POLITECNICO
DI TORINO

UNIVERSITÀ
DEGLI STUDI
DI TORINO

DOCTORAL THESIS

A Windblown Sand Transport Model for Large-Scale Industrial Applications

Candidate:
Roberto NUCA

Academic Supervisor:
Prof. Luigi PREZIOSI

Industrial Supervisor:
Dr. Nicolas COSTE

A thesis submitted in fulfillment of the requirements for the degree of Doctor of Philosophy in Pure and Applied Mathematics (XXXIII cycle)

in the framework of the

European Industrial Doctorate project SMaRT
(Sand Mitigation around Railway Tracks)

May 13, 2021

Declaration of Authorship

I, Roberto NUCA, declare that this thesis titled, "A Windblown Sand Transport Model for Large-Scale Industrial Applications" and the work presented in it are my own. I confirm that:

- This work was done wholly or mainly while in candidature for a research degree at this University.
- Where any part of this thesis has previously been submitted for a degree or any other qualification at this University or any other institution, this has been clearly stated.
- Where I have consulted the published work of others, this is always clearly attributed.
- Where I have quoted from the work of others, the source is always given. With the exception of such quotations, this thesis is entirely my own work.
- I have acknowledged all main sources of help.
- Where the thesis is based on work done by myself jointly with others, I have made clear exactly what was done by others and what I have contributed myself.

Signed: 

Date: May 13, 2021

Acknowledgements

First and foremost, I would like to express my heartfelt gratitude to my supervisors, prof. Luigi Preziosi[1] and Dr. Nicolas Coste[2]. I thank Luigi for his continuous guidance, support, and patience throughout these years. I thank Nicolas for teaching me a lot of practical knowledge about high performance computing in industry.

I would like express my gratitude to Dr. Andrea Lo Giudice[2], my colleague and friend. Our constructive discussions, his valuable suggestions and thoughtful comments have helped for the completion of this work and for my growth as scientist.

Last but not least, I would like to thank all member of the project, prof. Luca Bruno[3] for the management of the project, prof. Giles Wiggs[4] from Oxford University for the opportunity to familiarize myself with the topic of Geomorphology. Dr. Eric Delboulbe[2] and Dr. Sami Khris[2] for all the effort and time provided to me during the industrial secondment at Optiflow Company, my colleagues Dr. Lorenzo Raffaele[3], Marko Horvat[3] and Ciaran Nash[4].

The research for the PhD has been carried out within the project: "Sand Mitigation around Railway Tracks" (SMaRT). The SMaRT project was conducted in the framework of Marie Skłodowska-Curie Actions (MSCA), Innovative Training Networks (ITN), European Industrial Doctorate (EID), call H2020-MSCA-ITN-2016 (www.smart-eid.eu). The project received funding from the European Union Horizon 2020 research and innovation program under grant agreement No721798. The consortium included partner organizations Ansaldo STS, Astaldi, Salcef group, whose contribution is highly appreciated.

Computational resources, without which the research would not have been possible, were provided by Optiflow Company and HPC@POLITO, a project of Academic Computing within the Department of Control and Computer Engineering at Politecnico di Torino (http://www.hpc.polito.it).

[1]Department of Mathematical Sciences "G.L. Lagrange", Politecnico di Torino, Torino, Italy
[2]Optiflow company, Marseille, FR
[3]Department of Architecture and Design, Politecnico di Torino, Torino, Italy
[4]Department of Geomorphology, University of Oxford, UK

Contents

Chapter 1

Introduction

1.1 Motivations

Describing and modeling aeolian sand transport is very challenging because of the presence of many contributing and influencing phenomena. Its study is not only interesting from the pure scientific viewpoint but it is also useful in several applications. Aeolian sand transport is naturally related to desert areas made up of sand because it modifies terrain morphology and it has a huge impact on surrounding flora and fauna. Furthermore, climate changes contribute to the formation of new arid area with consequent desertification. Therefore a correct understanding of this phenomenon and its modeling becomes interesting especially for environmental sciences applications. In fact, human actions over the natural environment in desert areas show up problems related to the effect of sand over artificial infrastructures such as buildings, agricultural fields, roads and railways. Many of these infrastructures cross very large desert areas and the interaction with sand is inescapable. The problem of sand with artificial infrastructure is a well known issue but its definitive solution is still far away from being found.

The development of mathematical models on aeolian sand transport and their numerical implementations is the main purpose of this dissertation because engineers need sufficiently advanced models to perform reliable numerical simulations and hopefully to design proper mitigation solutions.

In particular, in this framework my PhD fellowship was financed by European Commission under a project named SMaRT (Sand Mitigation Around Railway Tracks) with the aim of identifying proper mitigation measures to protect railways in desertic areas. In fact, the action of the sand over railways infrastructures in desert areas can be catastrophic for train traffic. The same problem is shared by coastal areas because the beach sand is moved by the wind action with a consequent interaction with surrounding natural and artificial structures.

Besides the industrial application a proper mathematical model for aeolian transport can help geomorphologists to analyze the physical mechanisms governing the formation of sand ripples and dunes motion on earth or even on other solid planets such as Mars. Moreover, it needs to be mentioned that the same methodology used in this thesis can be applied, with proper modifications, to similar contexts such as wind driven rain and snow transport, because they share several mathematical aspects.

1.2 Physical Phenomenon

Aeolian sand transport is the result of the physical interaction between wind and sand. In particular a cloud of sand particles is generated over the sand surface leading to a stream of sand in the mean wind direction. It is intrinsically a multiphysics and multiscale phenomenon because it involves both fluid dynamics and particles mechanics that can be treated at a continuum or discrete scale, i.e., describing the evolution of sand concentrations or sand particles. In addition, there are phenomena occurring at different time scales.

The wind driven cloud is the result of a complex chain of distinct physical events that involve the force exchanged between fluid and sand grains by means the pressure and viscous drag effect experienced by a solid immersed in a fluid in case of relative motion. In this phenomenon spatial and temporal aerodynamic scales plays a role at many level because it starts from the atmospheric flow, that acts on very large scales, down to the millimeter scale where the effect of turbulent fluctuations trigger the movement of grains (see Figure 1.1). Once that some particles are triggered the wind action transfers energy to them leading to a ballistic trajectory which can eventually trigger other particles when the grain hits the sandy surface.

Masses of sand interested by aeolian transport are composed by a relevant number of grains and each grain is microscopically different, though macroscopically similar. This simple observation suggests that one can expect to observe a stochastic behavior of occurring events. In a deterministic viewpoint each grain has its own unique shape therefore its aerodynamic behavior during the ballistic trajectory within the turbulent flow leads to different results in terms of trajectory. Moreover turbulence itself introduces stochastic fluctuations in the system. Ground impact properties are locally featured by the surrounding grains, therefore grain shapes an their arrangement characterize the result of a possible incoming grain impact. Last but not least, also air collisions are affected by both grain shape and flow status. Also the ground morphology at a medium/large scales has an remarkable effect on the physical system. Indeed it represents both the boundary for the fluid domain and a moving boundary that introduces/subtracts mass in the system.

The description above should be sufficient to justify the "multiphase" and "multiscale" adjective attached this physical phenomenon. The explorer and geologist Ralph Alger Bagnold was the first person to apply the scientific method to study in the 40s the aeolian sand transport and the mechanisms of dunes formation. He provided a robust documentation of this phenomenon at different spatial scales, emphasizing important aspects and remarkable physical fact. In his expeditions and tests he observed the physics of wind blown sand classifying physical features and measuring proper quantities. He collected all his discoveries in the monograph "The Physics of Blown Sand and Desert Dunes" [16] that is still a reference point today. He also proposed some models based on his measurements collected both in laboratory and wind tunnel. In this way he put the first brick for the theory of the windblown sand transport.

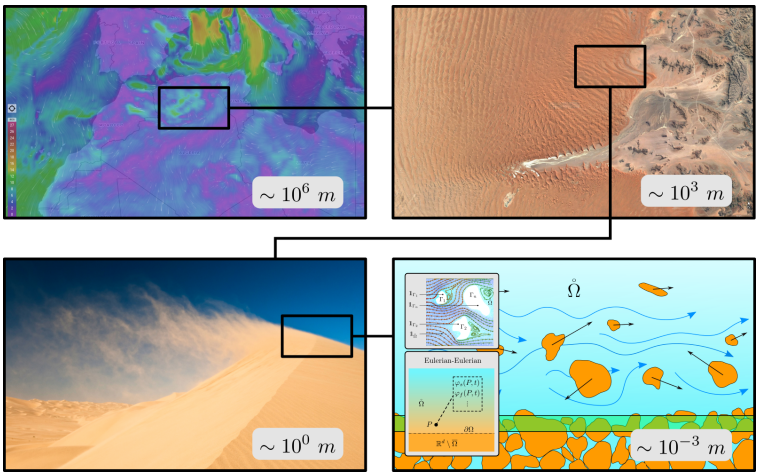

Figure 1.1: Aeolian sand transport viewed at different scales, from mesoscales to microscales.

1.3 Organization of the Dissertation

This dissertation is organized in six chapters. Chapter 2 contains a tailored reference to mixture theory and other mathematical modeling aspects that will be useful for the treatment of multiphase flows. Chapter 3 is a review of the state of the art of mathematical models applied to windblown particulate transport phenomenon. Chapter 4 contains a proposed mathematical model for the morphodynamic treatment of sand avalanches that can be integrated in the final multiphysics model. Chapter 5 describe the mathematical definition of a first order multiphase model by means of a data-driven approach. In the Chapter also two large scale industrial applications are simulated. Chapter 6 describe a particle-based model whose purpose is to catch fundamental physics of saltation dynamic. Its field of application is confined to hexahedral domains for scientific applications. Finally, in Chapter 7 the dissertation ends discussing future perspectives in this research area.

Chapter 2

Foundational Aspects

In this section we will briefly present some well known modelling aspects that will be useful in the following chapters.

2.1 Theory of Mixture Approach

The starting point in the model definition is the theory of biphasic mixtures ([13, 14], [21], [37–39], [162–164], [185, 188, 216]). This is one of the main approaches used to describe the macroscopic behavior of complex systems in which different continua interact at a microscopic level, which is one of the crucial points in modeling sand transport and erosion.

Using standard procedures of continuum mechanics based on balance laws, the following system of equations can be deduced in general

$$\frac{\partial \varphi_s}{\partial t} + \nabla \cdot (\varphi_s \mathbf{u}_s) = 0\,, \tag{2.1}$$

$$\frac{\partial \varphi_f}{\partial t} + \nabla \cdot (\varphi_f \mathbf{u}_f) = 0\,, \tag{2.2}$$

$$\rho_s \left[\frac{\partial}{\partial t}(\varphi_s \mathbf{u}_s) + \nabla \cdot (\varphi_s \mathbf{u}_s \otimes \mathbf{u}_s) \right] = \nabla \cdot \widetilde{\mathbb{T}}_s + \rho_s \varphi_s \mathbf{g} + \mathbf{m}_s^{\sigma}\,, \tag{2.3}$$

$$\rho_f \left[\frac{\partial}{\partial t}(\varphi_f \mathbf{u}_f) + \nabla \cdot (\varphi_f \mathbf{u}_f \otimes \mathbf{u}_f) \right] = \nabla \cdot \widetilde{\mathbb{T}}_f + \rho_f \varphi_f \mathbf{g} + \mathbf{m}_f^{\sigma}\,, \tag{2.4}$$

where the index s stands for the solid phase (sand) and f for the fluid phase (air). Furthermore, referring to the p-constituent

- ρ_p is the "true" density, i.e. the density of the material which is then used as p-constituent of the mixture;
- φ_p is the volume fraction, i.e. the volume occupied by the p-constituent over the total volume;
- $\mathbf{u}_p$ is the velocity;
- $\widetilde{\mathbb{T}}_p$ is the partial stress tensor;
- $\mathbf{g}$ is gravitational acceleration;
- $\mathbf{m}_p^{\sigma}$ is the momentum supply , also named internal body force or interaction force [37–39], and is related to the local interactions between the constituents across the interface separating them.

We refrain from writing the energy balance equation because we consider isothermal situations and phenomena for which thermodynamics is not relevant. Equations (2.3) and (2.4) can also be written in non-conservative form as follows

$$\rho_s \varphi_s \left(\frac{\partial \mathbf{u}_s}{\partial t} + \mathbf{u}_s \cdot \nabla \mathbf{u}_s \right) = \nabla \cdot \widetilde{\mathbb{T}}_s + \rho_s \varphi_s \mathbf{g} + \mathbf{m}_s^{\sigma} \,, \tag{2.5}$$

$$\rho_f \varphi_f \left(\frac{\partial \mathbf{u}_f}{\partial t} + \mathbf{u}_f \cdot \nabla \mathbf{u}_f \right) = \nabla \cdot \widetilde{\mathbb{T}}_f + \rho_f \varphi_f \mathbf{g} + \mathbf{m}_f^{\sigma} \,. \tag{2.6}$$

In addition, it is useful to write the usual balance laws for the mixture as a whole,

$$\frac{\partial \rho_m}{\partial t} + \nabla \cdot (\rho_m \mathbf{u}_m) = 0 \,, \tag{2.7}$$

$$\rho_m \left(\frac{\partial \mathbf{u}_m}{\partial t} + \mathbf{u}_m \cdot \nabla \mathbf{u}_m \right) = \nabla \cdot \mathbb{T}_m + \rho_m \mathbf{b}_m \,, \tag{2.8}$$

where

$$\rho_m = \rho_s \varphi_s + \rho_f \varphi_f$$

is the density of the mixture, and

$$\mathbf{u}_m = \frac{\rho_s \varphi_s \mathbf{u}_s + \rho_f \varphi_f \mathbf{u}_f}{\rho_m}$$

is the so-called mass average velocity, or simply mixture velocity. If the saturation condition

$$\varphi_s + \varphi_f = 1$$

holds, as in our case, adding the mass balance equations (2.1) and (2.2) gives

$$\nabla \cdot \mathbf{u}_c = 0 \,,$$

where

$$\mathbf{u}_c = \sum_p \varphi_p \mathbf{u}_p = \varphi_s \mathbf{u}_s + \varphi_f \mathbf{u}_f \tag{2.9}$$

is the so-called composite velocity.

Instead, summing up the momentum equations (2.3) and using (2.4) gives the momentum equation for the mixture (2.8) if one defines

$$\mathbb{T}_m = \widetilde{\mathbb{T}}_s + \widetilde{\mathbb{T}}_f - \rho_s \varphi_s (\mathbf{u}_s - \mathbf{u}_m) \otimes (\mathbf{u}_s - \mathbf{u}_m) - \rho_f \varphi_f (\mathbf{u}_f - \mathbf{u}_m) \otimes (\mathbf{u}_f - \mathbf{u}_m) \,,$$

where $\mathbf{u}_s - \mathbf{u}_m$ and $\mathbf{u}_f - \mathbf{u}_m$ are the so-called diffusive velocities, and, above all, if

$$\mathbf{m}_f^{\sigma} + \mathbf{m}_s^{\sigma} = \mathbf{0} \,. \tag{2.10}$$

Hence, the momentum supply appears in both the momentum equations with a different sign as should be for an interaction (action-reaction) force between the two constituents. It, then, represent the force exchanged between the solid and the liquid constituent. Its evaluation using particle-based approaches will be discussed in Chapter 2 on the basis of a stochastic Lagrangian model.

Remark 1 *When dealing with two constituents it may be convenient to consider the momentum equation for the mixture* (2.8) *in place of one of the momentum equation for the constituents. This is suggested for two reasons:*

- *It does not contain the interfacial term* $\mathbf{m}_p^\sigma$*;*
- *It is possible to perform experiments on the mixture as a whole in order to determine the stress constitutive equation. In fact, one can measure neither* $\widetilde{\mathbb{T}}_s$ *nor* $\widetilde{\mathbb{T}}_f$*, but only* $\mathbb{T}_s$*,* $\mathbb{T}_f$*, and* $\mathbb{T}_m$*, where* $\mathbb{T}_s$*, and* $\mathbb{T}_f$ *are the "true" stresses related to the constituents taken separately.*

2.2 Ensemble Average Approach

In order to understand in deeper details the origin of several terms characterizing the mixture model presented in the previous section, we here briefly report an alternative way to deduce them, using ensemble averaging. In fact, by a comparison of the different approaches, this procedure will allow to improve the understanding of some terms appearing in the equations posed in the previous section, e.g. the partial stresses $\widetilde{\mathbb{T}}_p$ and the interfacial force $\mathbf{m}_s^\sigma$ for which we are trying to identify the best constitutive equations. For instance, recalling Remark 1, the difference between $\widetilde{\mathbb{T}}_f$ and the constitutive equation for the fluid alone will be pointed out.

The ensemble average deduction is based on the following ideal procedure: consider a set of identical trials done on the same or similar specimens evolving according to the same initial and boundary conditions. At a certain time one observes if a particular position is occupied by the solid or the liquid component and measures there some physical quantities. Finally, distinguishing which component is found in that position, the averaged values are obtained by averaging the quantities over the number of trials having that component in the given position. In order to do that it is convenient to define an indicator function

$$H(t,\mathbf{x}) = \begin{cases} 0 & \text{if at time } t \text{ air is in } \mathbf{x}\ , \\ 1 & \text{if at time } t \text{ a sand grain is in } \mathbf{x}\ . \end{cases}$$

The average quantity

$$< H(t,\mathbf{x}) >= \varphi_s(t,\mathbf{x})$$

is the number of times we find that a sand material occupies the position $\mathbf{x}$ at time t over the number of trials, i.e. the solid volime fraction. Similarly,

$$< 1 - H(t,\mathbf{x}) >= \varphi_f(t,\mathbf{x})$$

is the fluid volume fraction.

In order to compute the average velocities, one has to use H or $1-H$ as weight functions to discriminate whether at time t the position $\mathbf{x}$ is occupied by sand or air,

measure the velocity of what is found there and divide by the number of measurements with that particular phase in $(t, \mathbf{x})$, that is

$$\mathbf{u}_s = \frac{< H\mathbf{u} >}{< H >}\,, \qquad \mathbf{u}_f = \frac{< (1-H)\mathbf{u} >}{< 1-H >}\,.$$

Similarly,

$$\mathbb{T}_s = \frac{< H\mathbb{T} >}{< H >}\,, \qquad \mathbb{T}_f = \frac{< (1-H)\mathbb{T} >}{< 1-H >}\,,$$

and so on.

The first step to deduce the model is to observe that $H(t, \mathbf{x})$ is a material variable. In fact, assuming no phase change, as it is true in the case of our interest, following the motion H will always assume the same constant value, 1 on the sand grain and 0 in air. This means that

$$\frac{\partial H}{\partial t} + \mathbf{u} \cdot \nabla H = 0\,.$$

Using the incompressibility of both constituents, $\nabla \cdot \mathbf{u} = 0$, and observing that averaging and differentiation are two independent operations that commute, one has

$$0 =< \frac{\partial H}{\partial t} + \mathbf{u} \cdot \nabla H >= \frac{\partial < H >}{\partial t} + < \nabla \cdot (H\mathbf{u}) > - < H \nabla \cdot \mathbf{u} >\,,$$

and, therefore,

$$\frac{\partial \varphi_s}{\partial t} + \nabla \cdot (\varphi_s \mathbf{u}_s) = 0\,.$$

Similarly, operating on $1 - H$, gives

$$\frac{\partial \varphi_f}{\partial t} + \nabla \cdot (\varphi_f \mathbf{u}_f) = 0\,.$$

So, one finds again the mass balances (2.1) and (2.2). The momentum equation for the solid component is derived by multiplying the momentum equation

$$\rho \left(\frac{\partial \mathbf{u}}{\partial t} + \mathbf{u} \cdot \nabla \mathbf{u} \right) = \nabla \cdot \mathbb{T} + \rho \mathbf{g}$$

by the indicator function and then averaging. Operating on the left hand side gives

$$< H\rho \left(\frac{\partial \mathbf{u}}{\partial t} + \mathbf{u} \cdot \nabla \mathbf{u} \right) > =< \rho_s \left[\frac{\partial}{\partial t}(H\mathbf{u}) + \nabla \cdot (H\mathbf{u} \otimes \mathbf{u}) - \mathbf{u} \left(\frac{\partial H}{\partial t} + \mathbf{u} \cdot \nabla H \right) \right] >$$

$$= \rho_s \left(\frac{\partial}{\partial t} < H\mathbf{u} > + \nabla \cdot < H\mathbf{u} \otimes \mathbf{u} > \right)$$

$$= \rho_s \left(\frac{\partial}{\partial t}(\varphi_s \mathbf{u}_s) + \nabla \cdot < H\mathbf{u} \otimes \mathbf{u} > \right)\,,$$

while operating on the right hand side gives

$$< H(\nabla \cdot \mathbb{T} + \rho \mathbf{g}) > = \nabla \cdot < H\mathbb{T} > - < \mathbb{T}\nabla H > + \rho_s < H > \mathbf{g}$$

$$= \nabla \cdot (\varphi_s \mathbb{T}_s) - < \delta_\sigma(\mathbf{x})\mathbb{T}\mathbf{n} > + \rho_s \varphi_s \mathbf{g},$$

where $\mathbb{T}\mathbf{n}$ is the traction vector at the interface σ between the solid and the fluid constituent ($\nabla H = \delta_\sigma(\mathbf{x})\mathbf{n}$), $\delta_\sigma(\mathbf{x})$ is the Dirac delta function across the solid-fluid interface and $\mathbf{n}$ is the outward normal to the solid constituent. Hence, one has

$$\rho_s \left[\frac{\partial}{\partial t}(\varphi_s \mathbf{u}_s) + \nabla \cdot (\varphi_s \mathbf{u}_s \otimes \mathbf{u}_s) \right] = \nabla \cdot [\varphi_s (\mathbb{T}_s + \mathbb{T}_s^{\Re})] - < \delta_\sigma(\mathbf{x})\mathbb{T}\mathbf{n} > + \rho_s \varphi_s \mathbf{g}, \tag{2.11}$$

where the following definition of Reynolds stress

$$\mathbb{T}_s^{\Re} := -\rho_s \frac{< H(\mathbf{u} - \mathbf{u}_s) \otimes (\mathbf{u} - \mathbf{u}_s) >}{\varphi_s} = \rho_s \frac{< H(\mathbf{u}_s \otimes \mathbf{u}_s - \mathbf{u} \otimes \mathbf{u}) >}{\varphi_s},$$

has been used. Similarly, multiplying the momentum equation by $1 - H$ and averaging gives

$$\rho_f \left[\frac{\partial}{\partial t}(\varphi_f \mathbf{u}_f) + \nabla \cdot (\varphi_f \mathbf{u}_f \otimes \mathbf{u}_f) \right] = \nabla \cdot [\varphi_f (\mathbb{T}_f + \mathbb{T}_f^{\Re})] + < \delta_\sigma(\mathbf{x})\mathbb{T}\mathbf{n} > + \rho_f \varphi_f \mathbf{g}, \tag{2.12}$$

where

$$\mathbb{T}_f^{\Re} := -\rho_f \frac{< (1 - H)(\mathbf{u} - \mathbf{u}_f) \otimes (\mathbf{u} - \mathbf{u}_f) >}{\varphi_f} = \rho_s \frac{< (1 - H)(\mathbf{u}_f \otimes \mathbf{u}_f - \mathbf{u} \otimes \mathbf{u}) >}{\varphi_f}.$$

Comparing (2.11) and (2.12) with (2.3) and (2.4), one obtains the following identifications

$$\widetilde{\mathbb{T}}_s = \varphi_s (\mathbb{T}_s + \mathbb{T}_s^{\Re}) = \varphi_s \mathbb{T}_s - \rho_s < (1 - H)(\mathbf{u} - \mathbf{u}_s) \otimes (\mathbf{u} - \mathbf{u}_s) >,$$

$$\widetilde{\mathbb{T}}_f = \varphi_f (\mathbb{T}_f + \mathbb{T}_f^{\Re}) = \varphi_f \mathbb{T}_f - \rho_f < H(\mathbf{u} - \mathbf{u}_f) \otimes (\mathbf{u} - \mathbf{u}_f) >,$$

and

$$\mathbf{m}_s^\sigma = -\mathbf{m}_f^\sigma = - < \delta_\sigma(\mathbf{x})\mathbb{T}\mathbf{n} > . \tag{2.13}$$

These relations emphasize the difference between $\widetilde{\mathbb{T}}_p$ and $\mathbb{T}_p$, which is assumed to be known from experiments on the single phase, and the meaning of the interaction force, included its action-reaction meaning. Though the same procedure can be repeated for the energy equation, we will not repeat it here because we are going to work in isothermal conditions.

2.3 Constitutive Equations

In principle, the above model holds both for the suspended sand and the packed sand in the sand bed. The main difference lies on the fact that in the former case there are no prolonged contact between sand grains, but possibly collisions. In the

latter case, one has continuous contacts between grains, though they may slide relative to each other giving rise to plastic-like phenomena, and there is the possibility to assume that the volume ratio in the sand bed is constant or at least nearly constant.

As already stated, one of the computational drawback of the *First Order Model* previously used was the remeshing step. This was needed because the model was only defined in the air and there are important deposition, erosion, and avalanching effects. Exploiting the fact that the basic *Second Order Model* is the same but with a constitutive equation that can change between the two regions we will discuss if and how we can get rid of the need of remeshing writing the model in a fixed domain with a well defined mesh that includes both the sand bed and air and identifying a constitutive model that can be used in transiting from one phase to the other.

As far as the second law of thermodynamics is concerned, it must be mentioned here that there is a basic question, well addressed in [69], [70], and [188], on whether the entropy inequality is valid for each constituent or only for the mixture as a whole. In mixture theory it is generally observed that entropy exchange can occur between the constituents, so while it is certainly true that the total entropy must be nondecreasing, the same thing may not be true for the single constituents (see [92–94], [162–164], [188], and reference therein). On the other hand, the ensemble average approach generates an entropy inequality for each constituent (see [69], [70], and references therein). Once this conceptual choice is done, classical methods of thermodynamics can be applied to deduce the form of the constitutive equations.

Most experiments are preformed using elastic solids in Newtonian fluids in isothermal conditions (see, for instance, [91]). Hence, also most models assume the fluid to be viscous or inviscid and the solid to be elastic. We will discuss this case in isotropic situation that are of our interest. We remark that, of course, a constitutive model for sand should include plastic phenomena because of relative motion of grains in the sand bed. However, this mainly occurs in the slidign layer when avalanching occurs. So, the idea is to treat the sand bed as plastic deformation where absent working in an elastic framework and then including avalanching as an external modulus determining the reshaping of the free surface.

Following thermodynamic arguments similar to the ones used by Crochet and Naghdi [59], Rajagopal and coworkers [60], [84], [189], [198], [210], one can distinguish in $\widetilde{\mathbb{T}}_s$, and $\widetilde{\mathbb{T}}_f$ a static and a dynamic component and study in detail the form of their constitutive equations for an elastic rubber-like solid constituent and a Newtonian liquid constituent in isothermal conditions under the assumption that the constitutive functions depend on

- the deformation gradient $\mathbb{F}$ of the solid,
- the volume fraction φ_s,
- the velocities of the constituents $\mathbf{u}_s$ and $\mathbf{u}_f$ and their gradients $\nabla\mathbb{F}$, $\nabla\varphi_s$, $\nabla\mathbf{u}_s$, and $\nabla\mathbf{u}_f$.

They concluded that $\widetilde{\mathbb{T}}_s$, $\widetilde{\mathbb{T}}_f$ and $\mathbf{m}_s^\sigma$ can only depend on

- the left Cauchy-Green strain tensor $\mathbb{B} = \mathbb{F}\mathbb{F}^T$,

- the velocity difference $\mathbf{u}_s - \mathbf{u}_f$,
- the rate of deformation tensors $\mathbb{D}_s$ and $\mathbb{D}_f$,
- the difference of the vorticity tensors $\mathbb{W}_s - \mathbb{W}_f$.

They suggest in the isotropic case the following expressions

$$\widetilde{\mathbb{T}}_s^{st} = -\varphi_s p\mathbb{I} + 2\rho_m \left[\left(\frac{\partial \Psi}{\partial I_B} + I_B \frac{\partial \Psi}{\partial \mathit{I\!I}_B} \right) \mathbb{B} - \frac{\partial \Psi}{\partial \mathit{I\!I}_B} \mathbb{B}^2 \right], \tag{2.14}$$

$$\widetilde{\mathbb{T}}_s^{dyn} = (\gamma_1 I_{D_s} + \mu_1 I_{D_f})\mathbb{I} + 2\gamma_2 \mathbb{D}_s + 2\mu_2 \mathbb{D}_f - c_1(\mathbb{W}_s - \mathbb{W}_f), \tag{2.15}$$

$$\widetilde{\mathbb{T}}_f^{st} = -\varphi_f p\mathbb{I} + \rho_m \varphi_f \frac{\partial \Psi}{\partial \varphi_f}\mathbb{I}, \tag{2.16}$$

$$\widetilde{\mathbb{T}}_f^{dyn} = (\gamma_3 I_{D_s} + \mu_3 I_{D_f})\mathbb{I} + 2\gamma_4 \mathbb{D}_s + 2\mu_4 \mathbb{D}_f + c_1(\mathbb{W}_s - \mathbb{W}_f), \tag{2.17}$$

$$\begin{aligned} \mathbf{m}_s^{\sigma} &= p\nabla\varphi_s - \rho_s \varphi_s \frac{\partial \Psi}{\partial \varphi_s}\nabla\varphi_s \\ &\quad + \rho_f \varphi_f \left(\frac{\partial \Psi}{\partial I_B}\nabla I_B + \frac{\partial \Psi}{\partial \mathit{I\!I}_B}\nabla \mathit{I\!I}_B \right) \\ &\quad - \varphi_f \varphi_s \widetilde{\mathbb{K}}(\mathbf{u}_s - \mathbf{u}_f), \end{aligned} \tag{2.18}$$

where Ψ is the Helmholtz free energy, I_B stands for the trace of $\mathbb{B}$ (i.e. the first invariant of $\mathbb{B}$) and $\mathit{I\!I}_B$ for the second invariant of $\mathbb{B}$

$$\mathit{I\!I}_B = \frac{1}{2}(I_{\mathbb{B}}^2 - \operatorname{tr}\mathbb{B}^2).$$

The presence of the same pressure term p in both constitutive models for the solid and the fluid and for the interaction force as well is due to the enforcement of the saturation constraint $\varphi_s + \varphi_f = 1$, implying (2.9), that in this case is convenient to write as

$$(\nabla\varphi_s)\mathbf{u}_s + (\nabla\varphi_f)\mathbf{u}_f + \varphi_s \nabla\cdot\mathbf{u}_s + \varphi_f \nabla\cdot\mathbf{u}_f = 0.$$

Considering that, for instance, $\nabla\cdot\mathbf{u}_s = I_{D_s} = \mathbb{I} : \mathbb{D}_s$ where : stands for the saturation product of tensors, one can then rewrite the last equation as

$$\nabla\varphi_s(\mathbf{u}_s - \mathbf{u}_f) + \varphi_s\mathbb{I} : \mathbb{D}_s + \varphi_f\mathbb{I} : \mathbb{D}_f = 0.$$

So, in the thermodynamic deduction involving Clausis-Duhem inequality, one need to add a term multiplied by a Lagrangian multiplier p that takes into account of the constraint above. So, one has

$$(CD) + p\left[\nabla\varphi_s(\mathbf{u}_s - \mathbf{u}_f) + \varphi_s\mathbb{I} : \mathbb{D}_s + \varphi_f\mathbb{I} : \mathbb{D}_f\right] \geq 0,$$

where CD stands for the classical formulation of Clausius-Duhem inequality. The term p is then identified as the interstitial pressure. Procedures that are standard in continuum mechanics then leads to Eqs.(2.14)–(2.18).

Assuming that the fluid is inviscid implies the drop of the dependency on the rate of strain tensor in the constitutive model, so that $\widetilde{\mathbb{T}}_s^{dyn}$ and $\widetilde{\mathbb{T}}_f^{dyn}$ vanish. This

means that we are left with the system

$$\widetilde{\mathbb{T}}_s^{st} = -\varphi_s p\mathbb{I} + 2\rho_m \left[\left(\frac{\partial \Psi}{\partial I_B} + I_B \frac{\partial \Psi}{\partial \mathit{I\!I}_B} \right) \mathbb{B} - \frac{\partial \Psi}{\partial \mathit{I\!I}_B} \mathbb{B}^2 \right], \tag{2.19}$$

$$\widetilde{\mathbb{T}}_f^{st} = -(1-\varphi_s) p\mathbb{I} - \rho_m (1-\varphi_s) \frac{\partial \Psi}{\partial \varphi_s} \mathbb{I}, \tag{2.20}$$

$$\begin{aligned} \mathbf{m}_s^{\sigma} = {} & p\nabla\varphi_s - \rho_s \varphi_s \frac{\partial \Psi}{\partial \varphi_s} \nabla\varphi_s + \\ & + \rho_f (1-\varphi_s) \left(\frac{\partial \Psi}{\partial I_B} \nabla I_B + \frac{\partial \Psi}{\partial \mathit{I\!I}_B} \nabla \mathit{I\!I}_B \right) + \\ & - (1-\varphi_s)\varphi_s \widetilde{\mathbb{K}} (\mathbf{u}_s - \mathbf{u}_f). \end{aligned} \tag{2.21}$$

We observe that, in this formulation, if we neglect the dependence of the Helmholts energy from $\mathbb{B}$, from (2.19) and (2.21) the momentum equation for the solid writes

$$-\varphi_s \nabla p - \rho_s \varphi_s \frac{\partial \Psi}{\partial \varphi_s} \nabla\varphi_s - \varphi_f \varphi_s \widetilde{\mathbb{K}} (\mathbf{u}_s - \mathbf{u}_f) = \mathbf{0}.$$

This leads to

$$\mathbf{u}_s = \mathbf{u}_f - \frac{1}{1-\varphi_s} \widetilde{\mathbb{K}}^{-1} \left(\nabla p + \rho_s \frac{\partial \Psi}{\partial \varphi_s} \nabla\varphi_s \right),$$

which gives the relationship for the class of models named *First Order Models*. So, most of the dynamics relays on the identification of the Helmholtz free energy. We can distinguish in it a part involving the invariants of $\mathbb{B}$ and another part that does not involve it, i.e.

$$\Psi = \Psi_{\mathbb{B}} + \Psi_{\varphi},$$

where, however, as we shall soon see, $\Psi_{\mathbb{B}}$ can still depend on the volume ratio. One easy form that is suggested in [84],[209], [210] is

$$\Psi = K(I_B - 3) + K' \left[\frac{1-\varphi_s}{\varphi_s} \ln(1-\varphi_s) + \chi(1-\varphi_s) \right], \tag{2.22}$$

where χ is called a mixing parameter, but, of course, this needs to be identified on the basis of experiment on sand. In the previous deliverable we discussed how and to what extent this can be done for the second term Ψ_{φ} using data on sand transport. We remark, however, that this implies that experiments are performed in a small volume ratio limit that does not hold when the sand is packed. So, when dealing with this case extra contributions may come out. In fact, constitutive models for granular materials are very complicated, even if one describes it as a monophasic continuum, i.e., neglecting the presence of air, mixture, or water.

The passage from sand transport in air to sand behaviour on the ground can be related to the dependency of the terms of the Helmholtz free energy that depend on the Cauchy-Green strain tensor $\Psi_{\mathbb{B}}$ on the volume ratio, represented by the term K in (2.22). Of course, we expect that this behaviour is highly nonlinear. It needs to vanish for small volume ratios and needs to blow up when the volume ratio tend to the close packing value φ_{cp}. In order to exploit the fact that the volume ratio of sand is nearly constant in the sand bed, one can work in the linear elasticity regime from

the close packing configuration, replacing $\mathbb{B}$ with the strain tensor $\mathbb{E}$. So, a possible idea is to work with a function K of the following type

$$K = \begin{cases} 0 & \text{if} \quad \varphi_s \leq \varphi_0 \,, \\ \dfrac{(\varphi - \varphi_0)^m}{(\varphi_{cp} - \varphi)^n} & \text{if} \quad \varphi_s > \varphi_0 \,, \end{cases} \tag{2.23}$$

where $\varphi_0 < \varphi_{cp}$ is the volume ratio at which the mechanical effects of close packing start being identifiable, m determines how they depart from zero and n how they tend to infinity when the volume ratio tends to close packing. The value of φ_0 is, however, close to the close packing one in order to maintain the validity of linear elasticity. In this respect we imagine that the value of m and n would have little influence on the outcome. So, as a first attempt we would have taken them equal to one (or two, if regularity issues showed up).

2.4 The Granular Kinetic Theory

One possible closure model for the constitutive terms presented in previous equations is the granular kinetic theory. This was derived from gas kinetic theory (see [48]) using the analogy between gas atoms/molecules with massive particles (e.g. sand grains). We report here the two-phase model proposed by Cheng and Colantoni [50] which is the basis of the *SedFoam* solver. This solver is implemented in the OpenFOAM framework. Therefore, it can be potentially interesting also for the *SMaRT* research activity.

The model resolves the multiphase flow both in the concentrated and diluted region of sediment transport because they consider both closures of particle stresses and fluid-particle interactions. For the turbulence modeling both $k - \varepsilon$ and $k - \omega$ closure are used. Authors developed and validated this model for water-sand mixtures. In particular they focused on the problem of momentary bed failure (or plug flow) under sheet flow conditions. However, the modeling approach is presented for general solid-fluid flows and the specific case of water is explicitly addresses when necessary.

These premises make this model interesting in the *SMaRT* context. However, as we shall see, some tests using *SedFoam* showed several issues when the solver is applied to physical conditions analogous to aeolian transport cases. Also the computational cost has proved to be too large for applications in large domains.

2.4.1 Inter-phase Momentum Transfer

We here limit ourselves to a comparison of the modelling with the terms presented in Section 2.3, also in view of the simulations that will be discussed at the end of this Chapter.

The inter-phase momentum transfer used in *SedFoam* considers dominant components, which are drag and buoyancy force. It can be expressed as

$$\mathbf{m}_s = \underbrace{-\varphi_s \beta(\mathbf{u}_f - \mathbf{u}_s)}_{(a)} + \underbrace{\beta \frac{\nu_{ft}}{\sigma_c} \nabla \varphi_s}_{(b)} + \underbrace{p \nabla \varphi_s}_{(c)} .$$

The terms (a) and (b) represent the drag forces by means the proportional coefficient β. In particular (a) models the average drag force due to mean velocity difference between fluid and particle. Instead (b) is the fluid turbulent suspension term. The last term (c) models the averaged buoyancy force. In [50] the authors remark that the correlation term between sediment concentration and fluid pressure is ignored in the turbulence averaged momentum equations. However, in the closure of eddy viscosity, the effect is included via buoyancy terms in the $k - \varepsilon$ equations. For the closure of β they suggest empirical formulas classically used in literature, switching between formulas with respect to the value of φ (see [50]). A comparison with (2.21) shows the following correspondence

$$\varphi_f \, \tilde{\mathbb{K}} \quad \longrightarrow \quad \beta \, \mathbb{I} \, ,$$

$$\rho_s \, \varphi_s \, \frac{\partial \Psi}{\partial \varphi_s} \quad \longrightarrow \quad \beta \, \frac{\nu_{ft}}{\sigma_c} \, ,$$

in addition to the assumption that the Helmholtz free energy does not depend on the invariants of $\mathbb{B}$.

2.4.2 Fluid Turbulence Model

In order to model the stress tensor of the fluid phase the authors write it as a sum of two components: a large-scale component $\mathbb{R}^{ft}$ (i.e. Reynolds stress) and a grain-scale component $\mathbb{R}^{g}$, which includes the viscous stress and an additional effect due to fluid-particle interaction at grain scale. However, they specify that this latter effect is then neglected. The considered formulation for the stress tensor reads

$$\mathbb{T}_f = \mathbb{R}_{ft} + \mathbb{R}^g = -\varphi_f p \mathbb{I} + \rho_f \varphi_f \left[2(\nu_{ft} + \nu_f) \left(\mathbb{D}_f - \frac{2}{3} \nabla \cdot \mathbf{u}_f \mathbb{I} \right) - \frac{2}{3} k_f \mathbb{I} \right]$$

that can be compared with the sum of (2.16) and (2.17).

The classical $k - \varepsilon$ formulation is modified because two additional terms are added to take into account the drag and buoyancy effect. It is important to remark that equations for k and ε are specifically studied for sand particles in water. Therefore, sand in air can eventually have completely different formulations. The k equation reads

$$\underbrace{\frac{\partial k}{\partial t} + \mathbf{u}_f \cdot \nabla k = \frac{1}{\rho_f} \mathbb{R}^{ft} : \nabla \mathbf{u}_f + \nabla \cdot \left[\left(\nu_f + \frac{\nu_{ft}}{\sigma_k} \right) \nabla k \right] - \varepsilon_f}_{\text{clean fluid}} \underbrace{- \frac{2\beta(1-\alpha)\varphi_s k}{\rho_f \varphi_f)}}_{\text{drag effect}} \underbrace{- \frac{\nu_{ft}}{\sigma_c} \frac{\partial \varphi_s}{\partial z} g}_{\text{buoyancy}} .$$

The transport equation for ε is made by analogy as classical turbulence modeling. It is interesting to remark the meaning of α, which is proposed to characterize to which

extent particles follow the fluid velocity fluctuations. This property can be quantified by the Stokes number. However, as Cheng and Colantoni themselves remarked, this turbulence model is tailored for water-sand flows. Therefore, its adaptation for air-sand flows is not immediate and needs to be studied. In particular, water and sand density are of the same order, instead sand and air differ of three order of magnitude. As we shall see in Section 2.4.5, we tried to apply the model in a sand-air case.

2.4.3 Particles Stress Closure

The particle stresses includes two components with different physical origin. For low to moderate sediment concentration the inter-granular interaction is assumed to be dominated by binary collisions. Hence, a closure based on kinetic theory is adopted. For large sediment concentrations, rather than binary collisions the inter-granular interaction is assumed to be dominated by enduring contact/frictional forces among particles. In particular, the authors assume that particle pressure and particle stress both consist of a collisional-kinetic component (subscript "sc") and a frictional component (subscript "sf"):

$$p_s = p_{sc} + p_{sf} \,,$$
$$\mathbb{T}_s = \mathbb{T}_{sc} + \mathbb{T}_{sf} \,.$$

The closure of the collisional-kinetic component is based on the kinetic theory of granular flow where particle stress and particle pressure are quantified by the granular temperature Θ, which is defined as one-third of the kinetic energy of particle velocity fluctuation. Analogously to the fluid turbulent kinetic energy k, balance equation of granular temperature can be derived, but a closure model is needed. Authors used a modified version of the original model which was derived for dry granular flow consists of smooth, slightly inelastic, spherical particles [112, 152]. The balance equation for granular temperature reads

$$\frac{3}{2}\left[\frac{\partial}{\partial t}(\rho_s \varphi \Theta) + \nabla \cdot (\rho_s \varphi \Theta \mathbf{u}_s)\right] = (-p_{sc}\,\mathbb{I} + \mathbb{T}_{sc}) : \nabla \mathbf{u}_s - \nabla \cdot \mathbf{q} - \gamma_s + J_{int} \,,$$

where $\mathbf{q}$ is the flux of granular temperature, γ_s is the dissipation rate due to inelastic collision and J_{int} is the production (or dissipation) due to the interaction with the carrier fluid phase. By means the granular temperature, the following closure formulas are used

$$\begin{aligned}
p_{sc} &= \rho_s \varphi_s \left[1 + 2(1+e)\varphi_s\, g_{s0}\right] \Theta \,, \\
p_{sf} &= \begin{cases} 0 & \varphi < 0.57 \,, \\ F\dfrac{(\varphi - 0.57)^m}{(0.635 - \varphi)^n} & \varphi \geq 0.57 \,, \end{cases} \\
\mathbb{T}_{sc} &= 2\,\mu_{sc}\,\mathbb{D}_s + \left(\lambda - \frac{2}{3}\,\mu_{sc}\right)(\nabla \cdot \mathbf{u}_s)\,\mathbb{I} \,, \\
\mathbb{T}_{sf} &= -2\,\mu_{sf}\,\mathbb{D}_s + \frac{2}{3}(\nabla \cdot \mathbf{u}_s)\,\mathbb{I} \,.
\end{aligned} \tag{2.24}$$

where g_{s0} is the radial distribution function, e is the coefficient of restitution during collision, μ_{sc} is the particle shear viscosity and μ_{sf} is the frictional viscosity. Notice also that the structure of (2.24) is the same as suggested in (2.23). Other terms are

detailed in [50] and involve a lot of coefficients and additional formulas coming from granular kinetic theory. They specifically claim that the kinetic contribution of particle stress is included, thus the sediment stress closure can be extended to very dilute conditions without an artificial cut-off, as discussed in [104]. Therefore, in principle, this modeling approach could be considered also for aeolian transport.

2.4.4 Interface representations

In aeolian transport the ground-surface region represents the most important spatial domain where multiphase physical interactions occur. In particular the air-side region close to the ground-surface identifies the spatial domain where sand cloud transport occurs. Figure 2.1 shows three schemes that emphasize spatial scales features of aeolian sand transport. Figure 2.1(a) focuses on the fluid-dynamics at the grain scale, Figure 2.1(b) on the smooth transition from a region with packed sand to a region with suspended particle and Figure 2.1(c) on the mathematical idealization of the sand as an Eulerian scalar field. Though modelling the sand-bed surface as a sharp interface holds its validity for simulation on the large scale, when one focuses on scales of the order of centimeters, or when the amount of flowing sand is not small, the thickness of the transititon layer might become relevant. This suggests that models taking care of the smooth transition from packed to dispersed phase, as the ones discussed above, might become of interest. Depending on the descriptive approaches for phases, numerical properties and techniques change.

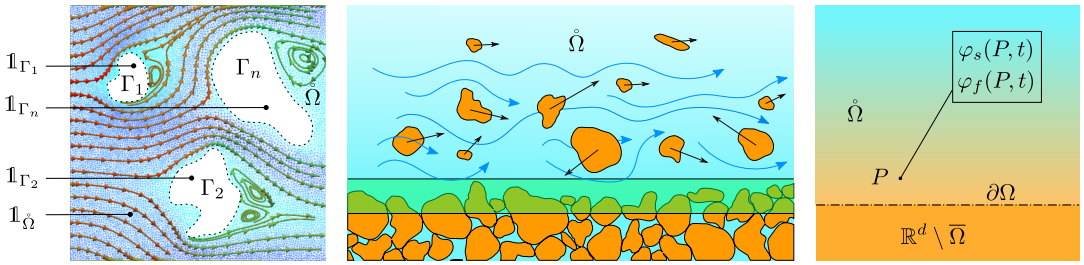

Figure 2.1: Schematic representation of the aeolian sand transport phenomenon: (a) flow around moving grains, (b) packed-to-dispersed transition near the sand bed (the green band represent the spatial region where the geometrical surface is contained and where the pneumatic conveying occurs) and (c) mathematical description of the sandy surface with sand transport in Eulerian models.

Explicit geometrical representation of the ground surface

One method to identify the ground-surface consists in an explicit geometric description of the surface using part of the boundary domain mesh. The boundary domain is splitted in different patches and some of them represent sandy surfaces where most of the phenomenon occurs. This approach has pros and cons, and in our research activity we figured out that there is a class of problems where this is feasible and others where this is not. Namely, this approach is convenient in scenarios where a complete phenomenological description on a large scale is desired. In this situation

the ground-surface is subjected to motion due to erosion-deposition effects, which generates the need to implement a proper mesh morphing algorithm to be included in the fully transient solver. This aspect leads to numerical problems of computational geometry: boundary mesh points need to be properly moved by the physical process and simultaneously preserve mesh quality of the geometrical description. Furthermore, internal mesh points have to be artificially moved as well. A description of practical implications due to this approach on complex real geometries is provided in Chapter 5.6.3.

The main advantage of an explicit ground-surface geometric description is the possibility to impose custom boundary conditions that take into account the wind-ground interactions. In Chapter 5 ad hoc formulations for solid phase boundary conditions are described. In general, they can be applied to *First Order Models* as well as *Second Order Models* depending on the boundary type. However, it is important to remember that a huge effort has been made into the fluid dynamics community in order to develop proper turbulence models and accurate boundary conditions over years. Things become even more difficult with the presence of a secondary phase into the leaden fluid, therefore the development of tailored wall functions from scratch could be very difficult and potentially inconclusive. A relevant advantage of the explicit ground surface description regards the computational cost if the remeshing step is applied occasionally. In fact, this approach completely neglects the spatial region under the soil. Therefore, no additional degrees of freedom are used to save in memory the computational description of steady sand.

For sake of completeness, we recall that an explicit representation of the ground surface calls for the inclusion of a module dealing with sand avalanching based on models developed in Chapter 4.

Implicit representation of the ground surface

The counterpart of the approach described above consists in the explicit representation of both phases over the entire range of concentration values without using an explicit geometric surface to define the sandy soil. In particular, the solid phase assumes the almost constant close packing value under the ground and it drops its value in just few millimeters changing its behavior from a viscoplastic fluid-like continuum constituent to a gas-like one. Therefore, in few computational cells the constitutive model has to drastically change its character. In particular, the entire wind-sand interaction that causes aeolian sand transport is controlled by the constitutive model of the differential system. This is the most relevant difference with respect to the geometric explicit representation where part of the phenomenon is delegated to the formulation of boundary conditions.

In the explicit geometric representation approach, the large interval of the solid phase concentration in a very small tubular region becomes a discontinuity. However, we have to account that OpenFOAM is a finite-volume-based computational platform, therefore, due to the intrinsic properties of the finite volume method, the sharp interface where the discontinuity occurs is naturally diffused. Mesh type and numerical fluxes drastically influence the final numerical solution leading to conditions where the distinction between numerical and modeling errors are not simply

discernible. From the computational point of view, avoiding mesh morphing represents an important advantage. However, the presence of high gradients for the concentration (and even fluid dynamic quantities such as k, ω and U_f) enforces to adopt an automatic mesh refiner to be able to practically obtain numerical solutions in a reasonable amount of time and with an acceptable numerical error where high gradients occur.

As already mentioned in the explicit geometric representation approach, in the extreme cases where no sand is transported in the air, the model should be able to recover the classical fluid dynamics for an incompressible fluid. In particular, all wall treatments for turbulence. A partial analogy can be found in the immerse boundary formulation where rigid walls are modeled by a Boolean function and the adopted constitutive model has to take into account the turbulence model (see [99]). Unfortunately, a proper knowledge transfer from this approach to the aeolian two-phase system requires a big effort in time and human resources, both for theoretical aspects and numerical implementation.

In order to highlight some numerical issues of *SedFoam* we tested two fundamental cases: The column collapse and the packing of a flat bed under sedimentation in water.

2.4.5 Sand column collapsing in water

The collapse of a sand column of granular material is a common test in the context of numerical models for granular materials (see [125, 146, 233] for numerical tests and [18, 148–150, 212] for experiments). Everything at the initial state is at rest and the dynamics is simply driven by gravity. Figure 2.2 shows six snapshots of the classical column collapse test. In order to reduce the numerical error as much as possible, the mesh is orthogonal and high order schemes has been adopted as suggested by the *SedFoam* developers. The ratio between fluid and solid density appears in the model formulation. Therefore, in order to keep the same order of coefficient values, we use water and sand, as done in [50] where *SedFoam* solver is presented. We can notice that immediately after the first iteration a numerical artifact appears on the top surface supplying a fake solid concentration. In real conditions we expect that the frictional actions among sand grains leads the column to a sort of cone until a critical angle is reached. In the simulation the process clearly proceed with unphysical states. We recall that the model involves multiple empirical coefficients that control numerical and modeling aspect of the simulation. Therefore, if they are set for a specific physical condition, they can eventually be not correct for others.

2.4.6 Sand sedimentation in air

The second test for *SedFoam* consists of simulating a homogeneous sedimentation until the equilibrium is reached starting from a non-critical condition (small perturbation of the equilibrium). The air density is almost a thousand time smaller than water density. Therefore, the model parameters drastically change the response of the model with respect to the water-sand behavior. We found only one converging configuration for air-sand mixture. Starting from a value of sand concentration close to the close packing value, the computation converges at each time step. However,

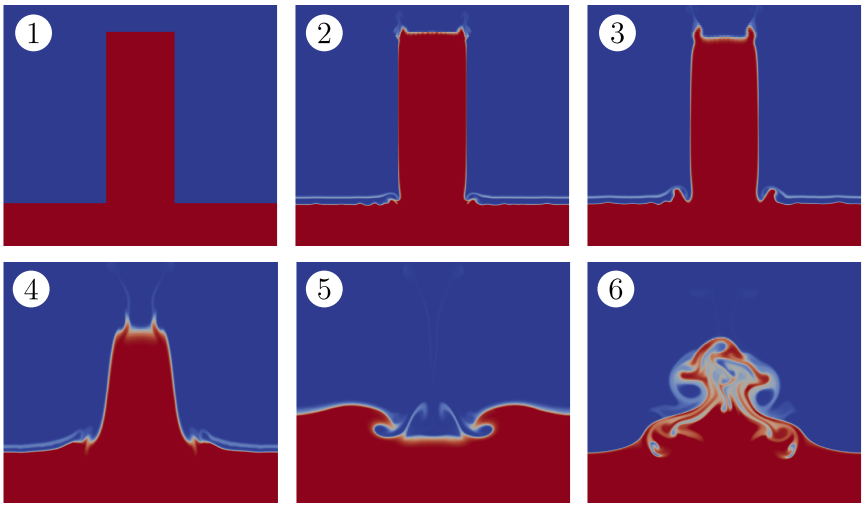

Figure 2.2: Testcase of the *SedFoam* solver in water-sand interaction, red is 0.4 (close packing concentration) and blue is 0. The column is $5cm$ height and $2cm$ width. (1) $t = 0$, (2) $t = 0.1s$, (3) $t = 0.5s$, (4) $t = 1s$, (5) $t = 1.5s$ and (6) $t = 3s$.

numerical oscillations appear just below the ground surface. In addition, a thin line of solid phase appears few centimeters above the ground similarly to the previous case of the sand column (see Figure 2.3).

These two previous test have been mainly performed to look at the computational capabilities of a second order solver in basic conditions. Even using two-dimensional cases and small domains the computational cost results too large for an application in large industrial domains. An adaptive mesh refinement algorithm appear to be necessary to reduce the overall computational cost. Furthermore, many numerical issues makes the model very tricky to set. These are the reasons why we proceeded with a surface morphing approach and a first order formulation. However, the *SedFoam* algorithm architecture is still very interesting for the second order model because it contains a splitting algorithm to solve the two momentum equation system. Further studies and tests have to be performed.

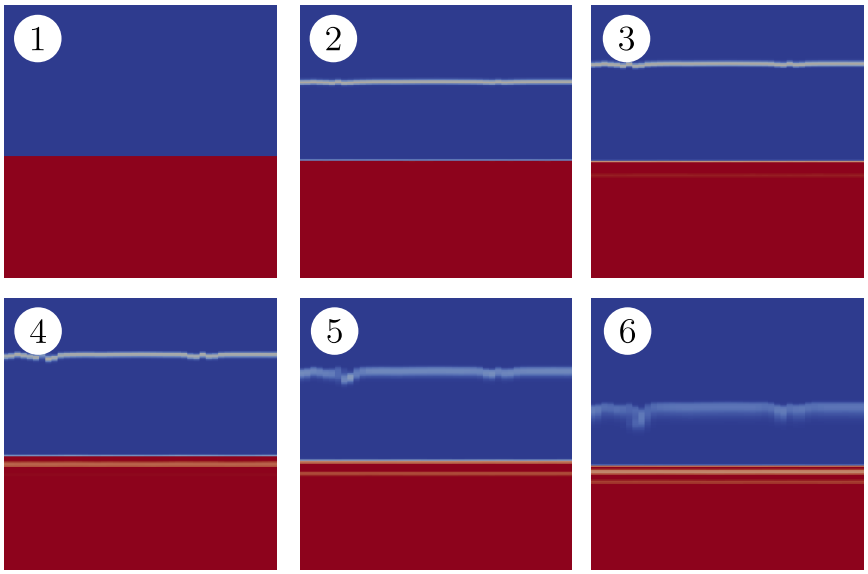

Figure 2.3: Air-sand packing test with *SedFoam* solver. The six images are separated in time of one tenth of second each other.

Chapter 3

Literature Review

The following content is based on the article [145] published during the initial period of the *SMaRT* research activity.

In this chapter the scientific literature which addresses mathematical models for the wind-driven particulate transport is resumed. The physical context of the reviewed models is not restricted just to the windblown sand, in fact other phenomena are included in the study such as rain and snow because their mathematical formulations exhibit similarities.

3.1 Introduction

Particle transport by the wind is a phenomenon of interest for civil engineering projects, environmental problems, and industrial applications. In fact, transport and consequent deposition of snow and sand on streets, railways, highways, roofs, and buildings can cause serious problems in terms of operation conditions and damages. Similarly, heavy rainfall and hail can cause discomfort and damages as well. Looking at the phenomena involved in the transport of particulate materials lying on the ground, such as sand and snow, one can observe that a crucial mechanism is their lift-off from the ground. Different phenomena contribute to it and their relevance mainly depends on two factors: particle size and wind velocity profile close to the ground.

This triggering transport mechanism, named *saltation* ([129]), is a phenomenon that takes place if the *wall shear stress* τ on the ground surface generated by the blowing wind exceeds a shear threshold value τ_t. This threshold value strongly depends on particles properties such as size and on chemical interactions among them, in conjunction with environmental conditions such as humidity, size and wetting. As reported in [110], it is also affected by the local slope of the ground surface.

Referring to Figure 3.1, after lifting-off, the smallest particles are entrained in the wind flow and remain in suspension for a long period. On the other hand, bigger particles, whose aerodynamic behavior is also strongly affected by their shape, follow ballistic trajectories before impacting again on the ground, transferring momentum to other particles which are then ejected from the soil. In this way saltating particles are also able to displace particles that are too heavy to lift-off, and induce very short trajectories that trigger a transport phenomenon called *reptation* (mainly occuring in sand transport). Another process involving big particles is *creep*, that

consists in particle rolling and sliding on the surface made of other deposited particles.

Erosion and subsequent sedimentation of particles on the ground determine the evolution of the ground surface. This fact makes the mathematical problem a free-boundary value problem. In cases that are severe for snow but not so severe for sand, the particles on the surface slide down forming avalanches, that also contribute to the shaping of the surface of the sedimented particulate.

The quantification of such phenomena suffers from the difficulties in performing experiments both in controlled environments and in-situ. In fact, from the experimental point of view, the presence of particles in the air and the need to monitor and measure their properties make wind tunnel experiments more difficult and onerous. Such kinds of tests have been performed mainly for sand, snow, and rain (see for instance [117, 118, 120, 207, 240]). However, in-situ measurements can be very expensive and time consuming as well. So, even though experiments are fundamental to shed light on the physical phenomena involved, nowadays they are more and more supported by computational simulations, because they are characterized by a high flexibility and can provide affordable results. In fact, thanks to significant improvements in terms of computational performance obtained in the last decade and to the continuous development of new mathematical models, computational simulations have become a catchy tool for all the people interested in these processes and in particular in testing civil and industrial applications. The interest is confirmed by the trend of integrating the dynamics of sand, snow, and rain in Computational Fluid Dynamics (CFD) commercial codes. Some examples of such CFD approaches are listed in [213] for snow and [28] for rain.

As usual, in dealing with pheomena involving many different phenomena a balance between modelling accuracy and simplicity is required and the choice mainly depends on the level of detail required by the specific application. In fact, on the one hand using over-simplified models may lead to unsatisfactory results compared to experimental data, though in particular situations they might show a qualitative agreement with the real natural phenomenon of interest. On the other hand, including more details leads to an increase of the complexity of the model, and consequently of the computational cost. In this respect, starting from the engineering needs of modeling the fall and transport of snow, sand, and rain, the aim of this review is then to describe and classify the different modelling approaches that have been proposed in the literature possibly mentioning their advantages and disadvantages.

The fundamental requirement of models dealing with particulate transport is their ability to accurately treat the wind dynamics in a very high Reynolds number regime and in a domain characterized by the presence of bluff bodies, like obstacles and infrastructures in general. Commonly, this is done by means of Navier-Stokes equations with suitable turbulence closure, e.g., Reynolds Average Navier Stokes equations (RANS), Large Eddy Simulation (LES) and Lattice Boltzamn models. Another key modelling aspect consists in how the interaction of the wind with the dispersed particles is described possibly with the modifications of the fluid dynamics

model because of the presence of dispersed particles. Following this modelling feature one of the classifications that we will use to review the literature is based on the coupling level [73, 74], namely, models with *1-way coupling* deal only with the influence of the flow on the particles, while models with *2-way coupling* take care of the mutual interactions. Finally, models with *4-way coupling* take also into account the effect of collisions between particles.

The difficulties in describing the dispersed phase (that can be solid in the case of sand and snow or liquid if small droplets are considered) arise because of the large number of particles transported, of the different shapes and sizes of each particle, of their interactions with walls, of the microscale description of the deposit, of the consequent large scale accumulation, and of the interactions between phases in terms of momentum, mass and energy. If the trajectories of each particles is described, then one has an approach that is here named *Lagrangian*. Alternatively, if the dispersed phase is described as an immiscible constituent of the air-solid (or air-liquid) mixture one has an approach that is named *Eulerian*. Turbulent dispersed multiphase flow approaches are described in [17].

As explained at the beginning of Section 3.3, in the fully Eulerian case a further classification can be done on the basis of the type of balance equations (mass and/or momentum) used for the dispersed phase. So, the plan of the review is as follows. In the next section we will first describe how wind, i.e. the driving flow, is classically modeled using computational fluid dynamics approaches, because this is shared by almost all the multiphase models presented. Then, in Section 3.3, we will focus on the dispersed particulate, listing the physical processes involved that need to be modeled. We will discuss separately Eulerian and Lagrangian approaches, analyzing the modeling strategies presented for all the physical processes mentioned above and, whenever possible, we will draw links between models and applications in order to highlight analogies and common features.

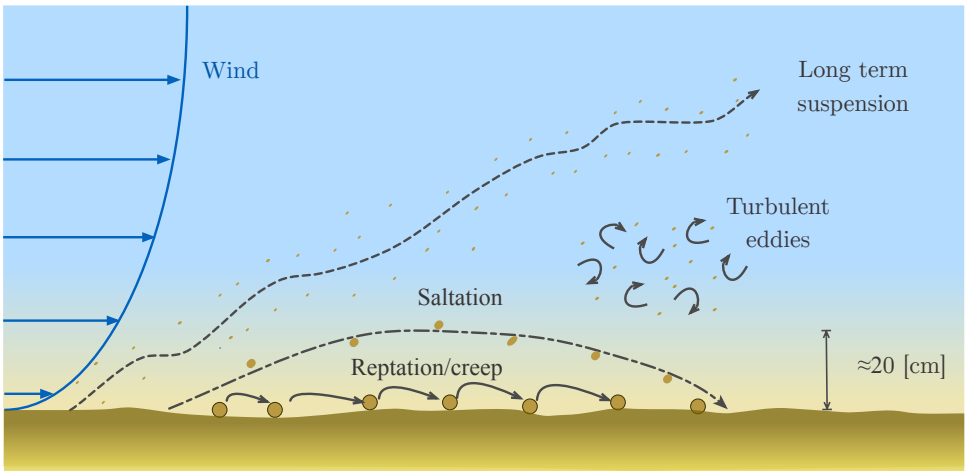

Figure 3.1: Schematic representation of different wind-driven transport modes: reptation/creep, saltation, suspension, and turbulent dispersion.

3.2 Wind flow modeling

The transport process of particulates takes place in the lowest atmosphere, namely the Atmospheric Boundary Layer (ABL), in a highly turbulent regime. Also commonly referred as Atmospheric Surface Layer (ASL), it just extends up to few meters above the ground and its dynamical structure is mainly influenced by the upper mixed layer, linked itself to the inversion layer reaching the geostrophic part, to finally form the planetary boundary layer. These ASLs represent only a small part of the planetary boundary layer and its highly turbulent character is mainly dominated by high gradients of the variables such as velocity, temperature, or moisture occurring in the mixed layer. Moreover, the shape and the properties of the ground surface affects not only the mean velocity profile, but also the level of turbulent fluxes. With the assumption that the ASL is a constant turbulent flux layer, in [160], [42] and [72] a similarity theory was derived, allowing to express the mean profile of different quantities as a function of the turbulent fluxes, the aerodynamic roughness of the ground, and a correction factor depending on a dimensional length scale describing the thermal state (stable, neutral, or unstable).

As reviewed in [27], in the last decade there was an increasing scientific effort in developing improved CFD models to describe the ABL in the computational wind engineering framework with dedicated attention to the roughness treatment. However, as shown in [29] the simulation of pure air in a neutral ABL requires a particular care.

In addition, as can be easily understood, the accurate reproduction of the driving flow plays a crucial role to achieve a reliable simulation of the behavior of wind-blown particulates both at a quantitative and at a qualitative level. Generally speaking, for a flat ground surface and assuming that thermal stratification plays a secondary role, it is known that the equilibrium mean velocity profile takes the following logarithmic expression

$$|\overline{\mathbf{u}}(z)| = \frac{u_*}{\kappa}\log\left(\frac{z+z_0}{z_0}\right), \tag{3.1}$$

where κ is the Von Karman constant ($\kappa \simeq 0.41$), and z_0 is the so-called roughness length. The parameter u_* in (3.1) is the *friction velocity* and represents the main bulk quantity to determine the erosion status. Close to the ground the *law of the wall* (see [123]) suggests that the velocity profile can be written in dimensionless form as

$$u^+ = \frac{1}{\kappa}\log(z^+) + B, \tag{3.2}$$

where $u^+ = \frac{u}{u_*}$, $z^+ = \frac{u_* z}{\nu_f}$, ν_f is the air kinematic viscosity and B is a constant. This expression holds true for $z^+ > 30$, in the so-called *logarithmic layer*. After a transitional regime for $5 < z^+ < 30$ called *buffer layer*, for $z^+ < 5$ the relation

$$u^+ = z^+ \tag{3.3}$$

holds. In this region, named *linear sublayer*, $\frac{\partial u}{\partial z} = \frac{u_*^2}{\nu_f}$. Therefore, by definition of wall shear stress

$$\tau = \mu_f \frac{\partial u}{\partial z}|_{z=0} = \hat{\rho}_f \, u_*^2 \, ,$$

where μ_f is the air dynamic viscosity, or

$$u_* = \sqrt{\tau / \hat{\rho}_f} \, .$$

However, in the presence of obstacles, this equilibrium profile is no longer valid and wind profile needs to be computed numerically, though some authors (for instance, [179]) try to avoid an explicit solution of wind velocity field applying small perturbation theories.

A more accurate fluid dynamics model would require to solve a set of conservation equations for air, usually restricting to mass and momentum balance. If the wind is treated as a one-constituent incompressible viscous fluid, then one has the classical *Navier-Stokes equations for incompressible flows*:

$$\nabla \cdot \mathbf{u} = 0 \, , \tag{3.4}$$

$$\frac{\partial \mathbf{u}}{\partial t} + \mathbf{u} \cdot \nabla \mathbf{u} = -\frac{1}{\hat{\rho}_f} \nabla p + \nabla \cdot [\nu_f (\nabla \mathbf{u} + (\nabla \mathbf{u})^{\mathrm{T}})] \, , \tag{3.5}$$

where $\mathbf{u}$ is the air velocity, and p is the pressure. On the right hand side, a momentum exchange term could be added to include the effect of the presence of particles. If particles laden wind is treated more realistically as a two-phase system (gas-solid or gas-liquid), it is useful to introduce the volume ratios φ_f and φ_s of air and of the dispersed phase, respectively. The mass and momentum conservation equations for the fluid flow then read

$$\frac{\partial (\hat{\rho}_f \varphi_f)}{\partial t} + \nabla \cdot (\hat{\rho}_f \varphi_f \mathbf{u}) = 0 \, , \tag{3.6}$$

$$\frac{\partial (\hat{\rho}_f \varphi_f \mathbf{u})}{\partial t} + \nabla \cdot (\hat{\rho}_f \varphi_f \mathbf{u} \otimes \mathbf{u}) = -\varphi_f \nabla p + \nabla \cdot [\mu_f \varphi_f (\nabla \mathbf{u} + (\nabla \mathbf{u})^T)] - \mathbf{f}_{drag} \, , \tag{3.7}$$

where $\mathbf{f}_{drag}$ is the interaction force between air and dispersed particles. Analogous equations should be written for the dispersed phase, as we will see in Section 3.3. This approach is more accurate but at the same time computationally more onerous. For this reason it has been rarely adopted for windblown particles models (for instance [34] for snow, GKT models in Section 3.3.1 for sand). Similarly, a complete Direct Numerical Simulation (DNS) of the incompressible Navier Stokes equations or of the mixture model is impossible for problems of engineering interest. In fact, practical problems typically involve highly turbulent separated flows in very large domains, requiring the use of unfeasibly small time steps and space discretization grids. Consequently, to describe the turbulent flow two different approaches are mainly used, either *Reynolds Average Navier Stokes equations* (RANS), or *Large Eddy Simulation* (LES). The choice between them depends on the particular application and on the level of detail required. For the sake of simplicity, we will briefly present these approaches for Eqs. (3.4)–(3.5), also because most of the models presented use

them for the fluid phase and refer to [229] for a more detailed treatment on Reynolds Average turbulence models. We also refer to works in which turbulent quantities equations present additional terms in order to introduce turbulence modulation due to the presence of a dispersed phase.

3.2.1 RANS approach

One way to simulate turbulent flows is to use a statistical approach consisting in splitting each quantity into mean (usually denoted with an overbar) and fluctuating component (usually denoted with a prime). For instance, referring to the velocity one has $\mathbf{u} = \overline{\mathbf{u}} + \mathbf{u}'$. Replacing them in Eqs. (3.4)-(3.5) and averaging over time one obtains the RANS equations:

$$\nabla \cdot \overline{\mathbf{u}} = 0 \,,$$
$$\frac{\partial \overline{\mathbf{u}}}{\partial t} + \overline{\mathbf{u}} \cdot \nabla \overline{\mathbf{u}} = -\frac{1}{\hat{\rho}_f} \nabla \overline{p} + \nabla \cdot \left[\nu_f \left(\nabla \overline{\mathbf{u}} + \nabla (\overline{\mathbf{u}})^T \right) \right] - \nabla \cdot \mathbf{R} \,, \tag{3.8}$$

where $\mathbf{R}$ is the so-called *Reynolds stress tensor* with components

$$R_{ij} := \overline{u_i' u_j'} \,.$$

It is the only term containing fluctuating components and consequently the one carrying information about turbulence. Most of Reynolds stress models are based on the *Boussinesq eddy viscosity assumption*, which states that turbulent momentum transfer can be represented by a viscous tensor:

$$\mathbf{R} = -2\nu_t \overline{\mathbf{D}} = -\nu_t \left(\nabla \overline{\mathbf{u}} + \nabla \overline{\mathbf{u}}^T \right) \,,$$

where ν_t is the so-called *turbulent viscosity* and $\overline{\mathbf{D}}$ is the mean strain rate tensor. This assumption implies in particular that turbulence is considered isotropic. The turbulent viscosity can be obtained using different modeling approaches that can be mainly divided into two families: *one-equation* and *two-equations turbulence models*. The most popular one equation turbulence model consists in relating ν_t to the normal component of the velocity gradient by means of the so-called *mixing-length* l_m:

$$\nu_t = l_m^2 \left| \frac{\partial \overline{\mathbf{u}}}{\partial z} \right| \,,$$

where l_m can be expressed in terms of the turbulent kinetic energy k and the turbulent dissipation ϵ. One-equation models, however, generally fail to predict complicate flows, with flow-separation and high reversed pressure gradients. Two-equations turbulence models recover the turbulent viscosity in terms of two other variables (k and ϵ, or k and ω), whose evolution is determined by suitable transport equations that are discussed below.

k-ε model

The *standard k-ϵ model* introduced in [116] has been widely used because of its robustness and affordability. By dimensional analysis, it is possible to define

$$\nu_t = C_\mu \frac{k^2}{\epsilon} \,,$$

where k is the turbulent kinetic energy and ϵ is the turbulent dissipation. Consequently, transport equations for k and ϵ are written as

$$\frac{\partial k}{\partial t} + \nabla \cdot (k\overline{\mathbf{u}}) = \nabla \cdot \left[\left(\frac{\nu_t}{\sigma_k} + \nu_f \right) \nabla k \right] + P_k - \epsilon \ , \tag{3.9}$$

$$\frac{\partial \epsilon}{\partial t} + \nabla \cdot (\epsilon\overline{\mathbf{u}}) = \nabla \cdot \left[\left(\frac{\nu_t}{\sigma_\epsilon} + \nu_f \right) \nabla \epsilon \right] + \frac{\epsilon}{k} C_{\epsilon 1} P_k - \frac{\epsilon}{k} C_{\epsilon 2} \epsilon \ , \tag{3.10}$$

where C_μ, $C_{\epsilon 1}$, $C_{\epsilon 2}$, σ_k and σ_ϵ are model constants. This turbulence model has been widely used for the fluid phase transporting snow [25, 26, 34, 85, 211], sand [83, 118], and rain [133, 138, 178]. Different modifications have been proposed in order to overcome well known drawbacks of the standard model, such as the over-estimation of the turbulent kinetic energy. Examples are:

- *RNG k-ϵ* model [234], this model is derived normalizing the equations in order to include the effects of smaller scales. The normalization procedure also helps in defining the model constants;
- modification in [124], where the turbulent production term is modified in order to reduce its over-prediction where the fluid is strongly accelerated or decelerated. The strain-rate in the turbulent production term is replaced by the vorticity;
- *realizable k-ϵ model* [200], where the ϵ-transport equation is obtained from an exact transport equation of the mean-square vorticity fluctuation, and C_μ is no longer constant. It has been used in [240] and [107], resepctively for snow and rain transport.

In Section 3.3.1 we will report in more details two versions of k-ϵ model, derived in [165] and [171] in order to take into account the effect of the dispersed particles on turbulence. Another modified version for including turbulence modulation by particles has been proposed in [89].

k-ω model

In [228] it was suggested to use the *specific dissipation* ω instead of ϵ. In this case a dimensional analysis suggests to use

$$\nu_t = \frac{k}{\omega} \ .$$

The transport equation for ω then reads

$$\frac{\partial \omega}{\partial t} + \nabla \cdot (\omega\overline{\mathbf{u}}) = \alpha \frac{\omega}{\kappa} \mathbf{T}_f \cdot \nabla \overline{\mathbf{u}} - \beta\omega^2 + \nabla \cdot \left[\left(\nu_f + \nu_t \sigma_\omega \right) \nabla \omega \right] \ ,$$

where $\mathbf{T}_f = 2\mu_f \overline{\mathbf{D}}$ is the stress tensor, $\alpha = \frac{5}{9}$, $\beta = \frac{3}{40}$, $\sigma_\omega = \frac{1}{2}$. As k-ϵ models, different modifications of k-ω model have been proposed in order to improve its performance. The standard model has been for instance revisited in [227] by the Author himself, adding a closure coefficient and modifying the dependence of eddy viscosity on turbulence.

Another relevant version is the *Shear-Stress Transport (SST) k-ω model* presented in [156], successively revised in [157]. Basically, it consists in applying the k-ω model in the inner boundary layer smoothly switching to the k-ϵ model outside it. The kinetic energy production term is modeled by introducing a production limiter to prevent the build-up of turbulence in stagnation regions. Transport equations for k and ω read

$$\begin{cases} \dfrac{\partial k}{\partial t} + \nabla \cdot (k\overline{\mathbf{u}}) = \nabla \cdot [(\sigma_k \nu_t + \nu_f)\nabla k] + \tilde{P}_k - \beta^* k\omega \,, \\ \dfrac{\partial \omega}{\partial t} + \nabla \cdot (\omega\overline{\mathbf{u}}) = \nabla \cdot [(\sigma_\omega \nu_t + \nu_f)\nabla \omega] + \alpha \dfrac{\omega}{k} P_k - \beta\omega^2 + (1 - F_1)\dfrac{2\sigma_\omega}{\omega}\nabla k \cdot \nabla \omega \,, \end{cases} \tag{3.11}$$

where the definitions of the model coefficients can be found in [157].Different authors have preferred k-ω *SST* to k-ϵ models for its proven accuracy when the presence of obstacles induces flow separation and adverse pressure gradients (see for instance [157]). This model has also been used for sand transport in [182].

3.2.2 LES approach

The semi-empirical nature of RANS models requires the identification of several parameters, based on approximations obtained for specific flow classes. In addition, Reynolds average approaches are capable to evaluate mean wind-flow fields only. Conversely, Large Eddy Simulations (LES) solve most of the turbulence scales getting more information and accuracy, paying the cost of an increase in computational time and storage memory required. LES is based on spatial filtering of quantities, justified by energetic considerations done on the basis of Kolmogorov's theory of turbulence (see [131]). The filtering operation for a generic quantity $\varphi(\mathbf{x}, t)$ reads

$$\tilde{\varphi}(\mathbf{x}, t) = \int_\Omega \mathcal{G}(\mathbf{x}, \xi)\varphi(\xi, t) d\xi \,,$$

where $\mathcal{G}$ is the filter and Ω is the domain. Whence $\varphi(\mathbf{x}, t) = \tilde{\varphi}(\mathbf{x}, t) + \varphi'(\mathbf{x}, t)$, where $\varphi'(\mathbf{x}, t)$ represents subgrid scales. Filtered Incompressible Navier-Stokes equations read

$$\begin{cases} \nabla \cdot \tilde{\mathbf{u}} = 0 \,, \\ \frac{\partial \tilde{\mathbf{u}}}{\partial t} + \tilde{\mathbf{u}} \cdot \nabla \tilde{\mathbf{u}} = -\frac{1}{\tilde{\rho}_f}\nabla \tilde{p} + \nabla \cdot \left[\nu_f \left(\nabla \tilde{\mathbf{u}} + \nabla \tilde{\mathbf{u}}^T\right)\right] - \nabla \cdot \tau^s \,, \end{cases} \tag{3.12}$$

where $\tilde{\cdot}$ represents the filtering operation and τ^s is the so-called *subgrid stress tensor* with components

$$\tau^s_{ij} := \widetilde{u'_i u'_j} \,.$$

Analogously to RANS, τ^s_{ij} can be modeled guessing the effects of unresolved scales (Sub Grid Scales, shortened as SGS) and can be summarized by a viscous stress tensor using the so-called *subgrid viscosity* ν^{sgs}, hence

$$\tau^s = -2\nu^{sgs}\tilde{\mathbf{D}} = -\nu^{sgs}\left(\nabla \tilde{\mathbf{u}} + \nabla \tilde{\mathbf{u}}^T\right) \,.$$

The first way used to close the equation with an expression for ν^{sgs} is the *Smagorinsky SGS model* ([201]). Using dimensional analysis one can write

$$\nu^{sgs} = \epsilon^{1/3}(C_S \Delta_g)^{4/3} \,,$$

where C_S is the *Smagorinsky constant* and Δ_g is the spatial filtering length. Requiring local equilibrium of scales in inertial subranges (i.e., k production equal to dissipation):

$$P_k = 2\nu^{sgs}\|\tilde{\mathbf{D}}\|^2 = \epsilon \ ,$$

where

$$\|\tilde{\mathbf{D}}\|^2 = \sum_{ij} \tilde{\mathbf{D}}_{ij}^2 \ ,$$

whence:

$$\nu^{sgs} = \sqrt{2}\|\tilde{\mathbf{D}}\|(C_S\Delta_g)^2 \ .$$

LES approach has been used for windblown sand simulations, for instance in [139, 220, 239]. A more evolute model is the *dynamic SGS model*, developed in [87]. In this model C_s is no longer constant, but computed dynamically, getting a model applicable to a wider range of turbulent flow fields. This model was used in [215] to simulate saltating particles. A recent variant of the dynamic model developed in [108] was adopted in [106] for wind driven rain impacting building facades. Other models have been introduce along the years to improve the accuracy of the results. For instance Kobayashi et al. [127, 128] proposed the *coherent structure Smagorinsky model*, which is more robust with respect to the classical formulation because the Smagorinsky constant is always positive. This model has been used in [170] for Lagrangian simulation of snow transport. More details about Large Eddy Simulation for incompressible flow problems can be found in [192]. In the following we will omit $\bar{\cdot}$ and $\tilde{\cdot}$ for averaged or filtered velocity.

3.3 Dispersed phase modeling

The most important distinction that can be done to classify the type of models used to describe the dispersed phase is based on how the particulate is considered:

- In a *Lagrangian approach* each particle is followed along its trajectories;
- in an *Eulerian approach* the ensemble of particles is treated as a continuum dispersed in the air and its behaviour is described using mass conservation and momentum balance.

Considering that wind flow is always described from an Eulerian point of view, in the following the first approach is called *Eulerial-Lagrangian* while the second approach is called *Eulerian-Eulerian* or *fully Eulerian*.

The second distinction is relates to the type of equations solved to obtain particulate density and velocity. Accordingly, in this work we introduce the following categorization:

- *0^{th}-order models*: No equations are solved for the dispersed phase. Fluxes are computed using algebraic formulas based on empirical relations. This kind of models are used in simplified conditions;
- *1^{st}-order models* or *1-fluid formulation*: Mass and momentum balance equations are solved for the fluid phase, while only mass conservation equation is solved for the dispersed phase, which is considered as a passive scalar convected by

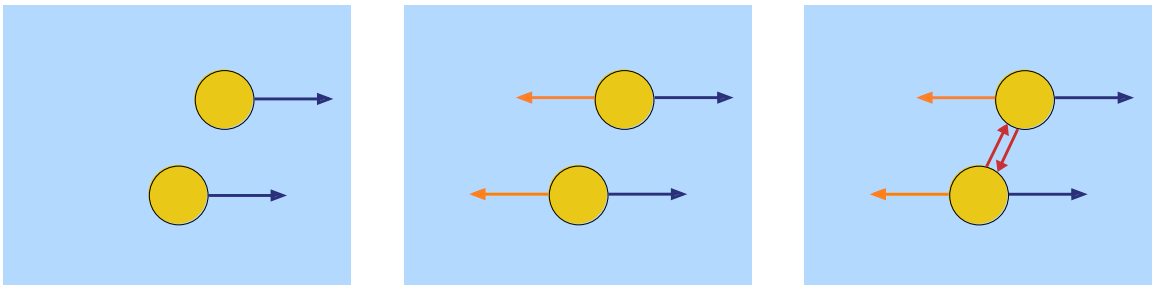

1-way coupling 2-way coupling 4-way coupling

Figure 3.2: Schematic representation of different degrees of coupling taken into account in the models. Blue arrows refer to the effect of the flow on the particles, orange arrows to the effect of the particles on the flow, red arrows to the effect of the interactions among particles.

air (carrying phase). Therefore, the velocity field of the dispersed phase is given by theoretical/empirical relations. This is a reasonable approach for highly-diluted flows, in which the dispersed phase is assumed to have the same velocity as the carrying phase. Alternatively, other terms are added in order to take into account of some differences in velocity fields (drift-velocity/slip velocity models);

- *2^{nd}-order models* or *2-fluid formulation*: Both mass and momentum balance equations for the dispersed phase are solved. Air and dispersed phase are coupled through interaction forces. These models are more difficult to be set up, due to the number of modeling parameters. Moreover, the computational costs are higher. Consequently they are not commonly used for the considered class of problems.

Furthermore, referring to Fig. 3.2, we will group the models according to the degree of coupling between wind-flow and dispersed phase. The approach mainly depends on the volume fraction of the dispersed phase and three different situations can be distinguished [73, 74]:

- *1-way coupling*: The wind field is used to compute the dispersed phase field which is treated as a passive scalar without any feedback on the flow. *0^{th}-order* and *1^{st}-order* models usually have this basic level of coupling;
- *2-way coupling*: The presence of the dispersed phase is taken into account in the computation of the wind flow. A *2-fluid formulation* is always *2-way coupled* because of the presence of coupling terms in the momentum equations;
- *4-way coupling*: Particle-particle interactions are considered as well as the particulate feedbacks on the wind flow.

Regarding wind-blown particulate transport, as we have previously mentioned, different physical mechanisms are involved and need to be taken into account. Most of the situations deal with particulate material settled on the ground which can start moving thanks to momentum transfer from the wind-flow to the particles by means of the wall shear stress. As we shall see in the following section, this process generates both erosion and deposition zones, as well as initializes particulate material drift at the ground, large air entrainment and transport.

3.3.1 Eulerian-Eulerian approach

Eulerian modeling of the dispersed phase was largely used for wind-blown snow, in order to predict erosion and deposition maps. From a mathematical point of view, whatever is the granular material considered, the modeling approach is the same. The advantage of an Eulerian-Eulerian approach mainly consists in the fact that it requires less computational resources compared to Lagrangian simulations, which were not even affordable years ago for industrial purposes. Very early attempts of predicting particulate mass drift were done computing physical quantities along a constant wind direction. These models used two-dimensional domains and the variables are computed along a vertical plane. Recently, they have been also used to model dune migration, avoiding to compute the real sand transport in the air. Liston et al. [141] considered a quasi-steady two-dimensional case; only saltation is considered using the empirical expression in [180] to get snow saltation flux Q_{sal} from the ground based on friction velocity (see Eq.(3.16) below). This idea was further developed in several other papers [7, 8, 71, 83, 175, 179, 194, 195, 239].In this work we do not describe such models in further details, because they do not explicitly solve for the transport of particulate in the air. The earliest attempt to obtain accurate deposition maps and snowdrift fields computing dispersed particle transport was done in the early nineties in [217]. In this model a diffusion equation for suspension transport is solved including a term accounting for the particle fall terminal velocity, while for the saltation flux a theoretical model based on friction velocity is employed. Wind flow fields are obtained by means of RANS approach with mixing-length turbulence closure. Erosion is computed using a heuristic expression for the saltation flux, while particle deposition is obtained assuming it to be proportional to the product of the density in the saltation layer and the settling velocity of particles. Erosion-deposition balance allows to compute the evolution of the ground surface. The model is then applied to both two-dimensional and three-dimensional cases with an assumed initial flat topography. Gauer [85] has proposed a two-layer model applied to more complicated topographies. His idea consists in dividing the domain in two zones: In one of them saltation is relevant, in the other one only suspension is considered. In the suspension layer an Eulerian-Eulerian approach with 1-way coupling is used. Wind flow fields are obtained by means of RANS k-ϵ model. In the saltation layer a 2-way coupling model is used, but the effect on turbulence due to the presence of particles is assumed negligible. Similarly, Naaim et al. [165] presented an Eulerian-Eulerian 1^{st}-order model with 1-way coupling based on mass conservation equations for fluid and dispersed phase separately, and a momentum equation for the mixture of air and particles, solved by RANS with a modified k-ϵ turbulence model, in order to considered the effect of the dispersed phase on turbulence. In particular, wind-blown particle transport is modeled distinguishing between saltation and suspension layer, yielding two different equations for particle concentrations, while a single momentum equation for the air-solid mixture. In a slightly different way, a single transport equation is used in [2] and [3] adding a saltation source term at the first cell centers above the ground. Bang et al. [19] and Sundsbø [206] paved the way to the use of *Volume Of Fluid (VOF)* for wind-blown particulate simulations, proposing a model of slip velocity between phases. Successively Beyers et al. [25, 26] presented an Eulerian-Eulerian 1^{st}-order model with 1-way coupling, in which the balance equations of mass and momentum are solved for the mixture. Suspension and saltation are modeled separately. The former is

described by a transport equation where the advection velocity is the sum of the velocity of the mixture and the slip velocity obtained using the drift flux model in [19]. More recently, Tominaga et al. [213] published a review of the CFD modeling of snowdrift around buildings. In the same work, they propose a model of wind-blown snow that solves suspension and saltation transport without distinguishing between them. It is an Eulerian-Eulerian 1^{st}-order model with 1-way coupling, that treats the fluid-phase by means of the RANS k-ϵ model used in [165], but with optimized additional terms based on experiments. After few years a modification of the same k-ϵ model was proposed in [171]. Similarly to the above models, Eulerian-Eulerian models for wind-blown sand were used in [113] and [182] using 1-way coupling approaches, taking into account saltation by means of suitable viscosity coefficents. The first Eulerian-Eulerian 2^{st}-order model with 2-way coupling was presented in [34]. Another novelty of this work is that two particle size distributions are simultaneously taken into account, leading to a significant improvement with respect to wind tunnel validation tests. Furthermore, Zhou et al. [240] presented a methodology that used the model in [213]. Based on meteorological data, the duration T of certain snow drifts is divided into n time windows. A steady solution is computed for each time-interval and the domain is modified and remeshed according to the resulting particulate drift.

Modeling wind interaction with the ground and particle interaction with the wind

Eulerian approaches require suitable models describing interaction phenomena with the ground, that is, erosion, saltation-suspension transport, and deposit, as well as the effect of particles on turbulence. The models dealing with such phenomena will be described in the following subsections. As already mentioned, continuum approaches have been largely used for snow drift-prediction. Therefore, most of the Eulerian dispersed particle models refers to snow. For this reason, part of the next subsections is done following the wind-blown-snow review [213], complementing it with the latest development and models related to different particulate materials.

Saltation and suspension transport modeling Mathematical models developed for mass transport of sand and snow always consider saltation, because it is responsible of most of the particulate transport. Conversely, suspension has been usually considered negligible, or has been treated separately. Just few models have a single equation for both transport modes. In particular, Eulerian dispersed particle transport was mainly modeled using *one-fluid approaches*, because particle velocity is not explicitly evaluated. The passive scalar transport equation models suspension transport, while saltation is often considered aside in a separated layer, or using empirical expressions at the first cell centers above the ground. One of the earliest models was presented in [217] where the *drift density* Φ_s ($[kg/m^3]$) was used as a transported scalar and it was assumed that the velocity of the dispersed phase is equal to that of the wind plus the particle-fall settling velocity. The transport equation then reads

$$\frac{\partial \Phi_s}{\partial t} + \nabla \cdot [\Phi_s(\mathbf{u} - u_w \mathbf{e}_z)] - \nabla \cdot (\overline{\Phi_s' \mathbf{u}'}) = 0 \,, \tag{3.13}$$

where u_w is the fall velocity considered constant and equal to the terminal settling velocity, while the turbulent diffusion term is modeled by means of Boussinesq's

approximation

$$\overline{\Phi_s' \mathbf{u}'} = \nu_t \nabla \Phi_s \ .$$

This approach was chosen in [193], [161], [213], and [240], even though in the last two articles saltation is included in the transport equation originally written for suspension transport. In a slightly different way Gauer [85] and Naaim et al. [165] distinguished between saltation and suspension layers applying respectively two different transport equations there. The former used a 2-way coupling in the saltation layer, while no particle feedback on the flow is considered in the suspension layer. The latter considered a transport equation inside the saltation layer which takes into account of particle-mass exchange between saltation and suspension layers. They also considered a term present in the transport equation for the suspension layer as well with the opposite sign, in addition to particle-mass exchange between flow and ground surface. The equation for the suspension layer then reads

$$\frac{\partial \Phi_s}{\partial t} + \nabla \cdot [\Phi_s(\mathbf{u} - u_w \mathbf{e}_z)] - \nabla \cdot (\nu_t \nabla \Phi_s) = \int_{\Sigma_{sal}} \mathbf{q}_{ex} \cdot d\mathbf{\Sigma} \ , \tag{3.14}$$

while that in the saltation layer is

$$\frac{\partial \Phi_s}{\partial t} + \nabla \cdot (\Phi_s \mathbf{u}) - \nabla \cdot (\nu_t \nabla \Phi_s) = \int_{\Sigma_{ground}} \mathbf{q}_{ground} \cdot d\mathbf{\Sigma} - \int_{\Sigma_{sal}} \mathbf{q}_{ex} \cdot d\mathbf{\Sigma} \ , \tag{3.15}$$

where $\mathbf{q}_{ex}$ is the exchange between layers (obtained by the balance between diffusive and settling flux), $\mathbf{q}_{ground}$ is the flow-ground exchange term, which is equal to the *erosion-deposition flux*, whose expression will be detailed in the next section, Σ_{sal} is the interface between saltation and suspension layer, and Σ_{ground} is the interface between ground and saltation layer.

Other Authors (e.g., [25, 26, 193, 217]) evaluated the saltation flux Q_{sal} at the first cell center above the ground, using empirical formulas based on the existence of a *treshold shear velocity* $u_{*,t}$ above which there is a saltation flux, or solving a balance equation. Different empirical formulations for the saltation flux Q_{sal} in a saturated saltation layer in equilibrium conditions have been proposed. Defining $(f)_+ = (f + |f|)/2$ the positive part of f, the most used are the following:

- [109] proposes

$$Q_{sal} = C \frac{\hat{\rho}_f}{g} \frac{u_w}{u_{*,t}} u_*^2 \left(u_* - u_{*,t}\right)_+ \ ,$$

  where C is an empirical constant

- [180] proposes

$$Q_{sal} = 0.68 \frac{\hat{\rho}_f}{g} \frac{u_{*,t}}{u_*} \left(u_*^2 - u_{*,t}^2\right)_+ \ . \tag{3.16}$$

The former was for instance used in [217], the latter in [141], [161] and [26] and was sometimes used to evaluate an inlet particles-drift profile, [25]. Gauer [85] modelled saltation with a 2^{nd}-order model with mass and momentum equations solved for the dispersed phase, using a scale analysis to simplify the expressions.

In the VOF and mixture theory framework, a transport equation similar to (3.14) has been proposed. The variable used is the dispersed volume fraction φ_s, and the velocity used to advect it is the mixture velocity $\mathbf{U}$ plus the relative velocity $\mathbf{U}_r$:

$$\frac{\partial \varphi_s}{\partial t} + \nabla \cdot [\varphi_s(\mathbf{U} + \mathbf{U}_r)] + \nabla \cdot (\overline{\varphi_s' \mathbf{U}'}) = 0 \,, \tag{3.17}$$

where the turbulent diffusion term is modeled again with Boussinesq's approximation and in [19] the relative velocity is

$$\mathbf{U}_r = \frac{d^2}{18\nu_f}(1-\varphi_s)\varphi_s\left(\frac{\hat{\rho}_s - \hat{\rho}_f}{\hat{\rho}_f}\right)\frac{1}{\varphi_s\hat{\rho}_s + (1-\varphi_s)\hat{\rho}_f}\nabla p \,,$$

where d is the mean diameter of the particles, approximated as spheres, $\hat{\rho}_s$ is the dispersed phase density. This transport equation was also used in [211], [25], [26]. Instead, in [2] and in [3] Eq. (3.17) was adapted for the Fractional Area-Volume Obstacles Representation (FAVOR) method, which defines obstacles within a fluid computational domain, like VOF. Moreover, they added the following source term S_{sal} accounting for saltation:

$$S_{sal} = \beta_{sal}\nabla \cdot \left[\varphi_s(1-\varphi_s)\mathbf{U}_r \frac{({u_*}^2 + {u_{*,t}}^2)(u_* - u_{*,t})}{{u_{*,t}}^3}\right] \,,$$

where $\beta_{sal} \in [0.15, 0.6]$. The model presented in [206] also started from Eq.(3.17) (without diffusion term) to model saltation, while for suspension the drift velocity is assumed to be inversely proportional to air turbulence, in order to have that the laminar regime gives the highest vertical fall velocity:

$$\mathbf{U}_r = \frac{\mu_f}{\mu_f + \mu_t} u_w \mathbf{e}_z \,,$$

where $u_w = 0.3[\frac{m}{s}]$. In the same spirt, Ji et al. [113] and Preziosi et al. [182] proposed a 1^{st}-order model similar to (3.17), in which the convective velocity is the fluid velocity $\mathbf{u}$ plus a vertical component due to gravity. Moreover, saltation is included in the transport equation assuming a diffusive effect due to particles collision inside the saltation layer. This is done using an effective viscosity ν_{eff} inserted in the mass conservation equation:

$$\frac{\partial \varphi_s}{\partial t} + \nabla \cdot [\varphi_s(\mathbf{u} - u_w \mathbf{e}_z)] - \nabla \cdot \left(\nu_{eff}\varphi_s^k \nabla \varphi_s\right) = 0 \,. \tag{3.18}$$

While the model in [182] is a 1-way coupling, the one in [113] is a 2-way coupling model, due to the presence of momentum-extraction term in the fluid phase momentum balance equation. In fact, on the basis of experimental data, the following form for the effective viscosity was proposed in [113]:

$$\nu_{eff} = \beta \delta_D u_w \,,$$

where $\beta = 0.217$ and

$$\delta_D = \frac{(k_0 u_*)^2}{2g}$$

is the length scale of the saltation layer thickness and

$$k_0 = 1 + 1.673\left(1 - \frac{d}{d_1}\right) ,$$

where $d_1 = 2.5 \cdot 10^{-4}[m]$ and d is the particle diameter ([166]).

Regarding the sedimentation velocity u_w, it can be classically calculated by the balance of drag and buoyancy forces and it strongly depends on the grain size (see, for instance, [88] or [78]). For small *particle Reynolds numbers*

$$Re_p := \frac{(1-\varphi_s)|u_s - u|d}{\nu_f} .$$

Stokes law gives:

$$u_w = \frac{(\hat{\rho}_s - \hat{\rho}_f)gd^2}{18\hat{\rho}_f\nu_f} . \tag{3.19}$$

Snow flakes certainly satisfy this regime. In case of *particle Reynolds numbers* in the range $[100, 1000]$ the sedimentation velocity is usually given in terms of the drag coefficient C_D

$$u_w = \sqrt{\frac{4}{3}\frac{(\hat{\rho}_s - \hat{\rho}_f)gd}{C_D\hat{\rho}_f}} , \tag{3.20}$$

where C_D can be approximated according to several experimental fittings (see, for instance, [9, 11, 20, 23, 62, 75, 78, 88, 177, 208, 224]). In particular, in [113] has been used the relation

$$C_D = \frac{24}{Re_p}(1 + 0.15Re_p^{0.687}) , \tag{3.21}$$

also suggested in [197]. In [182] it was observed that it is useful to plot the experimental relationship between particle Reynolds number and drag in terms of a relationship between the grain size and the particle Reynolds number, as shown in Fig.3.3. For sand close to the ground the particle Reynolds number is typically between 1 and 100, while, as already stated, for snow flakes it is well below 1. Hence, while for snow it is possible to use Stokes law (3.19) for sand it is hard to find an explicit relationship and one has to rely on the experimental curves, such as those given in [20]. A further observation in [182] regards the effective viscosity ν_{eff} defined as the sum of molecular viscosity, turbulent viscosity and a term related to collisions inside the saltation layer. Regarding this last term, it is observed that the behavior of the sand particles is isotropic. Hence, objectivity implies that ν_{coll} is a scalar isotropic function of the rate of strain tensor $\mathbf{D} = \frac{1}{2}(\nabla\mathbf{u} + \nabla\mathbf{u}^T)$. By the representation theorem of isotropic function, ν_{coll} can then only depend on the invariants of $\mathbf{D}$ in addition to the dispersed particles. However, since the flow can be considered as a perturbation of a shear flow in the vertical plane, the leading contribution is the second invariant $II_{\mathbf{D}} = \frac{1}{2}[(\mathrm{tr}\mathbf{D})^2 - \mathrm{tr}(\mathbf{D}^2)]$. For this reason, one can assume that $\nu_{coll} = \nu_{coll}(II_{\mathbf{D}}, \varphi_s)$.

Boutanios and Jasak [34] proposed a 2^{nd}-order model (2-fluid formulation) with a 2-way coupling, where there is no need to approximate the dispersed phase-velocity.

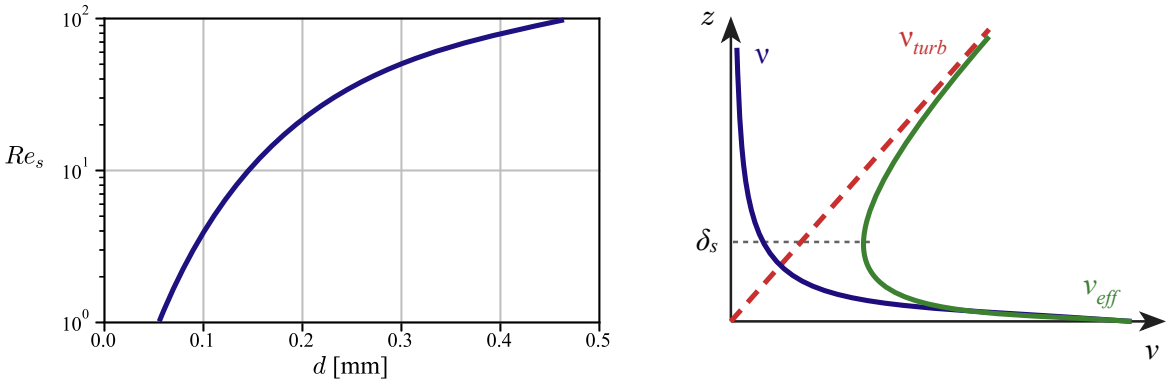

(a) (b)

Figure 3.3: (a) *Particle Reynolds number* as a function of the sand grains diameter of a sedimenting particles in air [182]. (b) Qualitative dependence of the diffusivity coefficient ν_{eff} on the distance from sand bed [182].

The conservation of mass and momentum for both phases read

$$\frac{\partial \hat{\rho}_k \varphi_k}{\partial t} + \nabla \cdot (\hat{\rho}_k \varphi_k \mathbf{u}_k) = 0 \,,$$

$$\frac{\partial}{\partial t}(\hat{\rho}_k \varphi_k \mathbf{u}_k) + \nabla \cdot (\hat{\rho}_k \varphi_k \mathbf{u}_k \otimes \mathbf{u}_k) = -\varphi_k \nabla p + \nabla \cdot (\varphi_k \mathbf{T}_k) + \hat{\rho}_k \varphi_k \mathbf{g} + (-1)^k \mathbf{m} \,,$$

where $k = 0, 1$ respectively for the fluid and the dispersed phase, $\mathbf{g} = -g\mathbf{e}_z$ is the acceleration of gravity, $\mathbf{m}$ is the momentum exchange term (with opposite sign in the two equations), $\mathbf{T}_f$ is modelled as a viscous stress tensor. Considering that the equations are written for two-dimensional cases corresponding to a vertical plane, the viscosity ν_s is obtained starting from momentum balance for two-dimensional fully-developed steady-state flow containing dispersed-phase bed particles in a control volume, getting

$$\nu_s = \frac{d}{6\epsilon_s}\frac{\partial p}{\partial x} + \frac{\tau_t}{2\hat{\rho}_s \epsilon_s} \,,$$

where ϵ_s is the rate of strain of the dispersed phase, x is the along-wind direction and $\tau_t = \hat{\rho}_s \varphi_s u_*^2$ is the threshold shear stress.

Saltation modeling If suspension has been neglected in some works ([141]), saltation is always taken into account, because it is the main cause of transport on the ground of snow or particles in general ([16], [129]).

Bed-surface evolution, erosion/deposit modeling Bed-surface changes due to erosion and deposition of granular material should be accurately reproduced in order to get a reliable morphodynamic evolution and mass-drift results. This aspect is relevant both for its influence on the aerodynamics and for the information it carries on the accumulation zones. Referring to Fig. 3.4, all models are based on a balance q_{net} between deposition q_{dep} and erosion q_{ero} fluxes, that is written either as

$q_{net} = q_{dep} + q_{ero}$ or as

$$q_{net} = \begin{cases} q_{ero} & \text{if erosion acts} \\ q_{dep} & \text{otherwise} \end{cases} .$$

Considering a cell laying on the bed surface, the height change in a time interval Δt is

$$\Delta z = \Delta t \frac{q_{net}}{A_{bed}\hat{\rho}_s} ,$$

where A_{bed} is the area of the ground-face of the cell considered. If $q_{net} > 0$ deposition occurs, otherwise the sand-bed is eroded.

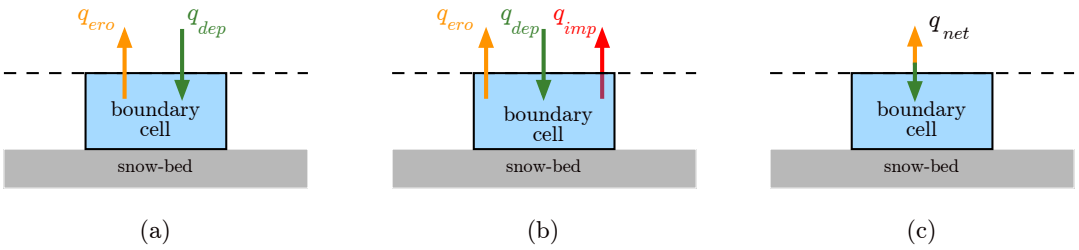

Figure 3.4: Schematic representation of different 1D models for erosion-deposition balance. (a) [217] and [182], (b) [25], (c) [165].

Several relationships have been suggested. For instance, referring to Fig. 3.4 (a), Uematsu et al. [217] proposed

$$q_{dep} = u_w \Phi_s , \tag{3.22}$$

$$q_{ero} = -u_w \frac{Q_{sal}}{u_{sal}\, h_{sal}} ,$$

where u_{sal} and h_{sal} are respectively wind velocity in the saltation layer and saltation layer height. Referring to Fig. 3.4c, Naaim et al. [165] suggested

$$q_{net} = \begin{cases} q_{ero} = C\hat{\rho}_f(u_{*,r}^2 - u_{*,t}^2) & \text{if } u_* \geq u_{*,t} \\ q_{dep} = \Phi_s u_w \dfrac{(u_{*,t}^2 - u_*^2)}{u_{*,t}^2} & \text{if } u_* < u_{*,t} \end{cases}$$

where $u_{*,r} = u_* - (u_* - u_{*,t})\frac{\Phi_s^2}{\Phi_{s,max}^2}$ and $\Phi_{s,max} = 0.248$ [Kg/m^3] for snow, recently used also in [205]. Referring to Fig. 3.4b, Beyers snd Sundsbø [25] computed fluxes differently and included a term taking into account of the *impinging flow* on the bed, so that the net flux is

$$q_{net} = q_{dep} + q_{ero} + q_{imp}$$

with

$$q_{dep} = u_w \Phi_s \left(\frac{u_{*,t}^2 - u_*^2}{u_{*,t}^2} \right)_+ ,$$

$$q_{ero} = -C\hat{\rho}_f(u_*^2 - u_{*,t}^2)_+ ,$$

$$q_{imp} = K u_p^n \Phi_s f(\alpha) ,$$

where C is a constant which represents the solid material pack bonding strength, K is another model constant, u_p is the flow velocity on the ground boundary cells, n is related to granular surface features, $f(\alpha)$ is a function of the flow incident angle α. Referring to Fig. 3.5, Beyers and Waechter [26] considered the mass balance equation

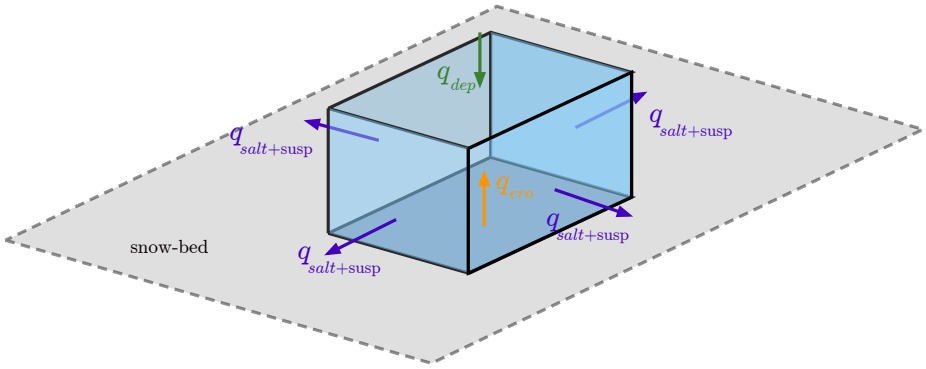

Figure 3.5: Schematic representation used in [26] to model erosion-deposition balance.

$$-q_{net} = \nabla \cdot (\mathbf{q}_{susp} + \mathbf{q}_{salt}) + q_{dep} + q_{ero} \ ,$$

where

$$\nabla \cdot \mathbf{q}_{susp} \approx \frac{\varphi_s z^{\beta}}{\ln \frac{z}{z_0}} \int_0^{z^{1-cell}} z^{-\beta} \ln \frac{z}{z_0} \, dz \, \nabla \cdot \mathbf{u}$$

with $\beta = \frac{u_w}{\kappa u_*}$ and it is stated that

$$\nabla \cdot \mathbf{q}_{salt} = \begin{cases} \dfrac{0.68 \hat{\rho}_f}{g} u_{*,t} \left(1 + \dfrac{u_{*,t}^2}{u_*^2}\right) \mathbf{t} \cdot \nabla u_* & \text{if } u_* > u_{*,t} \\ 0 & \text{otherwise} \end{cases} ,$$

where $\mathbf{t}$ is the direction of the flow. The quantities q_{dep} and q_{ero} are given by

$$q_{dep} = (u_{f,z} - u_w)\varphi_s - u_{wt}\varphi_s \ ,$$

where $u_{f,z}$ is the vertical component of fluid velocity and $u_{wt} = 0.4\sqrt{\frac{2}{3}k}$ is turbulent diffusion velocity, given by the isotropic turbulent velocity fluctuation approximation of the k-ϵ model, and

$$q_{ero} = -\rho_f C(u_*^2 - u_{*,t}^2) \ .$$

All the quantities are computed at the centers of the cells lying on the ground interface. Tominaga et al. [213] proposed to model erosion on a flat bed as a turbulent-diffusion process:

$$|q_{ero}| = \begin{cases} -\nu_t \left(\dfrac{\partial \Phi_s}{\partial z}\right)\Big|_{snowbed} & \text{if } u_* > u_{*,t} \\ 0 & \text{otherwise} \end{cases} .$$

This formula is used as a boundary condition for Φ_s (z is the vertical direction normal to the flat plane), computing q_{ero} by means of the empirical formula suggested in [4] for snow:

$$q_{ero} = -5 \cdot 10^{-4} \hat{\rho}_s u_* \left(1 - \frac{u_{*,t}^2}{u_*^2}\right) .$$

On the other hand, q_{dep} is modeled as in [217] (see Eq.(3.22)). A similar formula for the erosion flux was used in [182] on the basis of recent experiments reported in [102], [101] and [100], who proposed

$$q_{ero} = \frac{w_{ej} \alpha \hat{\rho}_f}{gd} \hat{\beta} \left(u_*^2 - u_{*,t}^2\right)_+ ,$$

where $w_{ej} = 0.5\ m/s$ is the *sand grain ejection velocity* evaluated experimentally in [102], [101], [100] and [58], α is a dimensionless free parameter to be fitted to experimental sand flux profiles, and

$$\hat{\beta} = A_H \sqrt{\frac{d}{g}} ,$$

where A_H is a model parameter depending of the physical properties of the granular material.

Erosion and deposition fluxes are almost always used in unsteady simulations to move the ground boundary or for domain re-meshing in order to have a boundary-fitted computational grid. Mesh-updating can take place at every time-step (as done in [25], [26], [213]), or when significant changes arise (as done in [165], [85]), because wind flow and particles-deposit evolve with different time scales. Another way used to take this difference into account is a quasi-steady procedure, that consists in computing a steady solution for the wind phase, which is then used to evaluate mass drift and modify the domain. This procedure is then repeated. In this framework, one of the most recent developments is a multi-time step domain decomposition method for transport problems proposed in [46].

Less recent studies adopted instead a fill-cell technique that consists in computing the amount of volume occupied by the dispersed phase in the ground boundary cells and to exclude them from the domain when they are filled ([141], [2], [3]).

Particle effect on turbulence In the suspension layer the concentration of particles is very low and the effect on turbulence is neglected in most of the articles. Naaim et al. [165] were the first to consider the influence of the dispersed phase on turbulence in a 1-way coupled model. They used a modified k-ϵ model ([49]) where the source terms

$$S_k = -\frac{2k}{t^*} 18 \mu_f \left[1 - \exp\left(-\frac{t^* \epsilon}{2k}\right)\right] \Phi_s \tag{3.23}$$

and

$$S_\epsilon = -\frac{2\epsilon}{t^*} \Phi_s \tag{3.24}$$

are respectively added to Eqs.(3.9) and (3.10) in order to take into account of the dissipative effect of the diluted phase. In Eqs. (3.23) and (3.24) $t^* = \frac{d^2 \hat{\rho}_s}{18 \mu_f}$ is the dispersed

particle relaxation time.

Tominaga et al. [213] used the same equations, but the additional terms were modified to:

$$S_k = -C_{ks} f_s \frac{k}{\hat{\rho}_s t^*} \Phi_s \,,$$
$$S_\epsilon = -C_{\epsilon s} \frac{\epsilon}{\hat{\rho}_s t^*} \Phi_s \,,$$

where C_{ks}, $C_{\epsilon s}$ are constants, and f_s is an exponential damping function. In Figure 3.6 the effect of the modified k-ϵ model on turbulent kinetic energy are shown. Okaze et al. [171] proposed a new k-ϵ modified model for particles dispersed in the wind. Particles are thought as moving obstacles and modeled using *vehicle canopy theory*, i.e. canopy model concept for moving obstacles (see [159]).

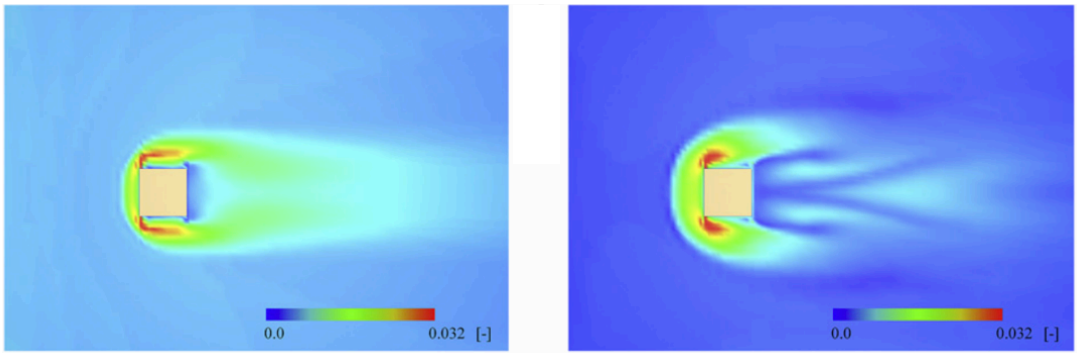

(a) (b)

Figure 3.6: Effects on turbulent kinetic energy by dispersed particles. Comparison between cases (a) wthout and (b) with k-ϵ model modifications ([213]).

Considering that the concentration of particles is higher in the saltation layer, the following modification (based on measured data) of standard rough wall functions is proposed in [25] (see also [29]):

$$u = \frac{u_*}{\kappa} \ln\left(\frac{z u_*}{\nu_f}\right) + B - \Delta B(k_s^+, s^+) \,, \tag{3.25}$$

where:

- $B = 5.5$ is an integration constant,
- $\Delta B(k_s^+, s^+) = \frac{1}{\kappa}\ln(1 + 0.3k_s^+ + 9,53s^+)$ represents the intercept of the profile, switched from the origin due to roughness height,
- $k_s^+ = \dfrac{k_s u_*}{\nu_f}$ is the so-called *dimensionless physical roughness height* or *roughness Reynolds number*,

- $s^+ = \dfrac{c_1 u_*^3}{2g\nu_f}$ is the additional parameter which models the effect of saltating particles, where c_1 is an empirical constant.

Defining:

- $z^+ = \dfrac{z_0 u_*}{\nu_f}$ the *dimensionless wall distance*,
- $u^+ = \dfrac{u}{u_*}$ the *dimensionless velocity*,

Eq. (3.25) can be written as $u^+ = \frac{1}{k}\ln(z^+) + B - \Delta B(k_s^+, s^+)$. Figure 3.7 shows the standard law proposed in [29] for different roughness regimes.

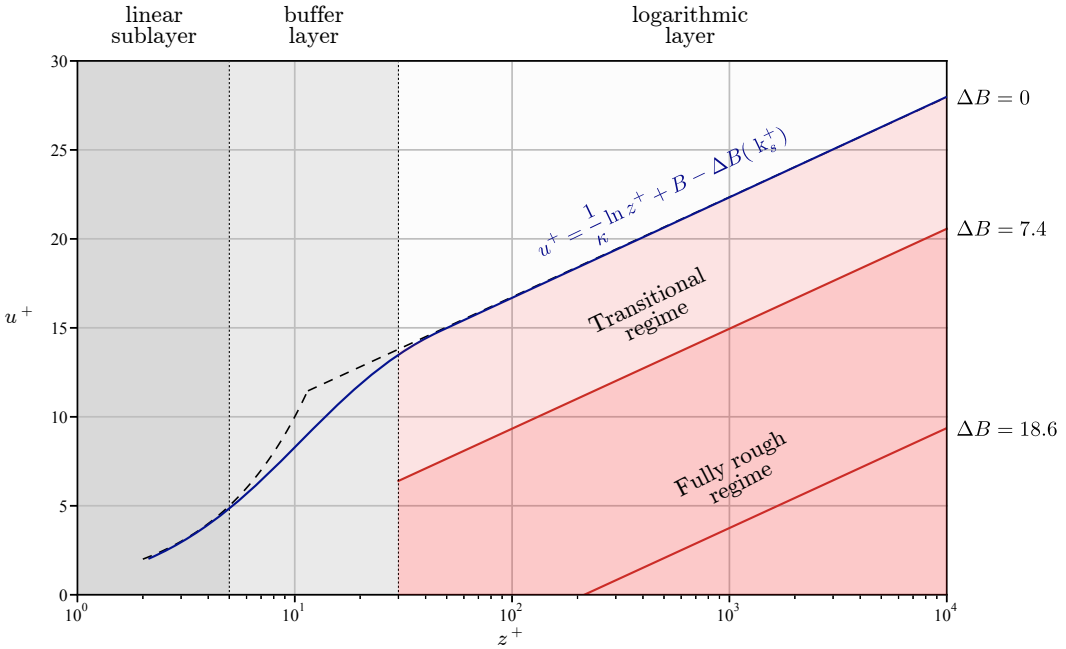

Figure 3.7: Wall function for fully rough surfaces proposed in [29].

Granular Kinetic Theory

A different Eulerian approach, called *Granular Kinetic Theory* (GKT) in analogy with the *Gas Kinetic Theory* [47], was proposed for dispersed particles multiphase simulations. The main idea of GKT consists in adopting a statistical and probabilistic approach to describe particle-particle interactions including both collision and friction, and random particles paths. In light of this approach, many quantities are introduced to describe sand dynamics. The most important one is the *granular temperature* that measures the energy level of the particle velocity fluctuations, which are then related to the air field by means of a turbulence model (generally a k-ϵ model). The *solid pressure*, that has the same meaning as pressure in gas standard models, describes the spherical component of the stress tensor for the dispersed phase. In this way, *GKT* models couple dispersed phase with carrying fluid behavior.

Specifically, Jenkins and Hanes [111] implemented a simple GKT model for a one-dimensional steady sheet flow focusing on a highly concentrated region of grains close to a sand bed, obtaining a qualitative good estimate of the erosion. The previous work was extended in [176] by implementing an extra term in the fluid momentum equation, following a modification suggested in [104]. They described an additional mechanism of suspension due to turbulence and *granular pressure gradient*. However, the results overestimated sand mass flux in comparison with experiments.

A further extension was proposed by Marval et al.[155] who considered slightly anelastic particle-particle collisions and incorporated an improved two-dimensional transient model with a frictional sub-model to describe the sustained contacts between particles. The simulation results provided a good estimate of mass flux in sediment transport layer.

To our knowledge, at present the latest extension of the model consists in a 2^{nd}-order model with 2-way coupling [151]. This type of models involves many equations and thermodynamic parameters, hence here we show the main equations only. Working under the *saturation assumption* $\varphi_f + \varphi_s = 1$, the mass and momentum balance equations for phases are:

$$\frac{\partial}{\partial t}(\hat{\rho}_s \varphi_s) + \nabla \cdot (\hat{\rho}_s \varphi_s \mathbf{u}_s) = 0 \,,$$

$$\frac{\partial}{\partial t}(\hat{\rho}_f \varphi_f) + \nabla \cdot (\hat{\rho}_f \varphi_f \mathbf{u}_f) = 0 \,,$$

$$\frac{\partial}{\partial t}(\hat{\rho}_s \varphi_s \mathbf{u}_s) + \nabla \cdot (\hat{\rho}_s \varphi_s \mathbf{u}_s \otimes \mathbf{u}_s) = -\varphi_s \nabla p - \nabla p_s + \nabla \cdot \mathbf{T}_s + \hat{\rho}_s \varphi_s \mathbf{g} + \beta(\mathbf{u}_f - \mathbf{u}_s) - \mathbf{F}_{Lift} \,, \tag{3.26}$$

$$\frac{\partial}{\partial t}(\hat{\rho}_f \varphi_f \mathbf{u}_f) + \nabla \cdot (\hat{\rho}_f \varphi_f \mathbf{u}_f \otimes \mathbf{u}_f) = -\varphi_f \nabla p + \nabla \cdot \mathbf{T}_f + \nabla \cdot \mathbf{T}_f'' + \hat{\rho}_s \varphi_s \mathbf{g} - \beta(\mathbf{u}_f - \mathbf{u}_s) + \mathbf{F}_{Lift} \,. \tag{3.27}$$

As mass and momentum conservation equation are present for both phases, then this model can be classified as a second order model. In the above equations

$$\mathbf{T}_s = \varphi_s \left[\mu_s \left(\nabla \mathbf{u}_s + (\nabla \mathbf{u}_s)^T \right) + \left(\lambda_s - \frac{2}{3} \mu_s \right) (\nabla \cdot \mathbf{u}_s) \mathbf{I} \right]$$

is the *solid stress tensor*,

$$\mathbf{T}_f = \mu_f \varphi_f \left[\left(\nabla \mathbf{u}_f + (\nabla \mathbf{u}_f)^T \right) - \frac{2}{3} (\nabla \cdot \mathbf{u}_f) \mathbf{I} \right] \,,$$

$$\mathbf{T}_f'' = \varphi_f \left[\mu_{t,f} \left(\nabla \mathbf{u}_f + (\nabla \mathbf{u}_f)^T \right) - \frac{2}{3} (\hat{\rho}_f k_f + \mu_{t,f} \nabla \cdot \mathbf{u}_f) \mathbf{I} \right]$$

are the *fluid stress tensors* and

$$\mathbf{F}_{Lift} = -\frac{1}{2} \hat{\rho}_f \varphi_f (\mathbf{u}_f - \mathbf{u}_s) \times (\nabla \times \mathbf{u}_f)$$

is the lift force. In addition, in (3.26) the pressure of the suspension phase is written as

$$p_s = p_{kin/coll} + p_{fric} \,, \tag{3.28}$$

where

$$p_{kin/coll} = \hat{\rho}_s \varphi_s [1 + 2\varphi_s (1+e) g_0] \Theta \,, \tag{3.29}$$

$$p_{fri} = \begin{cases} P_{fri} \dfrac{(\varphi_s - \varphi_{s,min})^n}{(\varphi_{s,max} - \varphi_s)^r} & \text{if} \quad \varphi_{s,min} < \varphi_s < \varphi_{s,max} \\ 0 & \text{if} \quad \varphi_s \leq \varphi_{s,min} \end{cases}$$

and $\mu_s = \mu_{kin} + \mu_{coll} + \mu_{fric}$. Formulas of these three viscosity terms are omitted for sake of brevity.

Lun et al. [153] derived all the involved expressions considering the anelastic nature of particle collision (instantaneous-binary collisions). Lugo et al. [151] claim that the most important idea of this model consists in introducing, as mentioned earlier, a quantity called *granular* or *solid temperature* Θ, which is a measure of the energy level due to the particle velocity fluctuation. In particular, splitting the solid velocity into a sum of mean and fluctuation components, i.e., $\mathbf{u}_s = \langle \mathbf{u}_s \rangle + \mathbf{u}'_s$, the definition of Θ is $\Theta := \frac{1}{3}\langle ||\mathbf{u}'_s||^2 \rangle$. Similarly to the classical gas theory, solving the equation

$$\begin{aligned} \frac{3}{2}\left[\frac{\partial}{\partial t}(\hat{\rho}_s \varphi_s \Theta) + \nabla \cdot (\hat{\rho}_s \varphi_s \Theta \mathbf{u}_s)\right] = \\ = \left(\mathbf{T}_s - \sum_{k=1}^{3} (\nabla p_s \cdot \bar{e}_k) \bar{e}_k \otimes \bar{e}_k\right) : \nabla \mathbf{u}_s + \nabla \cdot (\chi_s \nabla \Theta) - \gamma_s - 3\beta\Theta \end{aligned} \tag{3.30}$$

it is possible to obtain the pressure for solid phase through the constitutive relationship (3.29). Finally, the chosen equations for turbulence model are

$$\frac{\partial}{\partial t}(\hat{\rho}_f \varphi_f k_f) + \nabla \cdot (\hat{\rho}_f \varphi_f k_f \mathbf{u}_f) = \nabla \cdot \left(\varphi_f \frac{\mu_{t,f}}{\sigma_k} \nabla k_f\right) + \varphi_f G_{k,f} - \hat{\rho}_f \varphi_f \varepsilon_f \,,$$

$$\frac{\partial}{\partial t}(\hat{\rho}_f \varphi_f \varepsilon_f) + \nabla \cdot (\hat{\rho}_f \varphi_f \varepsilon_f \mathbf{u}_f) = \nabla \cdot \left(\varphi_f \frac{\mu_{t,f}}{\sigma_\varepsilon} \nabla \varepsilon_f\right) + \varphi_f \left(C_{1\varepsilon} \frac{\varepsilon_f}{k_f} G_{k,f} - C_{2\varepsilon} \hat{\rho}_f \frac{\varepsilon_f^2}{k_f}\right)$$

with

$$\mu_{t,f} = \hat{\rho}_f C_\mu \frac{k_f^2}{\varepsilon_f}$$

and

$$G_{k,f} = 2\, \mu_{t,f} \|\mathbf{D}\|^2 \,.$$

For sake of brevity, we omit the others 13 equations of the model, that involve many thermodynamics parameters that have to be chosen to characterize the sand type and the flow regime. However, for reader's use the "List of Main Symbols" is provided at the beginning of this article.

Many two-dimensional simulations were conducted with good qualitative results, in particular, the solid-like characteristics of the sand bed and the air free

flow outside the saltation zone were correctly reproduced, also from the quantitative point of view. On the other hand, at the large-scale *erosion* was overpredicted by 20% and at the small-scale the parameters of the model used in [103] (conductivity, solid viscosity, granular temperature and mean free path) strongly affect sediment transport layer thickness, which appears thinner than experimental measurements. As observed in [151] GKT models can provide a relatively good description of the saltation layer, but they require further studies on the coupling turbulence models and on the effect that the parameters have on the solution.

3.3.2 Eulerian treatment of wind driven rain

A somewhat different approach needs to be used for wind-blown rain, because the dispersed phase is liquid and is not entrained in the airflow from the ground apart from extreme situations of little practical interest, e.g., in presence of very strong winds. Moreover, the main transport process is due to convection and sedimentation. To the best of our knowledge, Eulerian-Eulerian approach for wind driven rain (WDR) have been introduced pretty recently by Huang and Li ([107], [106]) . They proposed a 2-fluid formulation for WDR with a 2-way coupling.

The air-phase is modeled with a 1-fluid approach (see Eqs.(3.4)-(3.5)) using both RANS with *realisable k-ϵ* [107] and LES [106] coupled with an SGS model proposed in [108]. The rain-phase is considered as a poly-dispersed fluid with k components, one per raindrop size class. Both mass and momentum conservation equations are solved:

$$\frac{\partial \hat{\rho}_\ell \varphi_k}{\partial t} + \nabla \cdot (\hat{\rho}_\ell \varphi_k \mathbf{u}_k) = 0 \,, \tag{3.31}$$

$$\frac{\partial}{\partial t}(\hat{\rho}_\ell \varphi_k \mathbf{u}_k) + \nabla \cdot (\hat{\rho}_\ell \varphi_k \mathbf{u}_k \otimes \mathbf{u}_k) = \hat{\rho}_\ell \varphi_k \mathbf{g} + \mathbf{F}_{k,d} \,, \tag{3.32}$$

where $\hat{\rho}_\ell$ is the water density, φ_k and $\mathbf{u}_k$ are respectively the volume fraction and the velocity of the k size range class. At variance with snow and sand-drift models, the Authors above do not model turbulent diffusion, justifying it by the discrete nature of rain. The motion of rain is obtained by the combined effect of gravity (the first term on the r.h.s. of Eq.(3.32)) and wind drag (the second term on the r.h.s. of Eq.(3.32)), that is taken to be given by Stokes law:

$$\mathbf{F}_{k,d} = \varphi_k \frac{18 \mu_f C_D Re_p}{24 d_k^2} (\mathbf{u}_f - \mathbf{u}_k) \,.$$

The sum of these last terms over all k size-range class is inserted with the opposite sign in the momentum equation for the air-phase for coupling.

In [133] a similar model is proposed, but there is no effect in the air momentum equations due to the interactions with the rain drops. The 1-way coupling approximation is justified by the fact that the volume ratio is smaller than 10^{-4}. The model is then extended in [134], where the effect of turbulent dispersion is included by means of Boussinesq eddy viscosity approximation for the Reynolds stresses modeling. This model has been successfully used for civil engineering application, involving different building set-ups and was validated with experimental measurements [132, 135, 136]. A similar model was also used in [178]. Finally, Wang et al. [223]

added the resulting drag term to the wind momentum equation so that the model can be classified as a 2-way coupling model. However, Huang and Li [106, 107] mentioned that other approaches (mainly Lagrangian and heuristics) can be selected for computational reasons. In fact, their model requires using very fine grids in order to reduce numerical diffusion, as well as solving partial differential equations for each class of raindrop size of the poly-disperse flow.

3.3.3 Eulerian-Lagrangian approach

While for wind-blown snow Eulerian-Eulerian approaches are always preferred, for sand Eulerian-Lagrangian approaches have been widely used, both for the persistent granular nature of sand and for the existence of previous studies on granular matter in general.

Eulerian-Lagrangian models allow to focus on phenomena related to the behavior of single grains and to get information at the grain scale that cannot be obtained by fully Eulerian models and that are hard to be obtained experimentally. On the other hand, in order to be statistically representative for the real ensemble of sand grains, a sufficiently large set of particles needs to be introduced in the domain, which makes the method computationally expensive. Basically, the method consists in solving the equations of motion for each particle including collision dynamics, to get individual trajectories. For these reasons, in general these methods are preferred to study local-scale phenomena.

After an earlier attempt by Anderson and Haff [4] and later by Lakehal et al. [138], only in the last two decades such computational approaches have taken hold in the particular fields of application of interest in this review. In fact, starting with [204], different discrete particles models have been proposed, specifically named as Discrete Particle Methods (DPM) and Discrete Element Method (DEM).

Before describing the models in some details, we give an overview of their main feaures. Kang and coauthors [117, 118, 120, 121] proposed a DPM for the granular phase joined with RANS two-phase equations for the transporting phase (see Eqs. (3.6) (3.7)), because of the lower computational cost of Reynolds-averaged approach. A 2-way coupling is employed. Particle distribution, velocity and drag force were analyzed and compared with wind-tunnel data [117, 118, 120]. The effect of Magnus and Saffman forces have been included and studied in [121]. A k-ϵ turbulence model was generally used, except in [117], where a simpler one equation mixing length model was preferred.

Concerning the particle tracking model, translational and rotational equations of motion are solved, taking into account the torque due to shear stress (except in [118]), and applying a *soft-sphere* model for inter-particles collisions. The simulation set-up used in [117] differs from the others because the domain bottom boundary coincides with the ground, while in the others the fluid-solid interface is inside the domain.

More sophisticated models were also proposed in order to improve the reliability of computational simulations. For instance, concerning the fluid phase, RANS

approaches were sometimes replaced by LES or Lattice-Boltzmann methods. Specifically:

- Tong and Huang [215] combined a DEM with 2-way coupling with LES (with dynamic SGS closure) to obtain a more realistic flow field;
- Li et al. [139] put more details and effort in the computation of the particle trajectories using a DEM with 4-way coupling combined with LES fluid simulation using Smagorinsky sub-grid model;
- Shi et al. [199] combined a 2-way Lagrangian tracking method with a Lattice-Boltzman approach for fluid flow.
- Jiang et al. [115] used LES with Lagrangian tracking to investigate the effect on turbulent flow structures, sand transport, and sand particle reverse motion over two-dimensional transverse dunes.
- Okaze et al. [170] used LES with coherent structure Smagorinsky model ([127], [128]), coupled with a snow transport model, based on the interaction between turbulent flow structures and snow particle dispersion.

Concerning the dispersed phase, different improvements were tried:

- Xiao et al. [230] extended the model presented in [118] where mono-sized sand was used, including different particle size distributions, both Gaussian and uniform.
- Lopes et al. [147] tackled the presence of different time scales by means of a quasi-steady procedure based on a RANS k-ϵ model with 1-way coupling.

Most of the works using Lagrangian methods studied local saltation phenomena over a flat bed. Instead, Jiang and coauthors ([114], [115]) has been used particle tracking over a sand dune in a two-dimensional configuration, and investigated the effect of the presence of grains on the air-flow.

The same kind of models has been used for rain droplets, with some simplifications. The first models to evaluate the impact of wind driven rain on buildings was presented in [53] and [52]. These models used a 1-way coupling and were based on steady air-flow simulation using RANS k-ϵ models. Lift forces were always neglected, as well as rebound, splash, run-off and resuspension. Similar models were proposed by Hangan [98] and Abadie and Mendes [1], who used both k-ϵ and k-ω RANS, according to the position inside the computational domain.

Finally, it is worth pointing out that Lagrangian models seem to treat all transport modes implicitly. Actually, this is true only if particle-particle and particle-bed interaction are taken into account. For instance, saltation is the result of complicate inter-particle collisions.

Particle equations of motion

As already mentioned, almost all Eulerian-Lagrangian models refer to Discrete Particle Methods (DPM) and Discrete Element Method (DEM). These methods solve the

equations of motion for each particle:

$$m_p \frac{d\mathbf{u}_p}{dt} = \mathbf{F}_p \ , \tag{3.33}$$

where m_p is the mass of the particle, $\mathbf{u}_p$ its velocity, and $\mathbf{F}_p$ the resulting force acting on the particle, that includes drag and gravity. In some cases the rotational degrees of freedom are considered as well, so that also the equations of angular momentum are solved:

$$I_p \frac{d\mathbf{\Omega}_p}{dt} = \mathbf{T}_p \ , \tag{3.34}$$

where I_p is the *momentum of inertia* of the particle (that is assumed spherical) and $\mathbf{\Omega}_p$ its angular velocity. Almost all Lagrangian models are 2-way coupled (except for [147]), because the effect of the presence of particles is included into the air-phase mass and momentum balance equations (Eqs. (3.6)-(3.7)), which depend on the air-phase volume fraction $\varphi_f = 1 - \sum_{i=1}^{N_d} \varphi_{s,i}$, where, considering poly-disperse flows, $\varphi_{s,i}$ is the volume fraction of the i-dispersed phase, and N_d is the number of dispersed phases. Moreover, in Eq. (3.7) there is the solid-fluid coupling term $\mathbf{f}_{drag}$ which is the resultant of the drag forces exerted by particles [230]:

$$\mathbf{f}_{drag} = \frac{1}{\Delta v} \sum_{p=1}^{N} \mathbf{F}_p^{dr} \ ,$$

where Δv is the volume of the considered computational cell, N is the total number of particles inside the cell and $\mathbf{F}_p^{dr}$ is the drag force acting on the p-particle, computed by means of empirical relations, for instance

$$\mathbf{F}_p^{dr} = -\frac{1}{8}\pi D^2 C_D |\mathbf{u}_f - \mathbf{u}_p|(\mathbf{u}_f - \mathbf{u}_p) \ , \tag{3.35}$$

where C_D is the *drag coefficient* [62]. As already stated after Eq. (3.21) several laws have been proposed for C_D to fit experimental data. In [204], [118], [147] and [139] the following relations generalizing Eq. (3.20) to high particle Reynolds numbers is used:

$$C_{D,l_1} = \begin{cases} \dfrac{24}{Re_p}(1 + 0.15 Re_p^{0.687}) & \text{if } Re_p < 1000 \\ 0.44 & \text{if } Re_p \geq 1000 \end{cases} \tag{3.36}$$

Instead, in [120], [117], [215] and [230] the following expression

$$C_{D,l_2} = \left(0.63 + \frac{4.8}{Re_p^{0.5}}\right)^2 \tag{3.37}$$

was used to express the drag coefficient laws (3.36) and (3.37) are compared in Fig.3.8, and they notably differs only for high Re_p. As observed above for sand particles close to the ground $1 \leq Re_p \leq 100$.

Also the models proposed in [215], [114] and [199] belong to the 2-way coupling category, because they included the effect of particles on the fluid.

In order to get 4-way coupling models like in [139] particle-particle and particle-bed interactions $\mathbf{F}^{coll}$ to $\mathbf{F}_p$ need be considered. In this case, the resulting force on

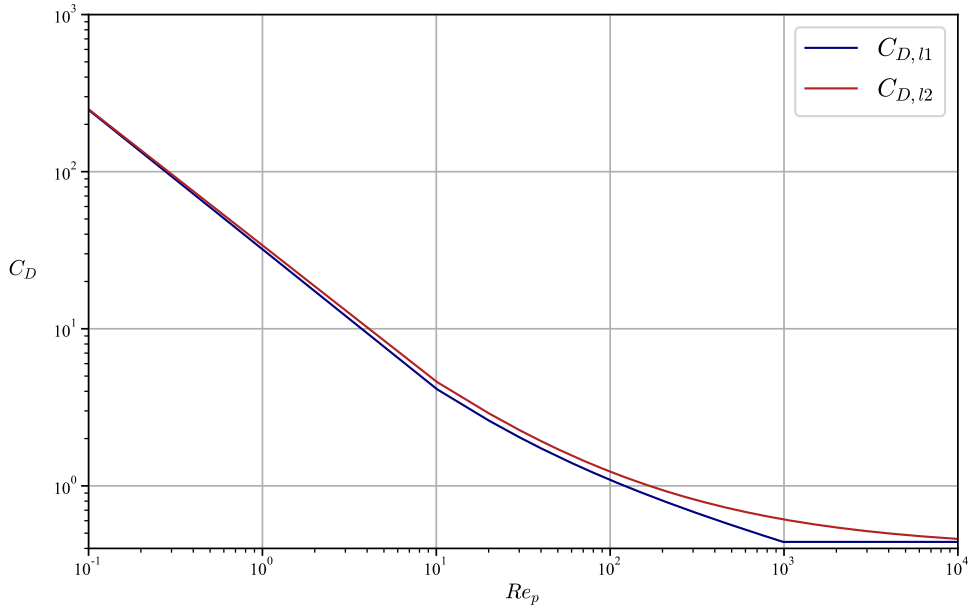

Figure 3.8: C_D coefficient according to Eqs.(3.36) and (3.37).

particle p generally reads

$$\mathbf{F}_p = m_p\mathbf{g} + \mathbf{F}_p^{dr} + \mathbf{F}_p^{coll} \ ,$$

where $\mathbf{F}_p^{coll}$ can be modelled with different levels of accuracy. DEM approaches are able to treat multi-contact interactions using mechanical elements (springs, dampers, etc...) to describe forces by means of hard-sphere and soft-sphere models, as well described in [61]. For instance, Kang and Guo [118] and Li et al. [139] split $\mathbf{F}_p^{coll}$ as

$$\mathbf{F}_p^{coll} = \sum_q (\mathbf{f}_{pq}^c + \mathbf{f}_{pq}^d) \ ,$$

where $\mathbf{f}_{pq}^c$ is a *contact force* and $\mathbf{f}_{pq}^d$ a *viscous damping force* which vanish when the particle q does not collide with the particle p. The expressions of the normal and tangential components of the contact and damping forces are:

- Normal contact force: $f_{pq,n}^c = -\frac{4}{3}E^*\sqrt{r^*\delta_n^3}$
- Tangential contact force: $f_{pq,t}^c = -\frac{\mu_s|f_{pq}^c|}{|\delta_t|}\left[1-\left(1-\frac{\min\{|\delta_t|,\delta_{t,max}\}}{\delta_{t,max}}\right)^{3/2}\right]\delta_t$
- Normal viscous damping force: $f_{pq,n}^d = -\eta\left(6m_{pq}E^*\sqrt{r^*\delta_n}\right)^{1/2}v_{pq,n}$
- Tangential viscous damping force:

$$f_{pq,t}^d = -\eta\left(6m_{pq}\mu_s|f_{pq}^c|\frac{\sqrt{1-|\delta_t|/\delta_{t,max}}}{\delta_{t,max}}\right)^{1/2}v_{pq,t}$$

where $\frac{1}{m_{pq}} = \frac{1}{m_p} + \frac{1}{m_q}$ and $\frac{1}{r^*} = \frac{1}{r_p} + \frac{1}{r_q}$ with r_p and r_q the radii of the particles p and q. In the same way

$$\frac{1}{E^*} = \frac{1-\nu_p^2}{E_p} + \frac{1-\nu_q^2}{E_q} ,$$

where E_p, E_q and ν_p, ν_q are respectively the Young modulus and the Poisson ratio of the particles p and q. In addition, μ_s is the friction coefficient, η is the damping coefficient, $\delta = (\delta_t, \delta_n)$ is the displacement vector between the particles p and q splitted in tangential and normal components and, similarly, $v_{pq} = (v_{pq,t}, v_{pq,n})$ is the relative velocity between the consider couple of particles, again splitted into tangential and normal components. In [120], [121], [117] the inter-particles interaction forces are given by

$$\mathbf{F}_p^{coll} = \sum_q \mathbf{f}_{pq}^c ,$$

where the summation terms are computed using a linear spring-damper model. In particular, the components of the interaction force are:

- Normal component
$$f_{pq,n}^c = -k_s\delta_n - \eta v_{pq,n}$$
- Tangential component
$$f_{pq,t}^c = \begin{cases} k_s\delta_t - \eta v_{pq,t} & \text{if } |f_{pq,t}^c| \le \mu_s |f_{pq,n}^c| \\ -\mu_s |f_{pq,t}^c| & \text{if } |f_{pq,t}^c| > \mu_s |f_{pq,n}^c| \end{cases}$$

where k_s is the stiffness coefficient and the other coefficients are as above. In addition, rotational degrees of freedom are also considered, adding the equation

$$I_p \frac{d\mathbf{\Omega}_p}{dt} = \sum_q \mathbf{T}_{pq} + \mathbf{T}_f , \tag{3.38}$$

where $\mathbf{T}_{pq}$ is the torque due to collision forces, $\mathbf{T}_f = 8\pi r^3 \mu_f \left(\frac{1}{2}\nabla \times \mathbf{u}_f - \mathbf{\Omega}_p\right)$ is the torque on a spherical particle due to the fluid shear stress. In [118] and [139] Eq. (3.38) is solved neglecting $\mathbf{T}_f$.

An alternative way to model particle-particle and particle-bed interactions consists in using a *hard-sphere* model with impulsive interaction forces.With this approach, particles restore their shape after impact. However, in this approach only instantaneous binary collisions are considered. Multiple interactions are neglected and so it can be used for dilute suspensions only and not close to the sand-bed. Considering two particles p and q, conservation of linear and angular momentum read

$$\begin{cases} m_p \left(\mathbf{u}_p - \mathbf{u}_p^{(0)}\right) = \mathbf{J} , \\ m_q \left(\mathbf{u}_q - \mathbf{u}_q^{(0)}\right) = -\mathbf{J} , \\ I_p \left(\mathbf{\Omega}_p - \mathbf{\Omega}_p^{(0)}\right) = \mathbf{r}_p \times \mathbf{J} , \\ I_q \left(\mathbf{\Omega}_q - \mathbf{\Omega}_q^{(0)}\right) = -\mathbf{r}_q \times \mathbf{J} , \end{cases}$$

where the index (0) refers to the values of velocity and angular velocity before the collision and $\mathbf{J}$ is the impulsive force. Such an approach was used by Sun el al. [204] who considered binary elastic collisions between non-deformable spheres, using analytical average normal and tangential impulses to compute velocity variations. In [230] hard-spheres were used to model both particle-particle and particle-bed interactions. As far as rain droplets are concerned, most of the models are based on Choi's work ([53], [52]). In his model only translation motion is considered and in Eq. (3.33) the resulting force on a particle is a balance between Stokes drag and buoyancy:

$$\mathbf{F}_p = m_p \mathbf{g} \left(1 - \frac{\hat{\rho}_f}{\hat{\rho}_s}\right) + 6\pi\mu r_p(\mathbf{u}_f - \mathbf{u}_p) \tag{3.39}$$

Instead Hangan [98] used

$$\mathbf{F}_p^{dr} = \frac{3\rho}{8r_p} C_D |\mathbf{u}_f - \mathbf{u}_p|(\mathbf{u}_f - \mathbf{u}_p) \tag{3.40}$$

for the drag force in the rain droplet translation equation of motion, where $C_D = a_1 + \frac{a_2}{Re} + \frac{a_3}{Re^2}$ is the drag coefficient given by Morsi-Alexander law. A similar quadratic dependence on the relative velocity was used in [1].

Particles-bed interaction

The Lagrangian approach allows to avoid dynamical re-meshing, because the integration cell can be fixed and even be crossed by the ground surface. However, this implies to accurately model the interaction of the dispersed particles in the saltation and creep layer with those particles laying on the ground. One simple way to do that is to compose the ground surface using a set of motionless particles and a restitution coefficient. Two different initial particles-bed configurations, with 3000 and 5000 particles were studied in [118]. The former reaches a steady state in 3.6 seconds, while the latter in 3.4 seconds, even if a direct comparison between the two set-ups can not be made because the simulations differ in other parameters. Similarly, 8000 particles were used in [120]. Differently, in [117] the ground interface is outside the domain, under its bottom boundary. Therefore, no boundary model is applied, and the dynamics is totally simulated by means of inter-particles collision models. On the contrary, Xiao et al. [230] focused on the effect of two different bed models:

- *Flat bed model*: the bed is considered as a motionless particle having an infinite mass (also used in [139]);
- *Rough bed model*: the bed is considered as a set of particles having mass and size of a settling particle; the velocity vector relative to an impacting particle and the wall is taken to be a Gaussian distribution.

The choice of bed models affects the results, and each of them seems to represent a particular type of sand surface (rough bed model) or desert areas (Gobi area, flat bed model). Tong and Huang [215] and Jiang [115] modelled the impacting-ejecting process on the basis of the *splash function* proposed in [225] and [220]. Specifically, the rebound and the ejected speeds v_{re} and v_{ej}, and the rebound and ejected angles α_{re} and α_{ej} are given by uniform probability densities with mean $|\bar{v}_{re}| = 0.3|v_{im}|$ and $\bar{\alpha}_{re} = 0.60$, where v_{im} is the *impinging speed* and α_{im} is the impinging angle. However,

the reported values of the standard deviation deserve more studies because they are sometimes unphysical. The number of ejected sand particles is

$$N_p^{ej} = \max\{0, 3.36 \sin\alpha_{im} (5.72|v_{im}| - 0.915)\} .$$

On the other hand, Shi et al. [199] chose the following Gamma distribution function

$$f(v_0) = \frac{13.5}{0.96u_*}\left(\frac{v_0}{0.96u_*}\right)^3 \exp\left(-\frac{3v_0}{0.96u_*}\right)$$

for the lift-off speed v_0 in order to capture the stochastic nature of the ejection process (see also [5]), while the number of particles ejected by splashing N_p^{ej} and the rebound velocity and probability are following [225]:

$$N_p^{ej}(v_{im}, \alpha_{im}) = 3.07 \sin\alpha_{im}\left(\frac{v_{im}}{18\sqrt{gd}} - 1\right) ,$$

$$v_{re} = \frac{1}{2} v_{im} ,$$

$$P_{re} = 0.95\left[1 - \exp\left(1 - \exp\frac{v_{im}}{10\sqrt{gd}}\right)\right] .$$

Different time-scale treatment

Air and particles have very different characteristic time-scales. From a computational point of view, this aspect is cumbersome and needs to be carefully considered in order to avoid waste of computational resources. In Lagrangian simulations the multi-time-scale issue is tackled using different time steps to integrate the equations for particles and air, as reported in Table 3.1. In all cases there is one order of magnitude difference between particle and air time-step.

Table 3.1: Examples of time-steps for air and dispersed phase in Eulerian-Lagrangian approaches.

Model	Air time-step [s]	Particle time-step [s]
[118]	$2 \cdot 10^{-5}$	$3 \cdot 10^{-6}$
[120]	$2 \cdot 10^{-5}$	$2 \cdot 10^{-6}$
[121]	$2 \cdot 10^{-5}$	$2 \cdot 10^{-6}$
[215]	$5 \cdot 10^{-4}$	$1 \cdot 10^{-4}$
[139]	$5 \cdot 10^{-5}$	$2 \cdot 10^{-5}$

Chapter 4

Avalanches

The content of this chapter is based on the article [169] published during the period of the *SMaRT* research activity.

The morphodynamic evolution of the shape of dunes and piles of granular material is largely dictated by avalanching phenomena, acting when the local slope gets steeper than a critical repose angle. A class of degenerate parabolic models are proposed closing a mass balance equation with several viscoplastic constitutive laws to describe the motion of the sliding layer. Comparison between them is carried out by means of computational simulations putting in evidence the features that depend on the closure constitutive assumption and the robust aspects of the models. The versatility of the model is shown applying it to the movement of sand in presence of walls, open ends, columns, doors, and in complicated geometries.

4.1 Introduction

Four phenomena contribute to wind-induced sand movement and eventually to the formation and evolution of dunes: erosion from the sand bed, transport by the wind, sedimentation due to gravity, and sand grain slides occurring when the slope of the accumulated sand exceeds a critical repose angle [40] that depends on the specific granular material [30].

In particular, erosion, sedimentation, and sand sliding determine the evolution of the free-boundary over which wind blows and transports the sand. As explained in detail in [143] and in the recent review [145], the need of coupling a multiphase turbulent fluid-dynamics model with the morphodynamics of the sand surface requires the deduction of mathematical models for such phenomena that are able to describe the evolution of the sand bed in a way that is at the same time accurate and computationally fast. However, applications are not restricted to sand dynamics but can be extended to debris and other granular material in general as they present similar behaviours.

Referring again to [145] for a more detailed review, many modeling frameworks were developed to study the phenomena involved, both for sand and snow, and for other granular materials in general. Savage and Hutter [196] proposed a hydrodynamical models, based on Saint-Venant equations. They start from the incompressibility condition and momentum conservation equations in the flowing layer and then integrate them over the thickness of the rolling layer, not considering erosion

and deposition. This gap was then filled, for instance, by Douady et al. [68], Khakhar et al. [126] and Gray [90]. A detailed analytical study of Savage and Hutter's model was performed by Colombo et al. [55].

Variational approaches have been proposed as well. Firstly, Aronsson et al. [12] introduced the p-Laplacian operator in order to model a non-homogeneous superficial diffusion to determine the height of a growing pile of a noncohesive sand. Mathematical properties were studied in a functional analysis framework by focusing on the theoretical results when the parameter p tends to infinity. Prigozhin [183] developed a variational model based on mass balance for the sand pile and assuming the surface flow is directed down in the direction of steepest descent subject to a slope constraint. Prigozhin et al. [184] allowed a leading coefficient to vanish if the slope is below a threshold corresponding to the repose angle.

Bouchaud and coworkers [31, 32] divided the sand pile in a static zone and a moving layer, giving rise to the so-called *two-layers models*. Such models are characterized by two state variables, the local height of the static part and the local density (or height) of the rolling layer, linked by an exchange term which governs the transfer of mass from one status to the other. Of course, in the static zone the advection velocity vanishes, while in the rolling layer it is usually considered constant and strictly positive downhill. Also de Gennes and coauthors [10, 35, 36, 86] and Prigozhin and Zaltzman [184] proposed modified versions of this type of models, with the latter that assumed a proportionality of the drift velocity with the gradient of the height of the sandpile. In the models proposed by Hadeler and Kuttler [95, 96, 137], velocity is again constant, though it is mentioned that it might depend on the slope (see, for instance, [97]). An exchange term proportional to the difference between the slope of the sand bed and the repose angle governs the transfer of sand between the static and the rolling layer.

A detailed analytical study of two-layers models was performed by Cannarsa and coworkers [43–45, 57] for different boundary conditions. Falcone and Finzi Vita [79–81] instead focused on the proper numerical method to integrate two-layers models putting in evidence some unrealistic features such as the presence of blow-ups when the boundary of the domain changes type, e.g., from a wall to an open end. Others are (i) the formation of artificial valleys on the top of the sand pile obtained by pouring sand on its top, due to the discontinuity of downhill velocities on the two slopes in 1D simulations, or in situations in which the maximum height of the sand pile should be reached close to a wall; (ii) the dependence of the evolution and of the final configuration from the non-uniquely defined initial partitioning of the sand pile in a static and a rolling region, e.g., if all the mass is set to be initially static, then there is no evolution even if the initial configuration exceeds the repose angle.

Starting from the just mentioned computational needs [143, 145], in [144] we proposed a model for the height of the sand pile that does not present the problems mentioned above. It is based on a reduction of a mass balance equation obtained assuming that (i) the thickness of the sliding layer is small, (ii) the grains move along the direction of steepest descent, (iii) the speed is given by the limit velocity of a body sliding down a slope under the action of gravity, Coulomb friction, and a drag

force taken to be proportional to the sliding speed.

It is proved that assumptions (i) and (ii) lead to an evolution equation for the height $h(\mathbf{x}, t)$ of the sand pile with the following structure

$$\frac{\partial h}{\partial t} = \nu \nabla \cdot \left[f_{sl}(|\nabla h|) \frac{\nabla h}{|\nabla h|} \right] + q \,, \tag{4.1}$$

where f_{sl} is called the sliding term, related to the mean sliding speed w through the relation $f_{sl}(|\nabla h|) = \frac{\delta}{\nu} w(|\nabla h|)$ where δ is the thickness of the sliding layer and ν is an effective diffusion coefficient. The last term q in (4.1) takes into accout of external volume supplies of sand per unit area. The existence of a repose angle triggering the motion of the sand grains reflects into the fact that the sliding term vanishes for slopes, and therefore $|\nabla h|$, below a threhsold value. This gives to the parabolic equation (4.1) a degenerate character, that justifies calling this type of models Degenerate Parabolic Sliding Models (in the following shortened as DPSMs). Specifically, in [144] assumption (iii) led to

$$f_{sl}(|\nabla h|) = \frac{(|\nabla h| - \tan \alpha_{cr})_+}{\sqrt{1 + |\nabla h|^2}} \,, \tag{4.2}$$

where $(g)_+ = (g + |g|)/2$ stands for the positive part of g, so that f_{sl} vanishes when $|\nabla h| \leq \tan \alpha_{cr}$, where α_{cr} is the repose angle.

Of course, it is possible to model in other ways the complex fluid-like behavior of the thin layer sliding on the top of the sand pile when the angle of steepest descent is larger than the repose angle (a configuration that will be called supercritical in the following), giving rise to different sliding terms f_{sl}. In particular, still working under the hypotheses (i) and (ii) above, we here consider several viscoplastic constitutive models named after Bingham, Casson, and Herschel-Bulkley (see, for instance [51, 154] for more details). All these models are characterized by the presence of a yield stress that must be overcome before the material can flow. This common feature is related to the existence of a repose angle for the sand pile. Exploiting the fact that for these models it is possible to determine the velocity profile of a flow down an inclined plane, our aim is to extend DPSMs to different closures and to point out robust features and evolutionary differences among the mathematical models.

As we shall see, regardless of the constitutive closure, in spite of their simplicity, all the models above reply many well known features of sand slides, such as the non-uniqueness of static configurations in subcritical conditions, i.e., with slopes always smaller than the angle of repose and the link between critical stationary configurations and the solution of the same eikonal equation. So, starting from supercritical conditions the solution of all models tends towards an equilibrium identified by the same equation. The difference is in the way this solution is reached, especially when the slope gets close to the repose angle, with the model (4.1)–(4.2) being the fastest to reach the equilibrium and the one in which the closure is achieved using a Herschel-Bulckley constitutive equations with a small power being the slowest.

The paper is organized as follows. In Section 4.2 we derive the viscoplastic closures of the DPSM, starting from different constitutive laws. Section 4.3 presents the result of comparative tests between the different models obtained, in order to evaluate the differences between them in terms of final configuration and convergence speed. Some examples of application of the models in practical situations are given in Section 4.4. A final discussion section concludes the paper.

4.2 Viscoplastic Models for the Sliding Speed

Modelling the motion of granular materials can be rather complicated, expecially when there is massive relative motion among the grains. Luckily, in many situations involving the redistribution of the granular mass, the motion is limited to a sliding layer that has a thickness much smaller than the characteristic dimension of the sand pile. This suggests to work with integrated variable on the thickness of the moving layer. Having this in mind, we will assume that the thickness of the sliding layer is small and constant δ and that the behaviour of the ensemble of sand grains is fluid-like with viscoplastic characteristics.

So, coming briefly to the deduction of the model and referring to [144] for more details, we consider a control volume $\mathcal{V}$ with vertical lateral surface and the basis $\mathcal{A}$ deep in the sand. The integral form of the mass balance equation then writes as

$$\frac{d}{dt}\int_{\mathcal{A}} \rho h \, dA = -\int_{\partial\mathcal{V}_{air}} \mathbf{q}\cdot\,\mathbf{n}\, d\Sigma - \int_{\partial\mathcal{V}\cap\mathcal{S}} \rho\mathbf{v}\cdot\mathbf{n}\, d\Sigma\,,$$

where ρ is the sand density and $h(x,y,t)$ is the height of the sand pile. The first integral on the rhs refers to the sand flux sedimenting through the top and the second one to that within the thin creep layer denoted by $\mathcal{S}$. We then assume that sand grains slide along the surface $h(x,y,t)$ in the direction of the steepest gradient

$$\mathbf{t} = -\frac{\nabla h + |\nabla h|^2\mathbf{k}}{|\nabla h|\sqrt{1+|\nabla h|^2}}\,,$$

with speed w, that depends on the local slope of the surface, so that $\mathbf{v} = w\mathbf{t}$. Therefore, one can re-write the sand flux within the thin creep layer as

$$\int_{\partial\mathcal{V}\cap\mathcal{S}} \rho\mathbf{v}\cdot\mathbf{n}\, d\Sigma = \int_{\partial\mathcal{A}} \rho w\delta \frac{\mathbf{t}\cdot\mathbf{n}}{|\mathbf{t}\cdot\mathbf{n}|}\, d\Gamma = -\int_{\mathcal{A}} \nabla\cdot\left(\rho w\delta\frac{\nabla h}{|\nabla h|}\right) dA\,,$$

where we used the fact that we can rewrite the surface element as $d\Sigma = \frac{\delta}{\cos\theta} w(|\nabla h|) = \frac{\delta}{|\mathbf{t}\cdot\mathbf{n}|} c$ where $d\Gamma$ is the line element along ∂A and that the lateral walls are vertical.

Defining $q := -\mathbf{q}\cdot\mathbf{k}/\rho$ and $\nu_{f_{sl}}(|\nabla h|) := w(|\nabla h|)\delta$ where ν is an effective diffusion coefficient and f_{sl} is a dimensionless term that we will call sliding term because of its dependence from $|\nabla h|$ we finally have

$$\frac{\partial h}{\partial t} = \nu\nabla\cdot\left[f_{sl}(|\nabla h|)\frac{\nabla h}{|\nabla h|}\right] + q\,. \tag{4.3}$$

The crucial point is now to evaluate the sliding speed w or equivalently f_{sl}. However, as we shall see the existence of a minimal slope triggering the motion of the grains implies that f_{sl} vanishes below a certain threshold for $|\nabla h|$ giving (4.3) a degenerate character. For sake of clarity, we explicitly remark that for this reason we extend to zero the value of the square parenthesis in (4.3) when $|\nabla h| = 0$.

In order to identify the mean sliding speed we work in the vertical plane containing the direction of steepest gradient $\mathbf{t}$ represented in Figure 4.1 and assume that in the thin sliding layer the velocity profile can be approximated to that of a viscoplastic fluid flowing down an inclined plane with slope α, such that $\tan\alpha = |\nabla h|$. In this geometry, neglecting inertia, the equilibrium of forces locally reads

$$\frac{\partial T_{x'y'}}{\partial y'} = -\rho g \sin\alpha\,,$$

where $T_{x'y'}$ is the shear stress and g is the gravitational acceleration.

The above equation joined with stress-free boundary condition at the free surface

$$T_{x'y'}\Big|_{y'=\delta} = 0\,,$$

can be trivially integrated to give the shear stress

$$T_{x'y'} = \rho g(\delta - y')\sin\alpha\,. \tag{4.4}$$

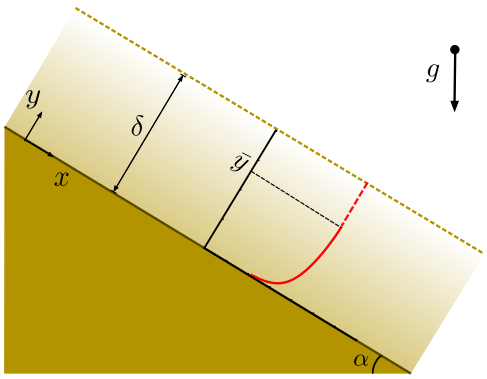

Figure 4.1: Velocity profile within a layer of moving sand behaving like a viscoplastic fluid in the vertical section containing the direction of steepest descent. The layer has thickness δ and $\bar{y}$ distinguishes the shear layer for $y' < \bar{y}$ (full red curve) from the plug layer for $y' > \bar{y}$ (dashed red curve).

If we take now constitutive models characterized by the presence of a yield stress τ, then there is flow only if an invariant measure of the stress is above it. One of the most common yielding criteria in viscoplastic flows is based on the second invariant of the stress tensor [51, 154], that in the two-dimensional section of our interest writes

$|T_{x'y'}| > \tau$: This means that there is flow only if

$$\sin\alpha > \sin\alpha_{cr} := \frac{\tau}{\rho g \delta},$$

so that α_{cr} represents the repose angle. We will call this case supercritical, while we will call subcritical a configuration with $\alpha < \alpha_{cr}$ everywhere. In this case, as shown in Fig. 4.1, the upper layer

$$y' > \bar{y} := \delta\left(1 - \frac{\sin\alpha_{cr}}{\sin\alpha}\right),$$

is a plug layer moving rigidly with the same velocity, while the lower layer $y' < \bar{y}$ where $T_{x'y'} > \tau$ undergoes a shear flow. We observe that at $y' = \bar{y}$ the shear stress is continuous and equal to τ. At this point, in order to proceed further and explicit the velocity profile in the supercritical case $\alpha > \alpha_{cr}$, we need to specify the constitutive equation. In the following we will use, as examples, the widely used models by Bingham, Casson, and Herschel-Bulkley because they allow to determine the analytical expression of the velocity profile.

4.2.1 Herschel-Bulkley model

The Herschel-Bulkley constitutive model writes as

$$\mathbf{T} = \left[k\sqrt{|\mathbb{I}_{\mathbf{2D}}|^{\gamma-1}} + \frac{\tau}{\sqrt{|\mathbb{I}_{\mathbf{2D}}|}}\right]\mathbf{2D}, \qquad \text{if} \quad \mathbb{I}_{\mathbf{T}} > \tau^2,$$

where $\mathbf{D} = \frac{1}{2}(\nabla\mathbf{v} + \nabla\mathbf{v}^T)$ is the rate of strain tensor, $\mathbb{I}_{\mathbf{2D}}$ is the second invariant of $\mathbf{2D}$ and $\mathbb{I}_{\mathbf{T}}$ the one of the stress tensor (see, for instance [51, 154] for more details). If, instead, $\mathbb{I}_{\mathbf{T}} < \tau^2$, then the shear rate vanishes. In two-dimensions it reduces to

$$T_{x'y'} = \tau + k\left|\frac{\partial v_{x'}}{\partial y'}\right|^{\gamma},$$

where $T_{x'y'} > \tau$ and $v_{x'}$ constant elsewhere. Then, in the shear layer $y' < \bar{y}$ Eq. (4.4) rewrites as

$$\frac{\partial v_{x'}}{\partial y'} = \left(\frac{\tau}{k}\right)^{1/\gamma}\left[\frac{\sin\alpha}{\sin\alpha_{cr}}\left(1 - \frac{y'}{\delta}\right) - 1\right]^{\frac{1}{\gamma}}, \tag{4.5}$$

that need be solved with the no-slip boundary condition at $y' = 0$. Because of the action of gravity, the flow will be downhill for small y'. So, there $\frac{\partial v_{x'}}{\partial y'} > 0$ and, actually, the positive sign will be kept because of the stress-free boundary condition. Therefore, overall the velocity profile is given by

$$v_{x'}(y') = \begin{cases} \dfrac{A}{\beta}\left[(\beta-1)^{1+\frac{1}{\gamma}} - \left(\beta - 1 - \beta\dfrac{y'}{\delta}\right)^{1+\frac{1}{\gamma}}\right] & \text{if } y' < \bar{y}; \\ \dfrac{A}{\beta}(\beta-1)^{1+\frac{1}{\gamma}} & \text{if } y' \geq \bar{y}. \end{cases} \tag{4.6}$$

where

$$A = \left(\frac{\tau}{k}\right)^{\frac{1}{\gamma}} \delta \frac{\gamma}{\gamma+1}, \qquad \beta = \frac{\sin\alpha}{\sin\alpha_{cr}},$$

with $\beta > 1$ when and where $\alpha > \alpha_{cr}$. In deducing (4.6) we also used the continuity of the shear stress in $y' = \bar{y}$, that implies that $\partial v_{x'}/\partial y'$ vanishes, in addition, of course, to the continuity of $v_{x'}$.

The mean speed across the moving layer $y' \in [0, \delta]$

$$w = \frac{1}{\delta}\left\{\int_0^{\bar{y}} \frac{A}{\beta}\left[(\beta-1)^{1+\frac{1}{\gamma}} - \left(\beta - 1 - \beta\frac{y'}{\delta}\right)^{1+\frac{1}{\gamma}}\right] dy' + \int_{\bar{y}}^{\delta} \frac{A}{\beta}(\beta-1)^{1+\frac{1}{\gamma}} dy'\right\},$$

can then be used to close (4.3). In fact, one can specify

$$\nu = \left(\frac{\tau}{k}\right)^{1/\gamma} \frac{\gamma}{(1+\gamma)(1+2\gamma)}\delta^2, \tag{4.7}$$

and f_{sl} as the product of two factors: a regular term f_{reg} and a degenerate term f_{deg}

$$f_{sl}(|\nabla h|) = f_{reg}(|\nabla h|) f_{deg}(|\nabla h|), \tag{4.8}$$

that, recalling that $\sin\alpha$ is a function of the slope $h(\mathbf{x}, t)$ given by

$$\sin\alpha = \frac{|\nabla h|}{\sqrt{1+|\nabla h|^2}},$$

write as

$$f_{reg}(|\nabla h|) = \frac{\sin\alpha_{cr}}{\sin\alpha}\left(1 + \gamma + \gamma\frac{\sin\alpha_{cr}}{\sin\alpha}\right), \tag{4.9}$$

which is always positive, while

$$f_{deg}(|\nabla h|) = \left[\left(\frac{\sin\alpha}{\sin\alpha_{cr}} - 1\right)_+\right]^{1+\frac{1}{\gamma}}, \tag{4.10}$$

vanishes when $\alpha \leq \alpha_{cr}$, i.e., when $|\nabla h| \leq \tan\alpha_{cr}$. In fact, if $\alpha < \alpha_{cr}$, $T_{x'y'} < \tau$ and there is no flow. The presence of this last term is the one that gives the parabolic equation (4.1) its degenerate character.

4.2.2 Bingham model

As well known, Bingham constitutive model is a particular case of a Herschel-Bulkley model with $\gamma = 1$ (and k replaced by μ) [51, 154]. Hence, from (4.7, 4.9, 4.10) we readily have

$$\nu = \frac{\tau\delta^2}{6\mu}, \tag{4.11}$$

$$f_{reg}(|\nabla h|) = \frac{\sin\alpha_{cr}}{\sin\alpha}\left(2 + \frac{\sin\alpha_{cr}}{\sin\alpha}\right), \tag{4.12}$$

and

$$f_{deg}(|\nabla h|) = \left[\left(\frac{\sin\alpha}{\sin\alpha_{cr}} - 1\right)_+\right]^2. \tag{4.13}$$

In particular, for the discussion to follow it is useful to observe that the degeneracy is quadratic, while for a Herschel-Bulkley model it goes like $1 + \frac{1}{\gamma}$.

4.2.3 Casson model

Casson's constitutive model can be written in three dimensions as

$$\mathbf{T} = \left[\sqrt{\mu} + \frac{\sqrt{\tau}}{|\mathrm{I\!I}_{\mathbf{2D}}|^{1/4}}\right]^2 \mathbf{2D} \qquad \text{if} \quad \mathrm{I\!I}_{\mathbf{T}} > \tau^2$$

(see, for instance, [51, 154] for more details) that in the two-dimensional section of our interest reduces to

$$\sqrt{T_{x'y'}} = \sqrt{\tau} + \sqrt{\mu\left|\frac{\partial v_{x'}}{\partial y'}\right|}.$$

Proceeding as in Section 4.2.1, one has then to solve the differential equation

$$\frac{\partial v_{x'}}{\partial y'} = \frac{1}{\mu}\left(\sqrt{\rho g(\delta - y')\sin\alpha} - \sqrt{\tau}\right)^2 = \frac{\tau}{\mu}\left(\sqrt{\beta}\sqrt{1 - \frac{y'}{\delta}} - 1\right)^2,$$

with no-slip boundary condition at $y' = 0$. The velocity profile is then

$$v_{x'}(y') = \begin{cases} \dfrac{\tau\delta^2}{6\mu\beta}\left[\left(\sqrt{\beta}-1\right)^3\left(3\sqrt{\beta}+1\right) - \left(\sqrt{\beta}\sqrt{1-\dfrac{y'}{\delta}}-1\right)^3\left(3\sqrt{\beta}\sqrt{1-\dfrac{y'}{\delta}}+1\right)\right] & \text{if } y' < \bar{y}, \\ \dfrac{\tau\delta^2}{6\mu\beta}\left(\sqrt{\beta}-1\right)^3\left(3\sqrt{\beta}+1\right) \qquad \text{if } y' \geq \bar{y}. \end{cases} \tag{4.14}$$

The mean speed across the moving layer $y' \in [0, \delta]$ can again be written as $w = \frac{\nu}{\delta} f_{reg}(|\nabla h|) f_{deg}(|\nabla h|)$ with $\nu = \frac{\tau\delta^2}{30\mu}$,

$$f_{reg}(|\nabla h|) = \frac{\sin^2\alpha_{cr}}{\sin^2\alpha}\left(10\frac{\sin^{3/2}\alpha}{\sin^{3/2}\alpha_{cr}} + 6\frac{\sin\alpha}{\sin\alpha_{cr}} + 3\frac{\sin^{1/2}\alpha}{\sin^{1/2}\alpha_{cr}} + 1\right), \tag{4.15}$$

and

$$f_{deg}(|\nabla h|) = \left[\left(\sqrt{\frac{\sin\alpha}{\sin\alpha_{cr}}} - 1\right)_+\right]^3, \tag{4.16}$$

where we also considered the fact that if $\alpha < \alpha_{cr}$, $T_{x'y'} < \tau$ and there is no flow.

4.3 Comparison of Slope Evolutions

From the structure of the equation it is clear that in absence of any mass input q, every subcritical configuration with $h(\mathbf{x})$ such that $|\nabla h| \leq \tan\alpha_{cr}$, $\forall \mathbf{x}$ is a stationary

solution, because f_{deg} in (4.10), (4.13), (4.16), as well as in (4.2), always vanishes being the angle of steepest descent $\alpha < \alpha_{cr}$.

On the other hand, starting from an initial condition such that $|\nabla h| > \tan\alpha_{cr}$ everywhere, then the evolution will tend to a solution of $f_{deg}(|\nabla h|) = 0$. Now, regardless of the closure assumption used, and therefore of the sliding model, this configuration is a solution of the eikonal equation $|\nabla h| = \tan\alpha_{cr}$, which then represents a robust feature of all the DPSMs proposed here and in [144]. Therefore, in order to put in evidence the differences among the models proposed above one should not look at the stationary configurations, but at transient behaviors. In order to do that, we will then integrate

$$\frac{\partial h}{\partial t} = \nu \nabla \cdot \left[f_{reg}(|\nabla h|) f_{deg}(|\nabla h|) \frac{\nabla h}{|\nabla h|} \right] + q \,, \tag{4.17}$$

with $f_{reg}(|\nabla h|) = 1/\sqrt{1+|\nabla h|^2}$ and $f_{deg}(|\nabla h|) = (|\nabla h| - \tan\alpha_{cr})_+$ in what we will call the Coulomb case, (4.9) and (4.10) in the Herschel-Bulkley case, (4.12) and (4.13) in the Bingham case, and (4.15) and (4.16) in the Casson case.

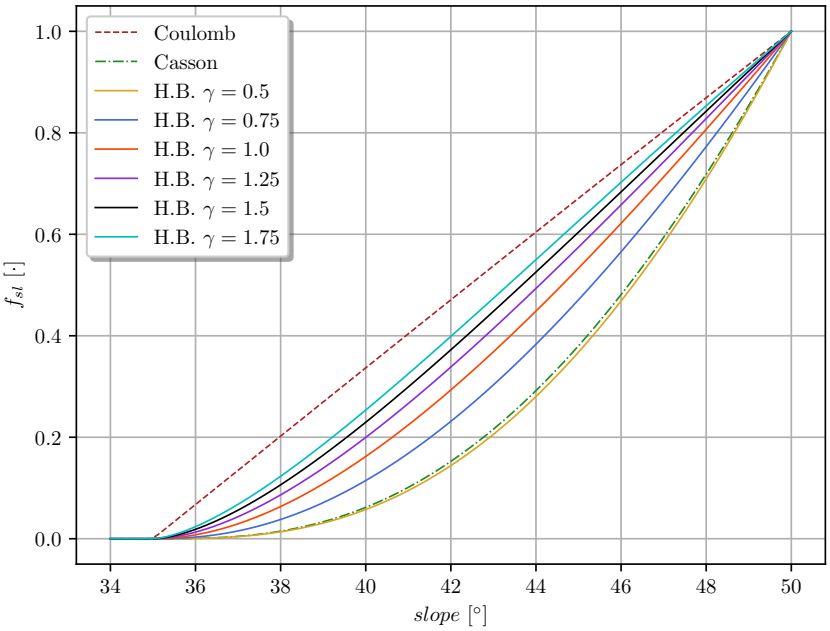

Figure 4.2: Sliding term $\hat{f}_{sl}$ normalized with respect to the value achieved for a slope of 50° and a repose angle of $\alpha_{cr} = 35°$ for different DPSM closure assumptions. We recall that Bingham fluids correspond to a Herschel-Bulkley model with $\gamma = 1$.

The main difference in the evolutions is due to the convexity of the curves representing the dependence of f_{sl} and specifically of f_{deg} on α close to α_{cr}. In fact, while the sliding term related to Coulomb's model goes linearly to zero, the other models have a stationary point there. More precisely, they behave like $(\alpha - \alpha_{cr})^n$ with $n = 2$

for Bingham model, $n = 1 + \frac{1}{\gamma}$ for Herschel-Bulkley models, and $n = 3$ for Casson model. This means that when approaching the repose angle the evolution becomes slower and slower especially for Casson fluids and Herschel-Bulkley models with $\gamma < 1$. The smaller γ is, the slower the process of approaching the stationary configuration is.

In Figure 4.2 we plot the sliding velocity normalized with their maximum value obtained for $\alpha = 50°$. From the figure it can be observed that at any angle the response to a Casson closure and to a Herschel-Bulkley one with $\gamma = 0.5$ are very close. So, we expect the evolutions related to them to be quite close.

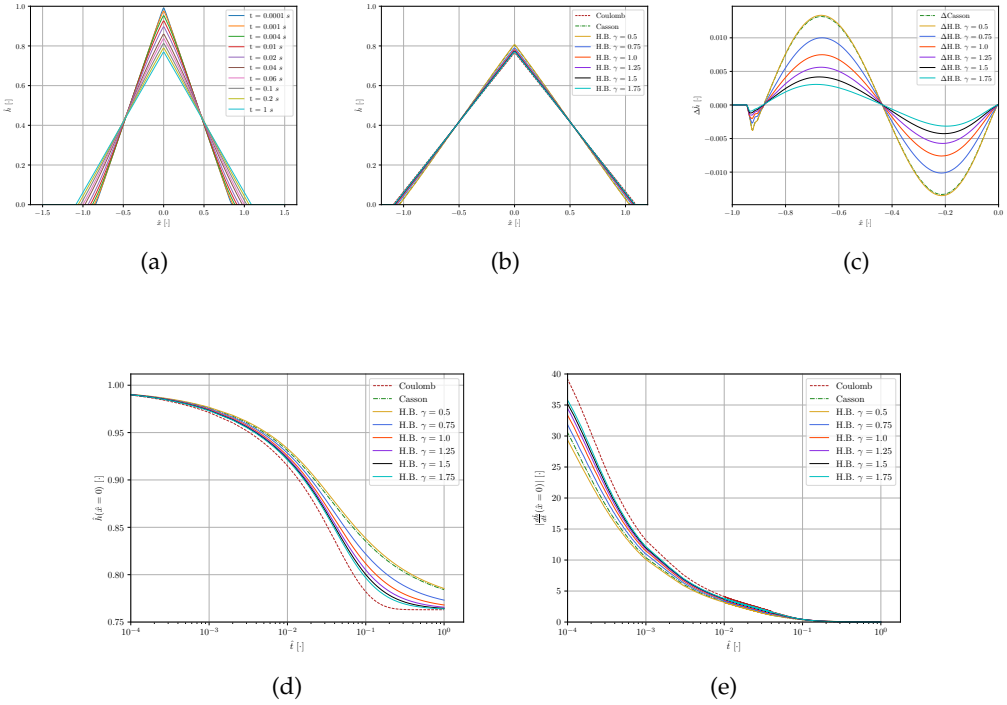

Figure 4.3: (a) Spatial evolution of the profile of an initially supercritical conical sand pile with repose angle $\alpha_{cr} = 35°$ at different times for a Bingham closure. (b) Comparison of the configurations achieved using the different DPSMs at $\hat{t} = 0.5$. (c) Differences between the heights of the left slopes as obtained using the different viscoplastic models with that obtained using Coulomb closure at the time for which the configurations have maximum height equal to 0.8. Temporal evolution of the height $\hat{h}$ (d) and of the velocity of the tip of the sand pile (e) for the different models. Bingham model corresponds to $\gamma = 1$.

Actually, it is useful to work in dimensionless variables scaling lengths with the reference size H of the sand pile, e.g., its height, and times with $T = \frac{H^2}{\nu f_{sl}(\alpha_*)}$ where

α_* is a reference slope angle, so that

$$\frac{\partial \hat{h}}{\partial \hat{t}} = \hat{\nabla} \cdot \left[\frac{f_{reg}(\alpha) f_{deg}(\alpha)}{f_{reg}(\alpha_*) f_{deg}(\alpha_*)} \frac{\hat{\nabla}\hat{h}}{|\hat{\nabla}\hat{h}|} \right] + \hat{q} \, ,$$

where the hats denote dimensionless variables.

In order to provide both a qualitative and quantitative comparison, DPMSs were implemented in the finite volumes open source code OpenFoam®. Finite-volume methods were successfully used for degenerate parabolic problems (see for instance [24, 76, 77]). As concerns spatial discretion, the diffusive term is evaluated by means of Gauss Theorem and Mean Value Theorem. A generic diffusive term $\nabla \cdot (f_{sl} \nabla h)$ is written by means of normal boundary fluxes [172]

$$\nabla \cdot (f_{sl} \nabla h) = \frac{1}{V} \int_V \nabla \cdot (f_{sl} \nabla h) \, dV = \frac{1}{V} \oint_{\partial V} f_{sl} \nabla h \cdot d\mathbf{S} = \frac{1}{V} \sum_{i}^{nFaces} f_{sl}^f (\nabla h)_i^f \cdot \mathbf{S}_i^f \, ,$$

where f_{sl}^f is the face-interpolated value of the sliding term and $\mathbf{S}^f$ is the face area normal vector. Cubic interpolation is used to get cell-face values from cell-center ones. Consequently, where the diffusivity becomes zero, the parabolic equation degenerates to $\frac{\partial h}{\partial t} = q$ which can be simply integrated in time. An implicit Euler scheme is used for time discretization.

In order to show the effect of the different constitutive closures, we simulate the motion of a sand pile with an initially conic shape with an angle of $\alpha_* = 50^\circ$ while the repose angle is 35°.

In Fig.4.3(a) the evolution is shown in the case in which the sliding layer is described as a Bingham fluid. The slope gradually decreases keeping an almost conical shape to eventually achieve the stationary configuration with an angle at the basis equal to the repose angle. In fact, as already stated, regardless of the closure assumption, all DPSMs relax an initial configuration that is supercritical everywhere, to the solution of the same eikonal equation, which in this case is a cone. In Fig.4.3(b) we plot the configurations achieved using the different closures at $\hat{t} = 0.5$.

In order to put in evidence how much the solutions differ and where, in Fig.4.3(c) we plot the difference between the solution obtained by the viscoplastic models considered here with respect to the one obtained using Coulomb closure as a reference. The maximum error is about 1.5% of the pile height.

The biggest difference among the evolutions stays in how fast the tip of the cone moves down and the basis of the cone enlarges. In fact, as shown in Fig.4.3(d) that plots the temporal evolution of the height of the sand pile, when the angle gets closer to the repose angle the asymptotic trend toward equilibrium differs more. In fact, the deceleration achieved using the different models deviate from each other because of the convexity properties mentioned above (see also Fig.4.2). A difference evidentiated in Fig. 4.3(d) is the location of the inflection points of the curves in the semilog graph and consequently the logarithm of the durations of the phases where

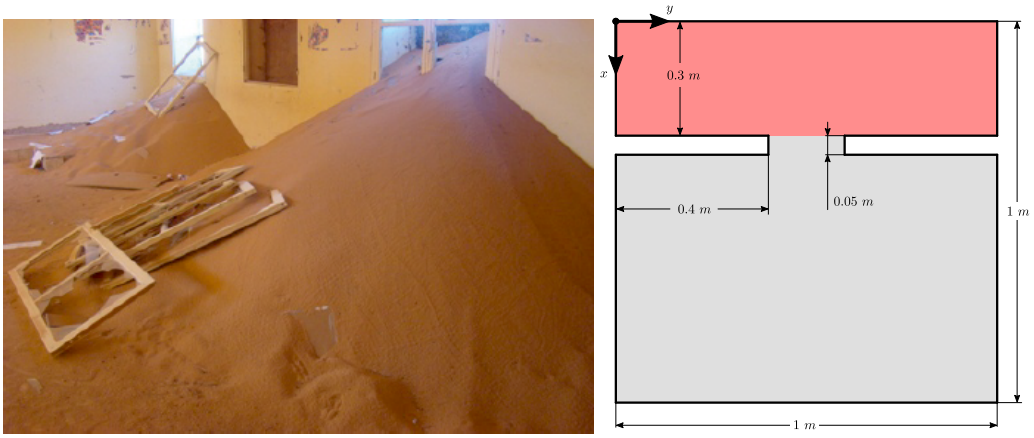

(a) (b)

Figure 4.4: Sand pile entering a room through an opening: (a) Real situation ([33], permission requested), (b) Sketch of the domain of integration close to one of the openings seen from the top.

the curve is convex and concave. As a consequence, as shown in Fig.4.3(e) the solution of the model with a Coulomb closure is the fastest and the one using a Casson fluid is the slowest (actually, the one using a Herschel-Bulkley fluid with $\gamma = 0.5$ is very close to it and if $\gamma < 0.5$ the asymptotic trend would be even slower).

The above discussion suggests that in order to identify the best closure, it is more useful to look at the temporal evolution of the sand pile tip or toe (e.g., Fig.4.3(d)) and in particular to their speed as in Fig.4.3(e), rather than focusing on the spatial evolution of the slopes because they are very similar as shown in Fig.4.3(a) and Fig.4.3(b). In this respect, Casson or Herschel-Bulkley closures with $\gamma < 1$ take much longer to reach asyntotically the stationary configuration with respect to Coulomb or Bingham closures and in this case even when the slope has an angle that is close to the repose angle, the solution still slowly moves so that it takes a long time to reach what can be considered a stop. On this basis we can state that Coulomb, Bingham or Herschel-Bulkley models with $\gamma > 1$ are more realistic than Casson or Herschel-Bulkley models with $\gamma < 1$.

On the other hand, if the main interest is in using a reliable model to get to the proper quasi-static configuration in a numerically efficient way, then Coulomb-like closure is certainly the best because it is the fastest to reach it without loosing accuracy.

4.4 Simulation in Realistic Setups

In this section we apply the model to more realistic setups, containing obstacles, walls and openings, also in presence of external sources. The first simulation regards the formation of a three-dimensional sand pile obtained constantly pouring sand in a region Ω_q on one side of a thick vertical wall (the shaded area in Fig.4.4(b)). The

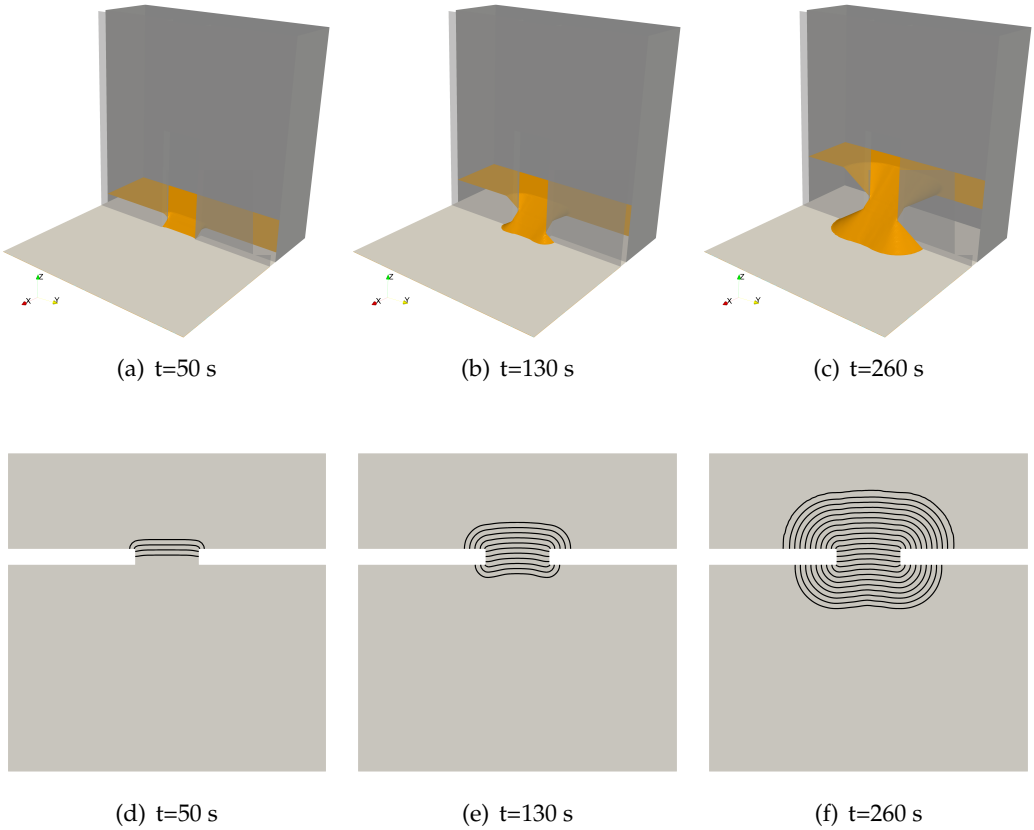

(a) t=50 s (b) t=130 s (c) t=260 s

(d) t=50 s (e) t=130 s (f) t=260 s

Figure 4.5: Profiles of sand poured in the space beyond the door and exiting from it at early times. The sliding is achieved using the DPSM with a Coulomb closure. The bottom row reports the contor plots of the 3D configurations plotted in the top row.

wall presents a 0.2 m wide and 0.05 m thick central opening Ω_d leading to a region Ω_0 having all other sides open, in the sense that when sand reaches these boundaries it can freely flow down. From the mathematical point of view, this corresponds to Dirichlet boundary conditions, while no-flux boundary conditions need be applied on the walls. The set-up can mimick situations like those shown in Fig.4.4(a) where sand came from outside the room and entered it through the openings in the walls.

Before starting the discussion, we observe that, as shown by Falcone and Finzi Vita [79–81] the change of boundary conditions may be troublesome leading to numerical problems and unphysical results more related to the mathematical model than to its numerical implementation. This is for instance the case of two-layer models. At variance with that, the DPSMs proposed here have no problem in dealing with changes in the boundary conditions and result very reliable in managing complex realistic situations and geometries. In the simulation shown in Fig.4.5 we modelled sand using a Coulomb-like closure with $\alpha_{cr} = 35°$, $\nu = 0.1\,\frac{\mathrm{m}^2}{\mathrm{s}}$, and $q = 10^{-3}\frac{\mathrm{m}}{\mathrm{s}}$ in Ω_q, but the results are very similar for all the other constitutive equations.

Coming to the description of the evolution, at the very beginning the profile is

flat between the walls in Ω_q, while close to the door sand flows down so that the sand profile takes a slope equal to the critical angle (see Fig.4.5(a)). The contour line where the surface is no longer constant is parallel to the wall in correspondence of the door and forms two circular arcs in correspondence of its jambs (see Fig.4.5(d)). After the sand slope with this triagular section has reached the other end of the wall, i.e. the boundary between Ω_d and Ω_0, the sand tends to spread also laterally to the right and to the left of the door. Closer to the jambs the shape is still conical (see Fig.4.5(b) and (e)). The foot of the sand pile advances faster on the right and on the left because more sand arrives there turning around the jambs. In the section corresponding to the middle of the door the slope is flat and the sand pile takes the shape of an inclined plane (see Fig.4.5(c) and (f)). Hence, the shape is prism-like closer to the center of the door and conic-like to its side. The steepest angle is always very close to the repose angle. Also within Ω_q the region in which the slope is non constant enlarges. Initially (see Fig.4.5(c) and (f)) it has more or less a prism-like shape corresponding to the door and a conic-like one to its side. Then at about $t = 400$ s the slope change in correspondence of the door hits the top boundary of Ω_q opposite to the door (see Fig.4.6(a) and (d)). After that, in Ω_q the sand profile takes a more funnel-like shape (see Fig.4.6(b) and (c)), while in Ω_0 the conic shape enlarges till just before $t = 650$ s the basis of the conic-like shape reaches the open end boundary. At this point also along the wall the conical shape becomes flat with an inclination close to the repose angle. Eventually, the stationary configuration is reached because the mass influx in Ω_q balances the mass outflux through $\partial\Omega_0$.

We remark that the entire simulation is very realistic and can be obtained with low computational cost, so that the update of the sand free surface does not represents a bottleneck for the entire multiphase fluid dynamics simulation that need be performed to describe sand transport in environmental problems. We notice, again, that the same final configuration is achieved with the viscoplastic closures and with Coulomb friction closure. Negligible differences in the evolution are present according to the constitutive closure used. Actually, as the flow is quasi-stationary, practically the configurations are a series of solutions of the eikonal equation. Differences increase with the ncrease of the flow rate q. However, we advise that the model might loose its validity for extremely high flow rates that may generate slopes that are much higher than the repose angle being closer to vertical slopes. In fact, in this case the hypothesis of small thickness of the sliding layer no longer holds. In spite of this, we mention that in [144] the model with a Coulomb-like closure was used to simulate experiments focusing on the collapse of initially cylindrical piles of sand, that of course start with a vertical wall, showing a satisfactory agreement.

As evident in Figs. 4.5–4.8, due to the degeneracy present in the model, a characteristic of the proposed DPSMs is the compact support of the solution starting from no sand and source term in a well defined area (and, of course, in other cases) and by the presence of slope discontinuities in the solutions. A basic example is the angle formed by the flat plane and the pile of sand or the angle between the horizontal profile in Ω_q and the sliding slope of the sand pile in Figs.4.5 and 4.6. This is a characteristic of the solution of the eikonal equation as well.

A similar thing occurs when two sand piles encounter. In order to show how the model can easily reproduce such effects and handle complicate geometries, in

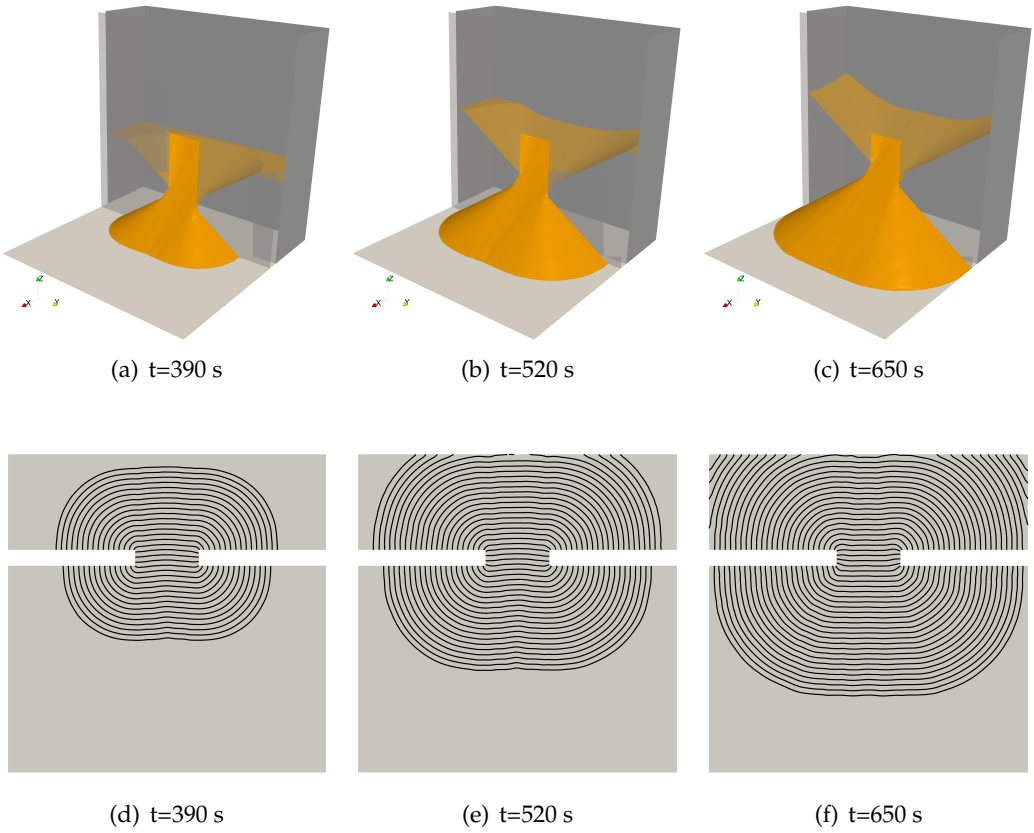

(a) t=390 s (b) t=520 s (c) t=650 s

(d) t=390 s (e) t=520 s (f) t=650 s

Figure 4.6: Profiles of sand poured in the space beyond the door and exiting from it at later times. The profile shown in (f) is almost stationary. All the sand poured between the walls falls off the open boundaries to the right and to the left. The sliding is achieved using the DPSM with a Coulomb closure. The bottom row reports the contor plots of the 3D configurations plotted in the top row.

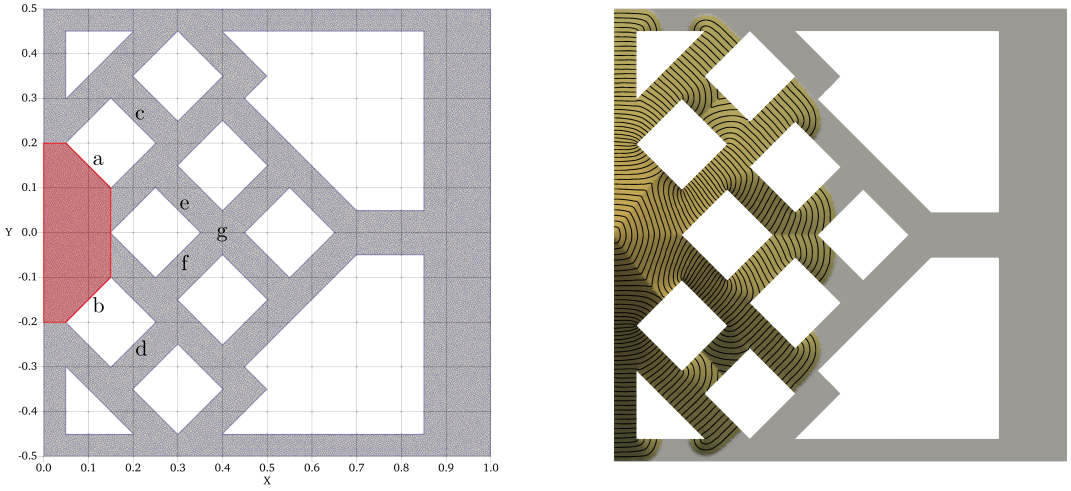

(a) (b)

Figure 4.7: (a) Domain of integration and numerical grid. The sand is poured in the region with a clearer grid. (b) Contour plot of the solution of the DPSM with Coulomb closure at $t = 840\ s$. Corners in the contour plots correspond to slope discontinuities of the sand profile.

Fig.4.7–4.8 we focus on the interaction of sand with several columns and corridors placed in the room with three open ends and a wall at $x = 0$. Sand is continuously poured close to the wall for $x \leq 0.15$ m and $|y| \leq 0.2$ m at a rate of 2 mm/s, that is, the shaded area in Fig.4.7(a).

Starting from an empty configuration, the sand continuously supplied starts accumulating in the pentagonal area sliding on its sides passing from a sort of truncated pyramidal shape (notice the flat rectangle on the top of the sand pile in Fig.4.8) to a full pyramidal-like shape with ridges, for instance, perpendicular to the sides of the columns denoted as **a** and **b** in Fig.4.7(a). In fact, the sand slides along the walls **a** and **b** from their centers in opposite directions turning around the corners with a dynamics similar to the one in Fig.4.5(b) and Fig.4.5(e). The ridge is also put in evidence in Fig.4.7(b) by the presence of corners in the contour plots. The sliding fronts then moves on the sides of the columns and then re-encounter on the other side of it forming a slope discontinuity. In fact, continuing to turn around the column, Fig.4.8 presents the configuration after the sand piles coming from the left and the right of the same corridor **c** (and symmetrically **d**) encounter forming an angle $\pi - 2\alpha_{cr}$. After that the distribution of sand in the corridor preserves the angles close to the repose value α_{cr} but the level rises up because of the continuously incoming mass flux. A similar dynamics occurs in the crossing identified by **g** in Fig.4.7(a) when the sand coming from the corridors **e** and **f** meets (see Fig.4.8). Again such slope discontinuities correspond to corners in the contour plots in Fig.4.7(b). As stressed several times along the paper, the evolution is very similar for all the closures considered above. For this reason, in Fig.4.7–4.8 only the result for Coulomb closure is shown.

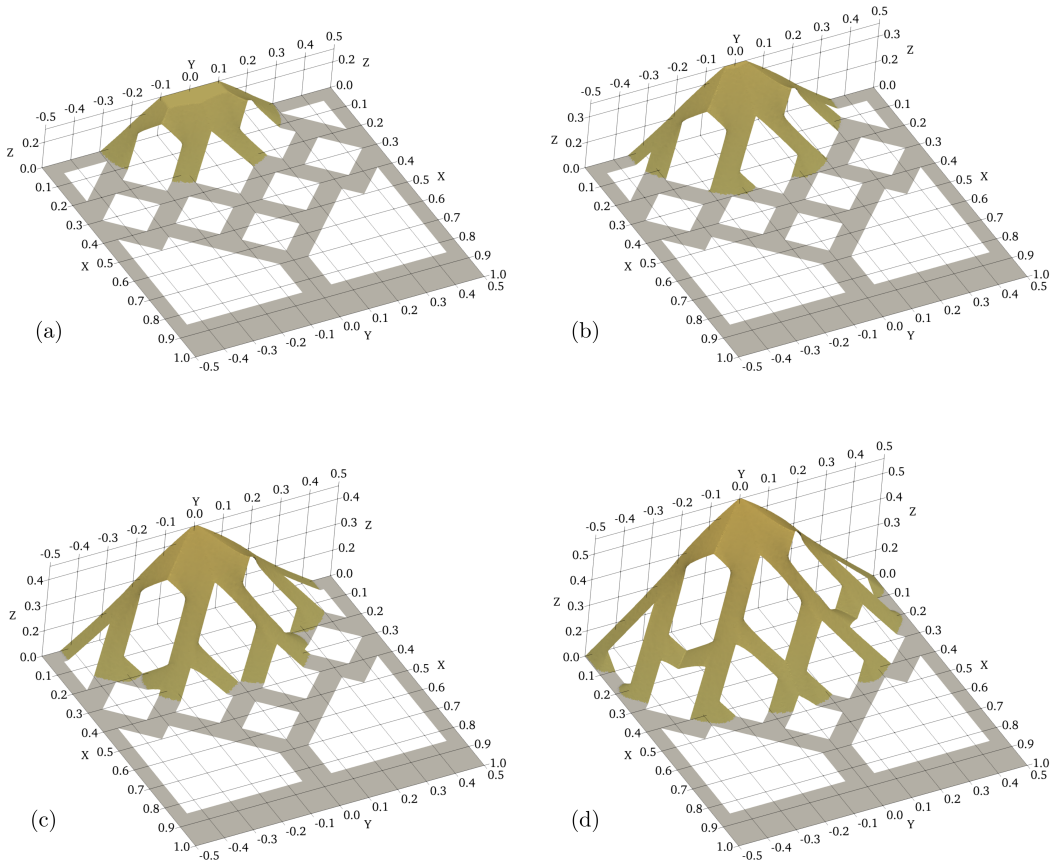

Figure 4.8: Configurations of the sand pile poured in the region highlighted in Fig.4.7a at different times $t = 150, 250, 450, 840$ s, respectively (a), (b), (c) and (d).

Chapter 5

The First Order Model

A fully Eulerian description for a multiphase flows system involves several mathematical variables. A robust validation procedure requires to have knowledge of all physical quantities in space and time. These last have to be measured from the experimental setup and then compared with the computational simulations obtained using the studied mathematical model. However, the possibility to measure all system variables at each time is the best case scenario. Unfortunately, for wind tunnel experiments - in particular in the presence of sand - this is almost impossible due to difficulties coming from the nature of fluid dynamics and the large number of degrees of freedom.

In a validation or a definition of a continuum differential model, the functions representing Eulerian quantities (and their derivatives) require a least amount of accuracy - both in space and time - in order to be reconstructed from an interpolation stage. Data reliability and quantity become even more important for boundary conditions where measurements can also involve derivatives. Measurements are discrete set of data, instead Eulerian fields are quantities described by functions over a continuum like domain. Therefore, an interpolation step is necessary to transfer the physical information from the discrete to the continuum domain. However this step can be a potential source of error if measurements are not accurate and refined enough, with the consequent risk to make mistakes in the model deduction.

In the context of aeolian sand transport there are two main categories of experiments used to take measurements and both of them have pros and cons. The first category is *infield tests* and the second is *wind tunnel tests*. A remarkable advantage of *infield tests* consists in being able to sample measurements in a natural environment, hence no artificial effects compromise the characteristics of the natural phenomenon (except for the presence of measure instruments). However, infield conditions are not under control and systematic measurements are practically unfeasible or, if possible, subjected to randomness of the atmospheric phenomena. Furthermore, in the best case scenario data can be collected in few spatial points (for the *First Order Model*'s purpose) and boundary conditions are almost impossible to determine. In addition, measure instruments are portable and usually less accurate than the instruments used in a laboratory. This because of the minor ability to take into account unpredictable events present in the natural environment.

In this chapter the purpose is to use *infield tests* results for macroscopic comparisons, i.e. once that the model is already defined its behavior is tested with plausible boundary conditions in order to verify qualitative results or macroscopic quantities

or trends. On the other side, *wind tunnel tests* are suitable for model validations because data can be collected with a decent spatial resolution, at least over one dimensional domains. Controlled like conditions allow scientists to test a wide range of physical states, hence to properly design a measurement system to perform systematic samplings. Furthermore, boundary conditions can be partially controlled. However, we remark that also classical wind tunnel tests (without sand) show several experimental difficulties, in particular in the cases of flows characterized by an high Reynolds number. The presence of particulate mass in the system obliges to adopt ad hoc wind tunnels and special equipment. In particular, due to the temporal evolution of the sandy surface the fluid domain keeps changing and eventually shows multiple fluid dynamic behaviors in the same sampling stage. This fact together with the system non-linearities can compromise the data sampling accuracy, and potentially leading to values that represent just a mean behavior in the entire experimental time span. This can eventually cause loss in the phenomenological and quantitative description of the system. Next in the chapter a list of experiments are considered and despite they share the basic experimental design, each experiment shows some difference, e.g. dimensions, sand bed shapes, measure instruments, sand types, data processing procedures. Therefore, comparisons or data aggregation are not possible in general.

In the following the focus will be on the interpretation of the general system of equations (2.1), (2.2), (2.3) and (2.4) providing the simplifications used to define the proposed *First Order Model*. We also propose a data driven algorithm to extract model coefficients depending on which turbulence model is chosen for the fluid dynamics side of the model. Furthermore, a potential generalization to multiple dispersed phases is proposed in Section 5.5, with the aim to make the model more general and suitable for future developments.

5.1 Mathematical Structure for the Single Dispersed Phase

The full set of equations (2.2), (2.1), (2.4) and (2.3) is in general not simple to solve and numerical approaches are usually tailored for the physical context that might suggests proper simplifications. As already remarked, experimental observations show that most of the physical domain is filled by clean air. Furthermore, the region where saltation occurs is small and confined nearby the ground surface where also the maximum concentration value of φ_s is small. Hence

$$\varphi_f \simeq 1 \,. \tag{5.1}$$

For the fluid phase, the approximation (5.1) together with the constant fluid density leads to Navier-Stokes equations for an incompressible Newtonian fluid

$$\begin{cases} \nabla \cdot \mathbf{u}_f = 0 \,, \\ \dfrac{\partial \mathbf{u}_f}{\partial t} + \mathbf{u}_f \cdot \nabla \mathbf{u}_f = -\dfrac{1}{\rho_f} \nabla p_f + \nabla \cdot \left(\nu_f \nabla \mathbf{u}_f \right) + \dfrac{1}{\rho_f} \mathbf{m}_f \,. \end{cases} \tag{5.2}$$

Though in the *First Order Model* mathematical structure the turbulence treatment can be generic, classical industrial domains are so large to suggest the usage of RANS models and for sake of simplicity a $k - \omega$ closure is reported here (other models

follow the same argument). Hence, the complete set of equations for the fluid phase reads

$$\begin{cases} \nabla \cdot \overline{\mathbf{u}}_f = 0 \,, \\ \dfrac{\partial \overline{\mathbf{u}}_f}{\partial t} + \overline{\mathbf{u}}_f \cdot \nabla \overline{\mathbf{u}}_f = -\dfrac{1}{\rho_f} \nabla \overline{p}_f + \nabla \cdot \left[(\nu_f + \nu_t) \nabla \overline{\mathbf{u}}_f \right] + \dfrac{1}{\rho_f} \mathbf{m}_f \,, \\ \dfrac{\partial k}{\partial t} + \nabla \cdot (k \overline{\mathbf{u}}_f) = \nabla \cdot [(\sigma_k \nu_f + \nu) \nabla k] + \tilde{P}_k - \beta^* k \omega \,, \\ \dfrac{\partial \omega}{\partial t} + \nabla \cdot (\omega \overline{\mathbf{u}}_f) = \nabla \cdot [(\sigma_\omega \nu_f + \nu) \nabla \omega] + \alpha \dfrac{\omega}{k} P_k - \beta \omega^2 + (1 - F_1) \dfrac{2 \sigma_\omega}{\omega} \nabla k \cdot \nabla \omega \,, \end{cases} \tag{5.3}$$

where k is the *turbulent kinetic energy*, ω is the *specific dissipation* and ν_t is the turbulent viscosity. Other parameters are defined as

$$k := \frac{1}{2} \left(\langle \tilde{\mathbf{u}}_{f,x}^2 \rangle + \langle \tilde{\mathbf{u}}_{f,y}^2 \rangle + \langle \tilde{\mathbf{u}}_{f,z}^2 \rangle \right) \,, \tag{5.4}$$

$$\omega := \frac{1}{0.09} \frac{\nu_f}{k} \sum_{i=1}^{3} \sum_{j=1}^{3} \left\langle \frac{\partial \tilde{\mathbf{u}}_{f,i}}{\partial x_j} \frac{\partial \tilde{\mathbf{u}}_{f,i}}{\partial x_j} \right\rangle \,, \tag{5.5}$$

$$\nu_t := \frac{k}{\omega} \,, \tag{5.6}$$

where $\tilde{\mathbf{u}}$ is the fluctuating velocity and $\langle \cdot \rangle$ is the mean operator (see [158] for details). The second main assumption regards the absence of the momentum equation (2.3) for $\mathbf{u}_s$. In fact, for cases where inertia is negligible, experimental observations suggest that while they sediment, particles are convected by the fluid with a velocity proportional to $\overline{\mathbf{u}}_f$ (see [17]), hence the solid velocity can be decomposed in a convective and diffusive flow as

$$\mathbf{u}_s = \underbrace{\alpha_s \overline{\mathbf{u}}_f + w_{sed} \mathbf{e}_z}_{\text{convective flow}} \underbrace{- \frac{\nu_{eq}}{\varphi_s} \nabla \varphi_s}_{\text{diffusive flow}} \,, \tag{5.7}$$

where w_{sed} is the particle sedimentation velocity and α_s is a function of the wall distance and the horizontal component of the fluid velocity. The term ν_{eq} is a diffusivity function named *equivalent diffusion*. It describes the diffusive-like behavior of the sand cloud when the dynamic equilibrium is reached and its analytical definition is the goal of Section 5.3 and 5.4.

The convection-diffusion formulation allow to use finite volume methods to solve numerical simulations for large scale industrial cases. Indeed in the *SMaRT* project, the computational tools have been chosen (a priori) in order to be suitable for industrial applications (in particular *OpenFOAM-extend-4.0* as computational package). However, these software packages has some limitations in the categories of partial differential equations that can be solved. We also remind that numerical analysis for an eventual special numerical methodology would be out of the scope of the thesis. Therefore, the development is a compromise between practical needs and theoretical aspects. As consequence the differential equations defining the model are developed by taking into account the available computational tools.

Substituting (5.7) in (2.1), the conservation equation for the solid phase reads

$$\frac{\partial \varphi_s}{\partial t} + \nabla \cdot \left(\left(\alpha_s \overline{\mathbf{u}}_f + w_{sed} \mathbf{e}_z \right) \varphi_s - \nu_{eq} \nabla \varphi_s \right) = 0 \, . \tag{5.8}$$

The function ν_{eq} is a generic function of the state variables and its realization, together with boundary conditions and (5.3), completely define the *First Order Model*. Section 5.4.2 introduces an algorithm to define ν_{eq} addressing the dependence from the system variables. The particles effect on turbulence is not taken into account but accordingly to [17, 145] the effect is negligible for small value of φ_s. Therefore, we suppose that k and ω are not function of φ_s and $\mathbf{m}_f \simeq \mathbf{0}$. Instead, the turbulent effect on the particles motion is taken into account by decomposing ν_{eq} in the sum of two separate diffusivities

$$\nu_{eq} = \lambda \nu_t + \nu_{coll} \, . \tag{5.9}$$

The turbulent diffusivity ν_t appearing in (5.3) is obtained from the turbulent model. The term λ is a tuning coefficient that allows to control the turbulence effect on the cloud dynamics and it provides more flexibility for experimental validations. The collisional diffusivity ν_{coll} aims to model the dynamics of the cloud particle system due to the action of the mean flow.

The errors of numerical and turbulence models make the particle feedback on the turbulence very difficult to evaluate with sufficient accuracy. As mentioned above, the effect of particles on turbulence is negligible for low concentrations. In conclusion, the system of equations for the *First Order Model* reads

$$\begin{cases} \nabla \cdot \overline{\mathbf{u}}_f = 0 \, , \\ \dfrac{\partial \overline{\mathbf{u}}_f}{\partial t} + \overline{\mathbf{u}}_f \cdot \nabla \overline{\mathbf{u}}_f = -\dfrac{1}{\rho_f} \nabla \overline{p}_f + \nabla \cdot \left[(\nu_f + \nu_t) \nabla \overline{\mathbf{u}}_f \right] + \dfrac{1}{\rho_f} \mathbf{m}_f \, , \\ \dfrac{\partial k}{\partial t} + \nabla \cdot (k \overline{\mathbf{u}}_f) = \nabla \cdot \left[(\sigma_k \nu_f + \nu) \nabla k \right] + \tilde{P}_k - \beta^* k \omega \, , \\ \dfrac{\partial \omega}{\partial t} + \nabla \cdot (\omega \overline{\mathbf{u}}_f) = \nabla \cdot \left[(\sigma_\omega \nu_f + \nu) \nabla \omega \right] + \alpha \dfrac{\omega}{k} P_k - \beta \omega^2 + (1 - F_1) \dfrac{2 \sigma_\omega}{\omega} \nabla k \cdot \nabla \omega \, , \\ \dfrac{\partial \varphi_s}{\partial t} + \nabla \cdot \left(\left(\alpha_s \overline{\mathbf{u}}_f + w_{sed} \mathbf{e}_z \right) \varphi_s - \nu_{eq} \nabla \varphi_s \right) = 0 \, . \end{cases} \tag{5.10}$$

5.2 Auxiliary Modeling Aspects

The analytical structure of the functions presented in (5.10) modifies the physical properties of outcoming solutions. In the following of this section some analytical aspects are discussed in the light of physical and modeling considerations.

5.2.1 Effects of the Mean and Turbulent Flow Decomposition

In a turbulence model the fluid velocity $\mathbf{u}$ is decomposed as

$$\mathbf{u} = \overline{\mathbf{u}} + \tilde{\mathbf{u}} \, , \tag{5.11}$$

where $\overline{\mathbf{u}}$ is the mean (respectively filtered) velocity and $\tilde{\mathbf{u}}$ is the fluctuating (respectively sub-filtered) velocity for RANS (respectively LES) approaches. This decomposition has direct consequences on the matematical quantities related to $\mathbf{u}$. In classical continuum mechanics, well known theorems concerning symmetries and constitutive axioms define analytical and algebraic properties of constitutive laws. Here is presented the second invariant of the strain tensor

$$\mathbb{D} := \frac{1}{2}\left(\nabla\mathbf{u} + \nabla\mathbf{u}^T\right) \tag{5.12}$$

which is used later in the model definition. Subscripts are omitted because statements are valid for every phase. Due to the linearity of the $\nabla(\cdot)$ differential operator

$$\mathbb{D} = \overline{\mathbb{D}} + \tilde{\mathbb{D}}\,, \tag{5.13}$$

where $\overline{\mathbb{D}}$ and $\tilde{\mathbb{D}}$ are defined using equation (5.12) respectively with $\overline{\mathbf{u}}$ and $\tilde{\mathbf{u}}$. The second invariant for the strain tensor reads

$$II_{\mathbb{D}} = \frac{1}{2}\left(tr^2\mathbb{D} - tr\mathbb{D}^2\right)\,, \tag{5.14}$$

where $tr(\cdot)$ is the trace operator for second order tensors. Substituting equation (5.13) in (5.14) the following relations hold

$$\begin{aligned} tr^2\mathbb{D} &= tr^2\overline{\mathbb{D}} + tr^2\tilde{\mathbb{D}} + 2\,tr\overline{\mathbb{D}}\,tr\tilde{\mathbb{D}}\,,\\ tr\mathbb{D}^2 &= tr\overline{\mathbb{D}}^2 + tr\tilde{\mathbb{D}}^2 + tr\overline{\mathbb{D}}\tilde{\mathbb{D}} + tr\tilde{\mathbb{D}}\overline{\mathbb{D}}\,, \end{aligned}$$

leading to the next final relation for the second invariant

$$II_{\mathbb{D}} = II_{\overline{\mathbb{D}}} + II_{\tilde{\mathbb{D}}} + tr\overline{\mathbb{D}}\,tr\tilde{\mathbb{D}} + tr\overline{\mathbb{D}}\,tr\tilde{\mathbb{D}} - tr\overline{\mathbb{D}}\tilde{\mathbb{D}}\,. \tag{5.15}$$

This decomposition highlights the effects of the field $\tilde{\mathbf{u}}$ in the second invariant $II_{\mathbb{D}}$. Once the turbulence model is chosen only the mean field $\overline{\mathbf{u}}$ is computed. The components of $\tilde{\mathbf{u}}$ can be estimated from the turbulent kinetic energy (5.4). This fact implies that only the term $II_{\overline{\mathbb{D}}}$ can be computed and the other terms must be modeled of neglected. Analogous arguments regard $I_{\mathbb{D}}$ and $III_{\mathbb{D}}$. As a consequence, in the context of the *First Order Model*, the choice of a turbulence model has a direct effect on the transport model of a solid phase because it is directly affect $II_{\overline{\mathbb{D}}}$.

5.2.2 Sedimentation Velocity and Drag Coefficients

Equation (5.7) includes the quantity w_{sed} which represents the sedimentation velocity. This is intended as an equilibrium settling velocity of a single solid particle in a motionless fluid resulting from the equilibrium of gravitational ($F_g = \rho_s V g$), buoyant ($F_b = \rho_f V g$) and drag forces ($F_d = 1/2 C_d \rho_f w_{sed}^2 A$) (see Figure 5.1). According to the particle Reynolds number ($Re_p = w_{sed} d/\nu_f$), the drag force shows different behaviors in different ranges of Re_p. In Stokes regime ($Re_p < 0.1$), the drag coefficient decreases with the particle Reynolds number and can be approximated by $C_d = 24/Re_p$. For the range of particle Reynolds numbers between 0.1 and 1000 (i.e. intermediate regime) the value of the drag coefficient continues to reduce increasing the Reynolds number, but with a lower rate than in the Stokes regime. In Newton's

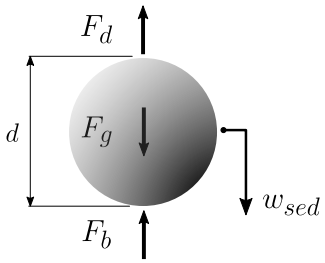

Figure 5.1: Forces on falling sphere

regime ($Re_p > 1000$) the drag coefficient is almost constant with a minimum value of 0.38 and maximum value of 0.5 (see [15]). Figure 5.2 (a) shows the representation of the explicit formula (5.16) for the drag coefficient suggested by [15] and its fitting with the experimental data from [41]:

$$C_d = \frac{24}{Re_p}(1 + 0.15Re_p^{0.687}) + \frac{0.42}{1 + \frac{42500}{Re_p^{1.16}}} \,. \tag{5.16}$$

From the balance of forces (F_b is neglected because $\rho_s/\rho_f > 10^3$) we obtain

$$C_d Re_p^2 = \frac{4\rho_s \rho_f g}{3\mu_f^2} d^3 \tag{5.17}$$

which is an equation only of physical properties of solid and liquid phase and the diameter of sphere. Substituting (5.16) in (5.17) we get the implicit relation (5.18) between d and Re_p. Hence

$$\frac{24}{Re_p}(1 + 0.15Re_p^{0.687}) + \frac{0.42}{1 + \frac{42500}{Re_p^{1.16}}} Re_p^2 = \frac{4\rho_s \rho_f g}{3\mu_f^2} d^3 \,. \tag{5.18}$$

Once the diameter is fixed, we can numerically find the value of Re_p such that equation (5.18) is satisfied. The outcoming values of Re_p and d allow to evaluate the sedimentation velocity by inverting the definition of Re_p, then

$$w_{sed} = \frac{\nu_f Re_p}{d} \,.$$

In Figure 5.2 (b), the sedimentation velocity for Stokes regime is plotted in red using the expression (5.19), the sedimentation velocity for Newton regime is plotted in green using the expression (5.20), while the blue line represents the sedimentation velocity obtained with Bagheri's drag coefficient formula (5.16) and the numerical approach explained above.

$$w_{sed,Stokes} = \frac{(\rho_s - \rho_f)g}{18\mu_f} d^2 \tag{5.19}$$

$$w_{sed,Newton} = \sqrt{\frac{4(\rho_s - \rho_f)g}{3\rho_f C_d} d} \tag{5.20}$$

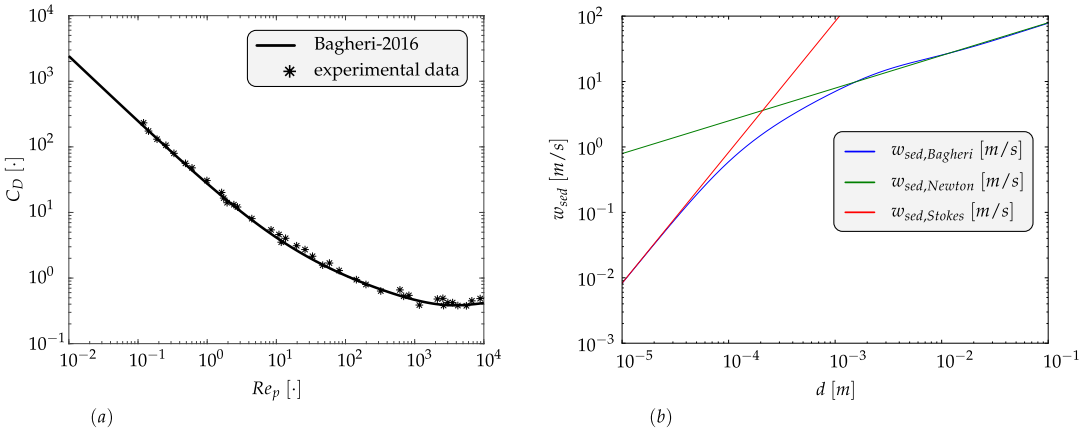

Figure 5.2: (a) Representation of the explicit formula from [15]. (b) Dependence of sedimentation velocity on diameter in different regimes.

Even though the sedimentation velocity is a value for a single particle falling in steady air, in the model it is used to quantify the convective vertical field in (5.7) for the solid phase.

5.2.3 Estimate of Momentum Exchange of Drag Force m

The momentum exchange term **m** in equations (2.3) and (2.4) describes the interaction between fluid and solid phase. Here we aim to calculate **m** addressing particles in a generic control volume. If the i index identifies the i-th particle inside of a generic control volume:

$$\delta \mathbf{u}_i := \mathbf{u}_f - \mathbf{u}_i \ . \tag{5.21}$$

$$\delta d_i := d_i - \langle d \rangle \ , \tag{5.22}$$

$$\Delta d := max\left\{|\delta d_i| \ such \ that \ \ i \in \{1, \cdots, N\}\right\} \ , \tag{5.23}$$

$$\langle d \rangle = \frac{1}{N}\sum_{i=1}^{N} d_i \qquad \text{mean particle diameter} \ , \tag{5.24}$$

$$\langle a \rangle = \frac{\pi}{4}\langle d \rangle^2 + O(\Delta d) + O(\Delta d^2) \qquad \text{mean particle frontal area} \ , \tag{5.25}$$

$$\langle v \rangle = \frac{\pi}{6}\langle d \rangle^3 + O(\Delta d) + O(\Delta d^2) + O(\Delta d^3) \qquad \text{mean particle volume} \ . \tag{5.26}$$

Equations (5.25) and (5.26) are derived by using definitions (5.22), (5.23) and (5.24). Supposing that the range of particle diameters is bounded around a mean value, the term $O(\Delta d)$, $O(\Delta d^2)$ and $O(\Delta d^3)$ can be neglected. The symbol $\mathscr{V}$ identifies a generic control volume where both solid and fluid phases can occupy its spatial region. The symbol $\mathscr{V}_s$ identifies the volume occupied by the solid phase within $\mathscr{V}$. Combining the formulae above it is possible to estimate the total number of particles N within the control volume. Indeed

$$\langle v \rangle N \simeq |\mathscr{V}_s| =: \varphi_s |\mathscr{V}| \ ,$$

$$\frac{1}{N} = \frac{\langle v \rangle}{\varphi_s |\mathscr{V}|} \ . \tag{5.27}$$

In the Eulerian-Eulerian approach it is necessary to express quantities in each point of the domain. In order to do that we relate the integral in a control volume of $\mathbf{m}$ with the sum of the Lagrangian force field acting on each particle. This can be viewed as the application of the third law of dynamics, hence

$$\overbrace{\int_{\mathscr{V}} \mathbf{m}\, d\mathscr{V}}^{\text{Integral}} = \overbrace{\sum_{i=1}^{N} \frac{1}{2}\rho_f C_d a_i \|\delta\mathbf{u}_i\|\delta\mathbf{u}_i}^{\text{Particles}}$$

$$\frac{1}{N}\int_{\mathscr{V}} \mathbf{m}\, d\mathscr{V} = \frac{1}{N}\sum_{i=1}^{N} \frac{1}{2}\rho_f C_d a_i \|\delta\mathbf{u}_i\|\delta\mathbf{u}_i$$

$$\frac{\langle v\rangle}{\varphi_s|\mathscr{V}|}\int_{\mathscr{V}} \mathbf{m}\, d\mathscr{V} \simeq \frac{1}{N}\sum_{i=1}^{N} \frac{1}{2}\rho_f C_d a_i \|\delta\mathbf{u}_i\|\delta\mathbf{u}_i \ .$$

With this equivalence we can evaluate the mean interaction force within the control volume

$$\begin{aligned}
\langle\mathbf{m}\rangle := \frac{1}{|\mathscr{V}|}\int_{\mathscr{V}} \mathbf{m}\, d\mathscr{V} &= \frac{\varphi_s}{\langle v\rangle}\frac{1}{N}\sum_{i=1}^{N} \frac{1}{2}\rho_f C_d a_i \|\delta\mathbf{u}_i\|\delta\mathbf{u}_i \\
&= \varphi_s \frac{1}{N}\sum_{i=1}^{N} \frac{1}{2}\rho_f C_d \frac{a_i}{\langle v\rangle}\|\delta\mathbf{u}_i\|\delta\mathbf{u}_i \\
&\simeq \varphi_s \frac{1}{N}\sum_{i=1}^{N} \frac{1}{2}\rho_f C_d \frac{\langle a\rangle}{\langle v\rangle}\|\delta\mathbf{u}_i\|\delta\mathbf{u}_i \\
&= \varphi_s \frac{1}{N}\sum_{i=1}^{N} \frac{3}{4}\rho_f C_d \frac{1}{\langle d\rangle}\|\delta\mathbf{u}_i\|\delta\mathbf{u}_i \\
&= \varphi_s \frac{3}{4}\rho_f \frac{C_d}{\langle d\rangle}\frac{1}{N}\sum_{i=1}^{N} \|\delta\mathbf{u}_i\|\delta\mathbf{u}_i \\
&= \varphi_s \frac{3}{4}\rho_f \frac{C_d}{\langle d\rangle}\langle\|\delta\mathbf{u}\|\delta\mathbf{u}\rangle \ ,
\end{aligned}$$

hence

$$\langle\mathbf{m}\rangle = \varphi_s \frac{3}{4}\rho_f \frac{C_d}{\langle d\rangle}\langle\|\delta\mathbf{u}\|\delta\mathbf{u}\rangle \ .$$

We can therefore compute the following limit

$$\mathbf{m} = \lim_{|\mathscr{V}|\to|\mathscr{V}_0|}\langle\mathbf{m}\rangle = \lim_{|\mathscr{V}|\to|\mathscr{V}_0|}\varphi_s \frac{3}{4}\rho_f \frac{C_d}{\langle d\rangle}\langle\|\delta\mathbf{u}\|\delta\mathbf{u}\rangle \ ,$$

where $\mathscr{V}_0$ is the smallest control volume for which ensemble mean operations make sense. Therefore, it is reasonable to write the interaction force as

$$\mathbf{m} = \frac{3}{4}\frac{C_d}{\langle d\rangle}\varphi_s\rho_f\|\mathbf{u}_f - \mathbf{u}_s\|(\mathbf{u}_f - \mathbf{u}_s) \Longrightarrow \mathbf{m}\, d\mathscr{V} = d\mathbf{F}_{drag} \ . \tag{5.28}$$

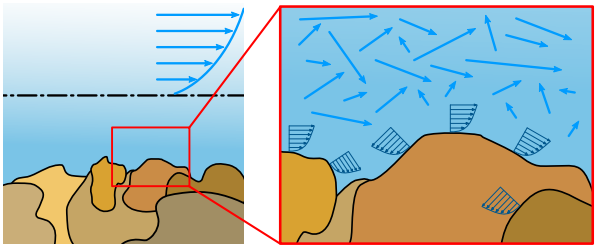

Figure 5.3: Qualitative representation of the flow around still particles near the ground.

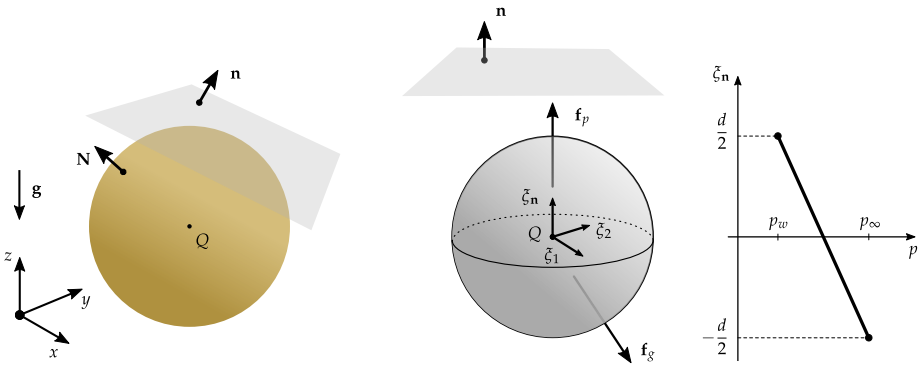

Figure 5.4: Geometrical representation of gravity and pressure forces acting on a spherical particle of diameter d. p_∞ is the constant atmospheric pressure and p_w is the wall pressure.

5.2.4 Density Force Acting on Ground Sand

The physical mechanism that causes the pneumatic conveying of sand grains within the flow depends on fluid dynamic forces acting on each still grain on the ground surface. For an incompressible Newtonian fluid the surface forces can be divided in the static pressure force and the viscous force. For low viscosity fluids the static pressure term is dominant with respect to the viscous term. Furthermore the fluid velocity is null on the ground surface because of the no-slip boundary condition (see Figure 5.3). This observation suggests that within the total force acting on the single grain the static pressure field is much larger than the viscous contribution. We also remark that we can not make general assumptions on the pressure field.

Starting from this assumption, a simplified formula is derived to estimate the force that determines whether erosion is effective or not (for a grain that lays on the ground). For sake of simplicity we consider a spherical particle of diameter d as shown in Figure 5.4.

In Figure 5.4 the symbols are defined as follow:

- **n** is the unitary vector normal to the ground surface
- **N** is the unitary vector normal to the particle surface
- **g** is the gravitational field
- p is the pressure field

- p_∞ is the constant atmospheric pressure
- p_w is the ground pressure
- $\mathbf{f}_g$ is the resulting force on the grain due to the gravity field
- $\mathbf{f}_p$ is the resulting force on the grain due to the pressure field

Assuming that the real pressure field has small variations near the spatial region surrounding a still particle, we can approximate p with a Taylor expansion

$$p(P) = p(Q) + \langle \nabla p(Q) | (P - Q) \rangle_{\mathbb{R}^3} + o(\|P - Q\|) \,. \tag{5.29}$$

Therefore, the resulting force due to the pressure field reads

$$\mathbf{f}_p = -\int_{\partial \mathscr{V}} p\, \mathbf{N}\, d\Sigma \;= \int_{\mathscr{V}} \nabla p \, d\mathscr{V} \overset{(5.29)}{=} |\mathscr{V}| \nabla p(Q) \simeq \frac{\pi d^3}{6} \left(\frac{p_\infty - p_w}{d} \right) \mathbf{n} \,,$$

where $\mathscr{V} := S^3(Q, \frac{d}{2})$ and $\mathbf{N}$ is the unitary vector orthogonal to the sphere surface, we therefore obtain

$$\mathbf{f}_p \simeq \frac{\pi d^3}{6} \left(\frac{p_\infty - p_w}{d} \right) \mathbf{n} \tag{5.30}$$

and the resulting force due to the gravity is

$$\mathbf{f}_g = \frac{\pi d^3}{6} \rho_s \mathbf{g} \,. \tag{5.31}$$

The resulting force acting on a still particle is made up by the summation of $\mathbf{f}_p$ and $\mathbf{f}_g$. In order to provide a practical interpretation let consider a flat ground surface, therefore all vectors have the same direction. The summation leads to the normal acting force

$$f_n = \frac{\pi d^3}{6} \left(\frac{p_\infty - p_w}{d} - \rho_s \|\mathbf{g}\| \right) \,. \tag{5.32}$$

If f_n is positive - for a large enough time span - the force magnitude is large enough to pull the grain and erosion could occur. On the contrary, for negative values the grain remains still. In (5.32) only p_w is a system variable, the others are known constants. Its value is strictly related to the flow surrounding the sand grain. In particular, it is related to the time variation of the pressure due to turbulent fluctuations. In case of an unsteady CFD simulation, p_w corresponds to the pressure boundary value. However, we must consider that turbulence models have relevant effects on the signal time spectrum (because they substantially operate a filtering process on signals). As a consequence, an ad hoc model has to be defined to overcome this problem. DNS simulations would be suitable for the spectral analysis, but Reynolds numbers characteristic of aeolian flows are too high for their application. Furthermore, very intricate geometries are not suitable for spectral methods that are typically used to speed up computational time and to increase the numerical accuracy. Possible alternatives to numerical simulations are ad hoc experiments to evaluate the gradient of pressure in the narrowed spatial region where the triggering mechanism occurs (see Figure 2.1(b)). For example, a series of pressure sensors can sample data for a time span that is large enough to apply Ergodic hypothesis.

Therefore, to come up with a statistically relevant amount of data. Another approach can consist in the analysis of slow motion videos by mean of computer vision algorithms. In conclusion, it is reasonable to chose a semi-empirical approach to face the industrial problems in the SMaRT context, hence the importance of experimental data quality results obvious. In this perspective, [54, 82] look interesting. However, a wide dataset is needed in order to perform reliable statistics.

5.2.5 General Structure of Boundary Conditions

Partial differential equations require a set of proper boundary conditions in order to be able to identify and compute a unique solution. In the context of multiphase flows, phases are described by sufficiently regular functions. In fluid dynamics and consequently in aeolian transport, boundary layers are created and high gradients occur for most of the quantities involved in mathematical models. They occur nearby wall regions because of the hyperbolic character of equations and the necessity to satisfy the no slip boundary condition. Wall functions are developed in the CFD context in conjunction with turbulence models. The definition of wall functions is based on the wall distance, which is the euclidean distance from the boundary geometric surface. Therefore a geometric surface has to be defined in order to be able to apply them in correspondence of no-slip boundary conditions. This is the main reason why in the *First Order Model* the interface between air-sand mixture and steady sand is described as an explicit geometric surface. In other words, the computational domain does not extend to the physical region under the soil. Other approaches are used in literature, e.g. [34], where a steady mesh is defined and the interface between fluid-solid mixtures and sediment phase does not explicitly exist. The main problem of this approach regards conditions where strong gradients occur. Without an explicit representation of a boundary surface the physical behavior have to be modeled by the stress tensor. Therefore, the model has to be able to replicate the effect of wall functions. Without a proper algorithm for mesh refinement, numerical and modeling errors risk to compromise the quality of numerical solutions.

According to [102], the final sand cloud behavior is massively affected by the ground mechanical properties. In particular grain size and ground impact properties influence the resultant boundary status. Because of this, it is necessary to formulate proper boundary models in order to mimic the physical boundary conditions. Furthermore, these must take into account morphodynamics of ground patch and satisfy mass conservation in the global domain.

Classical boundary conditions are used for the fluid phase, in this section the focus is on the variable φ_s because it is the most important one from the sand transport perspective. The combination of surface motion and mass conservation for an infinitesimal element $d\Sigma$ leads to

$$-\varphi_{cp} u_\Sigma \mathbf{n}\, d\Sigma\, dt = \varphi_s (\mathbf{u}_s \cdot \mathbf{n}) \mathbf{n}\, d\Sigma\, dt\,, \tag{5.33}$$

where $\varphi_{cp} \sim 0.6$ is the *close packing volume ratio of sand*, u_Σ is the *kinematic surface velocity* and $\mathbf{n}$ is the *surface unitary normal vector* which conventionally points into the air domain. Equation (5.33) represents a kinematic constraint linking together mass conservation and morphodynamics because it states that the mass introduced

in the computational domain by means of patch movement in the infinitesimal time dt must be equal to the net solid mass flux over the element $d\Sigma$. Equation (5.33) is general and it can contain a non-linear dependence from other system quantities.

The *First Order Model* formulation can be used to state mathematical expressions of boundary condition, in fact sand velocity $\mathbf{u}_s$ is approximated by splitting convective and diffusive term hence equation (5.33) leads to

$$\varphi_{cp} u_\Sigma = w_{sed}(\mathbf{e}_z \cdot \mathbf{n})\varphi_s + \nu_{eq}\frac{\partial \varphi_s}{\partial n} \,. \tag{5.34}$$

This equation represents a Robin boundary condition and in this form it can still contain non-linear dependencies. It can describe unsteady states but experimental data are not sufficiently accurate to determine the sandy surface kinematics.

Steady State The ground surface moves slowly under the action of sand erosion and deposition. If we consider a short period of time and we focus on the horizontal mass transport we can set the surface velocity to zero. The same condition occurs if erosion and deposition balance themselves. Mathematically speaking, a steady condition implies that each variable in the mathematical system does not depend on time, therefore the ground surface must be also steady. In the steady case equilibrium is reached by definition, therefore $u_\Sigma \equiv 0$, therefore (5.34) leads to

$$w_{sed}(\mathbf{e}_z \cdot \mathbf{n})\varphi_s + \nu_{eq}\frac{\partial \varphi_s}{\partial n} = 0 \tag{5.35}$$

which is the Robin boundary condition to be used for steady aeolian sand transport simulations. Equation (5.35) expresses the physical fact that the net flux of sand through the ground surface is null, and the analytical expression of ν_{eq} fully embeds ground mechanical properties. According to [102], ground conditions massively affect final results, therefore complex physical states of the surface must be well described by boundary conditions. In section 5.4.4 a possible data driven approach is proposed by considering the specific case of erodible surfaces. For non-erodible surfaces (5.35) applies also in unsteady simulations. However, for generic unsteady flows the boundary status can switch from erodible to non-erodible (and vice versa) due to the system evolution.

5.3 First Approach to Determine the Collisional Diffusivity

The first step in the data-driven modeling procedure is to find a proper experimental setup that can be tested by means of numerical simulations. It is important to collect as many details as possible from the experimental setups because each detail could affect sampled data. In particular - due to the fact that a best practice procedure and standard measuring protocols do not exist for wind tunnel aeolian tests - it is not always possible to directly compare data among different experiments. Furthermore, due to the instabilities of fluid systems the air flow can drastically change under small changes in the system. In fact, wind tunnel environments are notoriously difficult to be controlled due to the chaotic behavior of the fluid. Classical quantities used in fluid dynamics are problematic to measure because instruments themselves

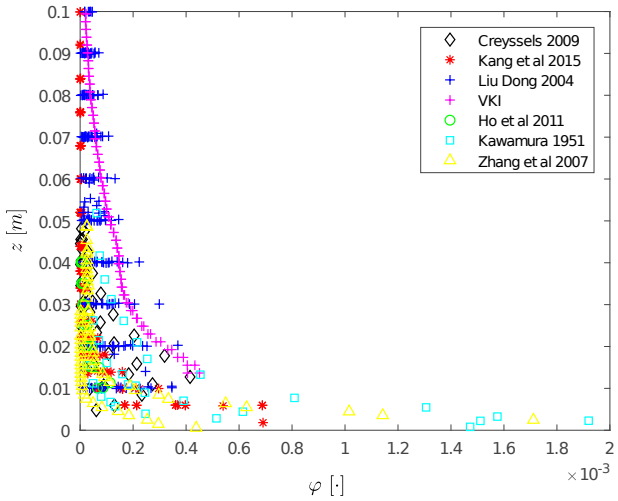

Figure 5.5: General representation of solid concentration profiles from several literature papers.

affect the flow state. Furthermore, the experimental scientific literature that we have considered shows that data are sampled over vertical array of points. Multiscale features of aeolian physics makes really problematic to build an easily controllable experimental setup that allows to provide data with high space-time accuracy.

Keeping this in mind, we searched through the scientific literature and selected seven scientific papers (Creyssels 2009 [58], Dong 2006 [64], Ho 2011 [102], Liu 2004 [142], Kang 2015 [122], Kawamura 1951 [203], Zhang 2007 [238]) as potentially useful. However, only three of them are taken into account in this first stage, because their data resolution is sufficient for the fitting procedure.

Particle concentration is the most important quantity to be monitored together with the other quantities describing the fluid dynamics field. There exist several technologies for the concentration data sampling and different units of measure are used by different authors. We represent the particle concentration by means of its volume fraction as dimensionless quantity. Figure 5.5 shows the particle concentration distribution from several papers with similar (but not equal) experimental setups. We remark that in all analyzed article the statistical characterization of data is missing. The first thing to notice in Figure 5.5 is the spread value of the particle concentrations. In particular we observe really small values of volume fraction φ_s with high gradients near the sand bed. Another relevant observation regards the spatial extension of the sand transport that only occupies approximately 10 cm from the ground. We remark that data reliability is also affected by post-processing analysis that processes raw data from instruments. Therefore, several source of errors could affect the final used data. In particular, very low particle concentrations correspond to the presence of few particle in control volumes (see Figure 5.6), hence the solid concentration might be questionable in the Eulerian context and need to be considered with care. The next sections are devoted to deal with part of these data and to justify the choices made in the *First Order Model* data-driven definition.

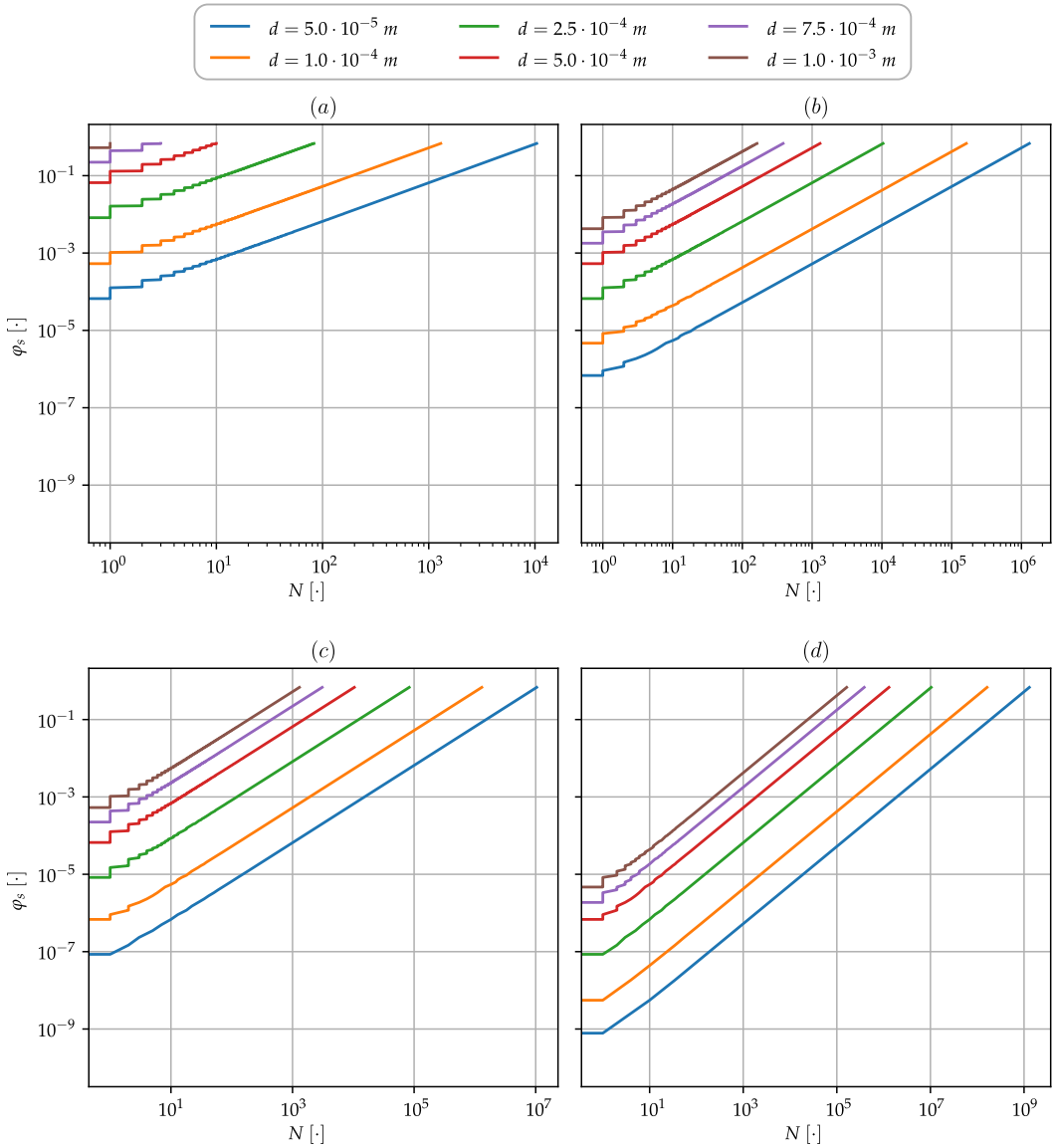

Figure 5.6: Solid concentration as a function of number of particles in four different cubes: (a) $1mm^3$, (b) $5mm^3$, (c) $1cm^3$ and (d) $5cm^3$

5.3.1 Fitting Models

Considering that the experiment descriptions are vague in several aspects, we suppose that the sand flow is measured when equilibrium is reached. This means to use a steady state of (5.8), hence

$$\nabla \cdot \mathbf{q}_s = \nabla \cdot \left(\left(\alpha_s \overline{\mathbf{u}}_f + w_{sed} \mathbf{e}_z \right) \varphi_s - \nu_{eq} \nabla \varphi_s \right) = 0 \, . \tag{5.36}$$

As discussed above, data are provided over a vertical line. In flat plane conditions we suppose that all quantities depend only on z, the vertical coordinate. Furthermore, $\mathbf{u}_f$ is horizontal and depends on z. We can then simplify (5.36) to a one-dimensional ordinary differential equation

$$\frac{d}{dz} \left(w_{sed} \varphi_s + \nu_{eq} \frac{d\varphi_s}{dz} \right) = 0 \, , \tag{5.37}$$

therefore

$$w_{sed} \varphi_s + \nu_{eq} \frac{d\varphi_s}{dz} = \text{constant} \, .$$

Since at infinity $\lim\limits_{z \to +\infty} \varphi(z) = 0$ and $\lim\limits_{z \to +\infty} \frac{d\varphi}{dz}(z) = 0$, then the constant in the above equation must vanish and the differential simplifies to

$$\begin{cases} w_{sed} \varphi_s + \nu_{eq} \frac{d\varphi_s}{dz} = 0 \, , \\ \varphi_s(z = 0) = \varphi_0 \, . \end{cases} \tag{5.38}$$

Instead of solving (5.38) to determine φ_s, we will try to use this equation to evaluate the coefficient ν_{eq} assuming that we can guess from experiments the analytic form of φ_s. So, from (5.38) we can calculate ν_{eq}

$$\nu_{eq} = -w_{sed} \frac{\varphi_s(z)}{\frac{d\varphi_s}{dz}(z)} \, . \tag{5.39}$$

The next step is then to correlate the z-dependence with a dependence from φ_s and of the flow conditions. The following fitting models are developed in order to accurately describe the experimental data behavior. In fact, data in Zhang's experiments show a peculiar knee in the logarithmic scale. This behavior is not physically explained by Zhang et al., therefore we develop two generic fitting models that can take into account these peculiar trends of φ_s data.

Fitting Model A

Assume that φ_s can be written in the form

$$\varphi_A(z) := e^{f(z)} \, , \tag{5.40}$$

where the subscript A is used to identify this first fitting model and

$$f(z) := \begin{cases} f_0 - cz & z < \overline{z} \\ f_\infty + \left[(f_0 - c\overline{z} - f_\infty) \, \exp\left(-\frac{c(z-\overline{z})}{f_0 - c\overline{z} - f_\infty} \right) \right] & z \geqslant \overline{z} \end{cases} \, . \tag{5.41}$$

From (5.40) and (5.41) we can compute

$$\frac{d\varphi_A}{dz}(z) = \frac{df}{dz}(z)\, e^{f(z)} = \frac{df}{dz}(z)\varphi_A(z)\,, \tag{5.42}$$

$$\frac{df}{dz}(z) = \begin{cases} -c & z < \bar{z} \\ -c\, \exp\left(-\frac{c(z-\bar{z})}{f_0 - c\bar{z} - f_\infty}\right) & z \geqslant \bar{z}\,. \end{cases} \tag{5.43}$$

With this structure the fitting problem consists in finding the optimal coefficients $f_0, f_\infty, \bar{z}, c$. In order to simplify the notation, model A is identified by

$$\varphi_A(z; f_0, f_\infty, \bar{z}, c)\,. \tag{5.44}$$

Analogously, the equivalent viscosity ν_{eq} can directly be written by using (5.39), (5.42) and (5.43) as

$$\nu_{eq}(z) := \begin{cases} \frac{w_{sed}}{c} & z < \bar{z} \\ \frac{w_{sed}}{c}\, \exp\left(\frac{c(z-\bar{z})}{f_0 - c\bar{z} - f_\infty}\right) & z \geqslant \bar{z} \end{cases}\,. \tag{5.45}$$

Fitting Model B

Assume that φ_s can be written in the form

$$\varphi_B(z) := \varphi_0\, e^{g(z)}\,, \tag{5.46}$$

where the subscript B is used to identify the second fitting model for the volume ratio and the function g is obtained by integrating its derivative

$$\frac{dg}{dz}(z) := a + b\arctan(c(z-\bar{z}))\,, \tag{5.47}$$

where

$$a := \frac{S_{max} + S_{min}}{2} \qquad b := \frac{S_{max} - S_{min}}{\pi}\,. \tag{5.48}$$

The integral of (5.47) reads

$$g(z) = az + b\left[(z-\bar{z})\arctan(c(z-\bar{z})) - \frac{\ln(1 + c^2(z-\bar{z})^2)}{2c}\right] + C\,. \tag{5.49}$$

By imposing that $g(0) = 0$ we can compute the value of C, hence

$$C = b\left[\bar{z}\arctan(-c\bar{z}) + \frac{\ln(1 + c^2\bar{z}^2)}{2c}\right]\,. \tag{5.50}$$

Adopting the same notation as the fitting model A we can address model B as

$$\varphi_B(z; \varphi_0, S_{min}, S_{max}, \bar{z}, c)\,. \tag{5.51}$$

Analogously, the equivalent viscosity ν_{eq} can be directly written by using formula (5.39) and (5.47) as

$$\nu_{eq}(z) := -\frac{w_{sed}}{a + b\arctan(c(z-\bar{z}))}\,. \tag{5.52}$$

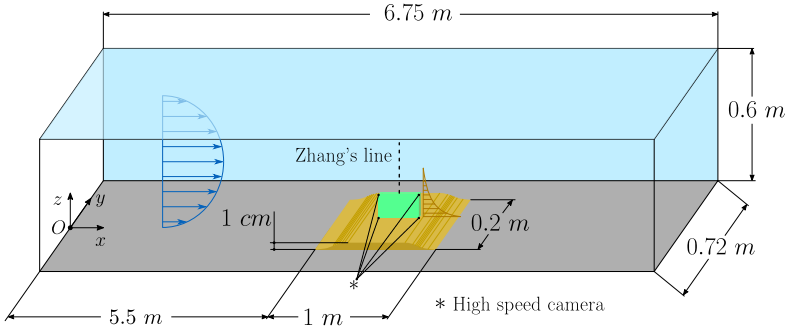

Figure 5.7: Geometric features of Zhang's wind tunnel. The dimensional proportions are not real because of the high ratio between length and height.

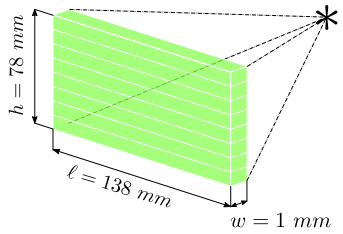

Figure 5.8: Scheme of sampling spatial section for Zhang experiment. Horizontal slices represent volumes in which number of particle are counted by an image processing algorithm.

In both the above models $\bar{z}$ aims to quantify the peculiar knee showed in the Zhang's experimental data.

5.3.2 Computational Setup

In this section we provide an overall description of Zhang's wind tunnel experimental setup and one possible computational model for its simulations. Figure 5.7 shows a scheme of Zhang's wind tunnel section with its main geometrical features: the sand bed is located at 5.5 m downstream the entrance and it is symmetric between front and back walls of the tunnel. In order to reduce possible undesired aerodynamics effects, a smoothing process is applied to the initial and final steps of the sand bed. In fact, sharp edges could generate a local production of turbulent kinetic energy and potentially lead to a chaotic evolution of the fluid flow. The green sheet on the sand bed represents the spatial region where the high speed camera records images; it is indicated with the symbol "$*$" in Figure 5.7. More details of the sampling slice are provided in Figure 5.8, the solid concentration is evaluated by counting the number of particles in each horizontal slice and the number of particles is determined by means of an image processing algorithm named *PIV*. The vertical line - where data are provided - is located at coordinate $x = 6.318\ m$ and it is symmetric with respect to the lateral walls. For sake of simplicity we name the vertical line as "Zhang's line".

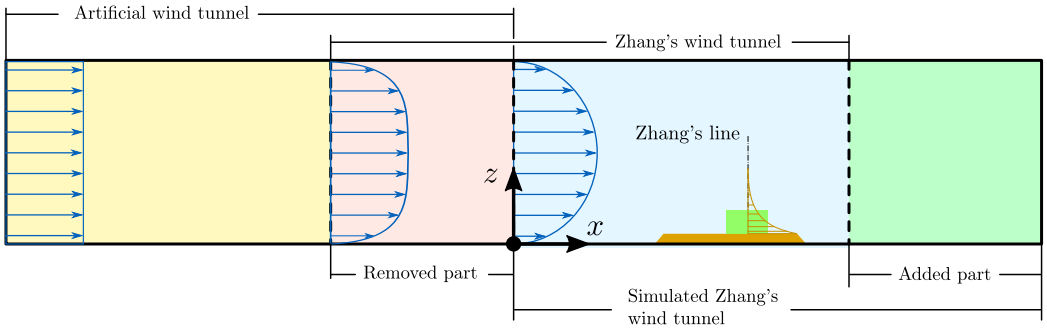

Figure 5.9: Conceptual structure of the computational wind tunnel. This figure do not respects real proportions because of high ratio between length and height.

Our computational setup is based on 2D simulations on a vertical slice which is virtually located at the symmetry plane of the wind tunnel. Preliminary CFD simulations were carried out to set acceptable boundary conditions for the fluid system, we recall that fluid boundary conditions have relevant effects for the *First Order Model*. The computational wind tunnel embed Zhang's experimental section, but it also includes two additional spatial regions. These two are located upwind and downwind Zhang's section, and their aim consists in uniforming the flow along the wind direction in order to reach the equilibrium before the sand bed. From these preliminary simulations we derived that a hybrid mesh with polyhedric cells in the domain's core and rectangular cells at the wall region can give results similar to a pure structured grid which are usually preferred because they avoid some finite-volume related numerical errors (e.g. non-orthogonality). The usage of a polyhedric mesh substantially decreases the computational execution time, which is a crucial factor in industrial context. Figure 5.9 shows the computational wind tunnel with its additional tunnel sections.

On the top and bottom surfaces we consider wall boundary conditions for smooth surfaces. Constant profiles for fluid velocity and turbulence quantities are used at the inlet. We also remark that the tunnel sections added to the original Zhang's section are used to fix the lack of information about boundary conditions, in particular for the pressure field. Proceeding along the horizontal direction aerodynamics quantities tend to stabilize toward a stationary equilibrium condition. The upwind additional section allows the flow to satisfies the fluid dynamics equilibrium imposed by the turbulence model and by wall functions. We recall that the adopted turbulence model is a standard $k-\omega$ SST.

Figure 5.10 b) shows the computational profiles of horizontal velocity and turbulent kinetic energy when the equilibrium is reached for the Zhang-46 case (see Table 5.1). In order to calibrate the integral mass flux, the velocity profile is scaled simply by multiplying it by a constant. Mass flux is calculated by fitting air velocity data on Zhang's line with an atmospheric logaritmic law and integrating it over z. The resulting integral flux is

Case	$d\ [mm]$	$u^*\ [m/s]$	$z_0\ [m]$	$Q\ [m^2/s]$
Zhang-46	$0.2 \div 0.3$	0.20031	$1.54 \cdot 10^{-8}$	4.545
Zhang-47	$0.1 \div 0.125$	0.44169	0.000825	3.103

Table 5.1: Fluid flow properties of the Zhang's experiment.

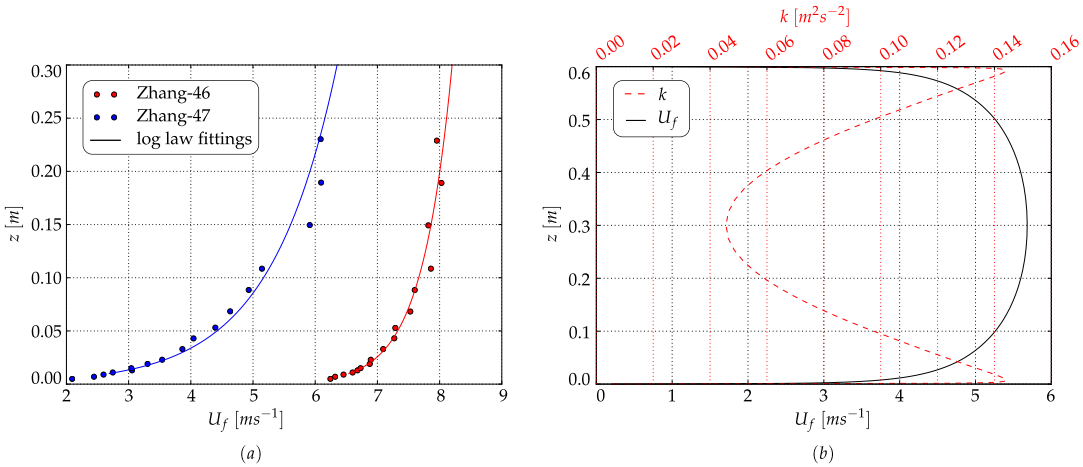

Figure 5.10: Figure (a) shows horizontal air velocity for both type of sand considered in Zhang's experiment. Figure (b) shows horizontal air velocity and turbulent kinetic energy profiles obtained from the virtual wind tunnel test for the Zhang-46 case.

$$Q = \frac{2u^*}{\kappa}\left[0.295 \ln\left(\frac{0.295}{z_0}\right) - 0.295 + z0\right] . \tag{5.53}$$

The magnitude of integral fluxes are given in Table 5.1. Figure 5.10 $a)$ shows the comparison between the experimental data and the their fittings via logaritmic law. Once the inlet boundary conditions are defined for Zhang's wind tunnel, simulations are prepared to match data shown in Figure 5.10 $a)$. Figure 5.11 shows a piece of the computational domain around the downwind sand step where also Zhang's line is visible. The plotted scalar field represents the turbulent kinetic energy and the streamlines visualize the air velocity field with magnitude and direction. The velocity field results horizontal around Zhang's line and no effect of turbulent kinetic energy are present due to the upwind steps. Therefore, we can visually see that horizontal gradients are not present around Zhang's line. This fact is relevant because the data analysis model requires that physical quantities change only over the vertical direction. Figure 5.12 shows a comparison among experimental data, fitting law and the CFD solution with optimized boundary conditions, for both regimes of the Zhang's experiment. We can observe that the Zhang-46 case is more accurate than Zhang-47. However we consider these results acceptable if we take into account uncertainties of experimental data.

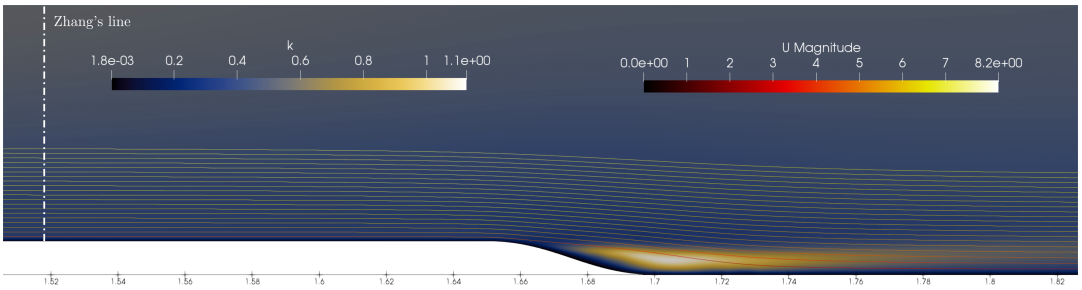

Figure 5.11: Subset of the computational domain for the case Zhang-46. Turbulent kinetic energy field and streamlines of the velocity field are also shown.

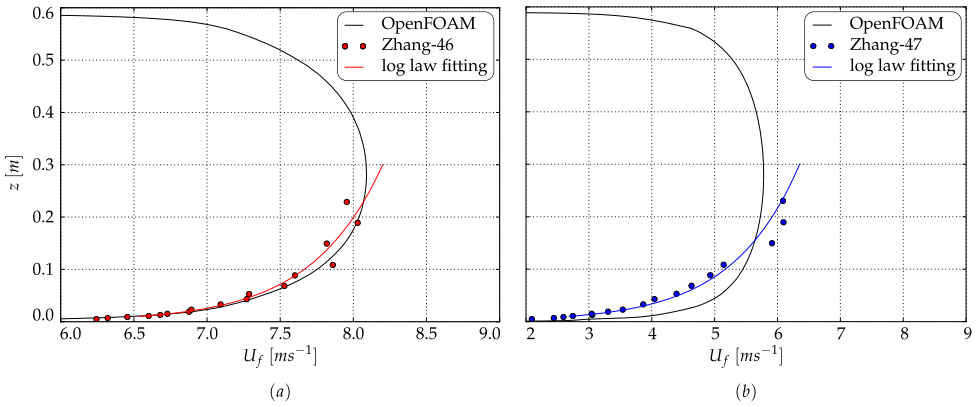

Figure 5.12: Comparison among experimental data, CFD simulation and logaritmic law used the case (a) Zhang-46 and (b) Zhang-47.

Case	$d \cdot 10^{-3}\ [m]$	$u^*\ [m/s]$	$z_0\ [m]$	Ref. Paper	Figure	Letters	Table
Zhang-46	$0.2 \div 0.3$	0.20031	$1.54 \cdot 10^{-8}$	[238]	5.19	$a_1)\ a_2)$	5.5
Zhang-47	$0.1 \div 0.125$	0.44169	0.000825		5.20	$b_1)\ b_2)$	
Kang-7	0.15	0.64	-		5.16	$a_1)\ a_2)$	
Kang-8	0.15	0.75	-	[122]	5.17	$b_1)\ b_2)$	5.3
Kang-9	0.15	0.82	-		5.18	$c_1)\ c_2)$	
Kawamura-43	0.25	0.2635	-		5.13	$a_1)\ a_2)$	
Kawamura-44	0.25	0.4929	-	[203]	5.14	$b_1)\ b_2)$	5.4
Kawamura-45	0.25	0.7857	-		5.15	$c_1)\ c_2)$	

Table 5.2: Identifiers and data for the analyzed experiments.

5.3.3 Particle Concentration Analysis

In this section we apply the fitting models presented in section 5.3.1 on three experimental setups. We address the experiments with Zhang for [238], Kang for [122] and Kawamura for [203]. The wind tunnel configuration for the Zhang's experiment is described in the previous section. Kang and Kawamura adopt a similar wind tunnel setup (see [122] and [203]), but their description is less accurate. We can observe that $\varphi \sim 10^{-3} = 0.1\%$ in all cases, hence the assumption (5.1) results correct. We can also note that the models for ν_{eq} (red and blue curves in Figures 5.19 and 5.20) quickly diverge over a certain value z . The reason of this is related to the analytic structure of the fitting models. Indeed Model A has an asymptote with value $\varphi_\infty := e^{f_\infty}$. In Figures 5.19 and 5.20 the presence of the asymptote is clear for both Zhang-46 and Zhang-47 cases.

The equivalent viscosity ν_{eq} exhibit appreciable differences between Model-A and Model-B, but yield small differences in particle concentration. Therefore, small errors committed for ν_{eq} do not drastically influence the distribution of particle concentration. Most of the particles are confined to the first few centimeter hence even a relevant error on ν_{eq} for high value of z does not lead to big differences in the overall transport rate. We also remark that when concentration becomes very low, very few particles are present in a control volume (e.g. if $d \approx 10^{-3}m$ and $\varphi_s \approx 10^{-3}$ in a cube of one cm^3 the are more or less a couple of particles).

All three experiments exhibit a kind of knee where the slope changes quickly. It is not clear whether this aspect is related to measurement issues or experimental conditions. However both models can embed this behavior if eventually high precision measurement might become available for future tests.

	coeff.	Kang-7	Kang-8	Kang-9	
$Model_A$	e^{f_0}	$1.112686380487 \cdot 10^{-3}$	$6.37883565464 \cdot 10^{-4}$	$4.01434347870 \cdot 10^{-4}$	$[\cdot]$
	e^{f_∞}	$1.170700574460 \cdot 10^{-7}$	$2.05716906258 \cdot 10^{-7}$	$2.52431433411 \cdot 10^{-7}$	$[\cdot]$
	$\overline{z}$	$-4.707577011080 \cdot 10^{-3}$	$-1.16774579047 \cdot 10^{-2}$	$-1.77645870617 \cdot 10^{-2}$	m
	c	$4.126800551370 \cdot 10^{2}$	$3.11103328150 \cdot 10^{2}$	$2.72109251904 \cdot 10^{2}$	$1/m$
$Model_B$	φ_0	$1.000000000000 \cdot 10^{-3}$	$1.45144205409 \cdot 10^{-3}$	$1.12844597347 \cdot 10^{-3}$	$[\cdot]$
	$\overline{z}$	$2.495728218540 \cdot 10^{-1}$	$2.05148318425 \cdot 10^{-2}$	$2.50247765609 \cdot 10^{-2}$	m
	c	$9.000000000000 \cdot 10^{1}$	$1.48168193661 \cdot 10^{2}$	$1.63596400000 \cdot 10^{1}$	$1/m$
	S_{min}	$-2.965365223190 \cdot 10^{2}$	$-2.59284228108 \cdot 10^{2}$	$-1.88047995605 \cdot 10^{2}$	$[\cdot]$
	S_{max}	$-5.194557242710 \cdot 10^{1}$	$-3.18946510000 \cdot 10^{1}$	$-3.15108410508 \cdot 10^{1}$	$[\cdot]$

Table 5.3: Fitting coefficients for Kang's case.

	coeff.	Kawamura-43	Kawamura-44	Kawamura-45	
$Model_A$	e^{f_0}	$1.21382718818 \cdot 10^{-3}$	$3.26422178877 \cdot 10^{-3}$	$3.39968915227 \cdot 10^{-3}$	$[\cdot]$
	e^{f_∞}	$2.53488955741 \cdot 10^{5}$	$3.52624139371 \cdot 10^{-5}$	$4.50466501634 \cdot 10^{-5}$	$[\cdot]$
	$\overline{z}$	$1.56259495587 \cdot 10^{-2}$	$6.32479014669 \cdot 10^{-4}$	$-1.24272078366 \cdot 10^{-4}$	m
	c	$2.91417588517 \cdot 10^{2}$	$3.89222876200 \cdot 10^{2}$	$2.15107022175 \cdot 10^{2}$	$1/m$
$Model_B$	φ_0	$1.99965840000 \cdot 10^{-3}$	$3.01140000000 \cdot 10^{-3}$	$3.19968915200 \cdot 10^{-3}$	$[\cdot]$
	$\overline{z}$	$3.05470000000 \cdot 10^{-3}$	$8.50687100000 \cdot 10^{-3}$	$1.27000000000 \cdot 10^{-2}$	m
	c	$1.00184687460 \cdot 10^{3}$	$1.69782620565 \cdot 10^{2}$	$8.00054850000 \cdot 10^{1}$	$1/m$
	S_{min}	$-6.59741178000 \cdot 10^{2}$	$-4.05001894378 \cdot 10^{2}$	$-2.38901568500 \cdot 10^{2}$	$[\cdot]$
	S_{max}	$-1.98074132000 \cdot 10^{2}$	$-9.87240000000 \cdot 10^{-1}$	0	$[\cdot]$

Table 5.4: Fitting coefficients for Kawamura's case.

	coeff.	Zhang-46	Zhang-47	
$Model_A$	e^{f_0}	$3.49888312206 \cdot 10^{-3}$	$7.24286231220 \cdot 10^{-3}$	$[\cdot]$
	e^{f_∞}	$2.60731732654 \cdot 10^{-5}$	$2.61597108238 \cdot 10^{-6}$	$[\cdot]$
	$\overline{z}$	$1.00828800000 \cdot 10^{-2}$	$1.04704711630 \cdot 10^{-2}$	m
	c	$2.96629674343 \cdot 10^{2}$	$4.39951826144 \cdot 10^{2}$	$1/m$
$Model_B$	φ_0	$3.61968280376 \cdot 10^{-3}$	$7.2397554 \cdot 10^{-4}$	$[\cdot]$
	$\overline{z}$	$1.48092639351 \cdot 10^{-2}$	$1.1915645 \cdot 10^{-1}$	m
	c	$3.86802967677 \cdot 10^{2}$	$9.89543654 \cdot 10^{2}$	$1/m$
	S_{min}	$-3.22086775070 \cdot 10^{2}$	$-4.71004838 \cdot 10^{2}$	$[\cdot]$
	S_{max}	$-1.00000000000 \cdot 10^{-1}$	0	$[\cdot]$

Table 5.5: Fitting coefficients for Zhang's case.

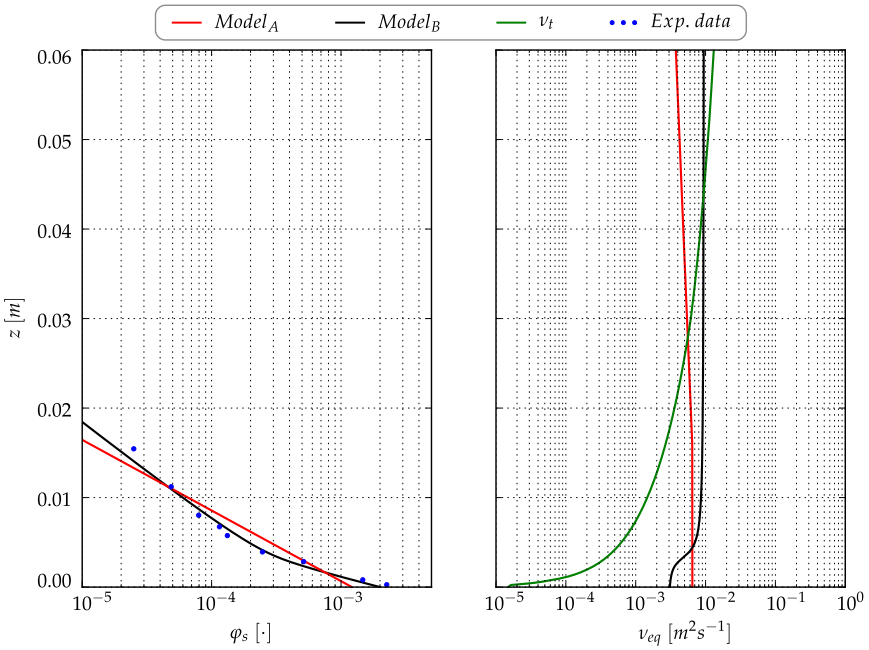

Figure 5.13: Results for Kawamura-43 case. See Table 5.2 for related data.

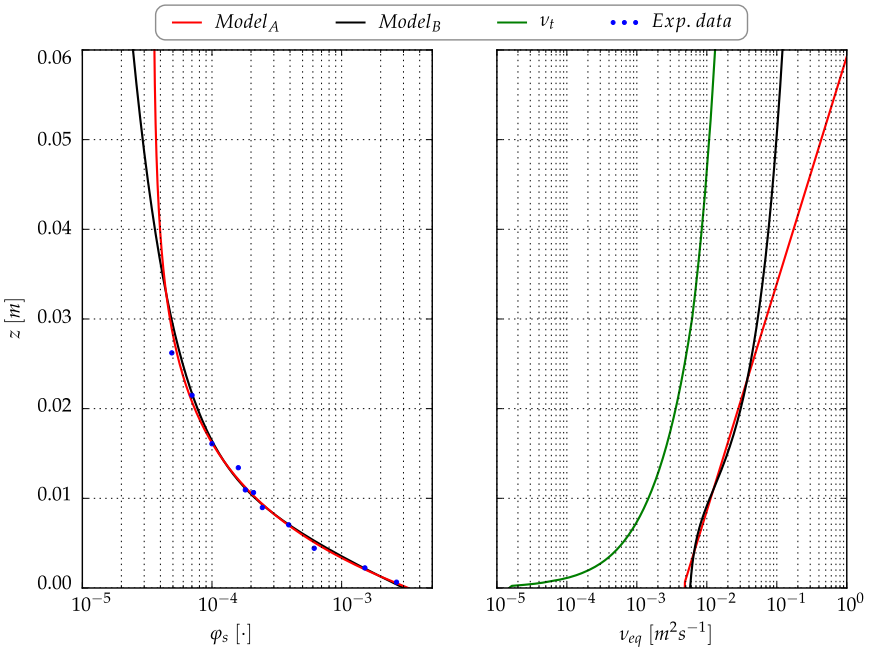

Figure 5.14: Results for Kawamura-44 case. See Table 5.2 for related data.

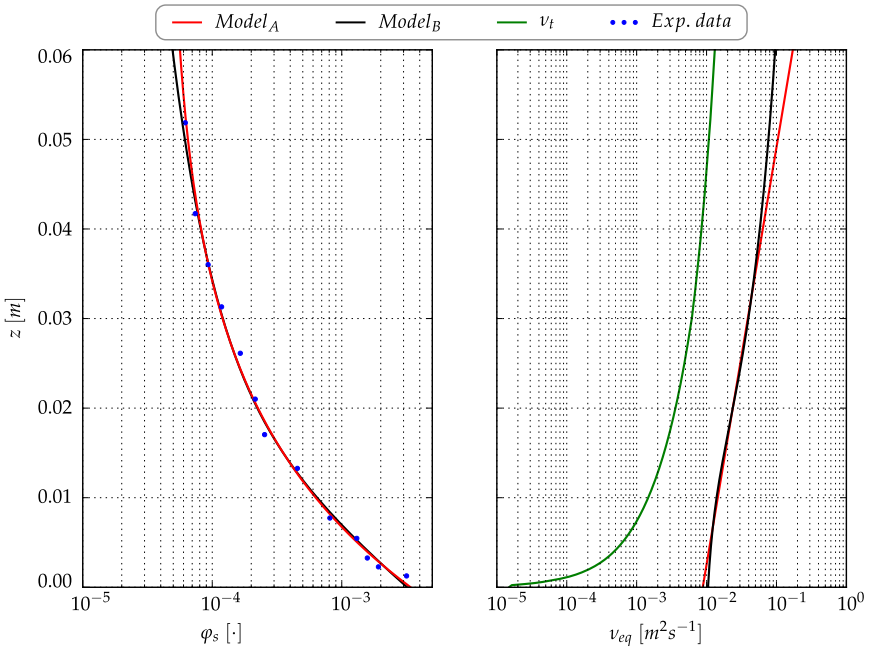

Figure 5.15: Results for Kawamura-45 case. See Table 5.2 for related data.

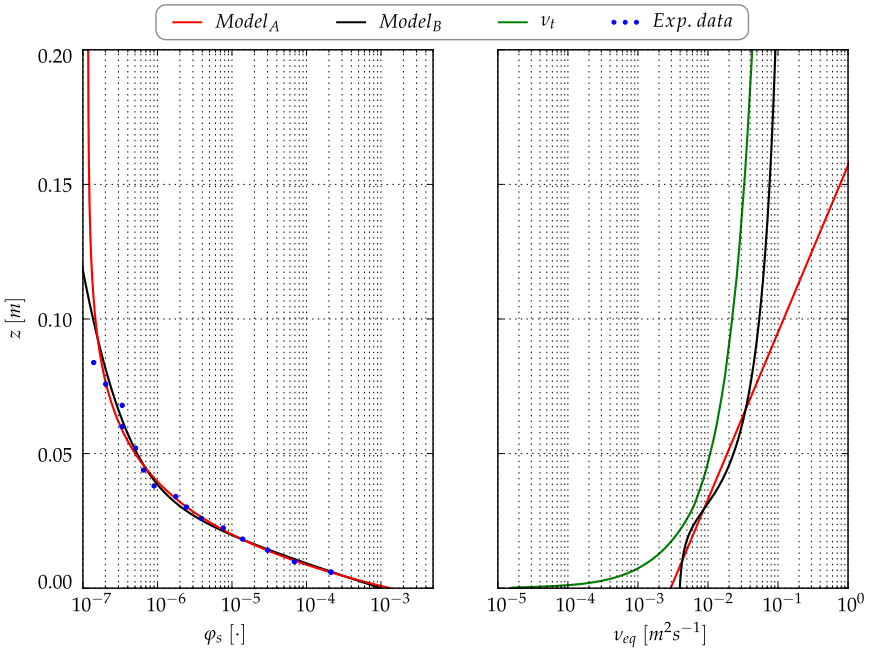

Figure 5.16: Results for Kang-7 case. See Table 5.2 for related data.

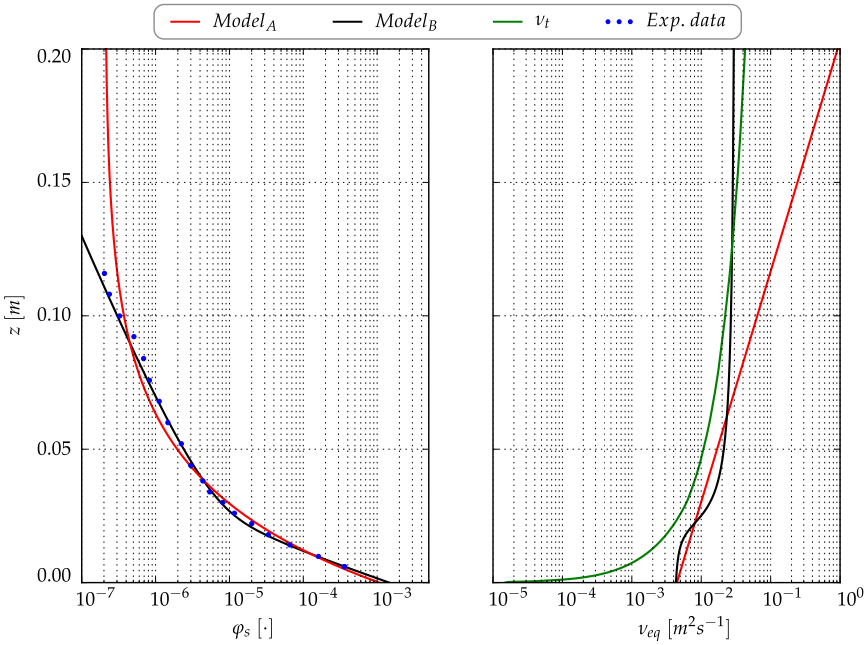

Figure 5.17: Results for Kang-8 case. See Table 5.2 for related data.

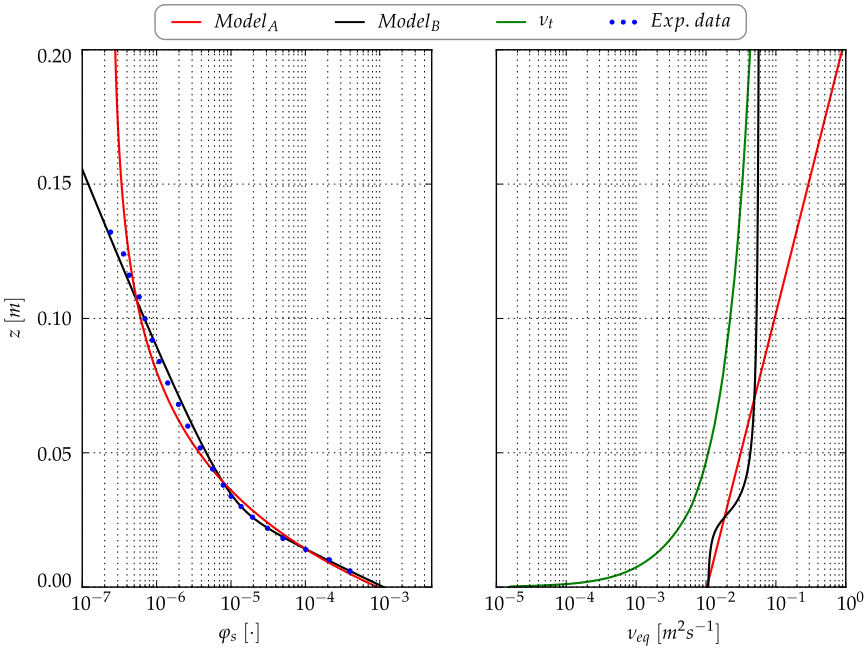

Figure 5.18: Results for Kang-9 case. See Table 5.2 for related data.

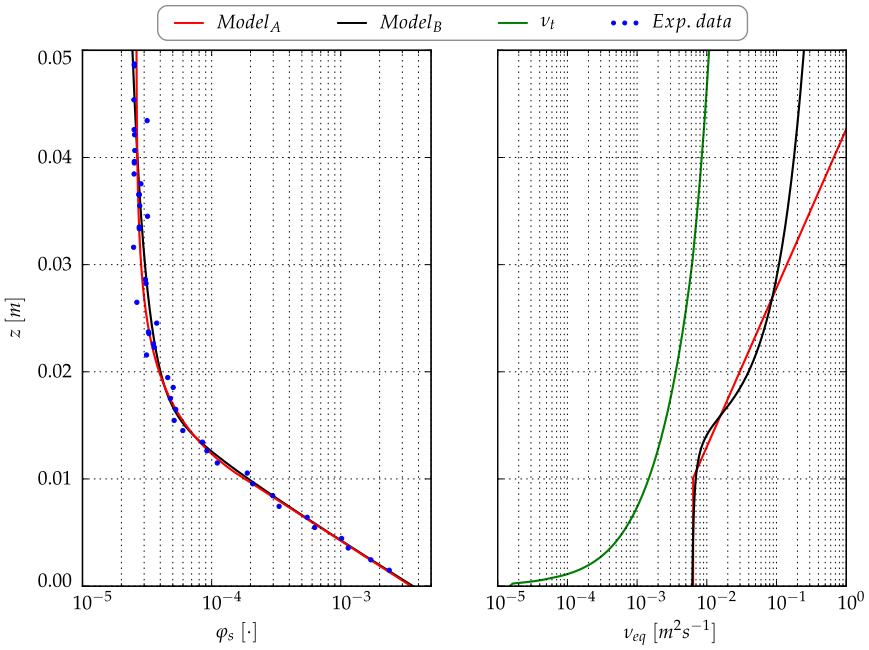

Figure 5.19: Results for Zhang-46 case. See Table 5.2 for related data.

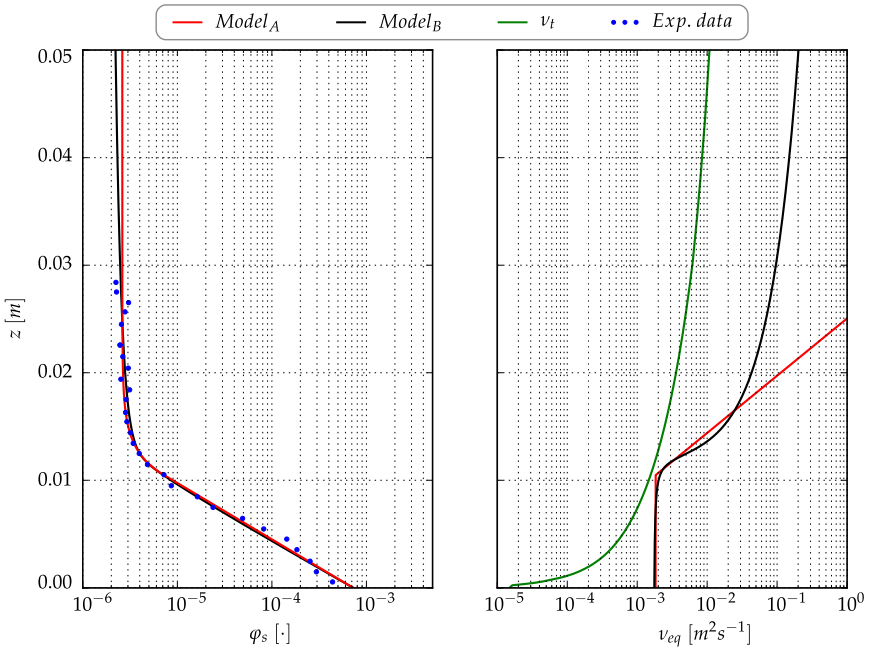

Figure 5.20: Results for Zhang-47 case. See Table 5.2 for related data.

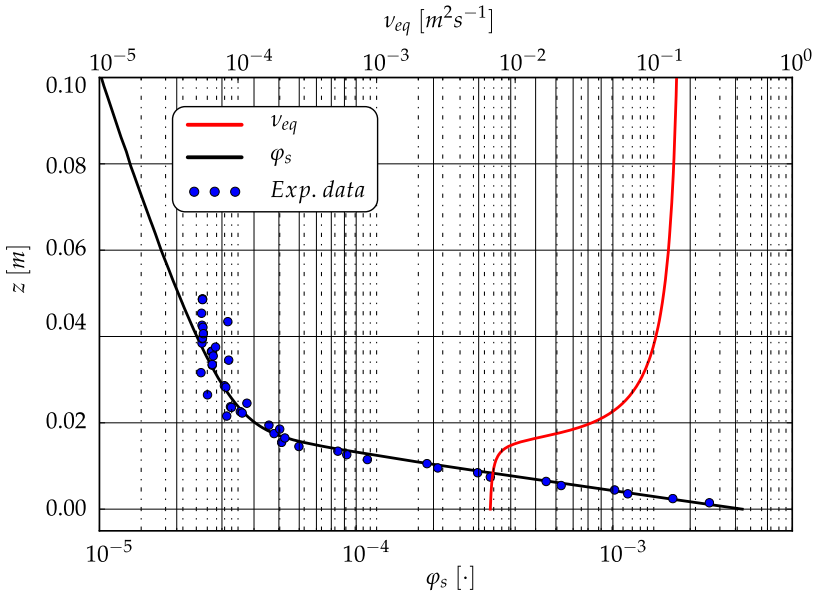

Figure 5.21: Simulation results in Zhang-46 case using the OpenFOAM implementation of the *First Order Model*.

5.3.4 Empirical Coupling Between Fluid and Solid Phases

Sections 5.3.1 and 5.3.3 describe how to represent ν_{eq} and φ_s as functions of the distance from the sand bed z. Section 5.3.2 describe the computational domain and fluid dynamics aspects of Zhang's case. We can therefore test the *First Order Model* in OpenFOAM with a prescribed function $\nu_{eq}(\cdot)$, which is still a function of the wall distance. Figure 5.21 shows the simulation result for Zhang-46 setup. The resulting concentration φ_s agrees with experimental data. We can therefore deduce that - qualitatively - numerical errors has small or negligible effects for this computational setup. As consequence, we suppose that this computational framework is suitable to study analytical aspects for the $\nu_{eq}(\cdot)$ formulation.

In the light of these results, the goal is therefore defining a model for ν_{eq} that replicates the correct spatial values, but its dependent variables has to embed physical properties of the flow. We anticipate that following model is not the final solution for the *First Order Model*; we report this result because its application to selected experimental setups leads to some anomalies. These last constitute the incipit for the idea that underlies the solution explained in Section 5.4.

In order to justify the following formulation (5.60) we need to consider three physical facts observed in all experiments that we have analyzed:

- most experiments refer to the shear velocity u^* which is a bulk parameter that determines if saltation occurs and its intensity,
- if $u^* > u_t^*$ saltation occurs, where u_t^* represent the threshold value.
- the fluid flow direction near the ground is horizontal and the fluid velocity varies with respect to the wall distance z, then we can write the fluid velocity

vector field as

$$\mathbf{u}_f(x,y,z) = u_x(z)\mathbf{e}_x \,. \tag{5.54}$$

We can use (5.54) to compute the second invariant as

$$\nabla \mathbf{u}_f = \begin{pmatrix} 0 & 0 & \frac{\partial u_x}{\partial z} \\ 0 & 0 & 0 \\ 0 & 0 & 0 \end{pmatrix} \,,$$

hence

$$\mathbb{D} := \frac{1}{2}\left(\nabla \mathbf{u}_f + \nabla \mathbf{u}_f^T\right) = \frac{1}{2}\begin{pmatrix} 0 & 0 & \frac{\partial u_x}{\partial z} \\ 0 & 0 & 0 \\ \frac{\partial u_x}{\partial z} & 0 & 0 \end{pmatrix} \tag{5.55}$$

and

$$\mathbb{D}^2 = \frac{1}{4}\begin{pmatrix} \left(\frac{\partial u_x}{\partial z}\right)^2 & 0 & 0 \\ 0 & 0 & 0 \\ 0 & 0 & \left(\frac{\partial u_x}{\partial z}\right)^2 \end{pmatrix} \,. \tag{5.56}$$

We can notice that the first and third invariants vanish for this specific flow

$$\mathbb{I}_{\mathbb{D}} := tr\ \mathbb{D} = \nabla \cdot \mathbf{u}_f = 0 \,, \tag{5.57}$$

$$\mathbb{III}_{\mathbb{D}} := det(\mathbb{D}) = 0 \,,$$

therefore they do not represent candidate quantities for the analytical structure of ν_{eq}. The last candidate is the second invariant, hence using (5.55), (5.56) and (5.57) we obtain

$$\mathbb{II}_{\mathbb{D}} := \frac{1}{2}\left((tr\ \mathbb{D})^2 - tr\left(\mathbb{D}^2\right)\right) = -\frac{1}{4}\left(\frac{\partial u_x}{\partial z}\right)^2 \,,$$

then we can consider

$$\left|\frac{\partial u_x}{\partial z}\right| = 2\sqrt{|\mathbb{III}_{\mathbb{D}}|} \,. \tag{5.58}$$

Equation (5.58) can be used to rewrite the definition of shear velocity in terms of $\mathbb{III}_{\mathbb{D}}$

$$u^* := \sqrt{\frac{\tau_{wall}}{\rho_f}} = \sqrt{\nu_f \left|\frac{\partial u_x}{\partial z}(z=0)\right|} \overset{(5.58)}{=} \sqrt{2\nu_f\sqrt{|\mathbb{III}_{\mathbb{D}}(z=0)|}} \,. \tag{5.59}$$

Using this relationship we can generalize the concept of shear velocity in every point of the computational domain, also away of the boundary, hence the

$$\tilde{u}^* = \sqrt{2\nu_f\sqrt{|\mathbb{III}_{\mathbb{D}}|}} \,.$$

For ν_{eq}^{emp} we propose

$$\nu_{eq}^{emp} := \alpha\left(\frac{\tilde{u}^*}{u_t^*} - 1\right)_+^{\gamma} = \alpha\left(\frac{\sqrt{2\nu_f\sqrt{|\mathbb{III}_{\mathbb{D}}|}}}{u_t^*} - 1\right)_+^{\gamma} \tag{5.60}$$

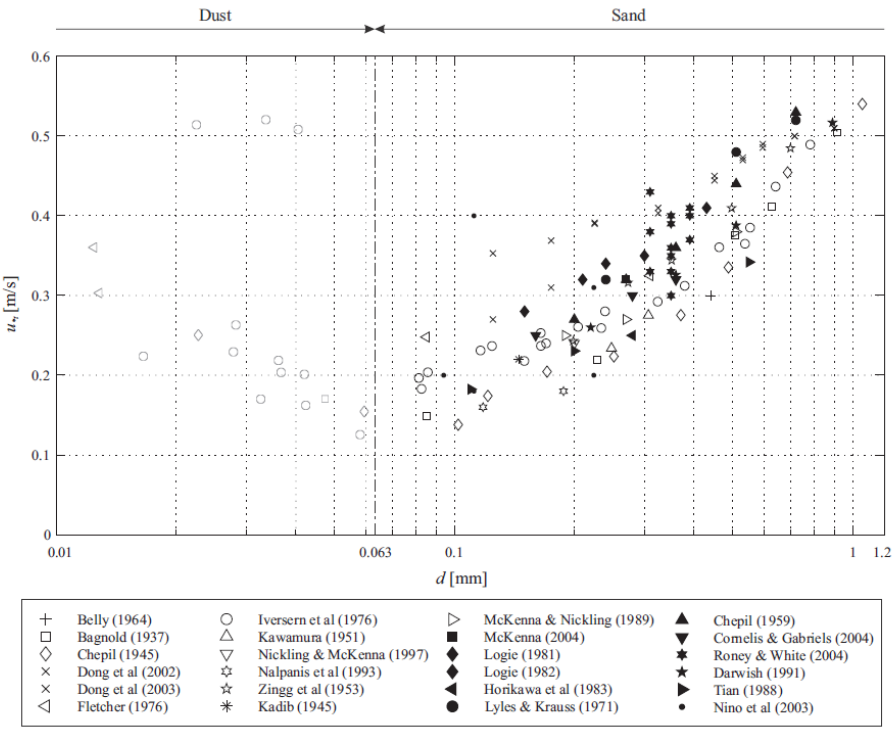

Figure 5.22: Experimental measurements of u_t^* with respect to d presented in [186].

where α, γ are model coefficients which have to be optimized for various physical conditions. In this formulation the diffusivity vanishes when the threshold value of u_t^* is not reached and uses $|\mathbb{II}_{\mathbb{D}}|$ as Eulerian field in a way that is compatible with the definition of u^* at the boundary i.e. $\tilde{u}^*(z=0) \equiv u^*$. In order to model the value of u_t^* we use

$$u_t^* = 0.124\sqrt{\frac{\rho_s - \rho_f}{\rho_f} g d + \frac{1.12 \cdot 10^{-4}}{\rho_f d}}\,, \tag{5.61}$$

which is proposed in [186] to fit the experimental data of Figure 5.22. Figure 5.23 shows the results of the optimization procedure for ν_{eq}^{emp} and the values of the analyzed experiments. The resulting coefficients are

$$\alpha = 0.00494232\,,$$
$$\gamma = 0.33717863\,.$$

5.4 Solid Volume Concentration Dependence of the Collisional Diffusivity

We can notice that in Figure 5.23 the dots are very scattered around the model curve. This result suggests that a model involving only the dependence from $\mathbb{II}_{\mathbb{D}}$ is not sufficiently general to embed effects of several physical conditions. In particular,

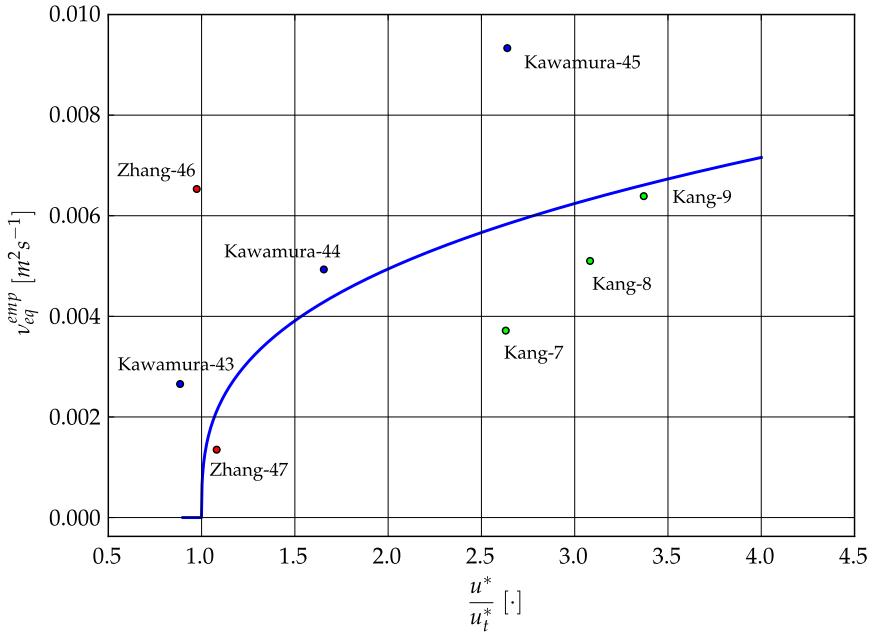

Figure 5.23: Results of the empirical model ν_{eq}^{emp} at the ground for several experiments.

the concentration φ_s is the important variable missing in the previous argument related to ν_{eq}^{emp}. We remark that including φ as a dependent variable in the model for ν_{eq} leads to a non-linearity in the differential operator of the convection-diffusion model. So, in this Section we face the problem of computing a possible analytical structure of ν_{coll} that is able to summarize the physical behavior of the saltation cloud. The following approach is the result of several theoretical and practical attempts to face this problem. The outcoming solution is a compromise between theoretical requirements and practical needs. Industrial applications - in addition to the accuracy control - require a certain flexibility in the model setting. Indeed, a generic setup can eventually show some characteristics that have not been taken into account when the model has been originally developed (e.g. the uncertainty of input data). Therefore, the model adopts some tuning parameters in order to be morphed when necessary.

5.4.1 Updated Literature of Experimental Data

4We have updated the experimental literature in order to identify one or more experiments to be used as prototype in for the data representation. An ideal scenario for an experiment describes each physical variable with good accuracy both in space and time. However, real case scenarios are very different and, as discussed in Section 5.3, data are provided in few spatial point, without temporal information of the system evolution. We recall that in Section 5.3 the set of articles [58, 64, 102, 122, 142, 203, 238] were selected as candidates for the data analysis. However, in order to expand the literature and avoid to lose potential good setups we also consider other experiments. Specifically, for aeolian flows [63–67, 168, 190, 214, 215, 219, 222, 232, 241] whose content can be summarized as follows

- The group of articles [64, 65, 168, 222, 241] contains a good description of the experimental setup, detailing the adopted wind tunnel and used instruments. The number of sand diameter values and the number of wind states are enough to extract quantitative information. In particular [241] focuses on energetic aspects and [65] provides some information of particles turbulence.
- The authors of [67] study a special case with gravel ground situated downwind with respect to the sand bed. This case is interesting to figure out the sand behavior over a non erodible and rough surface.
- In [63] interesting information can be extrapolated about the effect of particles on fluid velocity. In particular, to evaluate the interaction between phases, which is crucial for the Second Order Model.
- In [215] the case of sand ripple morphology is treated both with numerical and experimental approaches. This article is interesting as a comparison for tests on the soil morphology.
- In [214] a wind tunnel study of three dimensional flow over an obstacle is carried out. This article can be interesting for bulk comparison of a model where three dimensional effects of flows want to be studied.
- In [66, 190, 219, 232] other data and fitting formulas are proposed. These articles can be used as additional information to be included in the whole final dataset with the aim to increase number of samples for statistical analysis. However, they have some drawbacks compared to the previous articles.

We remark that the main issue of the entire literature considered her is the lack of completeness in the quantitative description of physical systems. In particular, all cases focus on few details and neglect others compromising the reproducibility of scientific results. Furthermore, statistical descriptions miss of accuracy because just two sand types or two regimes of flow are considered.

We remark that a limit of wind tunnel as a scientific tool in the study of the aeolian transport. In the articles cited above wind tunnels are similar, both in size and class (circulating or non-circulating wind tunnel). In particular, all cases use a non-circulating wind tunnel and their length and width of the cross section is around one meter in size. These aspect reduces the characteristic length in the *Reynolds Number* value and therefore the *Reynolds Number* of the entire flow. As consequence, results coming from these specific wind tunnels cannot be theoretically scaled out to atmospheric flows. As already discussed, infield tests are cost and time expensive, they also do not provide high resolution data, therefore wind tunnels are the only option to use in a data-driven development. Only once the model is complete benchmarks over infield data can be carried out. As already mentioned, accurate information about turbulence are almost impossible to be obtained. Therefore, this aspect is properly modeled in the following with a solution that can be easily modified when additional data are found.

In conclusion, we consider [142] as prototype of experiment, because it is the only one to combine several scenarios of flow conditions and sand types together, resulting in a useful grid of cases. Its quantitative details are described in the following Section.

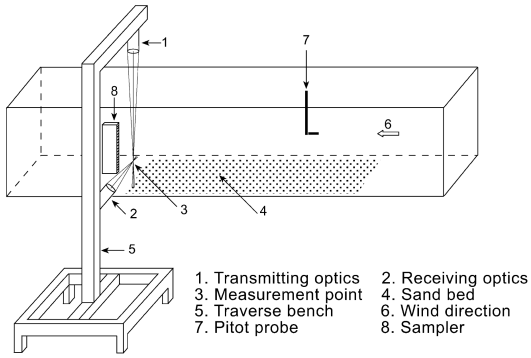

Figure 5.24: Scheme of the wind tunnel setup used in [142].

5.4.2 Analytic Formulation of the Collisional Diffusivity

In this section we finally describe the data-driven procedure to compute a possible formulation of ν_{coll} using the experimental setup presented in [142]. The flow regimes can be flagged using the so called *Free Stream Velocity*, addressed with the symbol U_∞ and measured in ms^{-1}. In particular, [142] tests six wind regimes

$$U_\infty \in \{8, 10,\ 12,\ 14,\ 16,\ 18\},$$

and five ranges of diameter measured in mm

$$d \in \{[0.1, 0.2],\ [0.2, 0.3],\ [0.3, 0.4],\ [0.4, 0.5],\ [0.5, 0.6]\}.$$

For clarity of notation, instead of using diameter intervals, in the following we use the mean value of the interval. Therefore, each interval has an alias diameter, hence

$$d \in \{0.15,\ 0.25,\ 0.35,\ 0.45,\ 0.55\}.$$

We remark that no further statistical properties of these intervals are provided. Therefore, we assume that diameter aliases can be used as reference values in the formulae evaluation. Whatever the real particle diameter spectrum, we commit an error for quantities that involve the dependence of d. In this case the diameter intervals are narrowed therefore we suppose that errors are negligible.

The combination of these settings leads to twenty-five wind tunnel runs providing a good data-mesh for statistical investigations. Figure 5.24 shows the scheme of the experimental setup adopted in [142], and we can suddenly notice the analogies with Zhang's setup. In particular, measurements are sampled over a vertical line in a downwind region of the sand bed.

Mean Wind Velocity Characterization

The first step consists in describing the mean wind velocity profile and its turbulence properties. A proper quantitative description of the mean wind velocity profile is important because we need to compute its spatial derivative in order to evaluate $|\mathbb{II}_{\mathbb{D}}|$ on the vertical line, where data is collected. In Section 3.2 we mentioned the two classical functions used to describe the mean velocity profile for a wind flow

(see (3.1), (3.3) and (3.2)). Their analytical formulation is based on experimental measurements with the aim to match the mean velocity profile (see [129]). For sake of clarity we recall here the fundamental relations

$$\text{ABL relation} \qquad U_f = \frac{u^*}{\kappa} \ln\left(\frac{z+z_0}{z_0}\right) , \tag{5.62}$$

$$\text{roughness Reynolds number} \qquad Re_\kappa = \frac{\kappa_s u^*}{\nu_f} , \tag{5.63}$$

$$\text{Nikuradse roughness} \qquad \kappa_s \sim 2 \div 5\, d , \tag{5.64}$$

$$\text{aerodynamic surface roughness} \qquad z_0 = \begin{cases} \nu_f / 9u^* & Re_\kappa < 4 \Leftrightarrow \text{smooth} \\ \kappa_s / 30 & Re_\kappa > 60 \Leftrightarrow \text{rough} \end{cases} , \tag{5.65}$$

where $\kappa \simeq 0.41$ is the Von Karman constant and u^* is the *shear velocity* defined in (5.59). Its value have to be intended as the mechanical stress on the surface.

In Figure 5.26 are reported the original wind mean velocity profiles presented in [142]. We remark that the mean wind velocity profiles refer to clean conditions, i.e. wind tunnel flow properties are tuned without the presence of sand in the domain. This is a standard practice for wind tunnel tests (also non-aeolian tests). Once these settings are defined, sand is introduced in the domain (making the sand bed) and the experiments run. We do not know the perturbed profile of mean wind velocity during the experiment. Which is a relevant aspect in the development of this model. Without measurements of the mean wind velocity during the saltation process we can not formally derive the perturbation involved in the transfer of momentum between sand and air due to the drag. As a consequence, we formally miss part of the physics involved in the process and we can only establish a cause-effect quantitative relation. On the other hand, as discussed in 5.1, the term $\mathbf{m}_f$ in (5.3) is almost negligible as well as the effects on turbulence. Therefore, we expect that the error due to this drawback is small. As a consequence, we do not include a feedback mechanism on the fluid velocity in this model because we do not have data for a validation step (see Figure 5.25). As soon as an aeolian system is fully described in all quantities, also this model can be easily updated with minor changes.

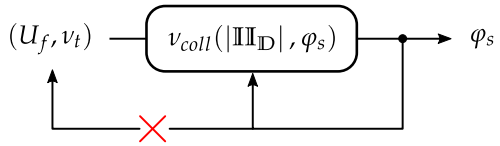

Figure 5.25: Abstract description of the model with its non-linearity. The red cross represent the missing feedback on the leading flow by the presence of particles.

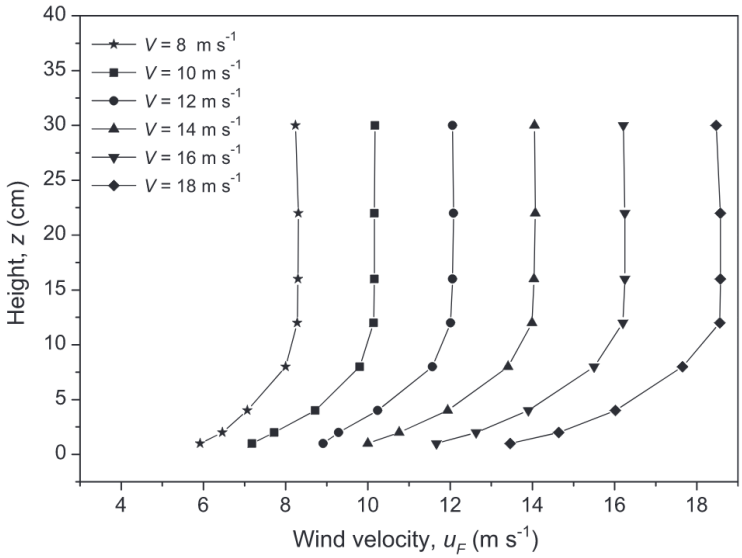

Figure 5.26: Original fluid velocity profiles at clean wind conditions provided in [142]. The symbol V stands for U_∞.

In order to model the flow we also propose a new formula inspired by the *law of the wall*. In particular, we properly formulate a function for the so-called buffer layer

$$u^+ = \begin{cases} z^+ & z^+ \in [0,5) \\ p_4(z^+) & z^+ \in [5,30) \\ \frac{1}{\kappa}\ln z^+ + C^+ & z^+ \in [30,\infty) \end{cases}, \tag{5.66}$$

$$z^+ = \frac{z u_\tau}{\nu_f}, \tag{5.67}$$

$$U_f(z) = u_\tau\, u^+(z^+(z)). \tag{5.68}$$

The p_4 is a fourth degree polynomial, whose coefficients are computed in order to fulfill following conditions

$$\begin{aligned} &p_4(5) = 5 && p_4'(5) = 1 && p_4''(5) = 0 \\ &p_4(30) = \tfrac{1}{\kappa}\ln(30) + C^+ && p_4'(30) = \tfrac{1}{30\kappa} \end{aligned}$$

In (5.67) and (5.68) the term u_τ can be intended as *friction velocity*, but it has to be intended as a mathematical parameter for the fitting law. This new formulation allows to solve a problem related to the computational wall shear stress τ_{wall} calculated with OpenFOAM. Indeed, the shear velocity have to satisfy the definition (5.59), but the outcoming values of u^* showed inconsistencies with computational outputs of the OpenFOAM simulations. In particular the wall shear stress is computed in relation to the selected boundary condition[1]

k	`kqRWallFunction`,
ω	`omegaWallFunction`,
ν_t	`nutRoughWallFunction`.

[1] we are referring to the distribution *OpenFOAM-extend-4.0*.

identifier	fitting function
new	(5.68) only u_τ as free parameter
opti	(5.62) and z_0 as free parameter
smooth	(5.62) with Nikuradse smooth condition (no dependence from κ_s)
rough-min	(5.62) with Nikuradse rough condition and $\kappa_s = \kappa_{s,min}$
rough-max	(5.62) with Nikuradse rough condition and $\kappa_s = \kappa_{s,max}$

$$d_{min} = 1 \cdot 10^{-4} \overset{(5.64)}{\longrightarrow} \kappa_{s,min} = 2 \cdot 10^{-4} \overset{(5.65)}{\longrightarrow} z_0 = 6.667 \cdot 10^{-6} \longrightarrow \text{rough-min}$$

$$d_{max} = 6 \cdot 10^{-4} \overset{(5.64)}{\longrightarrow} \kappa_{s,max} = 3 \cdot 10^{-3} \overset{(5.65)}{\longrightarrow} z_0 = 1.000 \cdot 10^{-4} \longrightarrow \text{rough-max}$$

	new	opti		smooth				rough-min		rough-max	
U_∞ $[ms^{-1}]$	u_τ $[ms^{-1}]$	u^* $[ms^{-1}]$	$z_0 \cdot 10^{-5}$ $[m]$	u^* $[ms^{-1}]$	$z_0 \cdot 10^{-6}$ $[m]$	Re_κ^{min} $[\cdot]$	Re_κ^{max} $[\cdot]$	u^* $[ms^{-1}]$	Re_κ $[\cdot]$	u^* $[ms^{-1}]$	Re_κ $[\cdot]$
8	0.3315	0.4062	2.815	0.3264	5.106	4.4	65.3	0.3368	4.5	0.4953	99.1
10	0.3959	0.5248	4.174	0.3899	4.274	5.2	78.0	0.4107	5.5	0.6041	120.8
12	0.4647	0.5291	1.227	0.4578	3.640	6.1	91.6	0.4908	6.5	0.7216	144.3
14	0.5281	0.6876	2.972	0.5204	3.203	6.9	104.1	0.5659	7.5	0.8320	166.4
16	0.6061	0.7533	1.905	0.5975	2.790	8.0	119.5	0.6595	8.8	0.9698	194.0
18	0.6875	0.8233	1.298	0.6778	2.459	9.0	135.6	0.7582	10.1	1.1150	222.9

Table 5.6: Results of mean wind velocity fittings for different models.

d $[mm]$	w_{sed} $[ms^{-1}]$	u_t^* $[ms^{-1}]$
0.15	0.76752	$2.41409 \cdot 10^{-1}$
0.25	1.42068	$2.95184 \cdot 10^{-1}$
0.35	2.02412	$3.43702 \cdot 10^{-1}$
0.45	2.58013	$3.87095 \cdot 10^{-1}$
0.55	3.09378	$4.26473 \cdot 10^{-1}$

Table 5.7: Sedimentation velocity w_{sed} computed as described in Section 5.2.2 and threshold shear velocity computed with (5.61).

d \ U_∞	8	10	12	14	16	18
0.15	✓	✓	✓	✓	✓	✓
0.25	✓	✓	✓	✓	✓	✓
0.35	×	✓	✓	✓	✓	✓
0.45	×	✓	✓	✓	✓	✓
0.55	×	×	✓	✓	✓	✓

✓	erosion
×	no-erosion
	correct prediction
	incorrect prediction

Table 5.8: Boolean predictions of erosion using (5.61) proposed by [186]. The comparison between the u_τ and u_t^* determines if erosion occurs. U_∞ is measured in ms^{-1} and d is measured in mm.

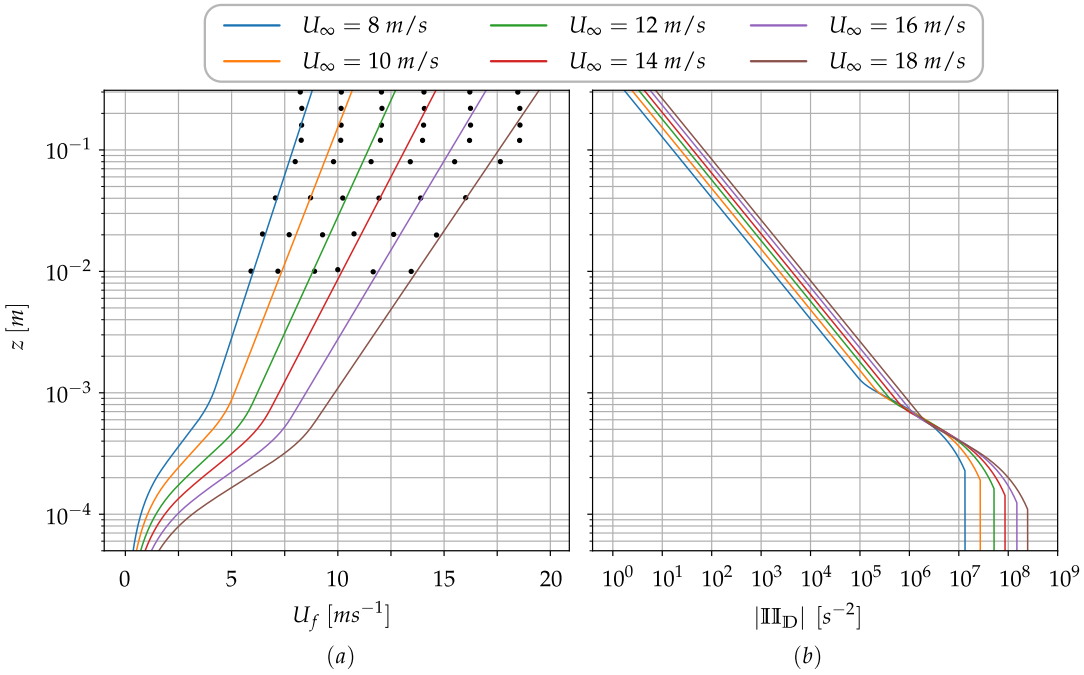

Figure 5.27: (a) Experimental data and fittings of the mean wind velocity of [142]. (b) Derived values of $|\mathbb{III}_\mathbb{D}|$ along z, see Table 5.9 for the related ground values.

$U_\infty\ [ms^{-1}]$	$max(\lvert\mathbb{III}_\mathbb{D}\rvert)\ [s^{-2}]$
8	$1.341 \cdot 10^7$
10	$2.728 \cdot 10^7$
12	$5.180 \cdot 10^7$
14	$8.640 \cdot 10^7$
16	$1.500 \cdot 10^8$
18	$2.482 \cdot 10^8$

Table 5.9: Values of the maximum absolute value of the second invariant with respect to experimental free-stream velocities.

Turbulence Profile

In order to properly quantify ν_t we need to set the turbulence properties. In [142] no data on turbulence are provided. Hence, we need to fill the lack of data. In view of a computational implementation, instead of using an explicit formula for ν_t we consider the $k-\omega$ system of RANS equations and we impose $\overline{\mathbf{u}}_f$ in order to match the mean wind velocity profile U_f. The velocity field defined by $U_f \mathbf{e}_x$ is divergence-free because it varies only over z. This approach fills the lack of data and allows to introduce the effect of a turbulence model, providing additional flexibility to the algorithm pipeline to compute the ν_{coll} formulation. Indeed, we could adopt a LES approach to compute a more accurate turbulence state and as a consequence to refine the model accuracy. Here we focus on RANS models because the industrial cases considered in the *SMaRT* context are so large to only leave the possibility to use these approaches.

The system of equation to be solved reads

$$\begin{cases} \nabla \cdot (k\, U_f \mathbf{e}_x) = \nabla \cdot [(\sigma_k \nu_f + \nu)\nabla k] + \tilde{P}_k - \beta^* k\omega \,, \\ \nabla \cdot (\omega\, U_f \mathbf{e}_x) = \nabla \cdot [(\sigma_\omega \nu_f + \nu)\nabla \omega] + \frac{\omega}{k}\alpha P_k - \beta\omega^2 + (1-F_1)\frac{2\sigma_\omega}{\omega}\nabla k \cdot \nabla\omega \,. \end{cases} \tag{5.69}$$

Therefore, solving for k and ω we can compute ν_t using its definition (5.6). In order to numerically solve (5.69) we modify the standard `simpleFoam`[2] solver of OpenFOAM. We substantially superimpose the fluid velocity vector field `U` (which is divergence free by construction). This new sub-solver is addressed as `expSimpleFoam`, and it can be used with several turbulence models for future tests. In order to make a comparison with literature formulae, we consider the approximation proposed in [191] with a correction factor of 0.81

$$\nu_t \simeq 0.81\, \kappa\, u_\tau\, z \,. \tag{5.70}$$

Figure 5.28 shows the comparison of ν_t between `expSimpleFoam` numerical results and the graph of (5.70). We can notice that both formulations provide similar values in the first ten centimeters, and suddenly diverge for higher value of z. However, we remark that most of the solid particles transport move in the first few centimeters. Hence, an error on ν_t for high values of z does not compromise the bulk behavior of the outcoming results.

Solid Concentration Model

Despite in Section 5.3.1 we considered special functions to mimic the φ_s behavior, the measurements of [142] are well described by

$$\varphi_s = \varphi_0 e^{-bz} \,. \tag{5.71}$$

According to (5.39) the equivalent diffusivity reads

$$\nu_{eq} = -w_{sed}\frac{\varphi_s}{\frac{d\varphi_s}{dz}} = -w_{sed}\frac{\varphi_s}{-b\varphi_s} = \frac{w_{sed}}{b} \,,$$

[2] `simpleFoam` is a standard solver in OpenFOAM which implements the SIMPLE algorithm.

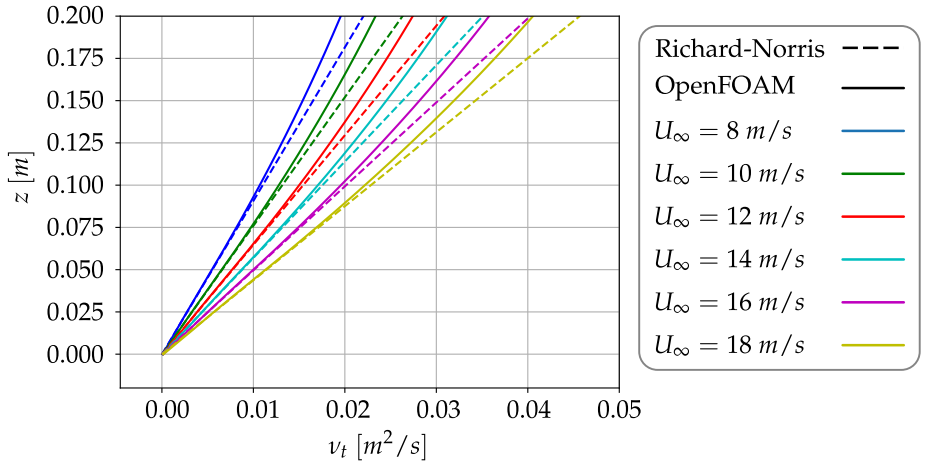

Figure 5.28: Comparison of the turbulent diffusivity obtained from OpenFOAM simulations and formula (5.70) (see [191])

d \ U_∞	10	12	14	16	18
0.15	$9.43 \cdot 10^{-5}$	$1.91 \cdot 10^{-4}$	$3.21 \cdot 10^{-4}$	$4.26 \cdot 10^{-4}$	$4.99 \cdot 10^{-4}$
0.25	$4.95 \cdot 10^{-5}$	$9.78 \cdot 10^{-5}$	$1.76 \cdot 10^{-4}$	$2.68 \cdot 10^{-4}$	$3.09 \cdot 10^{-4}$
0.35	$4.06 \cdot 10^{-5}$	$5.28 \cdot 10^{-5}$	$1.13 \cdot 10^{-4}$	$2.08 \cdot 10^{-4}$	$3.29 \cdot 10^{-4}$
0.45	$2.65 \cdot 10^{-5}$	$5.43 \cdot 10^{-5}$	$1.04 \cdot 10^{-4}$	$1.69 \cdot 10^{-4}$	$2.39 \cdot 10^{-4}$
0.55	$1.79 \cdot 10^{-5}$	$3.38 \cdot 10^{-5}$	$6.92 \cdot 10^{-5}$	$1.01 \cdot 10^{-4}$	$1.71 \cdot 10^{-4}$

Table 5.10: Value of φ_0 for all experimental cases of [142]. U_∞ is measured in ms^{-1} and d is measured in mm.

d \ U_∞	10	12	14	16	18
0.15	25.17	27.52	25.41	23.43	20.74
0.25	17.63	19.39	20.11	21.82	2.23
0.35	16.36	13.21	16.39	19.17	20.44
0.45	11.53	14.19	16.98	17.76	20.41
0.55	9.92	12.55	14.85	16.34	18.48

Table 5.11: Value of b for all experimental cases of [142]. U_∞ is measured in ms^{-1} and d is measured in mm.

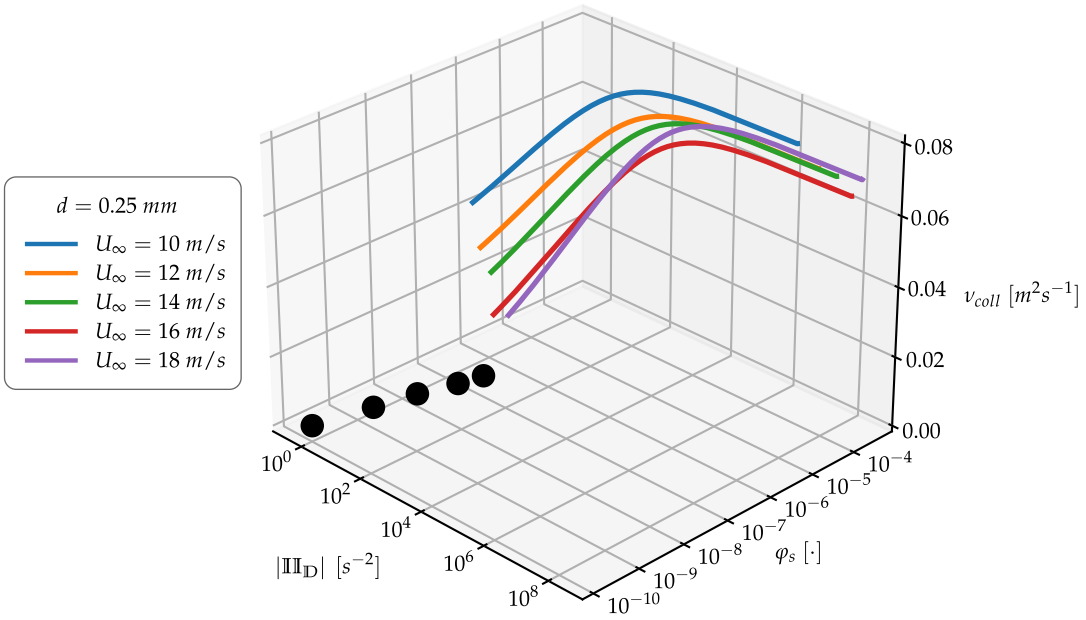

Figure 5.29: Embedding of the experimental data into the space $(\varphi_s, |\mathbb{III}_\mathbb{D}|, \nu_{coll})$.

which is constant because w_{sed} depends on the grain diameter (which is also constant for each experiment stage) and b is a parameter. According to (5.9) (with $\lambda = 1$) we can compute ν_{coll} as

$$\nu_{coll} = \frac{w_{sed}}{b} - \nu_t \ . \tag{5.72}$$

Therefore, for each combination of U_∞ and d we can extract the behavior of ν_{coll} on z.

Data Embedding

In the previous steps we basically described the behavior of φ_s, $|\mathbb{III}_\mathbb{D}|$ and ν_{coll} along z for each combination of U_∞ and d. Therefore, each pair (U_∞, d) identifies a curve in the space $(\varphi_s, |\mathbb{III}_\mathbb{D}|, \nu_{coll})$ which represents all the states of the flow along the vertical line. The diameter can be thought as an additional parameter, but it is not a real system variable because it is constant in each experimental run. Therefore, we take into account its effect only in a post processing fitting stage. Figure 5.29 shows the the curves for the diameter $d = 0.25\ mm$, where the black dots are the extrapolated intersections between the curves and the plane $\nu_{coll} = 0$. The spatial location of these curves suggests the existence of a surface which encodes the values experienced in all possible physical flows. Ideally, experimental data would populate the space $(\varphi_s, |\mathbb{III}_\mathbb{D}|, \nu_{coll})$ as a cloud of points and consequently we would compute a multivariate fitting with a generalized model instead of following the procedure presented here. However, due to the small amount of structured data of [142], instead of trying to compute a multivariate fitting we project the curves on the coordinate planes and we progressively build an analytic formula for ν_{coll}.

Projection on $(|\mathbb{III}_{\mathbb{D}}|, \nu_{coll})$ Figure 5.30 shows the projections of the experimental curves in the space $(|\mathbb{III}_{\mathbb{D}}|, \nu_{coll})$. The prototype function that we chose reads

$$\nu_{coll,\mathbb{III}_{\mathbb{D}}} = \nu_\infty \left(1 - \sqrt{\frac{\mathbb{III}_0}{\mathbb{III}_{\mathbb{D}}}}\right)_+$$

but, in order to facilitate the data regression we use the equivalent form

$$\nu_{coll,\mathbb{III}_{\mathbb{D}}} = \nu_\infty \left[1 - \exp\left(-\frac{1}{2}\left(\ln\left(|\mathbb{III}_{\mathbb{D}}|\right) - \ln(\mathbb{III}_0)\right)_+\right)\right] \tag{5.73}$$

where ν_∞ quantifies the horizontal asymptote showed by all curves, and $\mathbb{III}_0$ quantifies the value of $|\mathbb{III}_{\mathbb{D}}|$ such that the curve intersect the plane $\nu_{coll} = 0$. Figure 5.31 shows the values of ν_∞ for each pair (U_∞, d). The data suggest to adopt

$$\nu_\infty = m_\infty(d)\ln(\varphi_s) + c_\infty(d)\ , \tag{5.74}$$
$$m_\infty = S_m^\infty\, d + C_m^\infty\ , \tag{5.75}$$
$$c_\infty = S_c^\infty\, d + C_c^\infty\ . \tag{5.76}$$

See Table 5.12 for the results of the non-linear regressions.

Projection on (φ_s, ν_{coll}) Analogously to the previous projection, we consider the projections of the experimental curves in the space (φ_s, ν_{coll}). The prototype function that we chose reads

$$\nu_{coll,\varphi} = \mathcal{S}\left(\ln\left(\frac{\varphi_s}{\Phi_0}\right)\right)_+ . \tag{5.77}$$

This formulation allows to extract Φ_0 for each pair (U_∞, d). See Table 5.12 for the results of the non-linear regressions.

Zero threshold for the collisional diffusivity Figure 5.33 shows the combination of values Φ_0 and $\mathbb{III}_0$, which can be interpreted as the set of point such that ν_{coll} - intended as two variable function - nullifies (see Figure 5.35). We aim to model this set of points by means of (5.78), (5.79) and (5.80).

$$\ln(\mathbb{III}_0) = m_0(d)\ln(\Phi_0) + c_0(d)\ , \tag{5.78}$$
$$m_0 = S_m^0\, d + C_m^0\ , \tag{5.79}$$
$$c_0 = S_c^0\, d + C_c^0\ . \tag{5.80}$$

Final fomulation for the collisional diffusivity Combining all formulas described above we propose the following formula for ν_{coll}

$$\nu_{coll} = \left[m_\infty(d)\ln(\varphi_s) + c_\infty(d)\right]\left[1 - e^{-\frac{1}{2}\left(\ln(|\mathbb{III}_{\mathbb{D}}|) - [m_0(d)\ln(\varphi_s) + c_0(d)]\right)_+}\right]\ , \tag{5.81}$$

which is used in the OpenFOAM implementation of the *First Order Model*. Regardless of the analytic properties of this formulation we can notice that the strength of the wind is encoded in the action of $|\mathbb{III}_{\mathbb{D}}|$ and it increases the diffusive effect if the

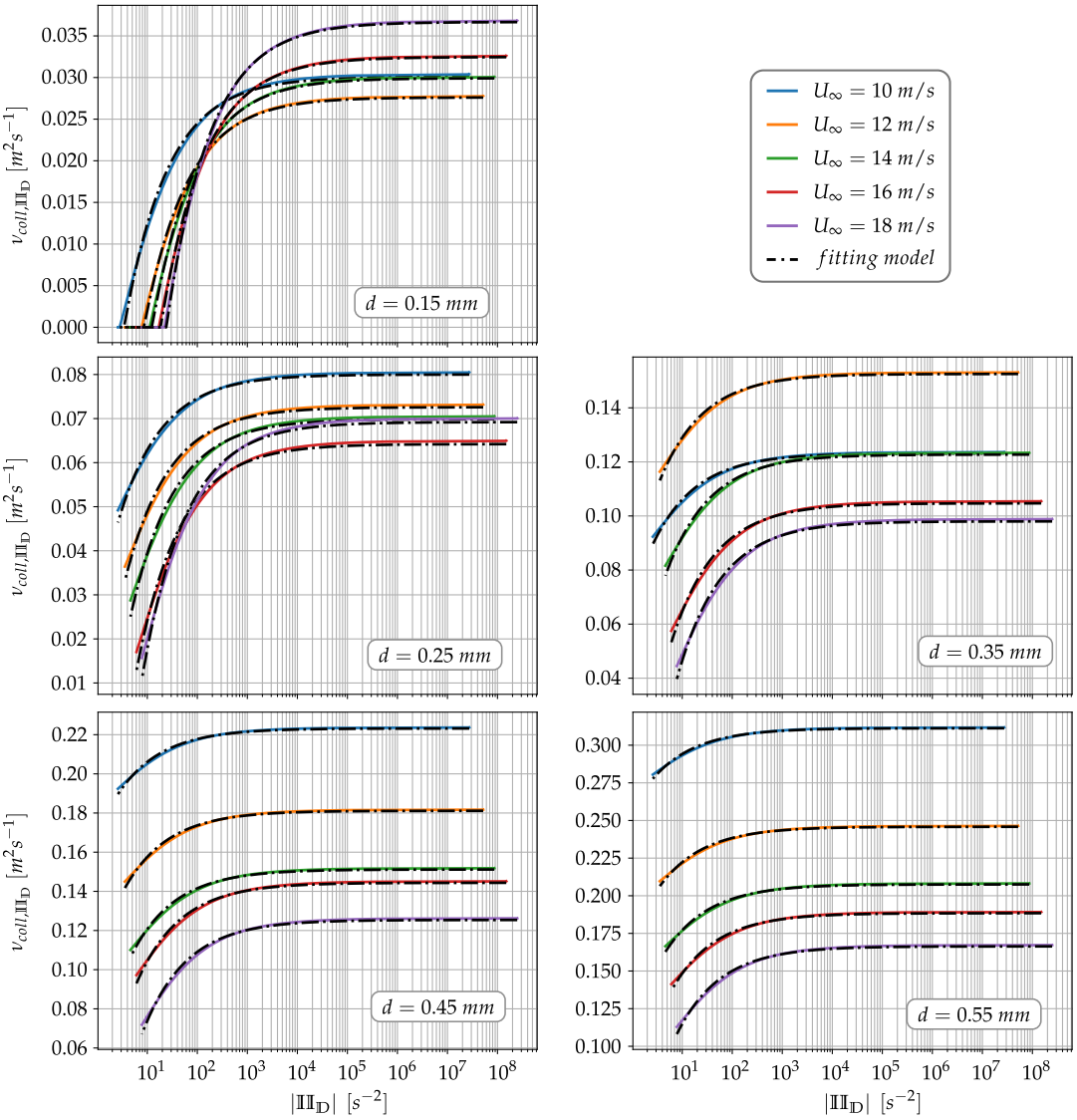

Figure 5.30: Projection of experimental curves in the plane $(|\mathbb{III}_\mathbb{D}|, \nu_{coll})$ and their non-linear regression with the model (5.73).

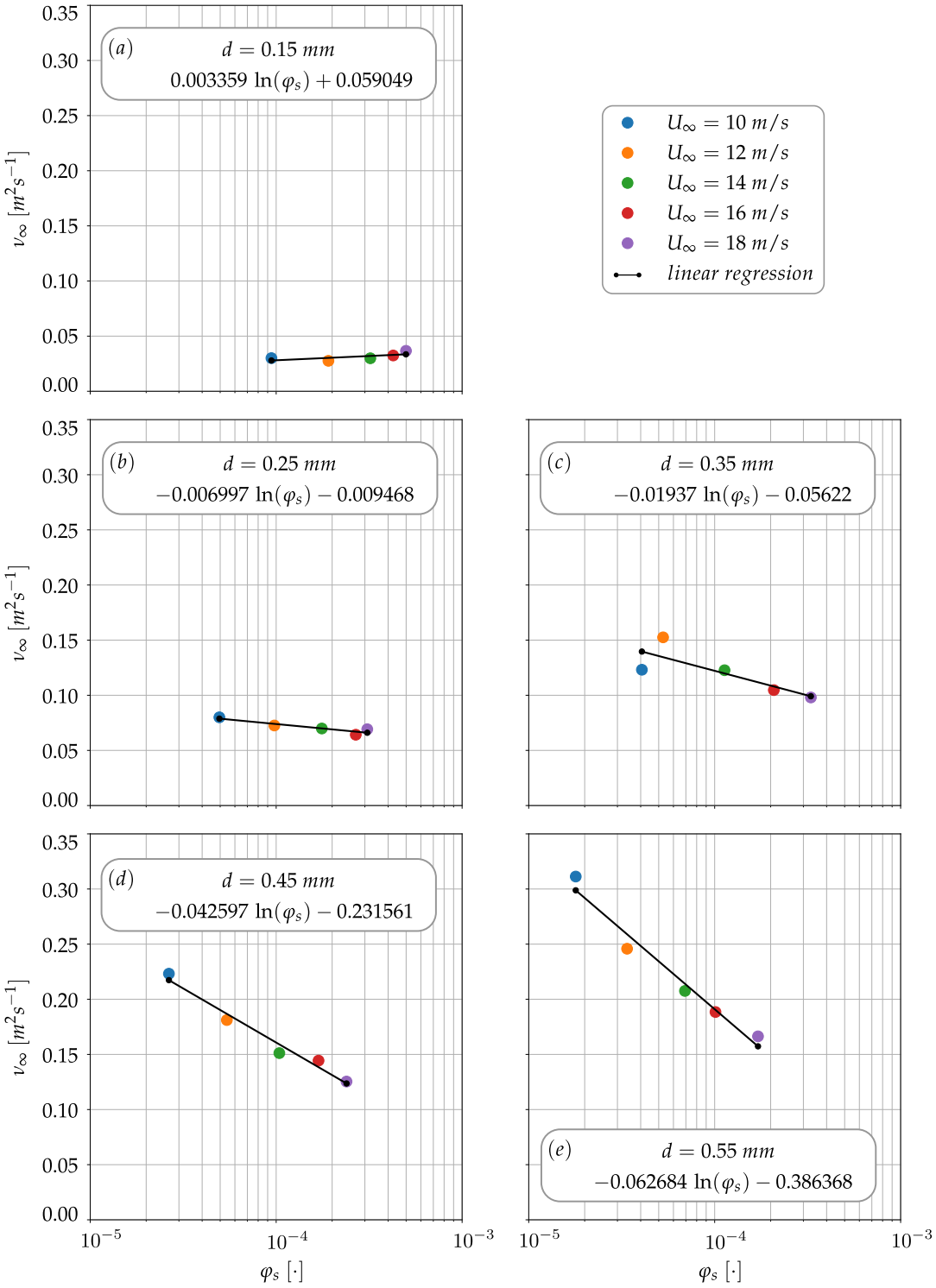

Figure 5.31: Values of ν_∞ for each pair (U_∞, d) and regressions with the model (5.74).

d $[mm]$	U_∞ $[ms^{-1}]$	ν_∞ $[m^2s^{-1}]$	$\ln(\mathbb{III}_0)$ $[\cdot]$	Φ_0 $[\cdot]$	$\mathcal{S}$ $[m^2s^{-1}]$
0.15	10	$3.0067 \cdot 10^{-2}$	$3.45317 \cdot 10^{0}$	$1.36428 \cdot 10^{-7}$	$4.59879 \cdot 10^{-3}$
	12	$2.7613 \cdot 10^{-2}$	$8.59804 \cdot 10^{0}$	$9.36303 \cdot 10^{-7}$	$5.19270 \cdot 10^{-3}$
	14	$2.9920 \cdot 10^{-2}$	$1.23881 \cdot 10^{1}$	$3.07236 \cdot 10^{-6}$	$6.43618 \cdot 10^{-3}$
	16	$3.2462 \cdot 10^{-2}$	$1.85277 \cdot 10^{1}$	$7.62087 \cdot 10^{-6}$	$8.06851 \cdot 10^{-3}$
	18	$3.6669 \cdot 10^{-2}$	$2.40308 \cdot 10^{1}$	$1.43770 \cdot 10^{-5}$	$1.03387 \cdot 10^{-2}$
0.25	10	$8.0005 \cdot 10^{-2}$	$4.56207 \cdot 10^{-1}$	$1.66954 \cdot 10^{-10}$	$6.34983 \cdot 10^{-3}$
	12	$7.2587 \cdot 10^{-2}$	$1.05248 \cdot 10^{0}$	$2.18338 \cdot 10^{-9}$	$6.77774 \cdot 10^{-3}$
	14	$6.9868 \cdot 10^{-2}$	$1.89473 \cdot 10^{0}$	$1.44423 \cdot 10^{-8}$	$7.42655 \cdot 10^{-3}$
	16	$6.4214 \cdot 10^{-2}$	$3.89189 \cdot 10^{0}$	$7.54107 \cdot 10^{-8}$	$7.85437 \cdot 10^{-3}$
	18	$6.9209 \cdot 10^{-2}$	$5.54308 \cdot 10^{0}$	$2.29763 \cdot 10^{-7}$	$9.60715 \cdot 10^{-3}$
0.35	10	$1.2315 \cdot 10^{-1}$	$1.92556 \cdot 10^{-1}$	$6.20390 \cdot 10^{-13}$	$6.84276 \cdot 10^{-3}$
	12	$1.5254 \cdot 10^{-1}$	$2.38306 \cdot 10^{-1}$	$1.15714 \cdot 10^{-11}$	$9.94855 \cdot 10^{-3}$
	14	$1.2272 \cdot 10^{-1}$	$6.14152 \cdot 10^{-1}$	$1.59972 \cdot 10^{-10}$	$9.11213 \cdot 10^{-3}$
	16	$1.0469 \cdot 10^{-1}$	$1.46416 \cdot 10^{0}$	$1.70689 \cdot 10^{-9}$	$8.94013 \cdot 10^{-3}$
	18	$9.8010 \cdot 10^{-2}$	$2.76399 \cdot 10^{0}$	$1.09791 \cdot 10^{-8}$	$9.50845 \cdot 10^{-3}$
0.45	10	$2.2320 \cdot 10^{-1}$	$5.86163 \cdot 10^{-2}$	$2.75155 \cdot 10^{-15}$	$9.70924 \cdot 10^{-3}$
	12	$1.8115 \cdot 10^{-1}$	$1.68995 \cdot 10^{-1}$	$1.73927 \cdot 10^{-13}$	$9.26148 \cdot 10^{-3}$
	14	$1.5117 \cdot 10^{-1}$	$4.04720 \cdot 10^{-1}$	$3.56860 \cdot 10^{-12}$	$8.79552 \cdot 10^{-3}$
	16	$1.4438 \cdot 10^{-1}$	$7.69828 \cdot 10^{-1}$	$3.56860 \cdot 10^{-12}$	$9.64990 \cdot 10^{-3}$
	18	$1.2540 \cdot 10^{-1}$	$1.68849 \cdot 10^{0}$	$4.56318 \cdot 10^{-10}$	$9.52243 \cdot 10^{-3}$
0.55	10	$3.1129 \cdot 10^{-1}$	$3.01336 \cdot 10^{-2}$	$1.87456 \cdot 10^{-17}$	$1.12850 \cdot 10^{-2}$
	12	$2.4583 \cdot 10^{-1}$	$9.17576 \cdot 10^{-2}$	$2.15463 \cdot 10^{-15}$	$1.04717 \cdot 10^{-2}$
	14	$2.0756 \cdot 10^{-1}$	$2.14698 \cdot 10^{-1}$	$7.53524 \cdot 10^{-14}$	$1.00571 \cdot 10^{-2}$
	16	$1.8844 \cdot 10^{-1}$	$4.51923 \cdot 10^{-1}$	$1.59027 \cdot 10^{-12}$	$1.04885 \cdot 10^{-2}$
	18	$1.6639 \cdot 10^{-1}$	$9.58953 \cdot 10^{-1}$	$2.29982 \cdot 10^{-11}$	$1.05169 \cdot 10^{-2}$

Table 5.12: Regression coefficient for each pair (U_∞, d) with models (5.73) and (5.77).

d $[mm]$	m_0 $[\cdot]$	c_0 $[\cdot]$	m_∞ $[\cdot]$	c_∞ $[\cdot]$
0.15	$4.09805 \cdot 10^{-1}$	7.75463	$3.35870 \cdot 10^{-3}$	$5.90491 \cdot 10^{-2}$
0.25	$3.48498 \cdot 10^{-1}$	7.02134	$-6.99684 \cdot 10^{-3}$	$9.46753 \cdot 10^{-3}$
0.35	$2.87059 \cdot 10^{-1}$	6.13155	$-1.93696 \cdot 10^{-2}$	$-5.62199 \cdot 10^{-2}$
0.45	$2.75252 \cdot 10^{-1}$	6.34857	$-4.25968 \cdot 10^{-2}$	$-2.31561 \cdot 10^{-1}$
0.55	$2.44961 \cdot 10^{-1}$	5.89985	$-6.26840 \cdot 10^{-2}$	$-3.86368 \cdot 10^{-1}$

Table 5.13: Regression coefficients for (5.75), (5.76), (5.79) and (5.80).

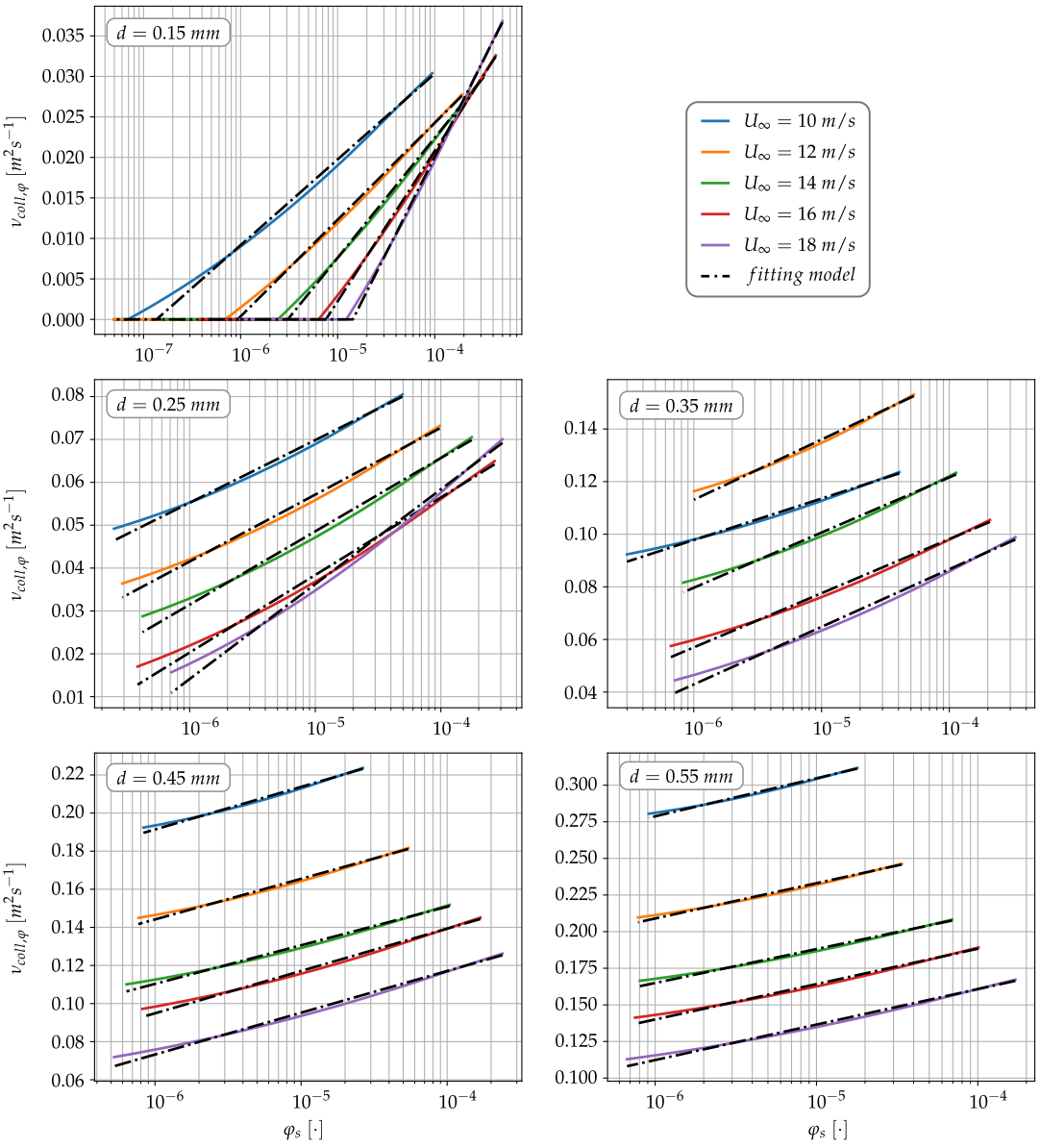

Figure 5.32: Projection of experimental curves in the plane (φ_s, ν_{coll}) and regression with the model (5.77).

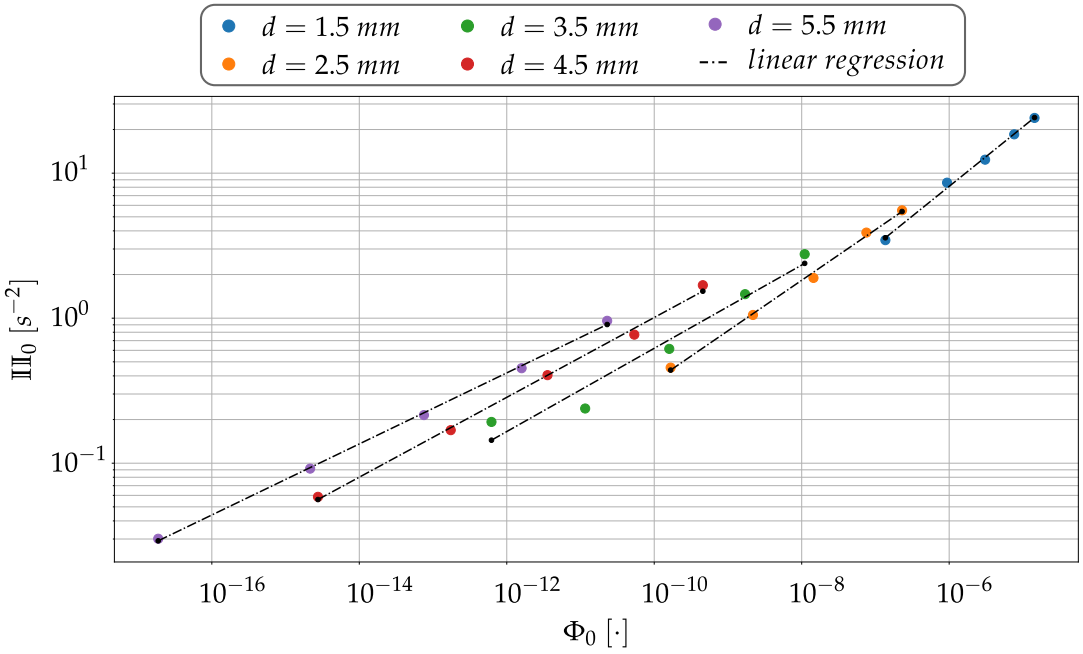

Figure 5.33: Location of points $(\Phi_0, \mathbb{II}_0)$ for all value of d and regression with the model (5.78).

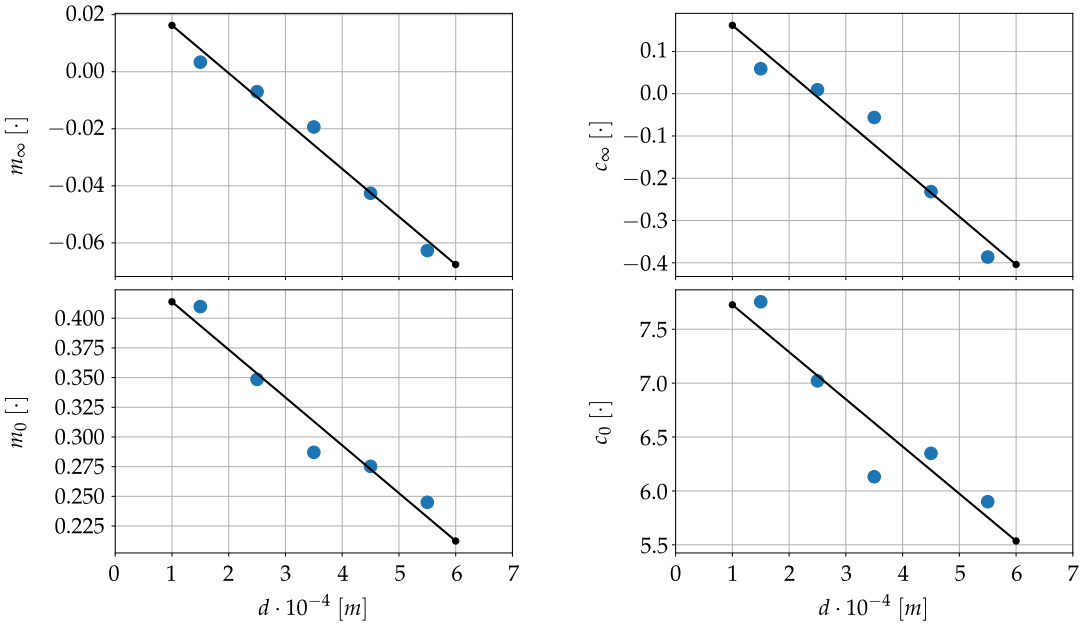

Figure 5.34: Parametrization with respect to d of (5.75), (5.76), (5.79) and (5.80).

S_m^∞	$-1.67685 \cdot 10^2$	S_m^0	$-4.02933 \cdot 10^2$
C_m^∞	$3.30322 \cdot 10^{-2}$	C_m^0	$4.54142 \cdot 10^{-1}$
S_c^∞	$-1.13186 \cdot 10^3$	S_c^0	$-4.38233 \cdot 10^3$
C_c^∞	$2.75026 \cdot 10^{-1}$	C_c^0	$8.16500 \cdot 10^0$

Table 5.14: Regression coefficients for (5.75), (5.76), (5.79) and (5.80).

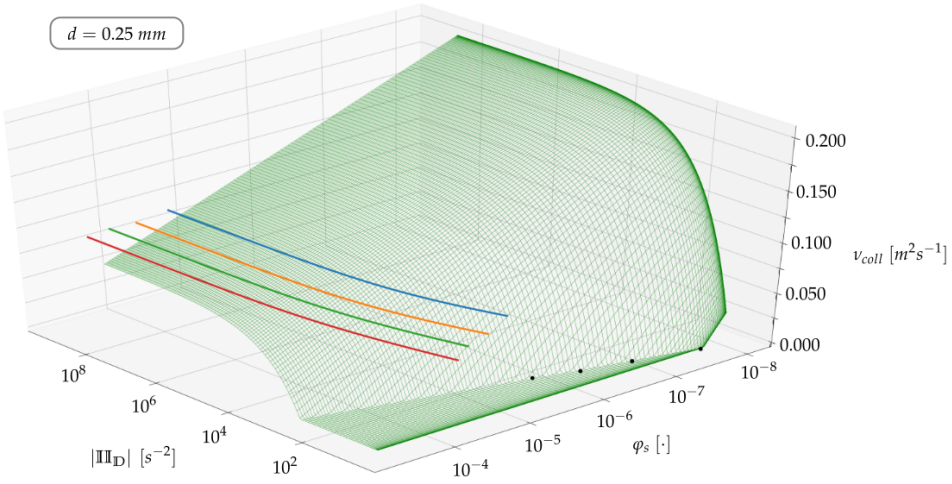

Figure 5.35: The resultant surface of ν_{coll} function for the case of $d = 0.25\ mm$. The colored curves represents the embedding of the experimental data in the space $(|\mathbb{II}_\mathbb{D}|, \varphi_s, \nu_{coll})$.

wind strength increases. Therefore, it is in accordance with experimental observations. Furthermore, φ_s determines both the threshold value for $|\mathbb{II}_\mathbb{D}|$ and the maximum value of ν_{coll}. Also this aspect is in accordance with experimental observation. Indeed, φ_s quantifies the presence of sand in a control volume, ν_{coll} is a diffusive coefficient that summarizes the collisional action of particles to each others. Indeed, if few particle are present in a control volume the collision probability decreases and the diffusivity is only due to turbulence effects (encoded by $\lambda\nu_t$). On the other hand, when many particles are present in a control volume the collision probability increases with a consequent increment of ν_{coll}. However, it cannot increase indefinitely because too many particle would lead to high dissipation. Hence, ν_{coll} has an asymptotic value ν_∞. The formulation also includes d as a parameter, which can be considered constant in a simulation.

5.4.3 The Flow Chart

All the steps described above can be conceptually summarized in the flow chart of Figure 5.36. We remark that this pipeline is highly modular. Indeed, most of sub-procedures can be substituted when new highly accurate data or new models eventually appear in literature. The bold symbols the flow chart address the computational arrays. In particular:

- $(z, \boldsymbol{\varphi}_s, \boldsymbol{U}_f)_{exp}$ is a triple of arrays, all with the same size, containing the experimental data.
- $(\boldsymbol{\varphi}_s, \boldsymbol{II}_{\mathbb{D}}, \boldsymbol{\nu}_{coll})_{CPU}$ is a triple of arrays obtained evaluating the non-linear models on the computational vector z_{CPU}. Also these arrays share the same dimension.

The showed diagram is mainly divided in two part. The upper part represents the treatment of the experimental data and the fix for the lack of data. The main output is the data embedding $(\boldsymbol{\varphi}_s, \boldsymbol{II}_{\mathbb{D}}, \boldsymbol{\nu}_{coll})_{CPU}$. However, data could directly come from measurements or from other procedures. The bottom part treats the triple just mentioned and it extract the analytic formula setting the vectors coefficients $\boldsymbol{cfs}_{\mathbb{III}_{\mathbb{D}}}$, $\boldsymbol{cfs}_{\varphi_s}$ and $\boldsymbol{cfs}_d$. The dashed boxes group main sub-steps of the flow. However, almost each detail can be easily updated without modifying the final result.

5.4.4 Quantitative Formulation of Boundary Conditions

In Section 5.2.5 we described the generic structure of boundary conditions for φ_s. However, we need to quantify the involved functions taking into account the experimental data. In the process of data analysis used to evaluate ν_{coll} we also indirectly have considered information about boundary conditions. In particular, the formulation of φ_s embeds the boundary value for the solid volume concentration and its normal derivative when an erodible surface experiences saltation.

Dirichlet Boundary Condition when a Dirichlet boundary condition is set the value of φ_s at the wall is directly obtained by φ_0 in (5.71). Table 5.10 collects the values of φ_0 for all combinations of U_∞ and d. Figure 5.37 (a) (respectively (b)) shows the relation between u_τ (respectively $|\mathbb{III}_{\mathbb{D}}(z=0)|$) and φ_0. We recall that u_τ and $|\mathbb{III}_{\mathbb{D}}(z=0)|$ are equivalent by (5.59), and in a simulation u_τ is evaluated computing the wall shear stress τ_{wall} and using the definition (5.59). In Figure 5.37 (a)-(b) the threshold values are plotted as black dots, and they are calculated using (5.61). Just taking inspiration by the data, the proposed prototype function reads

$$\varphi_s(z=0) = \varphi_0 \simeq A_w (u_\tau - u_t^*)_+^\gamma \,, \tag{5.82}$$

where A_w and γ are fitting coefficients depending on the grain diameter. For sake of simplicity the behavior of A_w and γ with respect of d is approximated using a polynomial of degree two. Hence

$$A_w, \gamma \sim a_2\, d^2 + a_1\, d + a_0 \tag{5.83}$$

where a_0, a_1 and a_2 are constants. Regression procedures lead to results of Table 5.15 and 5.16. Figure 5.38 shows the behavior of coefficients A_w and γ, and their fitting with (5.83).

Neumann Boundary Condition when a Neumann boundary condition is set, recalling (5.71) we have

$$-\frac{\partial \varphi_s}{\partial \mathbf{n}} = \frac{d\varphi_s}{dz} = -b\varphi_0 e^{-bz}$$

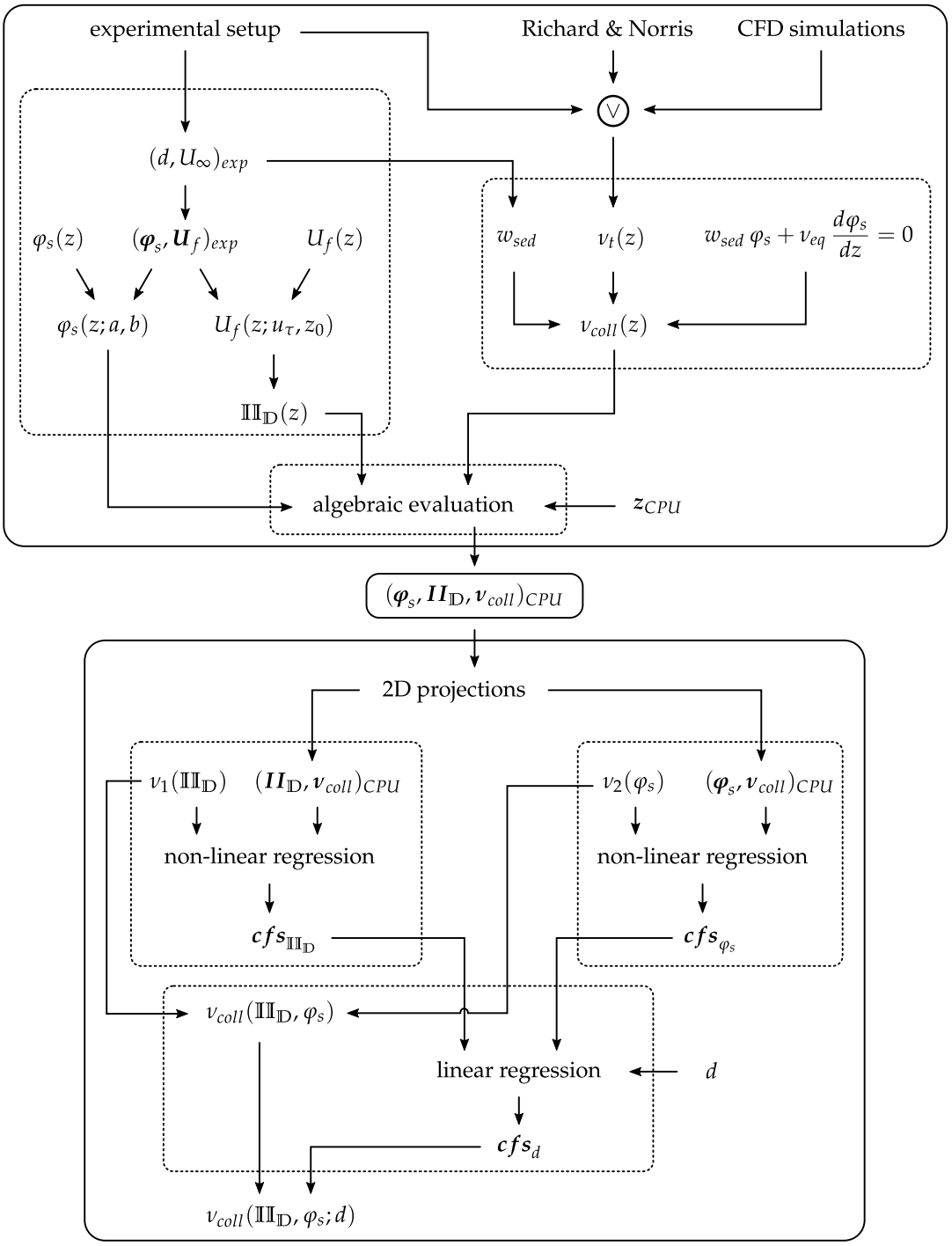

Figure 5.36: Flow chart representation of the model derivation.

d	A_w	γ
0.15	$1.55479 \cdot 10^{-3}$	1.34781
0.25	$1.06038 \cdot 10^{-3}$	1.26306
0.35	$1.89819 \cdot 10^{-3}$	1.64782
0.45	$8.46913 \cdot 10^{-4}$	1.05827
0.55	$6.33719 \cdot 10^{-4}$	0.99798

Table 5.15: Values of A_w and γ for the cases of [142].

	a_2	a_1	a_0
A_w	$-9.47604374 \cdot 10^{3}$	$4.57762211 \cdot 10^{0}$	$9.46966029 \cdot 10^{-4}$
γ	$-6.60991691 \cdot 10^{6}$	$3.72249022 \cdot 10^{3}$	$9.02030089 \cdot 10^{-1}$

Table 5.16: Fitting coefficients for A_w and γ.

and evaluating it at $z = 0$ we have

$$\frac{d\varphi_s}{dz}(z=0) = -b\varphi_0 \simeq B_w(u_\tau - u_t^*)_+^\beta \,, \tag{5.84}$$

where B_w and μ are fitting coefficients depending on the grain diameter. As well as the Dirichlet case, in order to compute B_w and μ with respect to d we use a polynomial of degree two

$$B_w, \beta \sim b_2\, d^2 + b_1\, d + b_0 \tag{5.85}$$

where b_0, b_1 and b_2 are constants. Regression procedures lead to the results in Tables 5.17 and 5.18. Figure 5.38 shows the behavior of the coefficients B_w and β, and their fitting with (5.85).

Non-Erodible Surfaces For non-erodible surfaces the Robin condition (5.35) applies. Regardless the formulation of ν_{coll}, the condition (5.35) guarantees that the flux through the boundary is null i.e. the surface is actually non-erodible. In [102] it is discussed the importance of the ground mechanical properties on the final concentration profile behavior. However, data are not quantitatively wide enough to be used in an upgrade for the model of ν_{coll}. Therefore the accuracy for this condition

$d\ [mm]$	$B_w\ [m^{-1}]$	$\beta\ [\cdot]$
0.15	$2.69893 \cdot 10^{-2}$	1.07731
0.25	$2.27284 \cdot 10^{-2}$	1.29662
0.35	$5.70430 \cdot 10^{-2}$	2.00124
0.45	$2.50325 \cdot 10^{-2}$	1.36977
0.55	$1.68559 \cdot 10^{-2}$	1.27222

Table 5.17: Values of B_w and β for the cases of [142].

		$b_2\ [m^{-3}]$	$b_1\ [m^{-2}]$	$b_0\ [m^{-1}]$
$[m^{-1}]$	B_w	$-5.29689595 \cdot 10^5$	$3.52820069 \cdot 10^2$	$-1.82764285 \cdot 10^{-2}$
$[\cdot]$	β	$-1.40701243 \cdot 10^7$	$1.03120446 \cdot 10^4$	$-2.00790156 \cdot 10^{-1}$

Table 5.18: Fitting coefficients for B_w, β and law (5.85).

is not guaranteed. On the other hand, in industrial cases the amount of area of non-erodible surfaces results to be negligible with respect to sandy surfaces. In Chapter 6 we consider a semi-stochastic Lagrangian model allowing to take into account local properties of surfaces. Its aim is not industrial but it can be used for future developments of boundary conditions.

We remark that both Dirichlet and Neumann boundary conditions involve the value of $|\mathbb{II}_{\mathbb{D}}|$ which is computed by the solution for $\overline{\mathbf{u}}$. This implies that the system of boundary condition for (5.10) is non-linear, requiring an iterative process to be solved. This fact shows the complexity that involve the modeling procedures in the case of tracking boundary approaches.

5.4.5 Implementation Accuracy

The arguments developed in previous Sections is based on a mixed approach between data-driven analysis and fundamental principles of continuum mechanics. Numerical approximations have been used for fitting procedures and for the generation of missing data. We remark that in most of the experimental literature the statistical properties of measurements are missing, therefore some discrepancies can be related to the summation of multiple error sources. However, in order to evaluate the effectiveness of (5.81) formulation we can test it in the OpenFOAM implementation of the *First Order Model* over the same conditions of [142]. Figure 5.39 shows the comparison between OpenFOAM results with Dirichlet boundary conditions (red curve) and the target curve obtained from experiments (black curve). Figure 5.40 shows the same comparison but the coefficient λ is set to be five. The results are organized in a grid of images where each row represents a value of d and each column represents a value of U_∞.

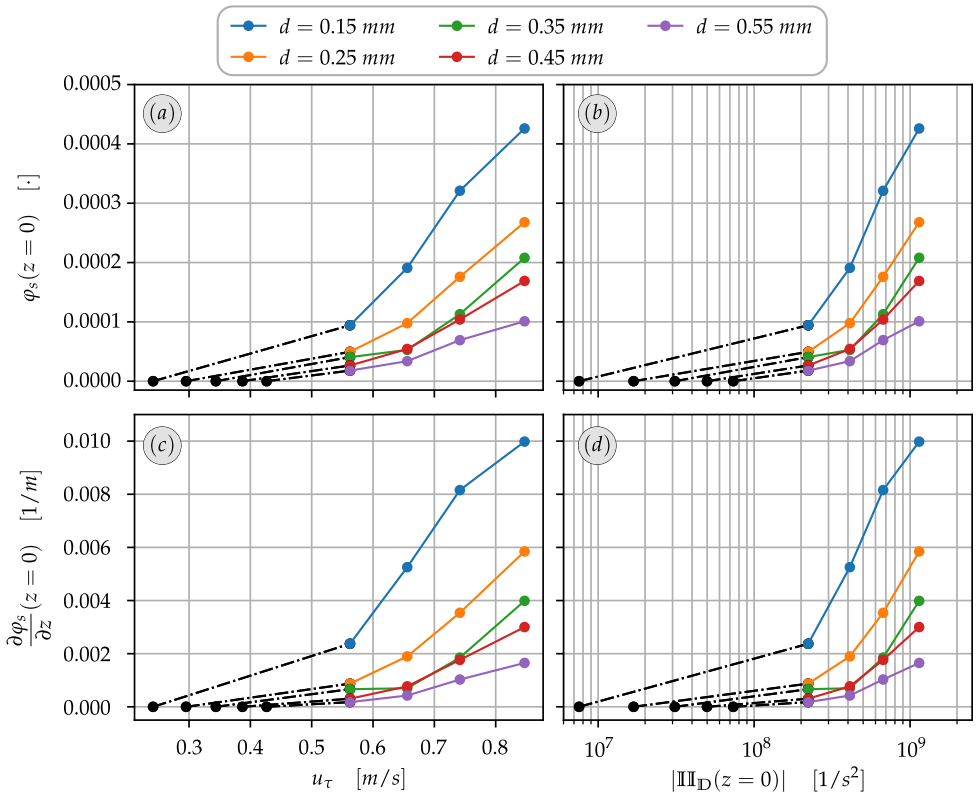

Figure 5.37: Boundary conditions values for different regimes. Colored dots represent extrapolations from experimental data, black dots represent the threshold values according to (5.61). (a)-(b) Dirichlet boundary condition. (c)-(d) Neumann boundary condition.

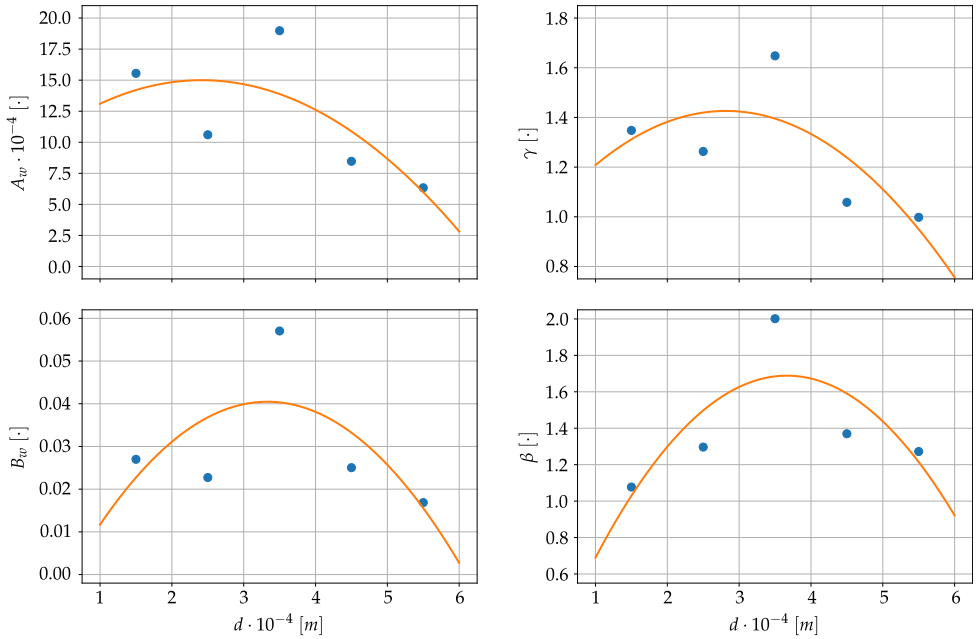

Figure 5.38: Parametrization of coefficients for boundary conditions with respect to d.

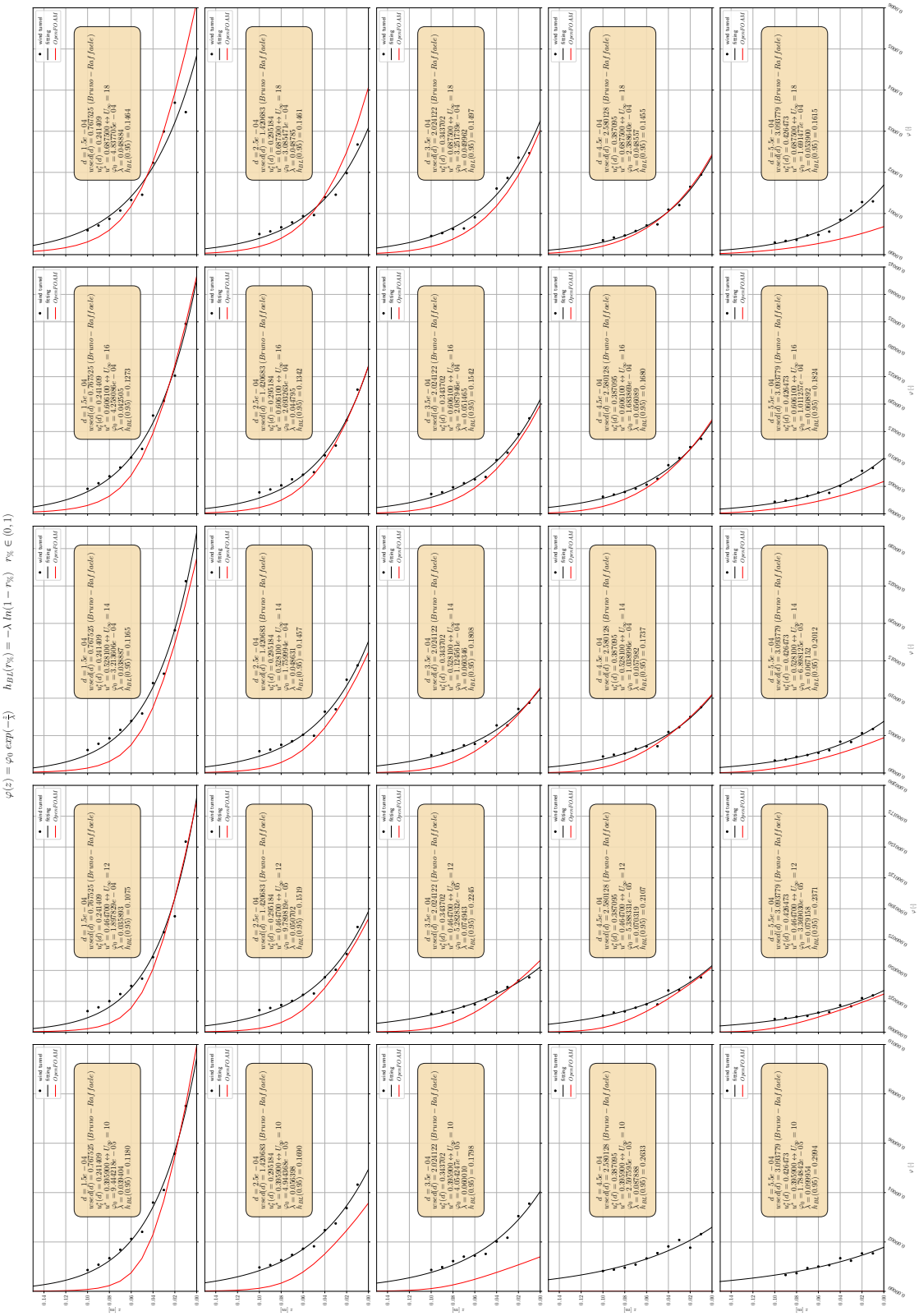

Figure 5.39: Implementation accuracy results with $\lambda = 1$.

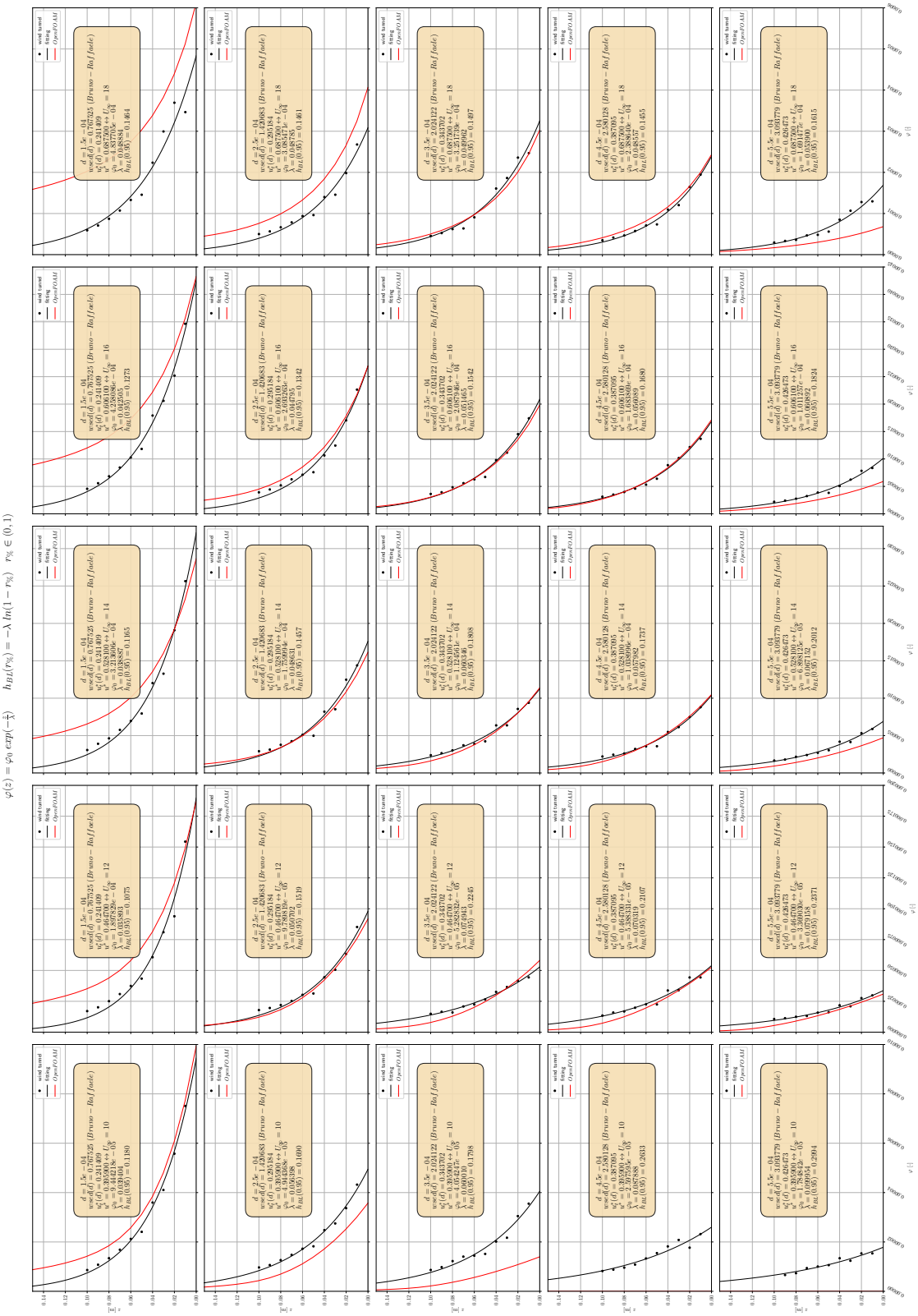

Figure 5.40: Implementation accuracy results with $\lambda = 5$.

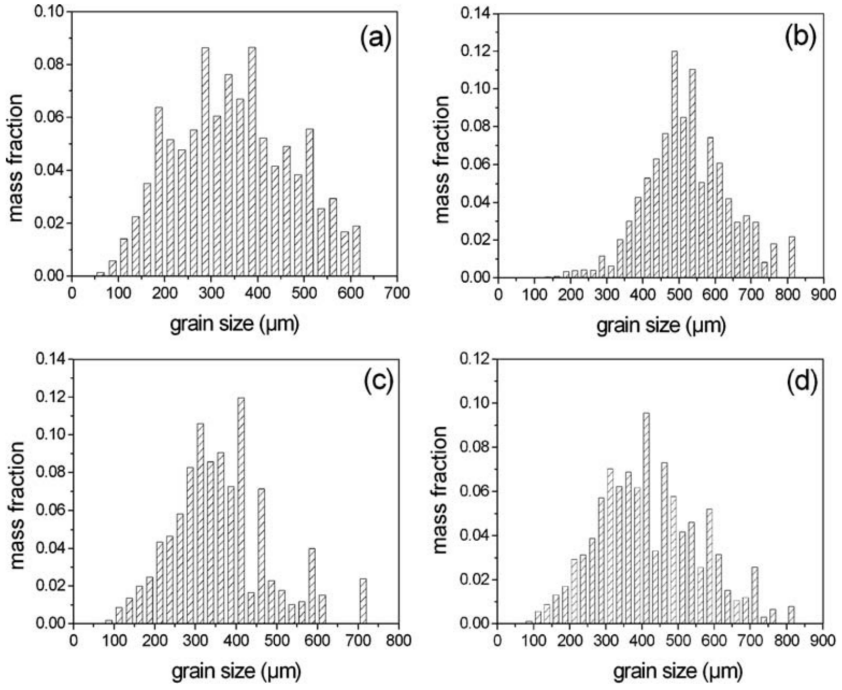

Figure 5.41: Sand samples of the experimental setup presented in [232].

5.5 Multi Solid Phases

The diameters range of natural sand grains is approximately $[10^{-5}, 10^{-3}]\ m$ (see [16]). It is true that in order to understand and describe the phenomenon in a controlled like environment - for example in wind tunnel - it is possible to precisely select the diameters to use in experiments. However, a natural sample of sand can also exhibits several diameter spectra (see Figure 5.41). The *First Order Model* used until now assumes one value for the characteristics sand diameter, but it can be improved to consider a multiple solid phase formulation that takes into account several diameters in one simulation.

The presence of heterogeneous sand has relevant effects on boundary condition modeling; Paragraph 5.5.1 will briefly discuss the effect of a non-homogeneous spatial distribution of the underground sand diameter spectrum. For sake of simplicity in this section we suppose that the diameter spectrum is homogeneous in all settled sand volume. The interaction between wind and particles changes significantly with respect to the particle diameter and shape. Therefore, we expect that distinct wind sources lead to significantly different sand clouds. We remark that natural atmospheric conditions are so variable that the case of a steady horizontal wind is not very plausible, mainly due to the turbulence effects. On the other hand, lack of data forces to adopt precautionary approximations that allow the *First Order Model* to perform predictions with a controlled error. In the industrial context a certain error is accepted.

For the sake of simplicity, we split the diameter spectrum in multiple contiguous intervals (i.e. a piecewise constant function) and we model each of them by means of

an Eulerian field. The diameter spectrum is therefore modeled using a list of diameters (i.e. interval) and for each diameter we pair a probability value. This table of values characterizes the sand sample used in a simulation. No further information of intervals widths are provided therefore the spectrum description can be thought also as a discrete probability distribution. This discrepancy can be justified supposing that the diameters in the same interval have same collisional properties. The model presented in Chapter 6 allows to take into account fine details of the aeolian transport. However, it has been only developed in the very last part of the *SMaRT* research activity. Therefore, its application on the Eulerian modeling is planned for future scientific researches.

Despite the model generality increases, to define several fields implies the allocation of a proper amount of memory for each field (the memory cost depends on the mesh domain). Consequently the computational number of phases is not arbitrary, and the interaction among different Eulerian fields have to be properly modeled. Furthermore, most of wind tunnel experiments in literature provide just a mean value for the grain size diameter rather than a full diameter spectrum; this results in uncertainties when model coefficients are defined.

We consider the system (5.3) for the fluid phase, and instead of using one equation we use the following system of transport diffusion equations for a system of N diameters:

$$\begin{cases} \dfrac{\partial \varphi_1}{\partial t} - \nabla \cdot (\alpha_s \mathbf{u}_f + w_{sed}(d_1)\mathbf{e}_z - \nu_{eq,1}\nabla\varphi_1) = 0\,, \\ \dfrac{\partial \varphi_2}{\partial t} - \nabla \cdot (\alpha_s \mathbf{u}_f + w_{sed}(d_2)\mathbf{e}_z - \nu_{eq,1}\nabla\varphi_2) = 0\,, \\ \qquad\qquad\qquad\qquad \vdots \\ \dfrac{\partial \varphi_N}{\partial t} - \nabla \cdot (\alpha_s \mathbf{u}_f + w_{sed}(d_N)\mathbf{e}_z - \nu_{eq,N}\nabla\varphi_N) = 0\,. \end{cases} \tag{5.86}$$

In (5.8) the nonlinear viscosity ν_{eq} is formulated as the sum of the turbulent viscosity ν_t and the collisional viscosity ν_{coll}. The derivation of ν_{coll} is based on the presence of one diameter value. We model the interaction among phases by analogy with (5.81), but instead of consider the presence of a single phase we use the total concentration. Therefore equivalent viscosities read

$$\begin{cases} \nu_{eq,i} = \nu_t + \nu_{coll}(\varphi_{tot}, II_{\overline{\mathbb{D}}}; d_i) \qquad i = 1, 2, \ldots, N \\ \varphi_{tot} := \sum_{i=1}^{N} \varphi_i \end{cases} . \tag{5.87}$$

We remark that the presence of φ_{tot} for each $\nu_{eq,i}$ realizes the nonlinear coupling among different diameters, otherwise a phase is not influenced by the presence of the others leading to an uncoupled system of equations. The algorithm to solve this system of equations is analogous to the iterative algorithm used to solve the *First Order Model*. But the number of internal cycles increases because of the presence of several equation and the nonlinear coupling. Its computational cost increases significantly therefore its industrial application is limited. We also remark that for each equation a different boundary condition applies because (5.82) and (5.84) depend

φ_i	$d\ [m]$	$w_i\ \%$	$u_t^*\ [m/s]$
0	$1.0 \cdot 10^{-4}$	5	0.220
1	$1.5 \cdot 10^{-4}$	15	0.260
2	$2.0 \cdot 10^{-4}$	35	0.275
3	$2.5 \cdot 10^{-4}$	25	0.310
4	$3.0 \cdot 10^{-4}$	15	0.320
5	$3.5 \cdot 10^{-4}$	5	0.365

Table 5.19: Discrete properties of the tested multi solid phase system.

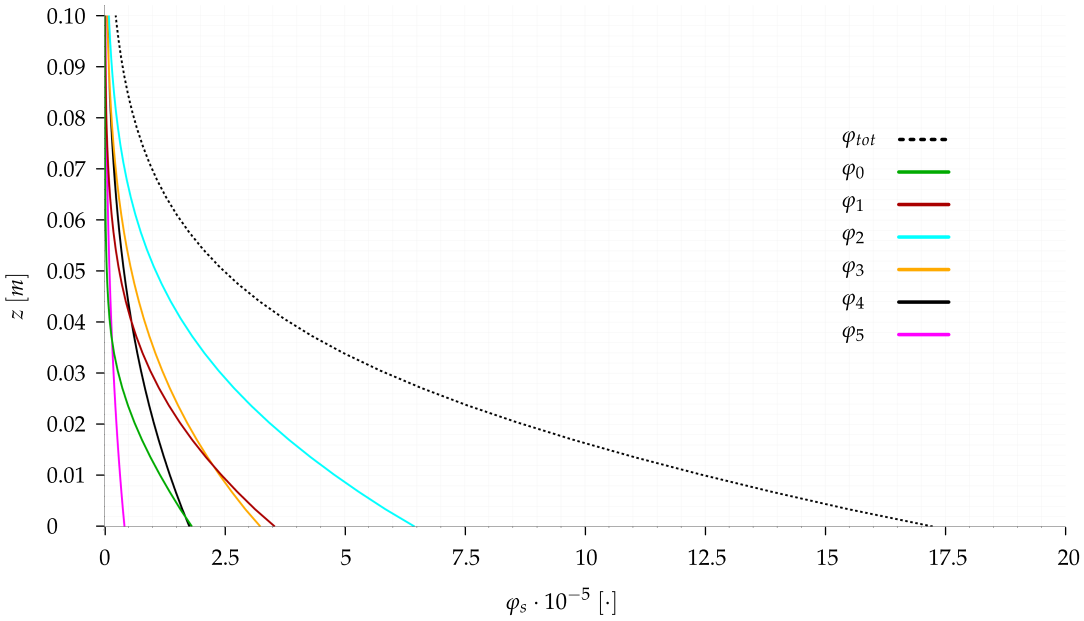

Figure 5.42: Numerical results of the multi solid phase solver for the setup described in Table 5.19 and 14 m/s for the free-stream velocity.

also to the diameter. For sake of simplicity boundary conditions are assumed uncoupled i.e. we use the same formulation for the single phase *First Order Model*.

Figure 5.42 presents the numerical results of this model for six solid phases system characterized by a free stream velocity of 14 m/s and sand properties defined in Table 5.19. The spatial setup is analogous to the Liu&Dong's experiments (see [142]) that is used for the v_{coll} derivation for the *First Order Model*. We do not have experimental data for a quantitative validation, however these results are qualitatively correct and the order of magnitude for outcoming concentrations are reasonable if compared with single phase results showed in Figure 5.39.

In conclusion, this preliminary version for the multi solid phases model is interesting, but future researches have to be combined with high accuracy results in order to be able to evaluate the quantitative error in a real heterogeneous sand condition.

5.5.1 Ground Memory Function

In this paragraph we want to discuss the effects on mathematical modeling if spatial heterogeneity of the diameter spectrum is taken into account in the model. As mentioned in the previous sections a sample of sand is characterized by its diameter spectrum, material density and grains shapes. In general these properties can change with respect to the sample point in the underground region. Figure 5.43 shows a scheme of the soil section subjected to erosion (red arrows) and deposition (green arrows) due to the wind action. The combination of several natural phenomena over time - aeolian transport, sand avalanches, earthquakes, fluvial phenomena, etc. - can lead to heterogeneous properties in the sediment material. We use the symbol $\Sigma(\cdot)$ to address the ground surface over time. Referring to Figure 5.43, the boundary conditions on $\Sigma(\cdot)$ are influenced by its dynamical states:

- **Erosion** occurs when some volume of sand is entrained in the air due to the wind action (see $\widetilde{AB} \to \widetilde{A'B}$ and $\widetilde{DE} \to \widetilde{DE'}$). Therefore boundary conditions for a truly representative mathematical model have to consider the diameter spectrum of the sand that is entrained in air (see P_1) when the surface $\Sigma(t)$ evolves toward $\Sigma(t + \Delta t)$.
- **Deposition** occurs when the sand suspended in air sediments, leading to a stratification of a steady volume of sand and consequently moving the from $\Sigma(t)$ toward $\Sigma(t + \Delta t)$ (see $\widetilde{BCD} \to \widetilde{BC'D}$). Unlike erosion, the deposition process creates the spatial information containing the diameter spectrum in the sedimented volume.
- **Equilibrium** occurs when there is not solid mass exchange through the surface $\Sigma(\cdot)$, i.e. the surface $\Sigma(\cdot)$ does not change in time (see points B and D in Figure 5.43).

The combination of actions described above results in an complex physical phenomenon where the flow behaves in relation to heterogeneous boundary conditions, but simultaneously the flow determines the status of boundary conditions for the future evolution. This argument suggest the *Ground Memory Function* name to address the function that maps each point in the underground spatial region to a space of functions for the sand diameter spectrum.

$$\begin{aligned} \textbf{GMF} : \Omega_s \subset \mathbb{R}^3 &\to V \subset L^2(\mathbb{R}_+) \\ P &\mapsto f(\cdot) \end{aligned} \tag{5.88}$$

The **GMF** definition depends in general on the complex combination of geomorphological phenomena mentioned above. However, its quantitative definition for an initial state could be performed by a systematic sampling and a consequent interpolation. This level of detail is out of the scope of the models developed in this thesis. However future researches can embed all previous modeling aspects. Chapter 6 a semistochastic Lagrangian model that allows to overcome several difficulties of the Eulerian modeling. Even though the discussion over the **GMF** is based on the mathematical description of $\Sigma(\cdot)$, analogous considerations are valid for second order models (e.g. models discussed in Chapter 2) where the spatial mesh includes also the sedimented region. In this case the surface $\Sigma(\cdot)$ is not explicit, and instead of describing the physical phenomenon via boundary conditions we would have to

define such a general stress tensor that is able to describe all physical state of the sand status, which means to be able to switch from a gas-like behavior to a plastic-like behavior almost discontinuously.

In conclusion, we want to remark that the introduction of multiple solid phases in a multiphase model leads to relevant modeling issues. This requires very an description of the physical system in each of its details, and most of the time these information are not totally available from experiments. Therefore, in a industrial context the use of several solid phases is not feasible if we consider also the additional computational cost.

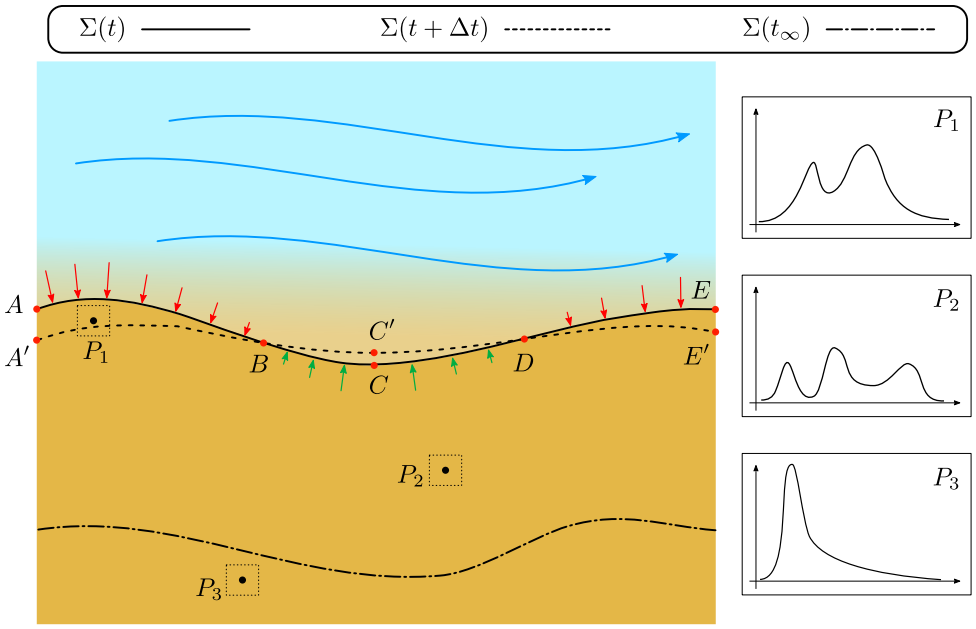

Figure 5.43: Schematic representation of a ground section.

5.6 Industrial Applications

Industrial applications represent the main goal for the *SMaRT* research activity, in particular for an engineering perspective for the railways industry. Therefore, we consider two railways-related cases in large domains. The first setup considers a spatial region surrounding the railway studied by the infield research activity of *SMaRT* during its Namibia campaign. This is a good benchmark because we can compare numerical results with macroscopic measurements. The second setup aims to test a complex geometry of the railway infrastructure, but no experimental data are available for this setup. In both cases we consider the *First Order Model* in the ultimate form obtained in Section 5.4.

5.6.1 T-track: Simulation of a Real Scenario from ESR-3 Experimental Research Activity

The term *T-track* refers to a special railway setup were a kind of concrete channel is created to support the rails (see Figure 5.51). This configuration induces sand

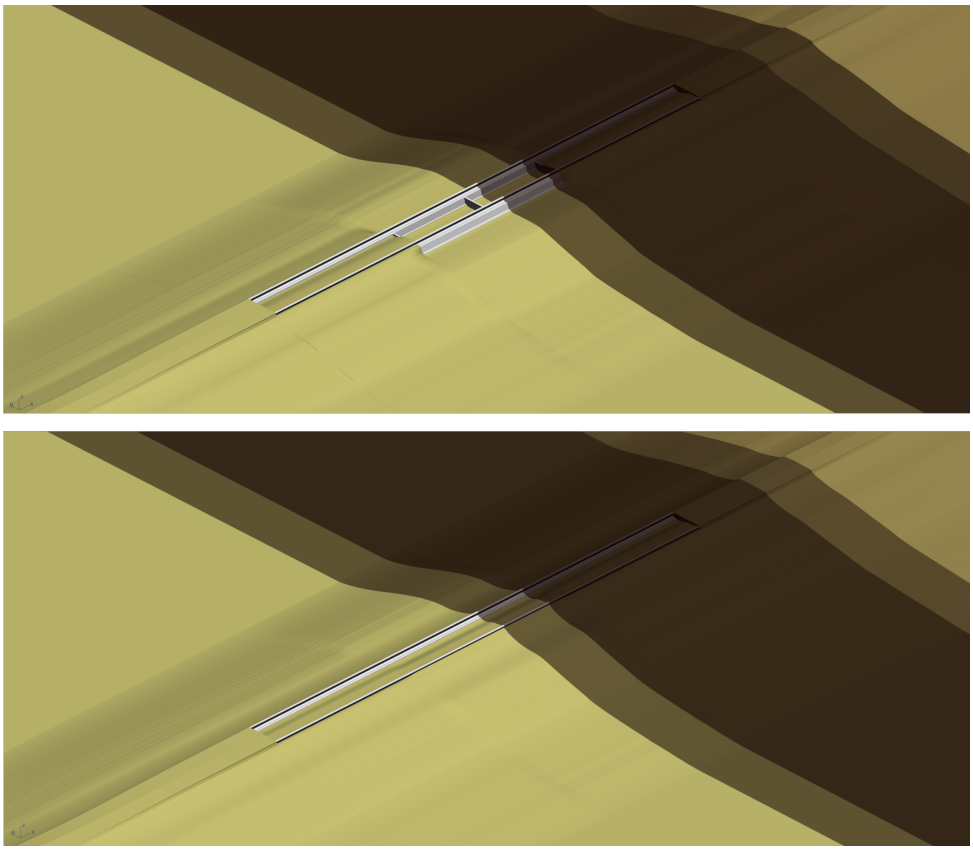

Figure 5.44: Laser scan measurements of the sand surface profile at the beginning (top) and end (bottom) of the temporal window with post-processing regularization of laser scan samples. In the top figure the railway is clean, in the bottom one the railway is full of sand.

deposition around the railway due to aerodynamic effects. By means a laser-scan the ground surface have been measured over time. Figure 5.44 shows the result of the laser sampling after the filtering procedure and an artificial extension of the domain. In particular, the top figure represents the ground surface before the sand deposition, while the bottom figure represents it at the end of the temporal window. The collected data can be used to create an erosion-deposition map to be used for comparison with numerical tests.

The computational domain for the simulation is the gray slice of the global domain showed in Figure 5.44. The flow is not perpendicular to the railway. Hence, in order to preserve the 3D effects, we consider periodic boundary conditions for the front and back slice of the domain. The boundary condition for the inlet matches infield experimental data (see [226, p. 17]). We considered a steady wind velocity with a given turbulence and a constant supply of sand. We set $u^* = 0.49\, m/s$, $u_t^* = 0.24\ m/s$, $z_0 = 10^{-3}\, m$ and the turbulence intensity to be around 8%. The domain sizes are large even considering a subset of the entire domain. Therefore, in order to keep the computational effort close to industrial standards, the mesh is not very fine (not as a scientific analysis would require). However, it satisfies the classical CFD requirements.

Figure 5.45(a) shows the wind streamlines and velocity magnitude. The zoom of the figure makes the recirculation zones very evident. We can recognize four main recirculation zones:

1. the first is a small recirculating zone at the foot of the downwind track (on its left)
2. the second recirculating zone, much larger, forms in the space between the tracks,
3. the third forms after the wind has passed the track and it is mainly due to the presence of the track, as it occurs on the upwind size of any obstacle passed by the wind,
4. the fourth forms right after the third one and it is mainly due to the downward slope of the enbankment

It is likely that in other geometries these two recirculating zones may merge into one.

The location of the recirculating zone is coherent with the patterns of the friction velocity and, therefore, of the identification of the sedimentation and erosion zones shown in Figures 5.45 (c) and (b), respectively.

Though a pure aerodynamic simulation with no sand transport may appear simplistic, however, it results useful as a preliminary metric, that can be sufficient to solve engineering problems in real working conditions. The addition of the *First Order Model* allows to quantify the free-surface speed i.e. the speed of sand erosion or deposition. Such an evaluation is useful, for instance, to plan maintainance operations of the railway.

Figure 5.46 shows a comparison of erosion-deposition patterns between numerical results and the infield data. Figures (a), (b) and (c) are different plots based on the same data. In particular, they measure the erosion-deposition pattern via the topographic changes over a temporal window of three days (see [226, p. 21]). In particular, Figure 5.46 (a) focuses on the erosion-deposition pattern obtained by numerical simulation. Figures 5.46 (b)–(d) point out the regions where there is an overall sedimentation or erosion comparing the ground levels at the end and at the beginning of the experiment.

We remark that, in addition to classical measurement errors, in this case difficult infield conditions trigger other potential sources of errors. In particular, the turbulence has an important effect on the aeolian process and we do not know much about that. Even very time localized event with a very strong wind can drastically change the morphology of surrounding areas. The assumptions for this numerical setup are far from being realistic in an in-situ experiment. In spite of this, numerical and experimental patterns are coherent and we consider these results positive for the industrial perspective.

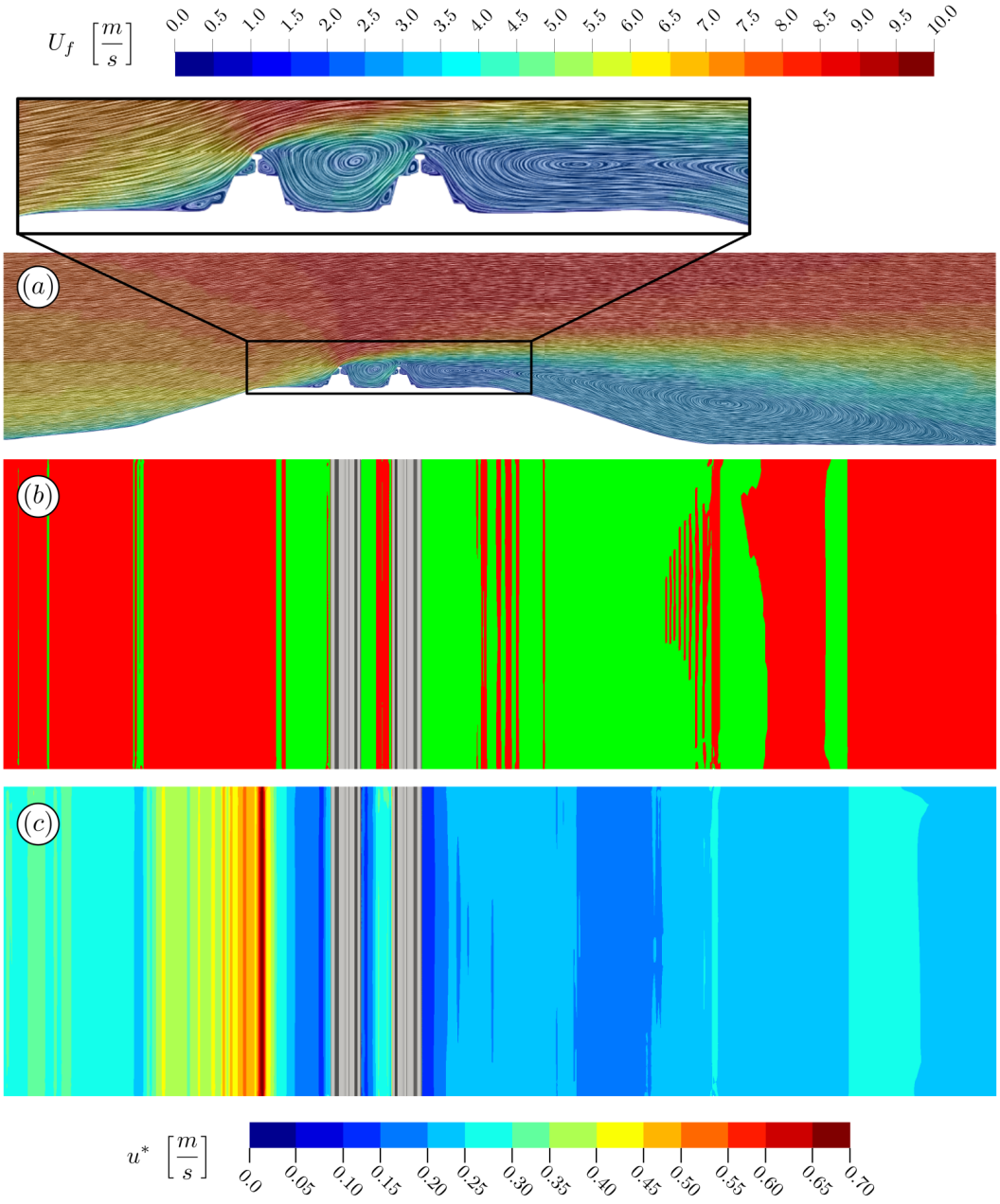

Figure 5.45: (a) Streamline of flow with velocity magnitude in a middle slice of the computational domain. (b) Boolean erosion-deposition pattern over the ground surface using our transport model (green is sedimentation and red is erosion). (c) Friction velocity pattern over the ground surface.

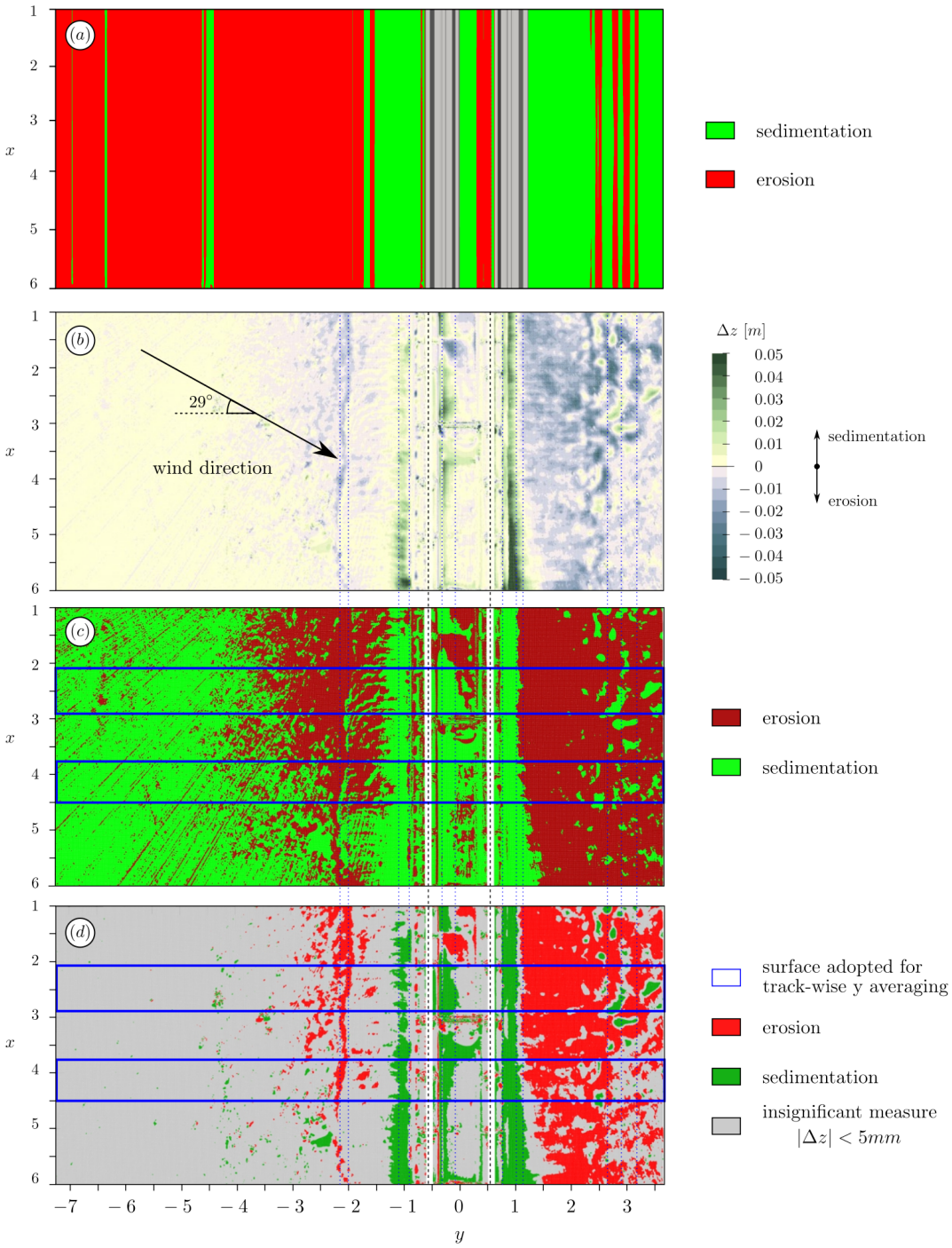

Figure 5.46: Comparison of the erosion-deposition patterns between the simulation and post processing of laser data from Period 1 in [226]: (a) Boolean erosion-deposition pattern obtained with numerical simulation, (b) exact topographic difference map between the start and end of the Period 1, (c) Boolean erosion-deposition pattern obtained with the topographic map and d Boolean erosion-deposition pattern filtering topographic difference under 5 mm, which are considered insignificant.

5.6.2 The Humped-Sleeper Case

We consider a railway equipped with the so-called *humped sleepers*. This configuration is interesting because it is designed to induce an aerodynamic effect under the rails. Figure 5.47 (top) shows the overall surface of the computational domain, Figure 5.47 (bottom) shows geometric details of the *humped sleepers* solution. This case is also interesting to highlight the main criticality of the mesh morphing approach presented in the next section.

The geometrical shape of concrete sleepers together with railways induce a particular flow which is interesting to study for sand transport. In this case we chose a wind direction orthogonal to the railways with a logarithmic atmospheric profile is used where $u^* = 0.5\,m/s$, $z_0 = 3 \cdot 10^{-3}\,m$ and $u_t^* = 0.32\,m/s$.

Figure 5.48 resumes the numerical results of the erosion/deposition patterns. This last is coherent with the scope of this kind of railway design. Indeed, the sleeper shape is designed to induce an acceleration to the flow under the rail in order to blow away the sand. The erosion pattern does not cover the whole area around the rail infrastructure. However, most of its performance depends on the free steam velocity of the incoming wind. This test shows that the industrial application of the *First Order Model* can be useful for engineers, for example, to perform systematic tests in order to evaluate different configurations or designs.

5.6.3 Influence of Local Shapes on Mesh Morphing

In section 2.4.4 we described two alternatives for the representation of the ground surface. We report here a criticality of the explicit representation of the ground surface. In classical mesh descriptions, the domain boundary is composed by the so-called patches. In 3D domains patches are surfaces, instead in 2D domains patches are curves. In case of domains that morph in time, points change their position and consequently they modify cell properties. Numerical approximation properties (consistency and stability) of finite volume method (as well as finite elements and analogous method) are heavily influenced by the cell deformation. Furthermore, flux corrections are requested to satisfy Reynolds transport theorem. All these aspects translate in additional computational costs.

Although the mesh morphing is computationally very expensive, in many cases it is an efficient way to take care of the evolution of free boundaries. Figure 5.49 shows a test for the surface displacement near a wall. The mesh morphing algorithm imposes the patch displacement as a boundary condition of an elasticity problem for an elastic solid. The solid shape matches with the fluid domain. The solution of this problem is obtained decomposing the finite volume mesh in tetrahedron, and solving the pseudo-elastic problem by means a finite element solver. The displacement solution is used as vector field to move mesh points. The case in Figure 5.49 shows that for high quality meshes even large displacement are allowed. But critical points, such as corners suffer from cells shrinking.

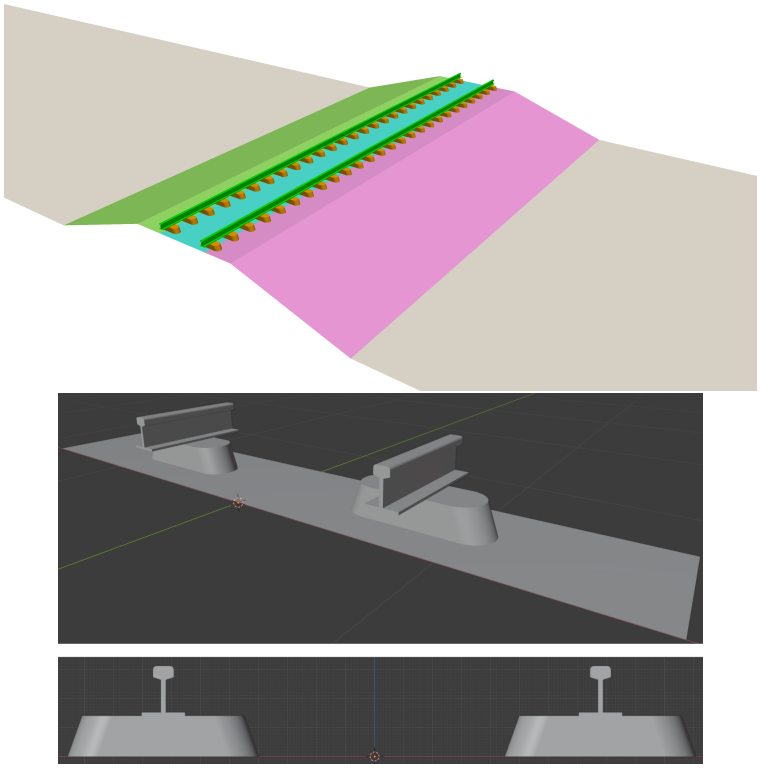

Figure 5.47: Schematic representation of the railway configuration used in the simulation of the railway with humped-sleeper (top) and detail representation of the track (bottom).

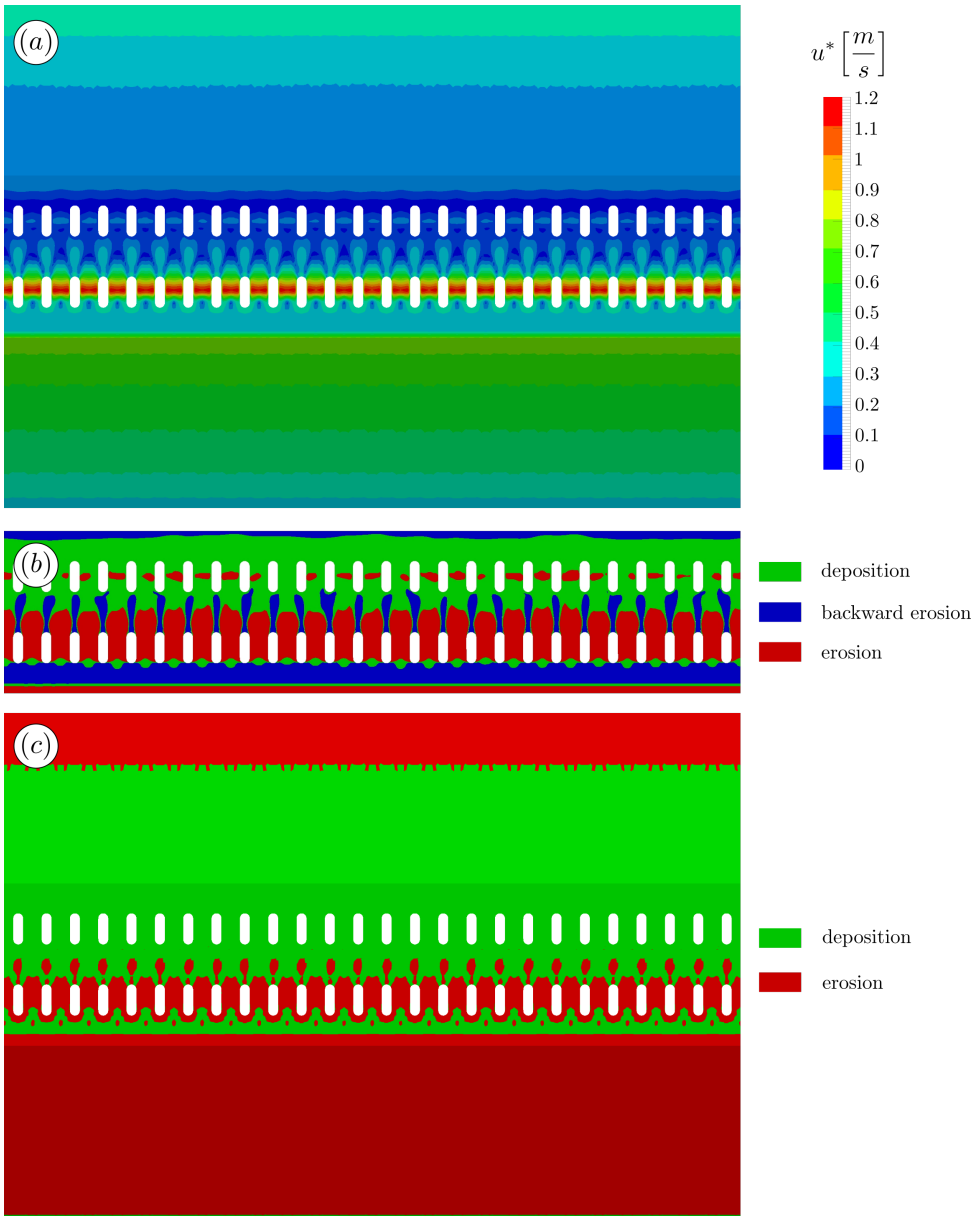

Figure 5.48: (a) Friction velocity pattern over the surface. (b) Erosion deposition pattern using basic method of the ratio between friction velocity and the threshold friction velocity (just for the area nearby railways). (c) Boolean erosion deposition pattern obtained using our model.

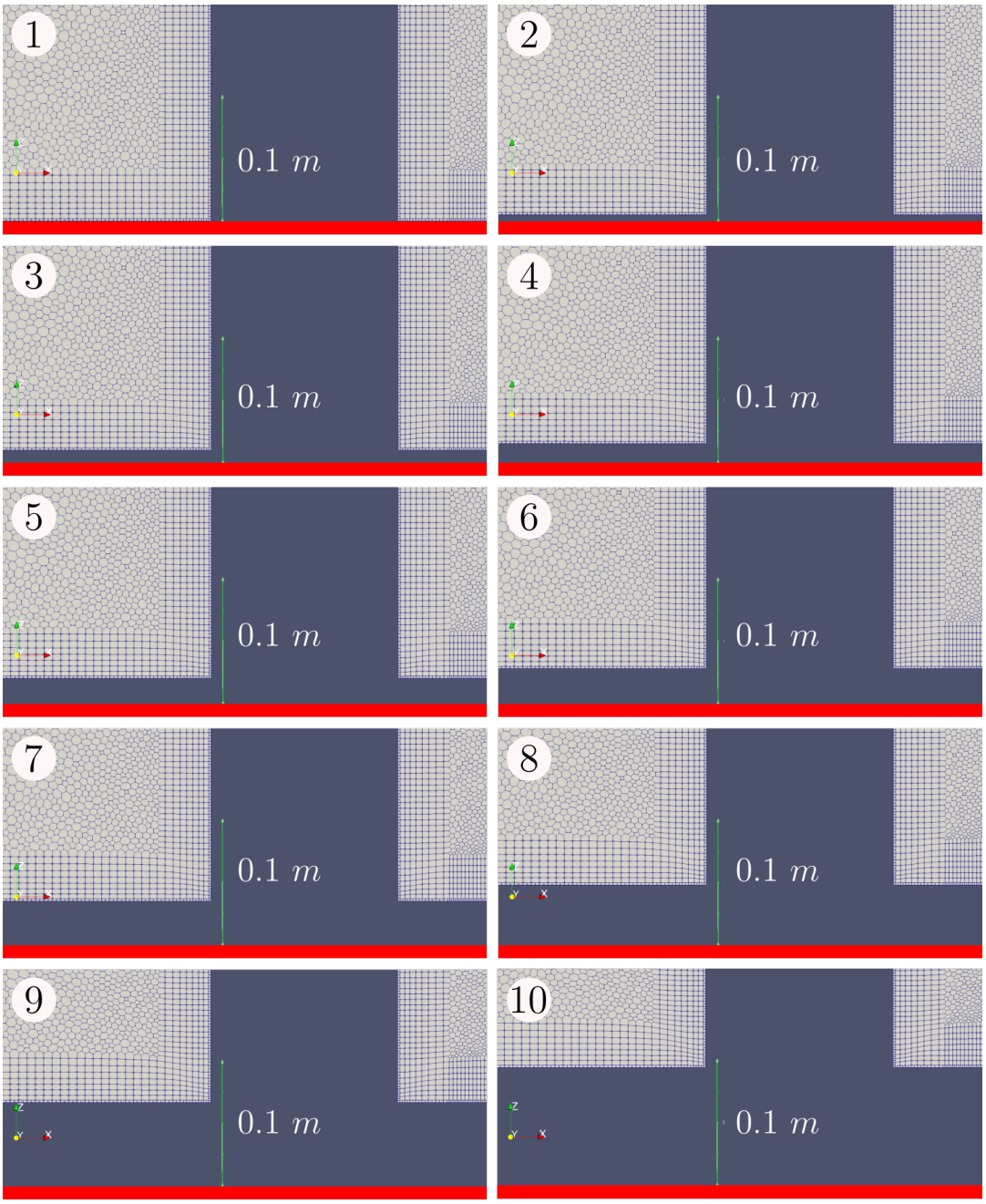

Figure 5.49: Temporal evolution of the surface morphing test.

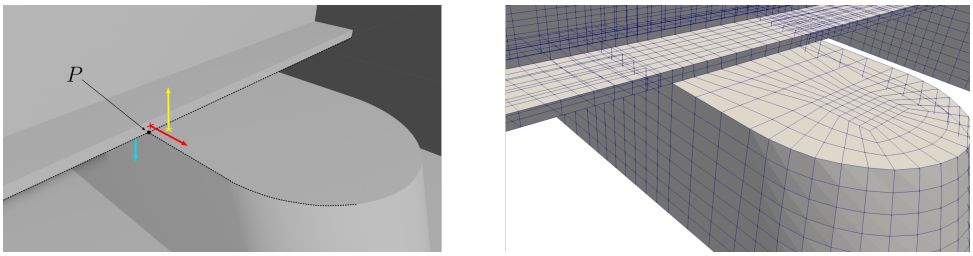

Figure 5.50: Geometric and mesh details of the mechanical coupling between rail and sleeper.

The criticality for the mesh morphing procedure becomes evident when geometric complexity rises up, like in the humped sleeper geometry or in the T-track configuration. Figure 5.50 shows a slice of a railway equipped with humped sleepers. The basal sand-concrete interactions is similar to the morphing showed in Figure 5.49. However, once the patch reaches the metal of the rail, a complex surface-surface interaction occurs leading to topological changes of the domain. In particular, in Figure 5.50 we highlight that close to the intersection between the rail and the concrete element (see different colors), there are three different surface normal vectors in the neighborhood of the point P (these are mutually nearly perpendicular). Even a very fine mesh presents a drastic variation of the normal vector around a single point, potentially leading to numerical issues.

Another tipping point is when the sand surface is about to touch the bottom of the rail, or when it covers the rail. Though undesirable from the practical point of view, these configurations are far from being unrealistic. In these cases there is a change of topology that requires a complete remeshing. Another analogous situation is shown in figure 5.51 where the metal feet of the rail creates a step. Once that the sand hypothetically reaches the connection between rail and concrete, the mesh points would be subjected to high deformations loosing the regularity and potentially leading to numerical errors.

We conclude recalling that these critical cases represent extreme conditions which do not likely occur in real computations. Indeed, the engineering goal is not to study very localized interactions, but to determine the bulk mass transfer over large domains and possibly to determine erosion/deposition patterns.

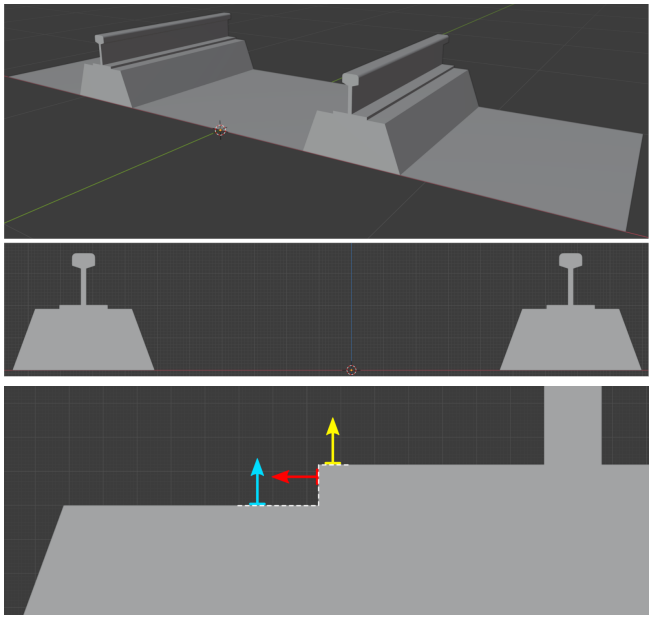

Figure 5.51: A whole representation of the T-track railway with the geometric detail about the drastic variation of the surface normal vector, for instance at the foot of the rail.

Chapter 6

Semi-Stochastic Periodic Box

The experience gained studying Eulerian models in the previous Chapters allowed to identify some criticalities of the Eulerian approach. In particular, we report three main aspects:

- High difficulties in finding highly accurate experimental data. In particular, experimental setups where all physical quantities are robustly described. So, having the possibility to validate the model by replicating the experiment with a computational simulation.
- Difficulties in distinguishing between numerical and modeling errors due to different discretization aspects.
- The necessity to evaluate the statistical quantities in control volumes in order to prove or disprove the statistical mechanics hypotheses for continuum like models in the context of aeolian transport.

In the very last part of the *SMaRT* research activity - in conjuction with my supervisor - I tutored the student Nicolò Perello for his master thesis titled *A Particle-Based Analysis of the Saltation Process: Models, Numerical Methods and Tests*. I developed autonomously the initial idea and the computational architecture for the main algorithm presented in this chapter, and together with Nicolò we improved it with a series of additional modeling details in order to increase the accuracy.

In Chapter 5 we considered a fully Eulerian continuum-like description for aeolian sand transport phenomena and we described how important the formulation and the identification of the constitutive equations are, especially those pertaining the interaction force and the boundary condition at the sand-bed surface. In order to understand more the physical processes involved in sand transport - and possibly to improve the modeling of such terms - in the present chapter we focus on a particle-based approach. It tracks the dynamics of each particle, including their collisions and interactions with the particles laying on the ground. In this respect, the granular kinetic theory briefly described in Section 2.4 pursues a similar aim, but it is grounded in statistical mechanics framework that requires a very large number of particles in a control volume. If this hypothesis does not hold, several steps in the model deduction do not apply, e.g. the concept of pressure is no longer valid in some common conditions and ensemble means have no statistical meaning.

Another issue is the fact that, classically, particles are treated as spherical entities, analogously to atoms or molecules. However, sand grains are not identical to each other (see Figure 6.1 and 6.2). Their shapes are significantly random and

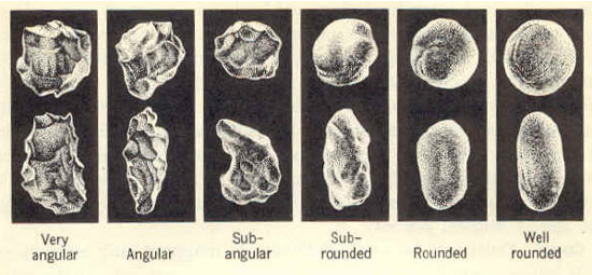

Figure 6.1: Classification of sand grain by shape from [181, p.118].

Figure 6.2: Sand photomicrography coming from many areas of the world [202]: (a) Kenya - Rift Valley - Samburu National Reserve, (b) United Kingdom - Isle of Wight (Beach at Brookgreen), (c) Indonesia - Bali - Bali island (Beach at Pemuteran), (d) Japan - Okinawa - Taketomi island (Kondoi beach), (e) South Africa - Western Cape - Cape Peninsula (Hout Bay) and (f) New Zealand - Northland (near Waipapa Bay).

the shape deviations from sphericity have important effects on collisions properties. Furthermore, when particles shape deviate from the sphere the formalization of kinetic theories becomes very complex or maybe even impossible. Indeed, most of the theories proposed in literature are developed under the hypothesis of perfect spherical particles. The material properties can eventually show heterogeneity, leading to further complexity in the modeling stages.

Eulerian-Lagrangian approaches are usually addressed with *Discrete Elements Method*[1] (DEM). For these models the particles are spheres in order to be able to model binary collisions with the Boltzmann approach (as mentioned just above). However, this hypothesis can be restrictive and can compromise the effect related to particles shape, which is relevant both for collision and aerodynamics. Furthermore, in DEM approaches the Lagrangian system is coupled with an Eulerian model, which is used to compute the fluid dynamics. We remark that particles volume does not influence the volume mesh used to solve the Eulerian flow even though in reality it involves a volume partitioning between solid and fluid. The particle presence is taken into account by means of a momentum term acting on fluid (e.g. the drag force, see Figure 6.3) and this closure requires a model; which can be an additional source of error.

[1] We are considering DEMs in the context of fluid-driven particle transport.

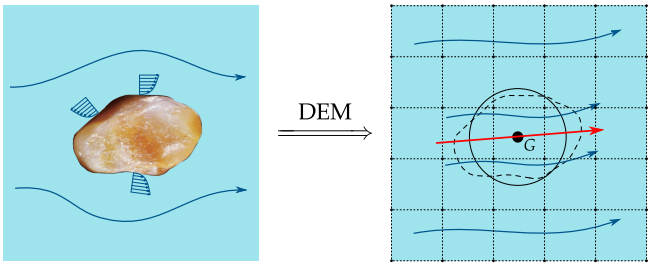

Figure 6.3: Conceptual representation of the DEM discretization. Particle volume does not influence the volume mesh used to solve the Eulerian flow even though in reality it involves a volume partitioning between solid and fluid. The red arrow represents the drag force acting on the particle.

In our framework we combine stochastic and deterministic models in order to catch most aspects of the saltation physics. In the next Sections we describe step by step the model and numerical techniques used to compute the solutions. The aim of this model is to study fundamental properties of aeolian transport for pure scientific purposes. A peculiar aspect of this model is the totally different paradigm of the experimental setups that can be used for validation or parameter setting. In particular, required experiments are much simpler than experiment in wind tunnel.

For sake of clarity, we recall the summarized description of the saltation flow which justifies the arguments of the following sections. When the air flow near the sandy soil is sufficiently strong, aerodynamic forces overcome gravitational and inter-particles forces providing initial condition for a ballistic trajectory into the air flow. The lifted particles - if sufficiently energized at the initial time - can gain energy due to the momentum transferred from the wind due to the drag force. The consequent particles impacts on the sandy soil can energize other still particles through collisions, leading to new initial conditions for new trajectories. Depending on the wind strength the process can be sustained and reach a stationary condition.

The qualitative description presented above suggests six hot topics that will be treated along this chapter:

- the particles trajectories
- the particles-ground impacts
- the ejection of new particles due to particles-ground impact
- the particles entrainment into the flow by the wind
- the momentum exchange between air and particles due to the drag force
- the wind flow characteristics

The source code for the developed solver has been written from scratch with basic numerical libraries for python. We do not involve any third party code for the physics simulation (contrary to previous *First Order Model* simulations that are based on OpenFOAM). This aspect allows a high versatility for the implementation of new features and for the code maintenance.

6.1 Particles Trajectories

We want to investigate the quantitative properties of a generic particle trajectory considering a pool of initial conditions and parameters. For sake of simplicity, we consider point-like particles (i.e. we do not consider the rotational dynamics) and steady wind profiles in the x direction, modeled by the atmospheric logarithmic law (5.62). In particular we are interested in linking initial conditions (i.e. ejection conditions) with final conditions (i.e. impact conditions). These last are crucial because they are interpreted as inputs of the impact model (see Section 6.2). Input and output data are collected in the *trajectory database*. This represents the map between the domain of ejection conditions and the codomain of impact conditions. The study of this map is the objective of this section. We remark that the argument presented in this chapter is easily extendable to particles with rotational dynamics and for fluid turbulent perturbations. However, the computational complexity increases and such detailed studies are out of the scope of this precursor analysis.

6.1.1 Trajectory Equation

Newton's law for a particle of mass m reads

$$m\frac{d^2\vec{x}}{dt^2} = \vec{\mathcal{F}}_{drag} + \vec{\mathcal{F}}_{gravity} + \vec{\mathcal{F}}_{g-pressure} \,, \tag{6.1}$$

where

$$\vec{\mathcal{F}}_{drag} = \frac{1}{2}\rho_f C_D(Re_p)\frac{\pi d^2}{4}\left\|\vec{u}_f(\vec{x}) - \frac{d\vec{x}}{dt}\right\|_{\mathbb{R}^3}\left(\vec{u}_f(\vec{x}) - \frac{d\vec{x}}{dt}\right) \,, \tag{6.2}$$

$$\vec{\mathcal{F}}_{gravity} = -mg\,\vec{e}_z \,, \tag{6.3}$$

$$\vec{\mathcal{F}}_{g-pressure} = -\frac{\pi d^3}{6}\nabla\tilde{p} \,, \tag{6.4}$$

$$m := \rho_s\frac{\pi d^3}{6} \,. \tag{6.5}$$

We recall that the shape of sand particles can be strongly irregular (see Figure 6.1 and Figure 6.2). Hence, in the equations above the particles diameter d is intended as the equivalent diameter of a perfect sphere of mass m and density ρ_s as stated in (6.5).

The term $\vec{\mathcal{F}}_{gravity}$ models gravitational action on grains. The term $\vec{\mathcal{F}}_{g-pressure}$ is derived from (5.30) and it models the action of the pressure fluctuations around a grain surface. This term can be useful in the region near the sandy soil because the fluid velocity nullifies the drag term. Therefore, it can become relevant to model particle entrainment into the flow. Due to the lack of data on turbulence for the moment we neglect this term.

The emission of particles due the pure wind action is treated in Section 6.3.3 by means of a probabilistic approach. The term $\vec{\mathcal{F}}_{drag}$ models the drag force exerted by the wind on particles. The drag coefficient C_D is computed with (5.16) (see Section 5.2.2 for a detailed discussion), but it can be easily substituted with a newer

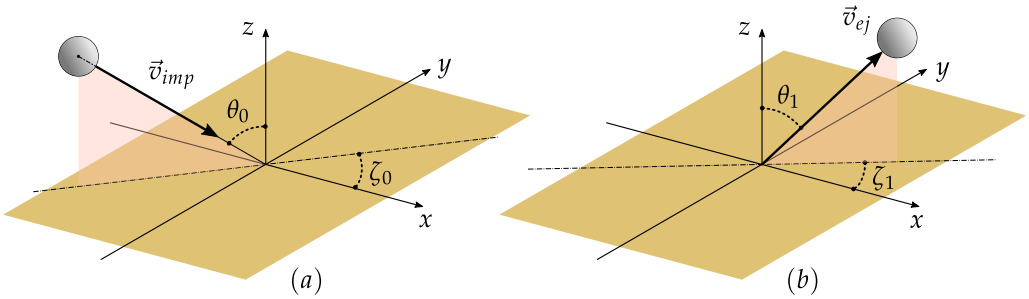

Figure 6.4: Diagrams for (a) particle impact and (b) particle ejection.

model whenever present in literature. Other forces can play a role in the process, e.g. *Magnus force* which is an aerodynamic force, and the electric force which play an important role for very small particles. We do not consider these forces because we want to prove the validity of this framework and consequently move to extend the accuracy in modeling details in future researches. Furthermore, also [129] suggest that the drag force is the most relevant term for the saltation process.

Equation (6.1) is solved for a grid of initial conditions. These are expressed in a polar coordinate system with angles θ_1, ζ_1 and kinetic energy e_1 instead of the velocity magnitude (see Figure 6.4). However, the computational implementation uses Cartesian coordinates and therefore we write

$$\vec{v}_{imp} = \left(\sqrt{\frac{2\,e_0}{m}} \cos\zeta_0 \sin\theta_0,\ \sqrt{\frac{2\,e_0}{m}} \sin\zeta_0 \sin\theta_0,\ -\sqrt{\frac{2\,e_0}{m}} \cos\theta_0 \right) , \tag{6.6}$$

$$\vec{v}_{ej} = \left(\sqrt{\frac{2\,e_1}{m}} \cos\zeta_1 \sin\theta_1,\ \sqrt{\frac{2\,e_1}{m}} \sin\zeta_1 \sin\theta_1,\ \sqrt{\frac{2\,e_1}{m}} \cos\theta_1 \right) , \tag{6.7}$$

$$\begin{cases} e_0 = \dfrac{1}{2} m \|\vec{v}_{imp}\|^2 , \\ \theta_0 = \arctan\left(\sqrt{(v^x_{imp})^2 + (v^y_{imp})^2} \Big/ \mid v^z_{imp} \mid \right) , \\ \zeta_0 = \arctan 2\left(v^y_{imp}, v^x_{imp} \right) , \end{cases} \tag{6.8}$$

$$\begin{cases} e_1 = \dfrac{1}{2} m \|\vec{v}_{ej}\|^2 , \\ \theta_1 = \arctan\left(\sqrt{(v^x_{ej})^2 + (v^y_{ej})^2} \Big/ v^z_{ej} \right) , \\ \zeta_1 = \arctan 2\left(v^y_{ej}, v^x_{ej} \right) , \end{cases}$$

where $\arctan 2(\cdot)$ is the "2-argument arctangent" which takes into account the quadrant of $\left(v^x_{ej},\, v^y_{ej}\right)$ in the plane $x - y$.

Given the flow conditions (u^*, z_0) and the diameter d, for each triple (e_1, θ_1, ζ_1) of initial conditions we numerically solve (6.1).

Parameter	Value	
e_1	$\{a \cdot 10^{-b} \mid a = 1, \dots, 9 \wedge b = 6, \dots, 9\} \cup \{10^{-5}\}$	J
θ_1	$10, 20, 30, 40, 50, 60, 70, 80$	deg
ζ_1	$0, 30, 60, 90, 120, 150, 180$	deg
$d \cdot 10^{-4}$	$2, 3, 4, 5, 6, 7, 8, 9, 10$	m
u^*	$0.2, 0.3, 0.4, 0.5, 0.6, 0.7$	m/s
z_0	10^{-3}	m

Table 6.1: Combination of initial conditions and parameters used to create the trajectory database.

d_m	$2 \cdot 10^{-4}$	m	$\Delta t(d_m, e_m)$	10^{-5}	s
d_M	10^{-3}	m	$\Delta t(d_M, e_m)$	10^{-6}	s
e_m	10^{-9}	s	$\Delta t(d_m, e_M)$	10^{-4}	s
e_M	10^{-5}	s	$\Delta t(d_M, e_M)$	10^{-5}	s

Table 6.2: Numerical time step for extrema values of e_1 and d. See Figure 6.5 for the graph of Δt.

The collected information for each trajectory are:

1. impact position
2. impact kinetic energy e_0
3. impact angles θ_0 and ζ_0 (see Figure 6.4 (b))
4. time T_{impact} required to execute the trajectory
5. maximum height H_{max} reached by the particle during its trajectory

Since the wind direction is constant along x the problem is symmetric with respect to the $x - z$ plane, hence $\zeta_1 \in [0°, 180°]$. Table 6.1 reports the combination of values used to compute the *trajectory database*. Equation (6.1) is numerically integrated using the Newmark method in the explicit form (see [167]). Small diameter particles ejected with high energies travel for long distances (and larger values of T_{final}); therefore we can use a relatively large time step. On the other hand, low values of energy and large values of diameter lead to very short trajectories where the traveled distance is of the same order of the diameter. Therefore, in order to reduce the overall numerical error and computational time, the numerical time step Δt is chosen as a function of e_1 and d. We use the polynomial expression

$$\begin{aligned}\Delta t(d, e) = &(\Delta t(d_M, e_M) + \Delta t(d_m, e_m) - \Delta t(d_M, e_m) - \Delta t(d_m, e_M)) \frac{d - d_m}{d_M - d_m} \frac{e - e_m}{e_M - e_m} \\ &+ (\Delta t(d_M, e_m) - \Delta t(d_m, e_m)) \frac{d - d_m}{d_M - d_m} + (\Delta t(d_m, e_M) - \Delta t(d_{min}, e_m)) \frac{e - e_{min}}{e_M - e_m} \\ &+ \Delta t(d_m, e_m)\end{aligned}$$

with parameters reported in Table 6.2. Figure 6.5 shows the time step function for parameter of Table 6.2.

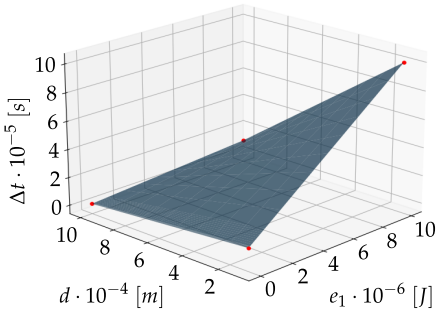

Figure 6.5: Graph of Δt as function of d and e_1. See Table 6.2 the reference values.

6.1.2 Geometry and Lifetime of the Particles Trajectories

We want to show and comment some results of simulated trajectories. The scope of these tests is to visualize and quantify the properties of particles trajectories in order to have a better overview of the saltation phenomenon.

Particle Footprint Figure 6.6 shows the projection on the coordinate planes of the trajectories for several ejection conditions. The aim of these plots is to give an idea of the spatial region involved by a trajectory as a function of d and u^*. In particular, the larger d is, the larger u^* must be to influence trajectory of particle. The term "Particle Footprint" derives by the fact that we can imagine to compute the hull set of all impact points in the plane $x - y$. If we refine the mesh-grid of initial conditions and parameters, the resultant hull set represents the larger soil area influenced by a generic particles.

Particle Displacement Figure 6.7 shows the particle displacement as the euclidean distance of the impact point from the origin. For sake of clarity we set $\zeta_1 = 0°$ which is the most representative angle to study the displacement of a particle (three-dimensional effects are reported later). The plots are organized in order to test several ejection conditions in accordance with Table 6.1. The red line indicate a displacement of one centimeter and it can be used as a reference. We can notice that the particle displacement is very sensible to initial conditions.

Maximum Height The maximum height H_{max} reached by a particle in its trajectory is interesting because it can be compared with bulk quantities used in geomorphology such as the *saltation layer*. Figure 6.8 shows H_{max} for several ejection conditions. We can also notice that the larger H_{max} is, the larger the air velocity is. Hence, the drag force exerted on a particle for a certain value of z is larger than the force exerted on a particle which does not reach the same height. We can also notice that the qualitative behavior of H_{max} plots is analogous to the particle displacement. Again, ζ_1 is set to zero.

Impact Time The impact time T_{impact} is the lifetime of a whole trajectory. Figure 6.9 shows T_{impact} for several ejection condition like other figures. Even in this case, the qualitative behavior of the plots are analogous to the maximum height and the particle displacement. Again, ζ_1 is set to zero.

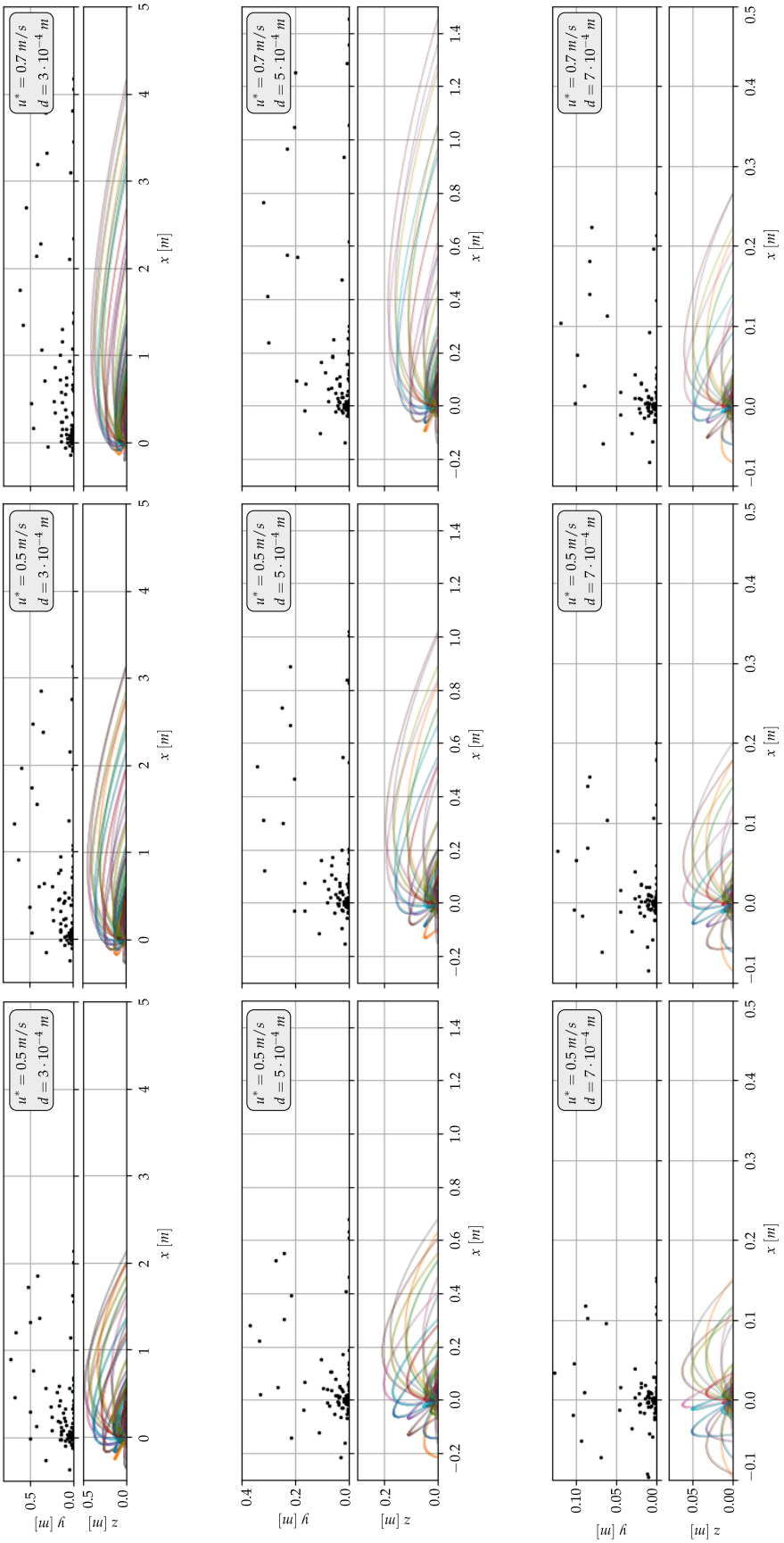

Figure 6.6: Trajectories of particle for $e_1 \in \{1 \cdot 10^{-9}, 5 \cdot 10^{-9}, 1 \cdot 10^{-8}, 5 \cdot 10^{-8}, 1 \cdot 10^{-7}, 5 \cdot 10^{-7}\}$ J and five equally spaced values of angles $\theta_1 \in [10°, 80°]$ and $\zeta_1 \in [0°, 175°]$.

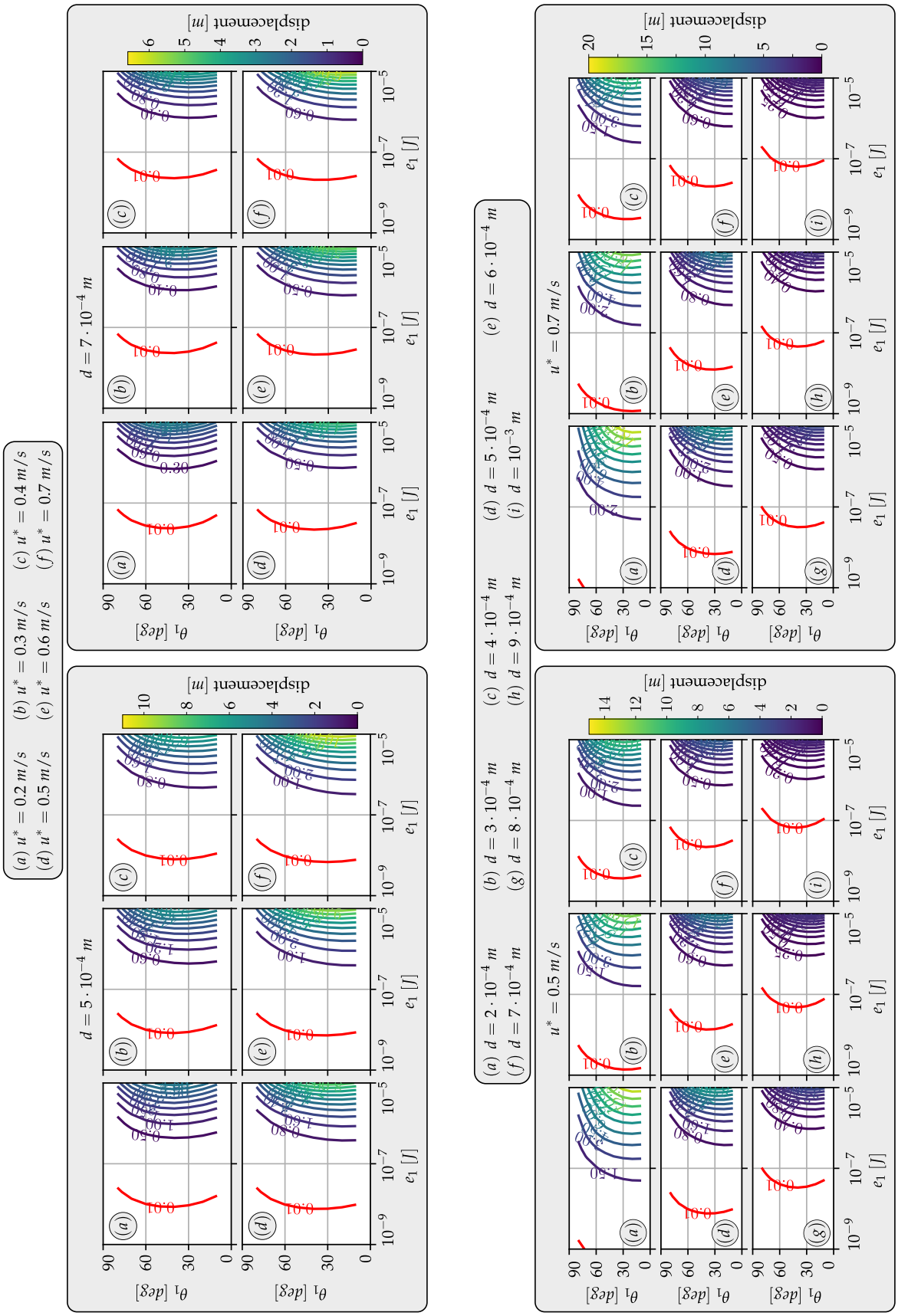

Figure 6.7: Particle displacement for several d and u^* with $\zeta_1 = 0°$.

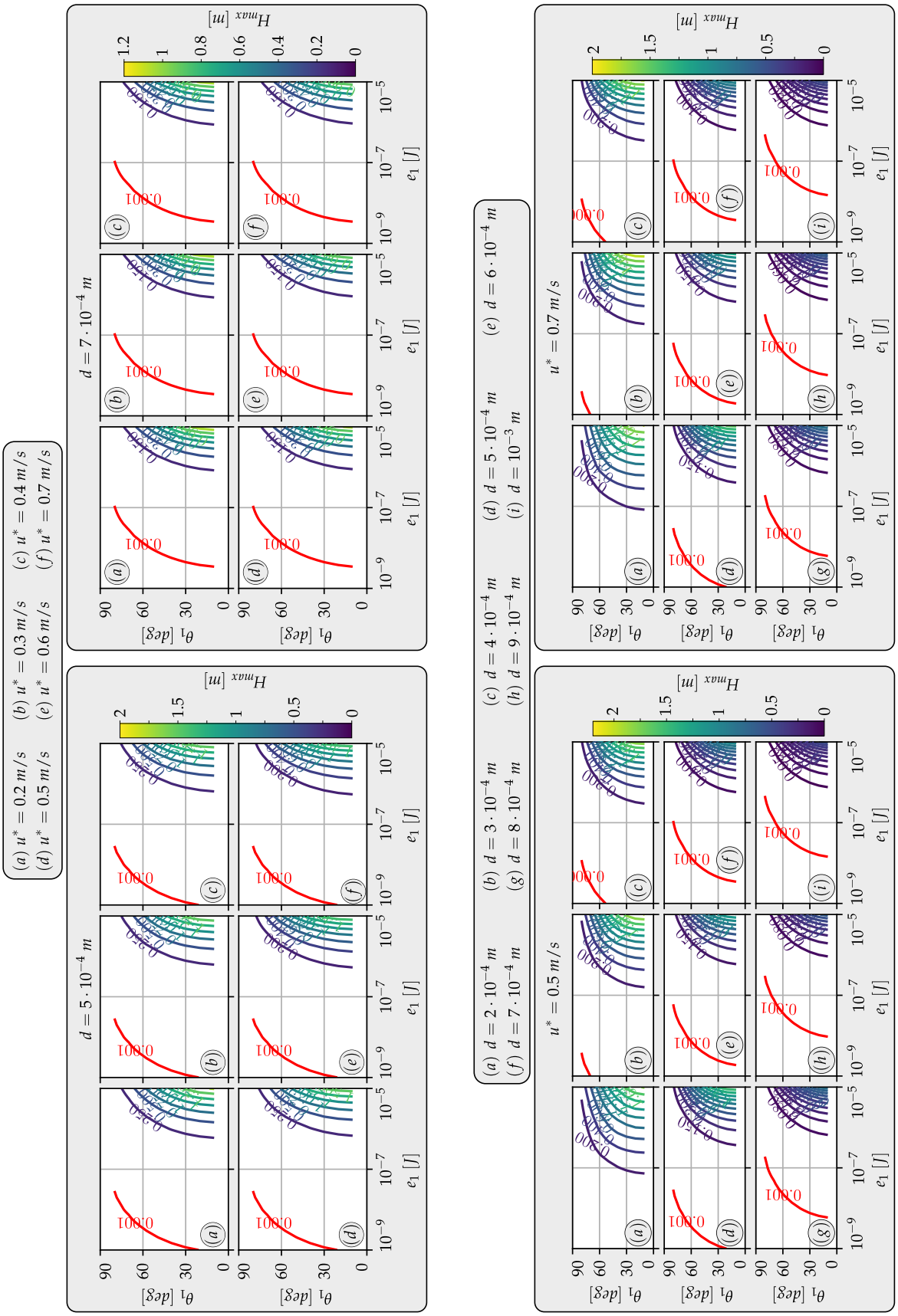

Figure 6.8: H_{max} for several d and u^* with $\zeta_1 = 0°$.

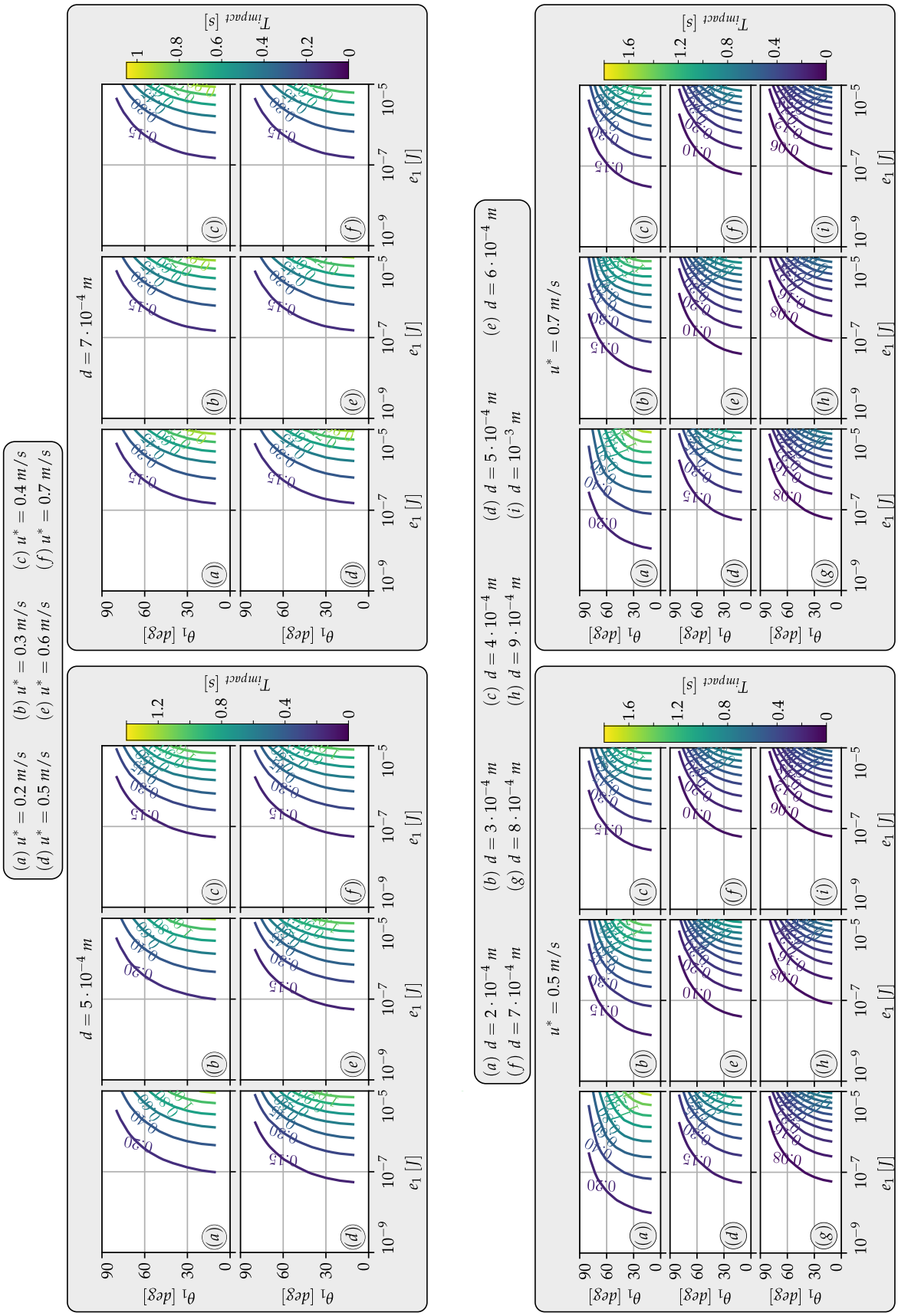

Figure 6.9: T_{impact} for several d and u^* with $\zeta_1 = 0°$.

6.1.3 Energy Gain

We consider the energetic properties of particles. In particular, we consider the ratio between e_0 and e_1. This value is important because it measures the energy gain of a particle during its trajectory. We can use the term "lifetime" to refer to the period spanning from the moment in which a particle lifts from the ground, to its eventual collision with the ground. Therefore, using the ratio e_0/e_1 we can classify which initial conditions certainly lead to finite lifetimes. The saltation process also involves particles emission and energy partition/dissipation (discussed in the next sessions). A particle has to gain energy in order to have the chance to trigger other still particles and consequently sustain the saltation process. e_0/e_1 is a representative indicator to visualize this aspect. Figure 6.10 shows the numerical results for the case $\zeta_1 = 0°$ and several combinations of d and u^*. Figure 6.11 shows the numerical results for four combination of d and u^* and for six values of ζ_1. Hence also three-dimensional effects are reported. We can notice that in all cases the level set of $e_0/e_1 = 1$ define a sort of boundary bubble in the space (e, θ, ζ) (see red lines).

6.1.4 Trajectories as Vector Field

Setting d, u^* and z_0, initial (i.e. ejection) and final (i.e. collision) conditions of a trajectory can be considered as connected by a vector map $\mathcal{T}_{(d,u^*,z_0)}$

$$\begin{aligned} \mathcal{T}_{(d,u^*,z_0)} : \mathbb{R}_+ \times [0, \pi/2] \times [0, 2\pi] &\longrightarrow \mathbb{R}_+ \times [0, \pi/2] \times [0, 2\pi] \\ (e_1, \theta_1, \zeta_1) &\longmapsto (e_0, \theta_0, \zeta_0) \end{aligned}$$

The *trajectory database* mentioned at the beginning of this Section aims to compute a discrete map of $\mathcal{T}_{(d,u^*,z_0)}$. We recall that for each (e_1, θ_1, ζ_1) we numerically integrate (6.1) parametrized by d, u^* and z_0. Figure 6.12 shows the grid of 2240 initial conditions for each combination of (d, u^*, z_0) for a total number of 120960 solved trajectories (see Table 6.1). Figures 6.13-6.14 show the mapping of $\mathcal{T}_{(d,u^*,z_0)}$ for two values of u^* and each figure shows the effect of changing d. We can notice that in all cases, as soon as the energy increases, there is a tendency to narrow down to a constant value of ζ_0 because the wind action tends to align particles along x. Less clear is the behavior of θ_0. However, the quantitative dependence of these two values from (d, u^*, z_0) need to be further studied. Three-dimensional visualizations can be not so representative. Therefore, in Figure 6.15 we show the special case of $\zeta_1 = 0°$ showing the components of the vector field $\mathcal{T}_{(d,u^*,z_0)}$.

All the studies above are related to a steady unperturbed wind condition. In future studies we will add the effect of turbulence in order to compute how strong is its effect with respect to the steady case.

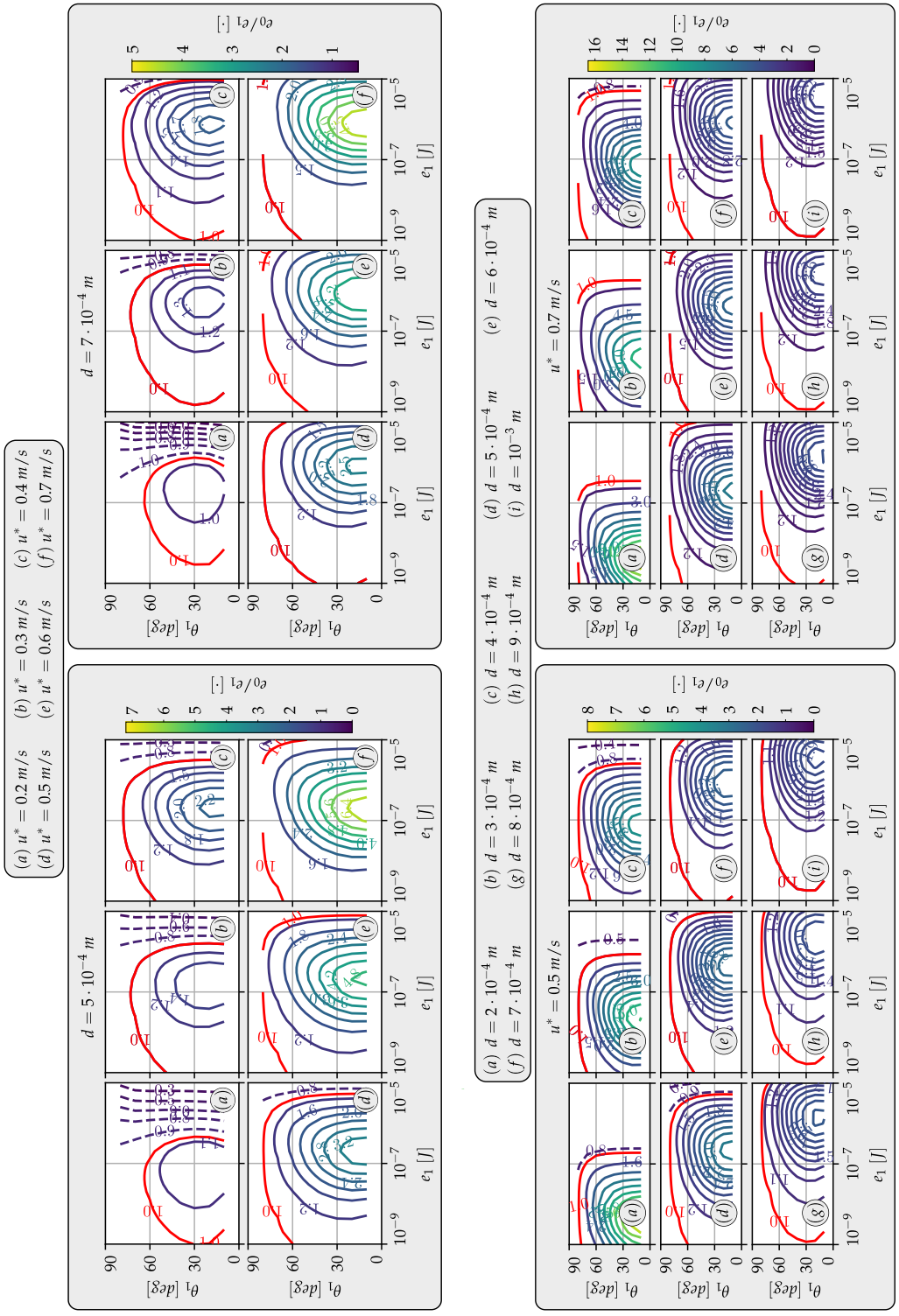

Figure 6.10: Ratio e_0/e_1 and $\zeta_1 = 0°$. Red lines delimit the regions where a particles gain energy (internal) or lose energy (external) in the trajectory.

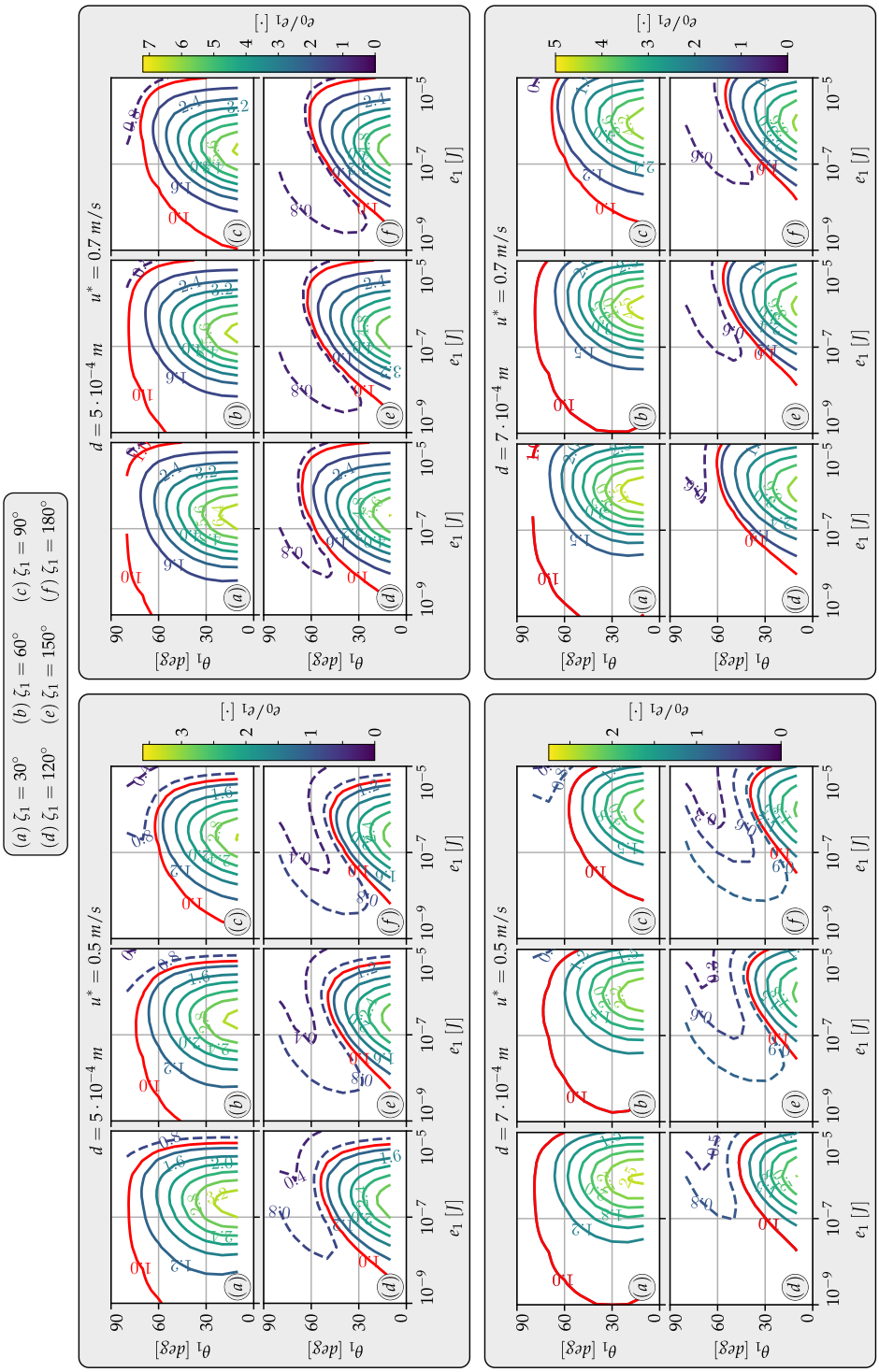

Figure 6.11: Ratio e_0/e_1 for several ζ_1. Red lines delimit the regions where a particles gain energy (internal) or lose energy (external) in the trajectory.

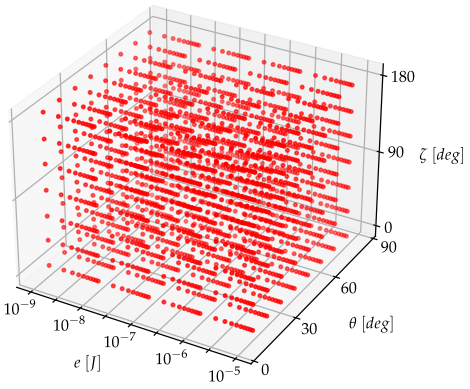

Figure 6.12: The red points correspond to the set of initial condition used to create the trajectory database.

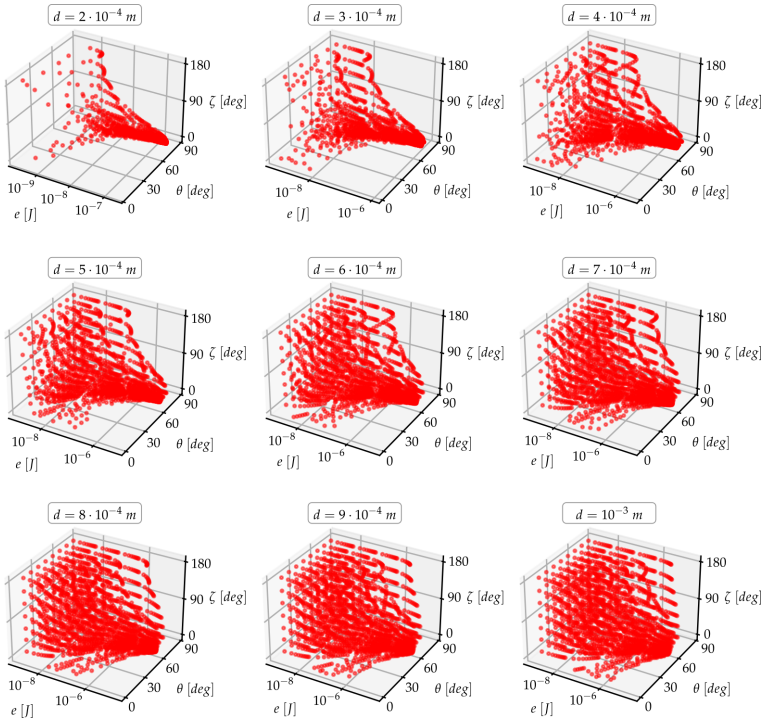

Figure 6.13: Impact conditions (e_0, θ_0, ζ_0) for nine values of particle diameter and $u^* = 0.5\ m/s$. Initial conditions correspond to Figure 6.12.

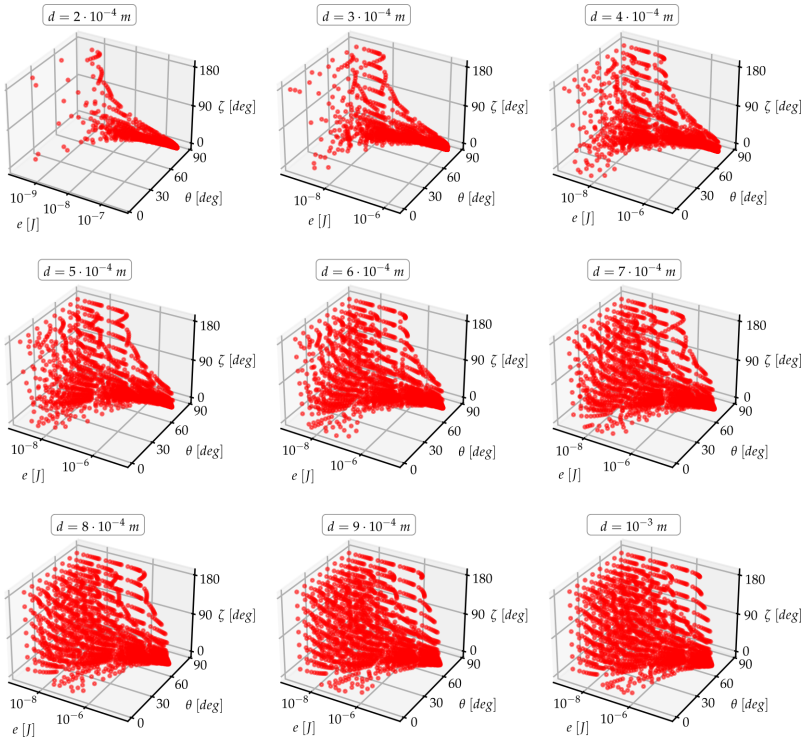

Figure 6.14: Impact conditions (e_0, θ_0, ζ_0) for nine values of particle diameter and $u^* = 0.7\ m/s$. Initial conditions correspond to Figure 6.12.

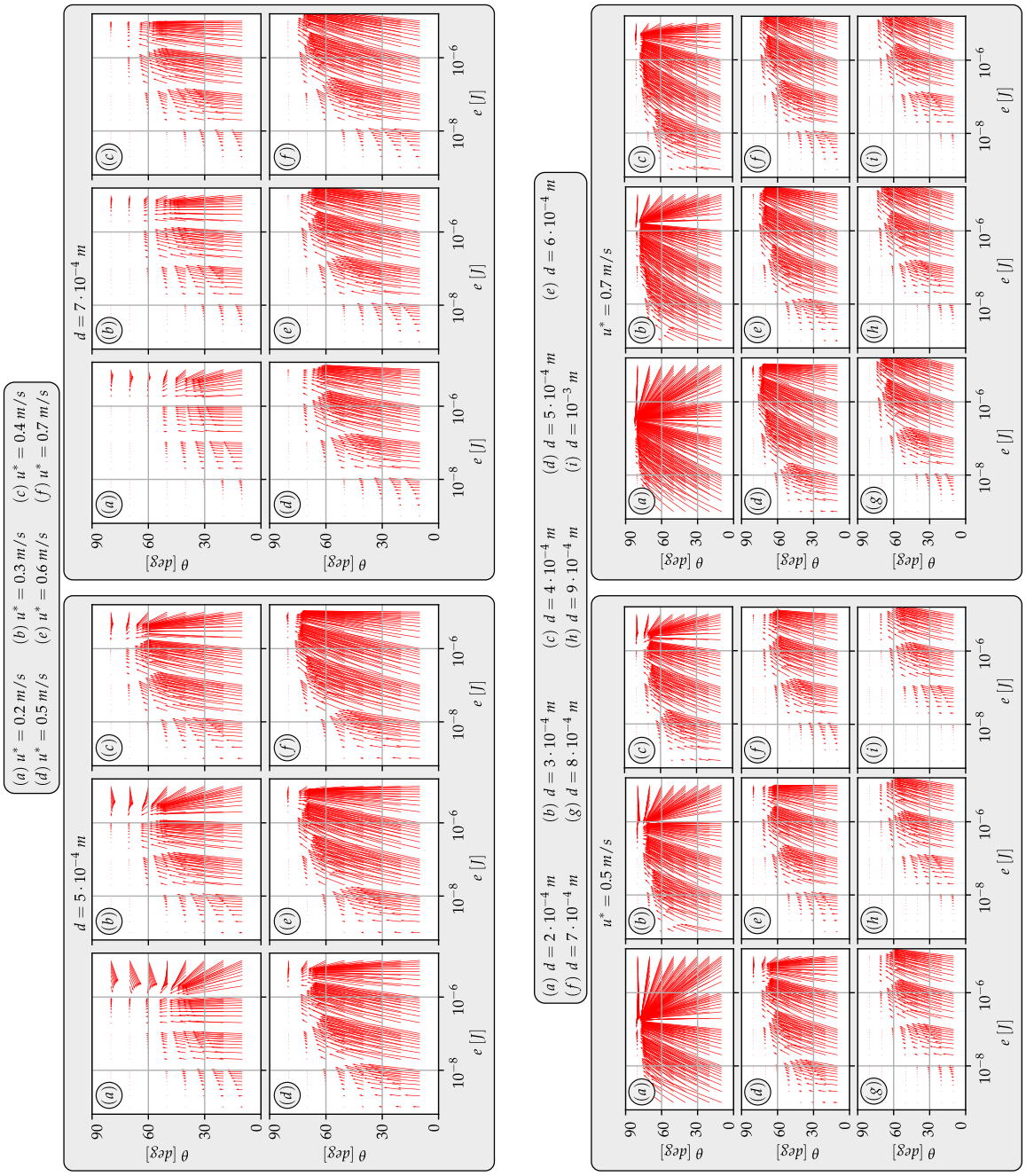

Figure 6.15: Trajectory function in the $e - \theta$ plane when $\zeta_1 = 0°$.

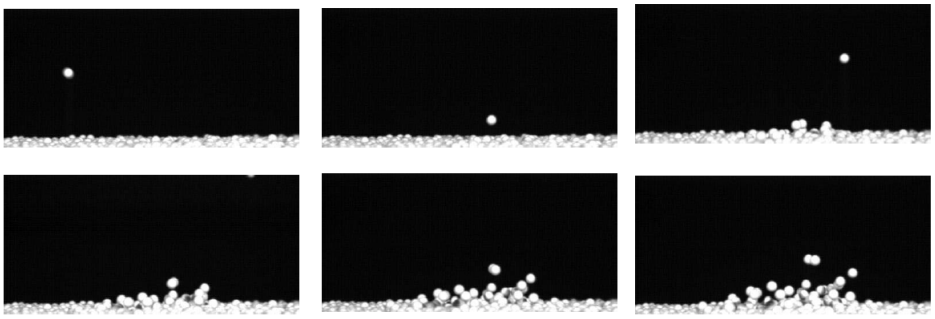

Figure 6.16: Temporal snapshots of a ground particle impact from [22].

6.2 Modeling of the Particle-Ground Impact

When a particle ends its trajectory, it hits the soil which is composed by other particles. As mentioned at the beginning on this chapter, the sand grain shapes can be very irregular (see Figures 6.1-6.2). Consequently, the local arrangement of particles around the region where the impact occurs is completely random. Even a particles system composed by perfect spheres wouldn't show, in general, a regular pattern unless if it is externally forced. Therefore, when a particle hits other soil particles the impact output properties is not deterministic. Randomness also affects the dissipation process and the ejection properties of outcoming particles. The aim of this chapter is to create a basic model to determine dynamic conditions and number of ejected particles as result of a particle-ground collision.

6.2.1 Literature Data

Before moving into modeling details we recall some useful articles describing the process from the experimental point of view

- The articles [221], [237], [231] and [119] perform wind tunnel tests in order to measure particles velocities while saltation occur. These experiments result not very useful in the quantitative study of impact models but they provide good qualitative information.
- The articles [22] and [236] study the effect of a particle impact against a bed of particles to study the probability distributions of kinematic quantities involved in the process. In particular, [22] aimed to prove that the characteristic time of the impact process is less than the characteristic time of turbulent structures. Hence, experiments involving just particle impact can characterize this aspect also in saltation. However, [174] reports that during the saltation process the soil condition also involves creeping particles, making the problem even more complex. To the best of our knowledge this is still an open problem. Furthermore, we report that [236] uses natural sand but [22] uses an artificial sample of ceramic spherical particles (see Figure 6.16).

In order to be coherent with cited papers we suspend the notation presented above only for this section. The presented symbols are self consistent.

Among the previous articles, in our opinion, the most relevant paper is [236] because it performs the study with natural sand. The data has been collected with a high-speed camera, and 1024 impact events are used for the statistics. Authors consider a particle as "ejected" if it reaches at least a height of one diameter. Denoting by θ_r the rebound angle, by V_r the rebound velocity, by θ_{ej} the ejection angle, by V_{ej} the ejection velocity and by n the number of ejected particles (see Figure 6.17).

Figure 6.18 reports the results for θ_r, the restitution coefficient ε defined as V_r/V_i and the number of ejected particles n (excluding the rebound particle). Figure 6.19 describes the probability density for θ_{ej} and V_{ej}. We report the probability distributions parametrized by V_i and θ_i:

Rebound angle θ_r:

$$f(\theta_r) = \frac{1}{\sqrt{2\pi}\sigma\theta_r}\exp\left(-\frac{(\ln\theta_r-\mu)^2}{2\sigma^2}\right) \qquad \begin{aligned}\mu &= 2.92 - 0.034V_i + 0.02\theta_i \\ \sigma &= 0.9 - 0.049V_i\end{aligned} \tag{6.9}$$

Restitution coefficient ε:

$$f(\varepsilon) = \frac{1}{\sqrt{2\pi}\sigma}\exp\left(-\frac{(\varepsilon-\mu)^2}{2\sigma^2}\right) \qquad \begin{aligned}\mu &= 0.62 + 0.0084V_i - 0.63\sin\theta_i \\ \sigma &= 0.19 - 0.0035V_i - 2.96\cdot 10^{-5}\theta_1^2\end{aligned} \tag{6.10}$$

Number of ejected particles n:

$$f(n) = \frac{1}{\sqrt{2\pi}\sigma\, n}\exp\left(-\frac{(\ln n-\mu)^2}{2\sigma^2}\right) \qquad \begin{aligned}\mu &= -0.3 + 1.35\ln V_i - 0.01\theta_i \\ \sigma &= 0.55\end{aligned} \tag{6.11}$$

Ejection angle θ_{ej}:

$$f(\theta_{ej}) = \frac{1}{\sqrt{2\pi}\sigma\theta_{ej}}\exp\left(-\frac{(\ln\theta_{ej}-\mu)^2}{2\sigma^2}\right) \qquad \begin{aligned}\mu &= 3.94 \\ \sigma &= 0.64\end{aligned} \tag{6.12}$$

Ejection velocity V_{ej}:

$$f(V_{ej}) = \frac{1}{\sqrt{2\pi}\sigma\, V_{ej}}\exp\left(-\frac{(\ln V_{ej}-\mu)^2}{2\sigma^2}\right) \qquad \begin{aligned}\mu &= -1.67 + 0.082V_i - 0.003\theta_i \\ \sigma &= 0.616\, m^2/s^2\end{aligned} \tag{6.13}$$

Figures 6.18 and 6.19 show the graphs of the probability distributions and data for different group of samples.

We report that [235] tries to replicate these experimental results with a fully deterministic DEM approach treating binary collisions with classical models and suffering of problems described in the introduction of this Chapter.

Due to the random nature of the impact entrainment, a stochastic description is typically adopted ([130], [140], [6], [105]). The grain-bed impact event in numerical models of saltation can be achieved in two ways:

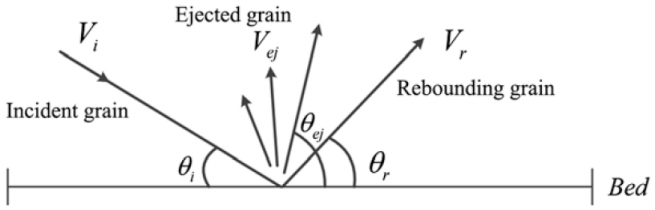

Figure 6.17: Scheme of a particle-ground impact showed in [236].

1. DEM-like approach: the interaction between the impacting particle and a still particle is computed via classical binary interaction (spring-dump models). [140] simulates a random ground particles arrangement in order to introduce the randomness. However, spherical particles are used.

2. *Splash Functions* approach: it is a function that links impact conditions to ejection conditions via probability distributions (see [130], [56], [218]). Its quantitative definition is based on experiments, as in [235] described above.

In [129, 173, 174] the impact entrainment is considered as the most relevant mechanism of the saltation process. But the impact dynamics is still poorly understood due to the phenomenon complexity. Furthermore, to the best of our knowledge only bi-dimensional solvers implement a model of *Splash Function*, and three-dimensional solvers are based on DEM-like approaches with perfect spheres[2].

6.2.2 Impact Model

We consider a *Splash Function* approach but we delineate formulas following the conservation of mass and energy. As notation, the rebounding particle is counted in the number N_{ej}, then the number of new ejected particles correspond to $N_{ej} - 1$. We suppose that if at least one particle is ejected, one of the ejected particles corresponds to the impacting particle. This hypothesis is based on the fact that the probability that a particle does not rebound but it ejects other particles is very low (see [236]).

Model's inputs are the impact energy, angles and diameter $(e_0, \theta_0, \zeta_0, d_0)$, accordingly to the polar coordinate system described in Figure 6.4 (a). Outputs are:

- the number of ejected particles N_{ej} (rebound plus new particles),
- the rebound energy and angles $(e_1^{reb}, \theta_1^{reb}, \zeta_1^{reb})$ accordingly to the polar coordinate system of Figure 6.4 (b),
- the energies, angles and diameters $\{(e_1, \theta_1, \zeta_1, d_1)\}_{i=1}^{N_ej-1}$ of the new ejected particles.

We divide the impact model in two parts:

1. the *Dissipation Model* aims to quantify the energy dissipated due to complex frictional interaction of sand grains when the impacting particle transfers its momentum,

[2] In some computational implementations the particles diameter varies but their shape remains spherical.

Group no.	V_i (m/s)		θ_i (°)	
	Mean	Standard deviation	Mean	Standard deviation
1	3.2	0.4	23.2	2.0
2	4.1	0.2	21.8	2.6
3	5.4	0.7	21.9	2.5
4	2.6	0.4	30.7	3.4
5	3.7	0.3	30.6	4.8
6	5.4	0.8	37.6	4.9
7	4.0	0.4	47.1	2.9
8	5.0	0.2	46.6	2.1
9	6.2	0.5	46.0	1.8

(a)

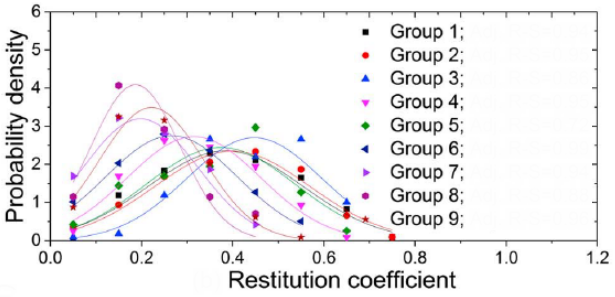

(b)

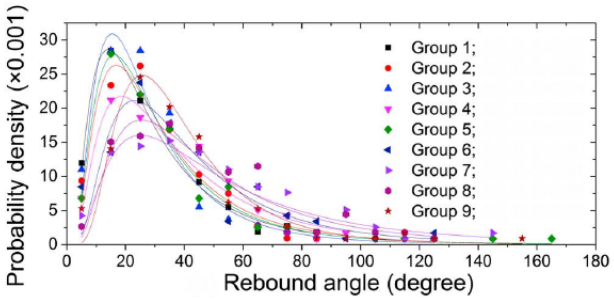

(c)

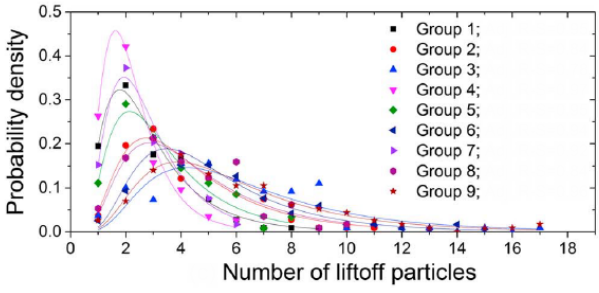

(d)

Figure 6.18: Results of experiments from [236]. (a) Data of the nine sample groups. Probability distributions: (b) restitution coefficient ε, (c) rebound angle θ_r and (d) number of liftoff particles n.

Group No.	V_i (m/s)		θ_i (°)	
	Mean	Standard deviation	Mean	Standard deviation
1	3.5	0.4	22.7	2.2
2	4.5	0.3	21.6	2.7
3	5.8	0.6	21.2	2.3
4	3.2	0.5	30.3	4.2
5	4.6	0.4	35.2	6.4
6	6.0	0.7	38.7	4.6
7	4.4	0.5	47.5	2.7
8	5.5	0.2	46.2	2.2
9	6.6	0.6	46.3	2.1

(a)

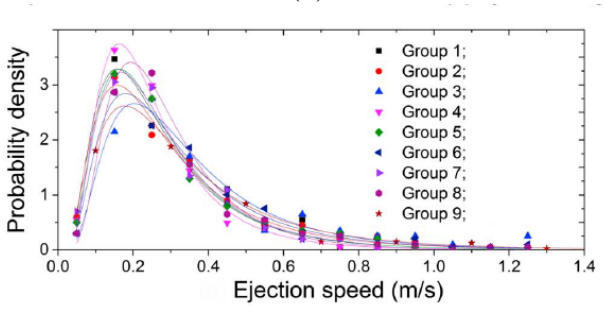

(b)

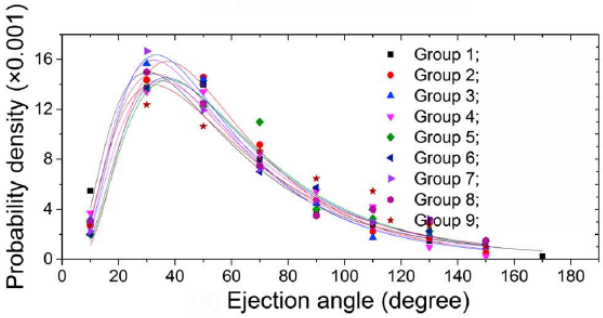

(c)

Figure 6.19: Results of experiments from [236]. (a) Data of the nine sample groups. Probability distributions for (b) ejection velocity V_{ej} and (c) ejection angle θ_{ej}

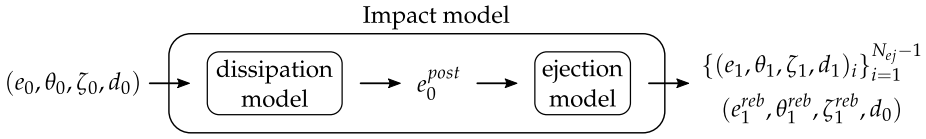

Figure 6.20: Conceptual diagram of the impact model.

2. the *Ejection Model* aims to determine how e_0^{post} is distributed on the N_{ej} ejected particles and their directions.

Figure 6.20 shows the general scheme for an impact model. This concept allow to split the complex chain of events involved in a ground-particle impact in two simpler parts, thought in a real phenomenon, frictional events, particles dislodgement and pneumatic conveying happen simultaneously.

We need to mention that the impact mechanism can be completely tracked with a high speed camera, even without using a wind tunnel. This implies that a massive number of tests can be easily performed with reasonably simple equipment.

6.2.3 Dissipation Models

We define the *coefficient of restitution* α as the ratio of the total (kinetic) energy just after and before the collision i.e. the sum of kinetic energies of the initial conditions of post-collision trajectories versus the one of impacting particle:

$$\alpha := \frac{e_0^{post}}{e_0} \in [0, 1) \ . \tag{6.14}$$

α can be thought as a stochastic variable and can be characterized by experiments changing impact conditions.

Uniform Distribution over a Fixed Interval The simplest probability distribution is the uniform distribution in a fixed interval:

$$\alpha \sim U(\alpha_{inf}, \alpha_{sup}) \ , \tag{6.15}$$

where $0 \leq \alpha_{inf} < \alpha_{sup} < 1$. We call this model "$dModel_1$".

Dependence on Energy and Angle of Impact Figure 6.21 classifies four types of collisions based of phenomenological observations. In particular, we can say that vertical impacts ($\theta_0 \simeq 0$) produce more dissipation than quasi-horizontal impacts ($\theta_0 \simeq \frac{\pi}{2}$). Furthermore, for high-energy impacts the available energy can be enough to eject particles even with high dissipation.

This idea is built on making α_{inf} and α_{sup} in (6.15) to be dependent on e_0 and θ_0, i.e.

$$\alpha \sim U(\alpha_{inf}(e_0, \theta_0), \alpha_{sup}(e_0, \theta_0)) \ ,$$

where

$$\alpha_k(e_0, \theta_0) = \alpha_0^k \left(1 - e^{-(e_0/e_k)}\right) \sin\theta_0 \qquad k = \{inf, sup\} \ . \tag{6.16}$$

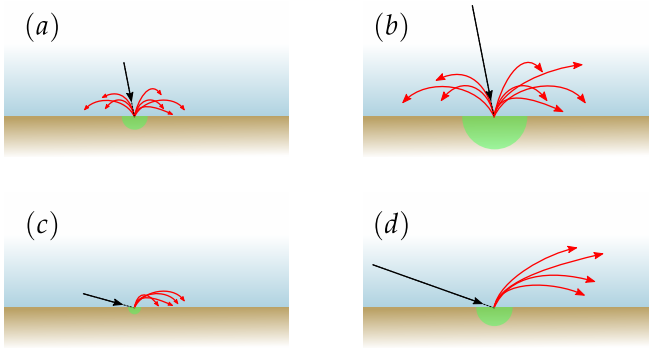

Figure 6.21: Four types of impact: (a) low energy and high dissipation, (b) high energy and high dissipation, (c) low energy and low dissipation, (d) high energy and low dissipation. The green region mimic the volume of particles influenced influence by the collision.

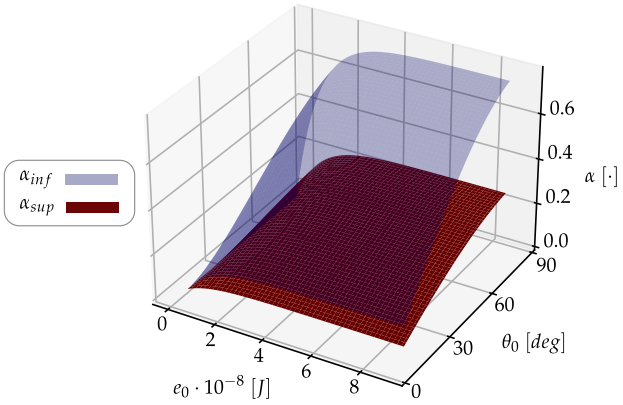

Figure 6.22: Graphs of α_k in (6.16) with $\alpha_0^{inf} = 0.3$, $\alpha_0^{sup} = 0.8$ and $e_{inf} = e_{sup} = 1 \cdot 10^{-8}\, J$.

Since $\alpha_{inf} < \alpha_{sup}$ for every pair (e_0, θ_0), the parameters have to satisfy the following conditions:

$$\begin{cases} \alpha_0^{inf} < \alpha_0^{sup} , \\ e_{inf} \geq e_{sup} . \end{cases} \tag{6.17}$$

For high-energy impacts

$$\alpha \in \left[\alpha_0^{inf} \sin\theta_0, \alpha_0^{sup} \sin\theta_0 \right] ,$$

while $\alpha \simeq 0$ for low-energy impacts or vertical impacts. The parameters e_{inf} and e_{sup} control how rapidly α_{inf} and α_{sup} reach their asymptotic values with respect to e_0. Figure 6.22 shows the behaviour of α_{inf} and α_{sup} for compatible values of α_0^{inf}, α_0^{sup}, e_{inf} and e_{sup}. We call this model "$dModel_2$". We remark that the analytical structure of (6.16) can be easily updated if experiments shows a new plausible behavior of α.

6.2.4 Ejection Models

Once α is determined by one of the methods described above, the particles can use the energy e_0^{post} to be ejected into the flow. Energy balance implies

$$\sum_{k=1}^{N_{ej}-1} e_{1,k} + e_1^{reb} \leq e_0^{post} \ , \tag{6.18}$$

where $\leq$ is used to take into account the sources of dissipation due to particles that are not entrained into the flow.

Particle Diameters Since a sand sample can be characterized by several types of sand we can directly use the probability distribution of d. If the particle size is composed by a constant value, the probability distribution becomes a Dirac delta. Therefore, when the number of particles is determined we can extract diameter values with the proper random distribution (see Figure 5.41 and Figure 6.46). In Section 5.5.1 we discussed the *ground memory effect*, but its application in this context is way beyond the scope of this preliminary study.

Ejection Angles The particle angle of ejection is another quantity strongly influenced by the particles shape and arrangement. In section 6.2.1 we mentioned the probabilistic description of the rebound angle proposed in [236] that however is only provided for the two-dimensional case. For sake of simplicity, we choose simple uniform distributions and we observe that we can assume the existence of an upper limit θ_1^{max} of θ_1 due to geometrical constraints of local particle arrangement (see Figure 6.23). Hence, $\theta_1 \in [0°, \theta_1^{max}]$.

In [231] the authors suggest the existence of a correlation between velocity and angle of ejection, but to the best of our knowledge this aspect is still debated. Because of the lack of experimental evidences on this correlation, we consider ejection angles independent from each other and from the ejection velocity. Since the fraction of particles involved in the backward motion is small (see [119, 237]) and considering the results on trajectories of Section 6.1.2 we simply consider

$$\begin{aligned} \theta_1 &\sim U(10°, 80°) \ , \\ \zeta_1 &\sim U(-30°, 30°) \ . \end{aligned} \tag{6.19}$$

As soon as new experiments provide new evidence on statistical correlations of ejection conditions, our model can be easily updated.

Minimum Value of Energy In order to distinguish between particles entrained by the wind and particles merely moved by their ejection energy we define a specific value of threshold energy. We address this value with the symbol e_{min}. The Boolean ejection condition reads

$$\begin{cases} e_1^{reb} \geq e_{min} \ , \\ e_{1,k} \geq e_{min} \qquad k = 1, 2, ..., N_{ej} - 1 \ , \end{cases} \tag{6.20}$$

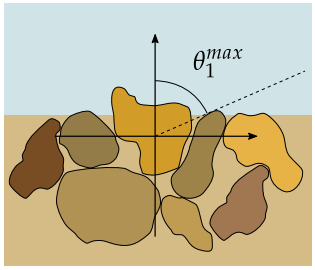

Figure 6.23: Schematic representation of particles arrangement that determine θ_1^{max}.

otherwise a particle is considered as not-ejected. Since e_0^{post} is partitioned among the ejected particles, if $e_0^{post} < e_{min}$ no particles are ejected. But, even if $e_0^{post} \geq e_{min}$ the model to extract the energy can eventually lead to no ejections (which corresponds to a dissipation of energy).

The value of e_{min} is related to the wind flow characteristics because for high values of u^* a particle requires little energy (i.e. smaller values of H_{max}) to be entrained into the flow. The functional dependence of e_{min} from flow variables is open to future researches. In Chapter 6.4 we will discuss the effect of e_{min} (as constant) in numerical tests.

Energy Equi-Ripartition

The model proposed here, called $eModel_1$, simply divides e_0^{post} equally among all ejecting particle. Since e_{min} determines the minimum value for the ejection, we can compute the maximum number of ejectable particles as

$$N_{ej}^{max} = \left\lfloor \frac{e_0^{post}}{e_{min}} \right\rfloor . \tag{6.21}$$

The relation (6.21) includes the case of $e_0^{post} < e_{min}$ which corresponds to no-ejections. The number of ejected particles N_{ej} is chosen randomly between 0 and N_{ej}^{max}. Hence

$$N_{ej} \in \{0, 1, ..., N_{ej}^{max}\} .$$

For sake of simplicity, we use the uniform discrete distribution. The mean number of ejected particles is

$$\overline{N_{ej}} = \frac{1}{2} N_{ej}^{max} .$$

Defining

$$S := \frac{e_{min}}{e_0^{post}} \tag{6.22}$$

previous relations read

$$N_{ej}^{max} = \left\lfloor \frac{1}{S} \right\rfloor \qquad \overline{N_{ej}} = \frac{1}{2} \left\lfloor \frac{1}{S} \right\rfloor$$

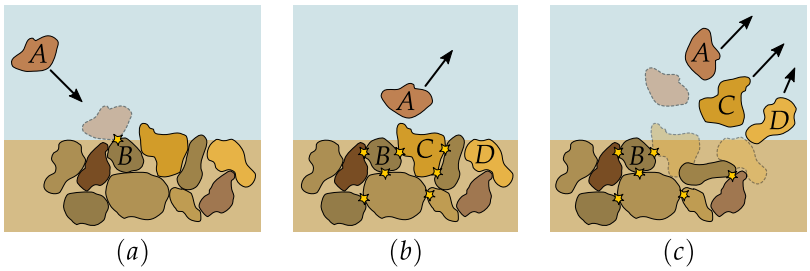

Figure 6.24: Scheme of the evolution of a ground-particle impact.

If $N_{ej} = 1$ only the rebounding particle is considered, while if $N_{ej} > 1$ other new particles are ejected. For $N_{ej} \geq 1$ the ejection model reads

$$\begin{cases} e_{1,k} = \frac{e_0^{post}}{N_{ej}} & \text{for } k = 1, ..., N_{ej} - 1 \ , \\ e_1^{reb} = \frac{e_0^{post}}{N_{ej}} \ . \end{cases} \tag{6.23}$$

Consecutive Extractions of Energy

Following the idea proposed in [56] and [218] we interpret a ground-particle impact as a sequence of binary collisions. The real physics can involve ternary or high order collisions but we suppose that higher order collisions are taken into account when α in (6.14) is computed. We can imagine to reproduce an impact dynamics using Figure 6.24 as reference.

1. particle A approaches the ground in direction of particle B, ending its trajectory with a binary collision (see Figure 6.24 (a)).
2. in the binary collision between A and B part of the energy and momentum of A is transferred to B. Meanwhile A rebounds (see Figure 6.24 (b)).
3. particle B is energized and it transfers its momentum to surrounding particles. Part of this leads to dissipation due to high-order collisions with underground particles (i.e. the value of α) and part is transferred to other particles in the surface region (see Figure 6.24 (b)).
4. particle B transfers momentum by means of binary collisions to C and D triggering the ejections (see Figure 6.24 (c)).

This sequence of events inspired the idea to interpret this phenomenon as a consecutive sequence of binary collisions. For each step of the sequence a fraction of e_0^{post} is extracted decreasing the total amount of available energy. The process stops when the available energy decreases below e_{min}. We call this model $eModel_2$.

In order to quantify ejection properties in accordance with this argument we set $e_{k=0}^{res} := e_0^{post}$. We define by E_k^{ex} the random variable of the k-th energy extraction and by e_k^{ex} its realization. We indicate by e_k^{res} the residual energy after the k-th extraction. We can formalize the sequence of extractions for each step with the following rules:

1. we sample e_{k+1}^{ex} according to the probability distribution of E_{k+1}^{ex} in

$$I_k := [0, e_k^{res}]$$

that is its probability space

2. the residual energy at the $k+1$ step reads

$$e^{res}_{k+1} := e^{res}_{k} - e^{ex}_{k+1} \, . \tag{6.24}$$

This determines $I_{k+1} := [0, e^{res}_{k+1}]$

3. we continue the iterations until

$$e^{res}_{k=N_{ex}} < e_{min} \, ,$$

where N_{ex} is the final number of extractions

In principle, the probability distribution for E^{ex}_{k+1} only requires that its probability space is finite and defined by I_k. For the sake of simplicity we consider

$$E^{ex}_{k+1} \sim U(0, e^{res}_{k}) \, . \tag{6.25}$$

We remark that e^{ex}_{k+1} could be smaller than e_{min}. Therefore an extracted energy does not necessarily correspond to an ejection, hence $N_{ej} \leq N_{ex}$. This aspect is relevant because it encodes the physical condition such that some particles are energized but they are not entrained leading to a loss of energy. $\{e^{ex}_i\}^{N_{ex}}_{i=1}$ is the sequence of extracted energies and $\{e^{ej}_i\}^{N_{ej}}_{i=1}$ is the sub-sequence of extracted energies greater than e_{min}. Figure 6.25 shows the process of extractions for three value of e^{post}_0. As observed in Section 6.2.1, most experiments associate the maximum value of energy with the rebounding particle (see for example [22]). In order to maintain this consistency we set

$$e^{reb}_1 = \max_{k=1,...,N_{ej}} \{e^{ej}_k\} \, .$$

We notice that the residual energy $e^{res}_{k=N_{ex}}$ when sequence stops is lost by dissipation. We also remark that N_{ex} and N_{ej} are random variables because they depend on the relation with the involved stochastic process. In order to estimate the maximum value of N_{ej} we can count the number of times that e_{min} can be potentially extracted consecutively. Hence

$$N^{max}_{ej} = \left\lfloor \frac{e^{post}_0}{e_{min}} \right\rfloor \, ,$$

which corresponds to (6.21). The minimum of N_{ej} is zero because all e^{ex}_k can potentially be less than e_{min}. In conclusion

$$N_{ej} \in \{0, 1, ..., N^{max}_{ej}\} \, .$$

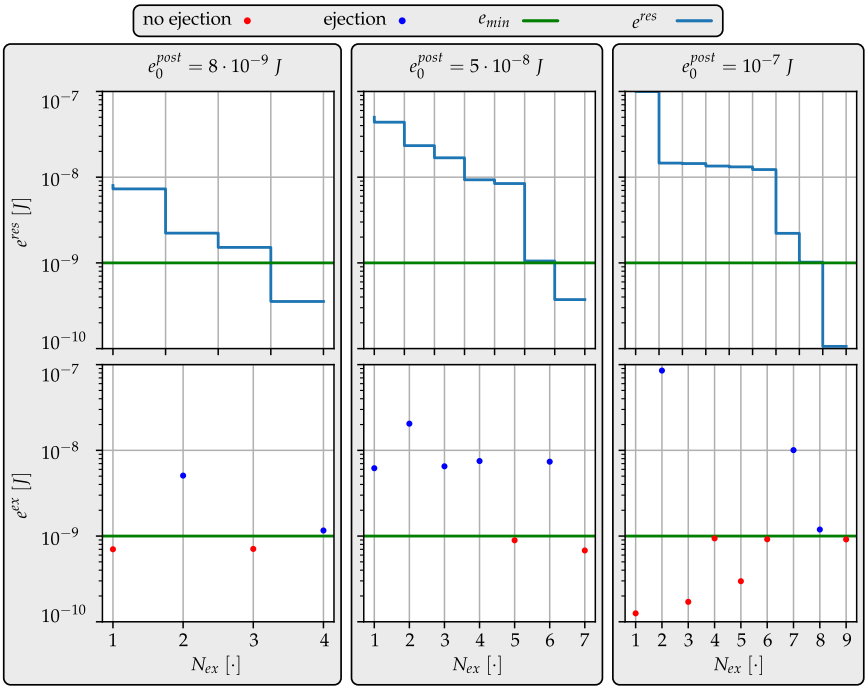

Figure 6.25: Numerical tests of the extraction process for three values of e_0^{post} and $e_{min} = 10^{-9}\ J$.

6.2.5 Energy Extractions as a Markov Process

In this section we aim to interpret the model in the context of Markov processes. We suppose to use a uniform distribution, hence we can use the residual energy e^{res} instead of the extracted energy e^{ex}. We recall that e_{k+1}^{ex} is the extracted energy at the $k+1$ step by the uniform distribution in $I_k = (0, e_k^{res})$. We denote E_k^{res} as the random variable for the residual energy and e_k^{res} its realization. The extraction rule allows to formulate the conditioned probability distribution as

$$f_{E_{k+1}^{res}|E_k^{res}}(e_{k+1}^{res}) = \frac{1}{e_k^{res}} \mathbb{1}_{((0,e_k^{res}))}(e_{k+1}^{res}) \qquad \text{for} \quad k = 0, 1, ..., N\ . \tag{6.26}$$

The sequence $\{E_k^{res}\}_{k=1}^N$ models the consecutive extraction process, where N is the number of extractions and $E_{k=0}^{res} := e_0^{post}$ is the initial energy. Equation (6.26) implies

$$f_{E_{k+1}^{res}|E_k^{res},E_{k-1}^{res},...,E_1^{res},E_0^{res}}(e_{k+1}^{res}) = f_{E_{k+1}^{res}|E_k^{res}}(e_{k+1}^{res})\ , \tag{6.27}$$

in other words the sequence of random variables can be considered as a Markov process. We recall that the sequence of realizations $\{e_k^{res}\}_{k=1}^N$ is decreasing and it stops as soon as $e_N^{res} < e_{min}$. Figure 6.25 shows some numerical tests of this process.

Normalization It is convenient to deal with fractions of energy. Therefore, we normalize the extracted energy dividing it by e_0^{post}. Therefore, we define $X_k := \frac{E_k^{res}}{e_o^{post}}$, and

x_k be its realization. Hence, the sequence of extractions stops as soon as

$$x_k < S := \frac{e_{min}}{e_0^{post}}$$

where S is the normalized energy threshold (i.e. (6.22)). Using (6.26) the conditional probability density function reads

$$\begin{cases} f_{X_1}(x_1) = \mathbb{1}_{((0,1))}(x_1)\ , \\ f_{X_k|X_{k-1}}(x_k) = \dfrac{1}{x_{k-1}}\mathbb{1}_{((0,x_{k-1}))}(x_k) \quad \text{for} \quad k = 2,3,...,N\ . \end{cases} \tag{6.28}$$

Probability Density of X_k For a generic joint probability distribution $f_{X,Y}$ of two random variables X and Y we can write

$$f_{X,Y}(x,y) = f_{X|Y}(x) f_Y(y). \tag{6.29}$$

We can compute the probability density function f_{X_k} for the generic random variable X_k using recursively (6.29). For the first m extractions we have

$$f_{X_1,X_2,...,X_m}(x_1,x_2,...,x_m) = f_{X_m|X_{m-1},X_{m-2},...,X_1}(x_m) f_{X_{m-1},X_{m-2},...,X_1}(x_{m-1},x_{m-2},...,x_1) =$$

$$= f_{X_m|X_{m-1},X_{i-2},...,X_1}(x_m) f_{X_{m-1}|X_{m-2},X_{m-3},...,X_1}(x_{m-1}) f_{X_{m-2},X_{m-3},...,X_1}(x_{m-2},x_{m-3},...,x_1) = \dots$$

and using (6.27) we have

$$f_{X_1,X_2,...,X_m}(x_1,x_2,...,x_m) = f_{X_1}(x_1) f_{X_2|X_1}(x_2) f_{X_3|X_2}(x_3) ... f_{X_m|X_{m-1}}(x_m)$$

and by (6.28) we have

$$\begin{aligned} f_{X_1,X_2,...,X_m}(x_1,x_2,...,x_m) &= \mathbb{1}_{((0,1))}(x_1)\frac{1}{x_1}\mathbb{1}_{((0,x_1))}(x_2)\frac{1}{x_2}\mathbb{1}_{((0,x_2))}(x_3)...\frac{1}{x_{m-1}}\mathbb{1}_{((0,x_{m-1}))}(x_m) \\ &= \frac{1}{\prod_{h=1}^{m-1} x_h}\mathbb{1}_{((0,1)\times(0,x_1)\times...\times(0,x_{m-1}))}(x_1,x_2,\dots,x_m)\ . \end{aligned} \tag{6.30}$$

We recall that the probability density function of X_k depends only on X_{k-1}. Therefore, we can sequentially integrate (6.30) in order to compute the related marginal probability distributions.

For X_2 we have

$$f_{X_2}(x_2) = \int_0^1 f_{X_1,X_2}(x_1,x_2)\,dx_1 = \int_0^1 \frac{1}{x_1}\mathbb{1}_{((0,1)\times(0,x_1))}(x_1,x_2)\,dx_1\ . \tag{6.31}$$

The domain region where the function is not null are identified by

$$\begin{cases} 0 < x_1 < 1 \\ 0 < x_2 < x_1 \end{cases}$$

or equivalently

$$\begin{cases} 0 < x_2 < 1 \\ x_2 < x_1 < 1 \end{cases}$$

hence (6.31) reads

$$f_{X_2}(x_2) = \int_{x_2}^{1} \frac{1}{x_1}\, dx_1 = -\ln x_2\, \mathbb{1}_{((0,1))}(x_2)\ .$$

For X_3 we have

$$\begin{aligned} f_{X_3}(x_3) &= \int_0^1 f_{X_2,X_3}(x_2, x_3)\, dx_2 \\ &= \int_0^1 f_{X_2}(x_2) f_{X_3|X_2}(x_3)\, dx_2 \\ &= \int_0^1 -\frac{\ln x_2}{x_2} \mathbb{1}_{((0,1)\times(0,x_2))}(x_2, x_3)\, dx_2 \end{aligned}$$

and again the integration domain can be expressed with respect to x_3 as

$$\begin{cases} 0 < x_2 < 1 \\ 0 < x_3 < x_2 \end{cases} \longrightarrow \begin{cases} 0 < x_3 < 1 \\ x_3 < x_2 < 1 \end{cases}$$

hence

$$\begin{aligned} f_{X_3}(x_3) &= \int_0^1 -\frac{\ln x_2}{x_2} \mathbb{1}_{([0,1]\times[0,x_2])}(x_2, x_3)\, dx_2 \\ &= \int_{x_3}^1 -\frac{\ln x_2}{x_2}\, dx_2 = \frac{\ln^2 x_3}{2} \mathbb{1}_{([0,1])}(x_3)\ . \end{aligned}$$

Iterating the procedure above we can define the probability density function for a generic index. Hence

$$f_{X_i}(x_i) := (-1)^{i-1} \frac{\ln^{i-1} x_i}{(i-1)!} \mathbb{1}_{([0,1])}(x_i) \quad i = 1, 2, ..., N\ . \tag{6.32}$$

Figure 6.26 shows the comparison of (6.32) and the numerical tests using 10000 samples.

Number of Extractions The joint probability distribution (6.30) allows to obtain the discrete probability distribution for N. We denote with N the stochastic variable of the number of extractions and with n its realization. Since the sequence of extraction stops when $e^{res}_{n-1} < e_{min}$ we have

$$\mathbb{P}(N = n) = \mathbb{P}(X_1 \geq S, X_2 \geq S, ..., X_n < S)\ . \tag{6.33}$$

For $n = 1$ we have

$$\mathbb{P}(N = 1) = \mathbb{P}(X_1 < S) = \int_0^S \mathbb{1}_{((0,1))}(x_1)\, dx_1 = S\ .$$

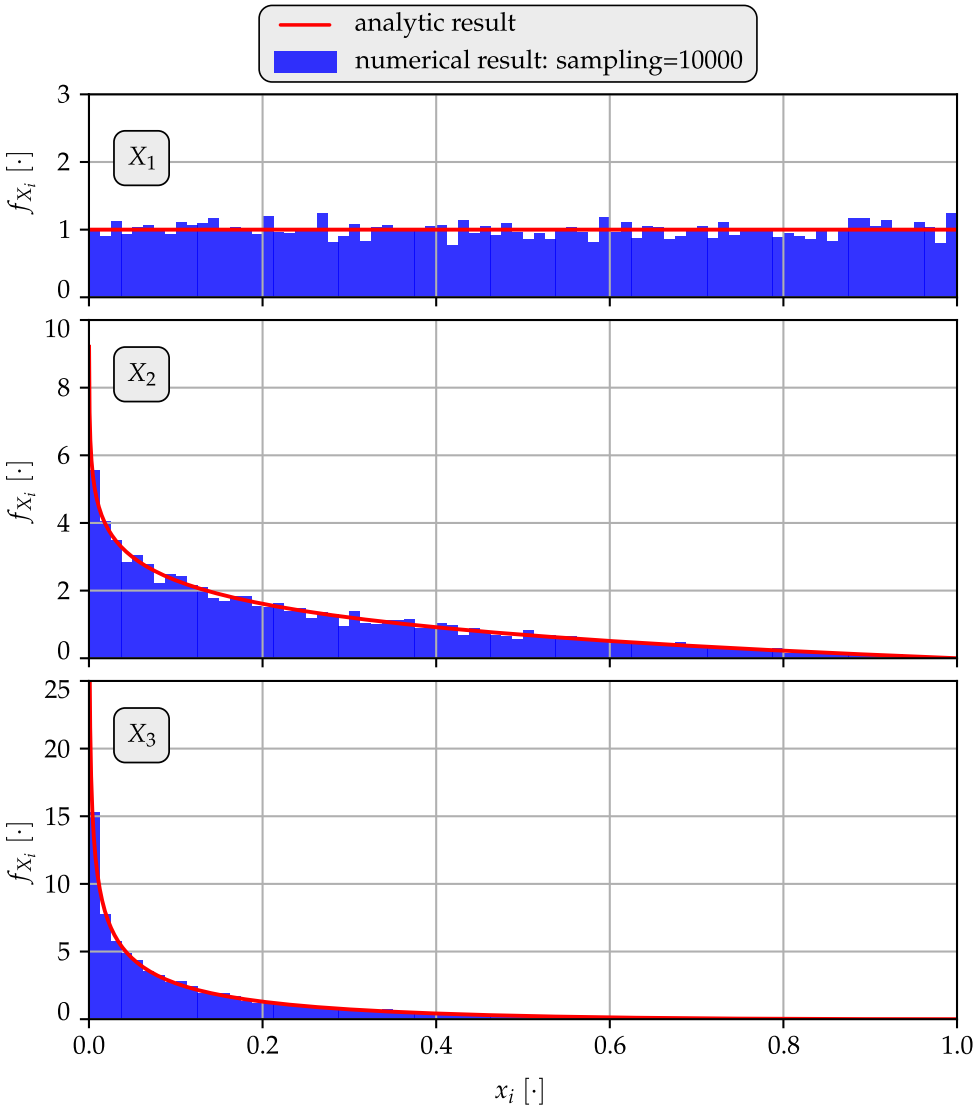

Figure 6.26: Comparison between numerical and theoretical results for X_k with $k = 1, 2, 3$. The showed histograms is obtained performing 10000 samples.

For $n = 2$ we define $\Omega_2 := \{x_1 \geq S, x_2 < S\}$. Hence

$$\begin{aligned}\mathbb{P}(N=2) &= \mathbb{P}(X_1 \geq S, X_2 < S) \\ &= \iint_{\Omega_2} f_{X_1,X_2}(x_1,x_2)\,dx_1\,dx_2 \\ &= \iint_{\Omega_2} \frac{1}{x_1}\mathbb{1}_{((0,1)\times(0,x_1))}(x_1,x_2)\,dx_1\,dx_2\end{aligned}$$

where

$$\begin{cases} 0 < x_1 < 1 \\ 0 < x_2 < x_1 \\ S \leq x_1 < 1 \\ 0 \leq x_2 < S \end{cases} \longrightarrow \begin{cases} S \leq x_1 < 1 \\ 0 < x_2 \leq S \end{cases}$$

hence

$$\mathbb{P}(N=2) = \iint_{\Omega_2} \frac{1}{x_1}\mathbb{1}_{((0,1)\times(0,x_1))}(x_1,x_2)\,dx_1\,dx_2 = \int_S^1 \int_0^S \frac{1}{x_1}\,dx_1\,dx_2 = -S\ln S\,.$$

For $n = 3$ we define $\Omega_3 := \{x_1 \geq S, x_2 \geq S, x_3 < S\}$. Hence

$$\begin{aligned}\mathbb{P}(N=3) &= \mathbb{P}(X_1 \geq S, X_2 \geq S, X_3 < S) \\ &= \iiint_{\Omega_3} f_{X_1,X_2,X_3}(x_1,x_2,x_3)\,dx_1\,dx_2\,dx_3 \\ &= \iiint_{\Omega_3} \frac{1}{x_1 x_2}\mathbb{1}_{((0,1)\times(0,x_1)\times(0,x_2))}(x_1,x_2,x_3)\,dx_1\,dx_2\,dx_3\,,\end{aligned}$$

where

$$\begin{cases} 0 < x_1 < 1 \\ 0 < x_2 < x_1 \\ 0 < x_3 < x_2 \\ S \leq x_1 < 1 \\ S \leq x_2 < 1 \\ 0 < x_3 < S \end{cases} \longrightarrow \begin{cases} S \leq x_1 < 1 \\ S \leq x_2 < x_1 \\ 0 < x_3 < S \end{cases}$$

hence

$$\begin{aligned}\mathbb{P}(N=3) &= \iiint_{\Omega_3} \frac{1}{x_1 x_2}\mathbb{1}_{((0,1)\times(0,x_1)\times(0,x_2))}(x_1,x_2,x_3)\,dx_1\,dx_2\,dx_3 \\ &= \int_S^1 \int_S^{x_1} \int_0^S \frac{1}{x_1 x_2}\,dx_1\,dx_2\,dx_3 = \frac{S\ln^2 S}{2}\,.\end{aligned}$$

We can iterate the procedure for a generic n obtaining

$$\mathbb{P}(N=n) = (-1)^{n-1}\frac{S\ln^{n-1} S}{(n-1)!} \quad \text{for} \quad n = 1, 2, \ldots\,. \tag{6.34}$$

Figure 6.27 shows the comparison of (6.34) and the numerical tests using 10000 samples. During the numerical simulations we can also track the number of ejected

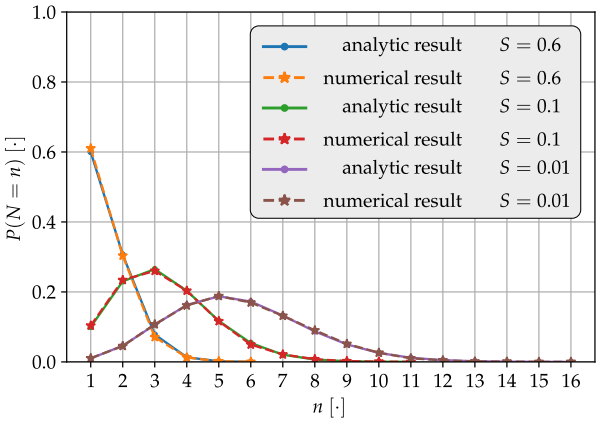

Figure 6.27: Comparison between (6.34) and the numerical tests using 10000 samples for several values of S.

particles which is smaller than the number extraction by construction. Figure 6.28 shows the mean value of N_{ej} as function of S over 10000 samples. Table 6.3 report some statistics on N_{ej}.

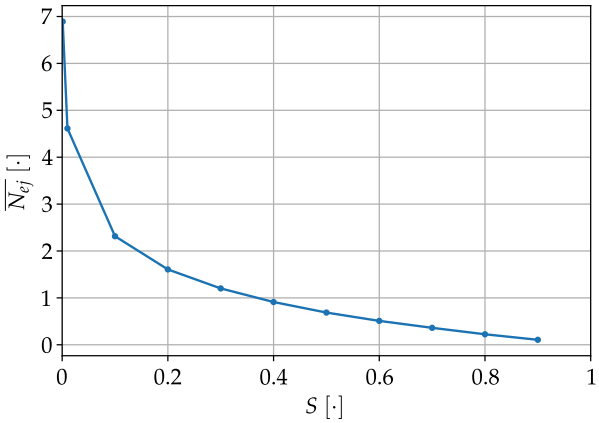

Figure 6.28: Numerical results of $\overline{N_{ej}}$ as function of S. The results are obtained over 10000 samples.

S	theoretical N_{ej}^{max}	numerical N_{ej}^{max}	nearest integer	$\overline{N_{ej}}$
0.9	1	1	0	0.11
0.8	1	1	0	0.22
0.7	1	1	0	0.36
0.6	1	1	1	0.51
0.5	2	1	1	0.69
0.4	2	2	1	0.91
0.3	3	3	1	1.20
0.2	4	4	1	1.61
0.1	10	6	2	2.31
0.01	100	12	4	4.61
0.001	1000	19	7	6.89

Table 6.3: Statistical report of N_{ej}.

6.3 Algorithm Architecture

In this Section we propose an algorithm that uses the models described in the previous section in order to simulate an aeolian system in a hexahedral domain. The system of particles evolves in time, tracking all events and physical interactions. For sake of simplicity we neglect the explicit treatment of mid-air collisions because the probability of their occurrence is marginal with respect to the effects of ground-particle collisions (see [130]). However, during the algorithm description we report where it could be implemented.

The algorithm involves a temporal loop where all the system properties are updated over time iterations. The temporal loop (see Figure 6.29) can be descriptively summarized in four main sequential steps:

Input step At the generic time t we introduce particles in the system due to the pure wind action, for example due to pressure fluctuations induced by the eddies near the soil. The rate of particles introduction depends on the sand concentration and wind strength. Details are discussed in Section 6.3.3.

Predictor step Positions and velocities of old and new emitted particles are used as initial conditions in a one-step ODE integrator[3] to solve (6.1) for each particle. Here all the forces, and possibly the turbulence effect, are taken into account. New positions and velocities are candidates for the particles positions and velocities at the time $t + \Delta t$. Details are discussed in Section 6.3.2.

Impact step Candidate positions computed in the previous step are used to detect ground-particle collisions (see Figure 6.31 (a)). This is also the step where mid-air collisions can be detected and taken into account in the computation.

Corrector step Positions and velocities of colliding particles are corrected or removed in order to be compatible with the rules of the impact model. Also new particles can be emitted using the impact model rules (see Figure 6.31 (b)).

6.3.1 Wind Flow and Turbulence

In the algorithm framework we intentionally decide to impose the fluid velocity as a known function. A similar approach is used in [130] for a two-dimensional solver with good results. As usual, the fluid velocity can be thought as the sum of mean and fluctuating terms. Hence

$$\vec{u}_f = \vec{U}_f + \vec{u}'_f \, .$$

Both these terms are imposed as known functions. $\vec{U}_f$ represent a steady (or quasi-steady) horizontal flow which only varies along z, therefore it is divergence-free by definition. The turbulent fluctuations are described by $\vec{u}'_f$. Since $\vec{u}'_f$ is applied pointwise in the particle position, its analytic formulation is not required to be divergence-free i.e. $\vec{u}'_f$ can be thought as a divergence-free vector field but we only sample its value in the point occupied by the particle. In particular, once turbulence properties are set, we do not need to compute a divergence-free Eulerian field.

[3] For sake of simplicity we use the Newmark method (see [167]) but other methods can be used.

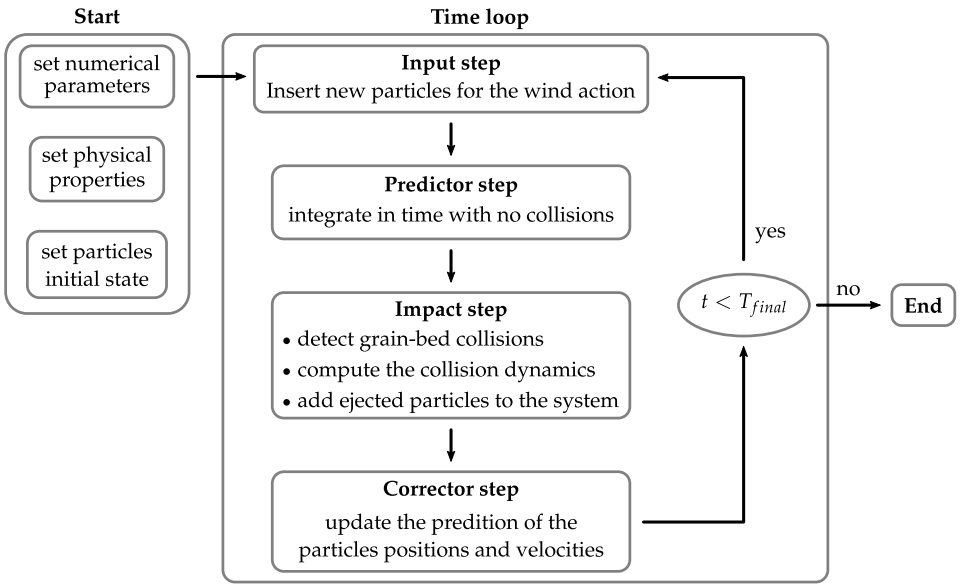

Figure 6.29: Flow chart of the presented algorithm.

Steer clear to solve the (incompressible) Navier-Stokes equations[4] drastically reduce the computational costs. We set $\vec{u}'_f = 0$ due to the lack of robust data on turbulence for high Reynolds flows within the saltation layer. However, in future tests we can conjecture the space-time properties of $\vec{u}'_f$ in order to compute sensitivity studies and eventually perform ad hoc CFD simulations to get turbulence data.

The particles feedback on the mean flow requires to solve a momentum equation in order to perturb the steady profile of $\vec{U}_f$ taking into account the drag force that particles exert on the air. Also the particles feedback on $\vec{u}'_f$ is postponed to future studies. All these aspects combined together lead to a strongly coupled system which is similar (but not equal) to DEM approaches and also similar to second order models for multiphase continuum flows. In fact, the final goal of the *Semi-Stochastic Periodic Box* is to gain quantitative knowledge to be transferred to fully Eulerian multiphase models.

6.3.2 Computational Aspects

Computational Domain

Since we consider a saltation state in a steady condition we imagine to simulate a volume region in the middle of the cloud of saltating sand. Therefore, boundary effect are negligible and all quantities change only in z. We consider an hexahedral domain of sides L_x, L_y and L_z because we can easily apply periodic conditions on

[4] In form of DNS or with a turbulence model, e.g. RANS or LES.

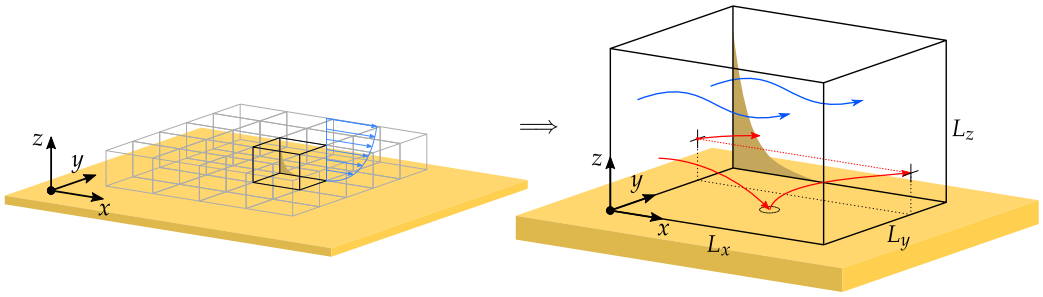

Figure 6.30: Schematic representation of a box domain for a flat surface. The red curve describe an example of particle trajectory.

particles trajectories. For a generic active k-th particle, at each time step we compute

$$\begin{cases} x_k = mod\left(\frac{x_k}{L_x}\right) , \\ y_k = mod\left(\frac{y_k}{L_y}\right) . \end{cases} \tag{6.35}$$

Hence, when a particle pass through the downwind surface (i.e. the plane $x = L_x$) it is reintroduced from the upwind surface (i.e. the plane $x = 0$, see Figure 6.30). The sand bed can be described by the graph of a smooth periodic function

$$\begin{aligned} f_{bed} : [0, L_x] \times [0, L_y] &\to \mathbb{R} \\ (x, y) &\mapsto \mathbb{R} \end{aligned} \tag{6.36}$$

Therefore, a ground-particle collision occurs if

$$z_k \leq f_{bed}(x_k, y_k) \quad \text{for} \quad k = 1, ..., N . \tag{6.37}$$

For sake of simplicity we consider flat surfaces i.e. $f_{bed} \equiv 0$. Therefore ground-particle collisions are detected by

$$z_k \leq 0 \quad \text{for} \quad k = 1, ..., N$$

However, a generic f_{bed} can be potentially used to study sand ripples or other periodic structures showed in the aeolian science.

Predictor-Impact-Corrector Chain

Here we want to discuss the process involved in a collision event from the computational perspective. In particular we want to clarify why we adopt a one-step method. The explicit Newmark method applied to the particle system at the time t reads

$$\begin{cases} \vec{\mathbf{x}}(t + \Delta t) = \vec{\mathbf{x}}(t) + \Delta t\, \vec{\mathbf{v}}(t) + \frac{\Delta t^2}{2} \vec{\mathbf{F}}(t) , \\ \vec{\mathbf{v}}(t + \Delta t) = \vec{\mathbf{v}}(t) + \Delta t\, \vec{\mathbf{F}}(t) , \end{cases}$$

where $\vec{\mathbf{x}} = (\vec{x}_1, \vec{x}_2, \ldots, \vec{x}_N)$ is a N-tuple of positions, $\vec{\mathbf{v}} = (\vec{v}_1, \vec{v}_2, \ldots, \vec{v}_N)$ is an N-tuple of velocities and N is the number of particles at time t. We are practically solving

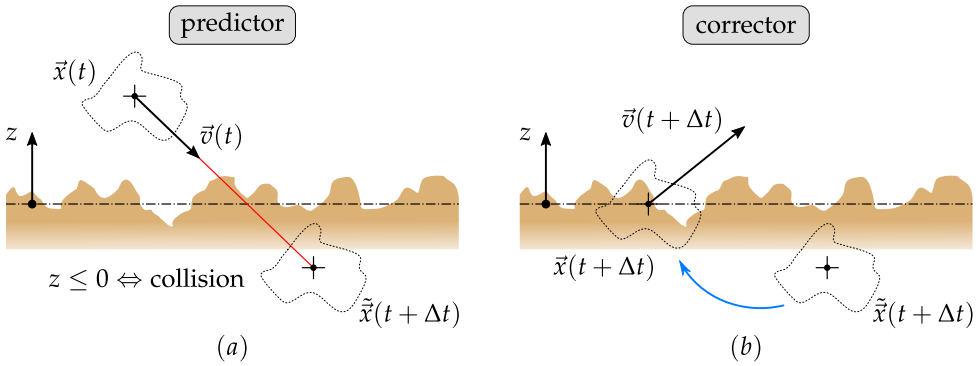

Figure 6.31: (a) Predictor step for a particle involved in an incoming collision. (b) Detection of the collision and correction with a new position and velocity.

(6.1) for each moving particle. In the *predictor step* we compute $\vec{\mathbf{x}}(t+\Delta t)$.

We can take Figure 6.31 as reference and focus on a generic particle in a status of incoming collision. In the interval of time Δt the observed particle moves approximately along the red line (see Figure 6.31(a)) and other particles in the system may lie in an similar condition. Therefore, a collision certainly occurs in the time interval Δt. The *impact step* checks which particles are subjected to collision and it applies the impact model. Since Δt is small to keep a small numerical error, the difference between $\vec{x}(t)$ and $\tilde{\vec{x}}(t+\Delta t)$ is small. Therefore, instead of computing the intersection of the particle trajectory with the ground surface (and the related impact time), we simply impose the new position $\vec{x}(t+\Delta t)$ as the projection of $\vec{x}(t)$ to the plane $z=0$ (see Figure 6.31(b)). This approach reduces the computational cost but the small error committed does not affect the system evolution. The *corrector step* addresses the procedures to update the positions of colliding particles.

We remark that when a ground-particle collision occurs the impact model applies and new particles could be ejected. These do not exist for times preceding $t+\Delta t$. Therefore, multistep methods would take into account several time steps and apply low order methods for initial times of a particle trajectory. The one-step explicit methods avoid this problem and this is the reason why we use the Newmark method in its explicit form. Indeed, since the particle moves in air without mid-air collisions the trajectories could be solved with an high accurate multistep methods. We also remark that the smaller Δt is, the smaller is the number of impacts in that time interval. Therefore the overall error committed computing new positions reduces.

Active and Passive Particles

Due to the impact model, saltating particles can stop their trajectory in a rest condition and new particles can be ejected from the soil. Since in our approach we do not treat binary collisions deterministically (like in DEM models) there is no reason to waste computational memory to save still particles on the ground. Therefore, only moving particles are involved in the system evolution. This approach leads to deal with dynamic containers where pointers to particles are continuously created (for

ejected particles) and deleted (for removed particles). The computational optimization of the source code is under development. However, the current implementation allows to consider an acceptable number of particles for numerical tests. One of the reasons why we neglect mid-air collisions is also the computational cost. In fact, if N is the number of *active particles*, handling ground-particle collisions requires to check the condition (6.37) i.e. N operations, while Mid-air (binary) collisions require to check the distance for each pair of active particles i.e. $N^2/2$ operations.

This framework is also coherent with physical observations. It allows to mimic the continuous creation and removal of particles in their saltation trajectories. Contrarily to DEM methods where the number of particles in the system is constant, our approach is capable to deal with dynamic lists of particles. Therefore, all computational resources are used only to compute moving particles.

6.3.3 Fluid Entrainment Model

When no particles are present in air the triggering mechanism is due to the aerodynamics structures that eventually lift the particles into the flow. The stronger the wind is, the higher the number of lifted particles is. We address to this phenomenon with the term "fluid entrainment". In Section 5.3.4 we have discussed the existence of a threshold value u_t^* which determines if the saltation occurs or not (see [174, 187]). Since the value of u_t^* is still debated here we use another approach.

When the saltation process become steady under a steady wind condition the fluid entrainment and the particles ejection due to the impact model balance each other. Therefore, we associate the emission rate due to fluid entrainment to the concentration of particles present in air. We introduce a specific flux of particles p_{wind} from the sandy soil

$$p_{wind} := P\, e^{-\varphi_{ground}\,/\,\varphi_{sat}}\ , \tag{6.38}$$

where φ_{ground} is the volume concentration of particles near the ground, φ_{sat} represents the concentration of saturation and P measures the specific rate of emission in clean air with dimensions $[m^{-2}s^{-1}]$. We remark that P would depend on the wind strength (e.g. u^*) because phenomenological observations show that the stronger the wind flow is, the higher the emission rate is. In this preliminary stage we keep it as a free parameter.

The number of entrained particles N_{input} is computed by the formula

$$N_{input} = \lfloor p_{wind}\, L_x\, L_y\, \Delta t \rfloor\ .$$

Since the presence of the *floor* function introduces a relevant error for very small Δt, we use a specific time step Δt_{input} for the fluid entrainment such that $\Delta t_{input} > \Delta t$. Therefore, the number of particles N_{input} entrained into the system is then computed as

$$N_{input} = \lfloor p_{wind}\, L_x\, L_y\, \Delta t_{input} \rfloor\ . \tag{6.39}$$

The different discrete time advancement is taken into account during the *input step* of the temporal loop. Using Figure 6.32 as reference, we verify whether the input time (green time-line) falls within the interval $[t, t + \Delta t]$. If the emission occurs N_{input}

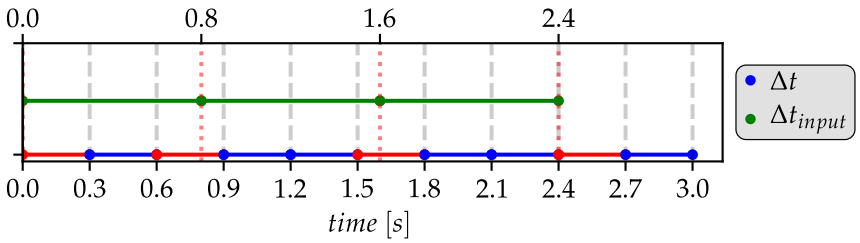

Figure 6.32: Scheme of fluid entrainment times. The final time T_{final} is set to $3\,s$, the integration time (blue line) proceeds with a time step of $\Delta t = 0.3$ and the input time (green line) with a time step of $\Delta t_{input} = 0.8$. In red are highlighted the steps in which a fluid entrainment event occurs.

particles are added to the computational list of the *active particles* with compatible positions and velocities. In particular

- $x \sim U(0, L_x)$, $y \sim U(0, L_y)$ and $z = 0$,
- new diameters are sampled using the diameter probability distribution for the sand.

Ejection energies and angles would be chosen using probability distributions defined by experiments as a functions of u^*. Due to the lack of data, we use uniform distribution for e_1, θ_1 and ζ_1 over a fixed interval

$$\begin{aligned} e_1 &\sim U(5 \cdot 10^{-8}\, J, 5 \cdot 10^{-7}\, J)\ , \\ \theta_1 &\sim U(30°, 80°)\ , \\ \zeta_1 &\sim U(-80°, 80°)\ , \end{aligned} \tag{6.40}$$

where the cartesian coordinates can be computer using (6.7).

The Pseudo-Code

In this section we show the pseudo-code of the Semi-Stochastic Periodic Box algorithm. For sake of simplicity we do not show all the implementation details. However, the presented pseudo-code is complete in all major details. The source code is implemented in *python-3.6* using *numpy* and *scipy* libraries.

6.4 Numerical Simulations

In this Section we perform some numerical tests using the algorithm presented above. We systematically change the models parameters in order to explore how the results change. We track the evolution of following quantities:

- the system kinetic and potential energy
- the total number of moving particles
- the number of particles introduced in the domain due to the fluid entrainment
- the number of particles introduced in the domain due to the impact model

set temporal and domain properties;
set wind properties;
set sand properties;
set properties of impact model and fluid entrainment model;
set a number of initial particles $N(t = 0)$ and set their positions and diameters;
$t = 0$;
while $t \leq T_{final}$ **do**
  save the state of the system for post-processing routines;
  Input step: **if** *fluid entrainment occurs* **then**
    compute the ground concentration φ_{ground} of particles;
    compute the number of new particles N_{input};
    set energies e_1, angles θ_1, ζ_1, diameters and positions of new particles;
    convert input information into cartesian velocities;
    add the new particles to the system;
  end
  calculate forces on particles;
  Predictor step: compute new positions and new velocities if no collisions occur;
  Impact step: **for** *particle p in the system* **do**
    if *p is involved in a mid-air collision* **then**
      treatment of binary collision (neglected);
    else if *p is involved in a ground collision* **then**
      compute kinetic energy e_0 and angles θ_0, ζ_0 of the impact particle;
      Impact model: compute energies e_1, angles θ_1, ζ_1 and diameters of the ejected particles and the rebounding particle;
      convert outputs of impact model into cartesian velocities;
      set the particles positions;
  end
  Corrector step: compute corrections for positions of the new particles;
  add the new particles to the system;
  remove impact particles;
  update the state of particles;
  t = t + Δt;
end

Algorithm 1: Pseudo-code of the Semi-Stochastic Periodic Box algorithm.

- the sum of the previous two
- the number of particles exiting from the domain due to the impact model

In order to perform a significant statistical analysis we collect 100 system samples equally distributed over time once the stationary state is reached ($t \simeq 1\,s$). Although $L_z = 1\,m$, we consider a $20\,cm$ height volume; L_x and L_y remains the same. We divide this volume in twenty slices, one centimeter each. In each slice we compute:

- the particles concentration φ_s summing the particles volume and dividing it by the total volume
- the mean and standard deviation of the particles velocity components v_x, v_y, v_z
- the mean and standard deviation of the particles velocity magnitude
- the mean and standard deviation of particle diameters for the polidisperse case
- the horizontal mass flux $q := \rho_s \varphi_s \langle v_x \rangle$

where $\langle v_x \rangle$ is the average of the x-component of particle velocity among particles in a slice. Each slice is basically a control volume.

6.4.1 Simulations of the Monodisperse Case

In this section we show a series of numerical tests with a single value of diameter. Table 6.5 reports the default values shared by presented results. Then, we change parameters one by one in the presented figures. Table 6.4 reports the changed parameters and the related figures. Figures 6.33, 6.34, 6.35 and 6.36 show the result for default values of Table 6.5, to be used as a reference for the parameter changes.

changed parameter/s	Figure/s	related equation
e_{inf}, e_{sup}	6.37	(6.16)
$\alpha_{inf}, \alpha_{sup}$	6.38	(6.15)
e_{min}	6.39	(6.20)
P	6.40	(6.38)
φ_{reb}	6.41	(6.38)
u^*	6.42-6.43	-
$\langle d \rangle$	6.44-6.45	-

Table 6.4: Map of the changed parameters and related figures.

L_x	0.05	m
L_y	0.05	m
L_z	1	m
T_{final}	3	s
Δt	10^{-3}	s
Δt_{input}	$5 \cdot 10^{-3}$	s
$N(t=0)$	100	$[\cdot]$
ρ_f	1.225	kg/m^3
ρ_s	2700	kg/m^3
u^*	0.5	m/s
z_0	0.001	m
$N(t=0)$	100	$[\cdot]$
$\langle d \rangle$	$5 \cdot 10^{-4}$	m
d $p.d.f.$	$\delta_{\langle d \rangle}$	
dissipation model	$dModel_1$	
α interval	$[0.2, 0.7]$	$[\cdot]$
ejection model	$eModel_2$	
e_{min}	$5 \cdot 10^{-8}$	J
P	$1 \cdot 10^{6}$	$m^{-2}s^{-1}$
φ_{sat}	10^{-3}	$[\cdot]$

Table 6.5: Default values used in the presented numerical tests.

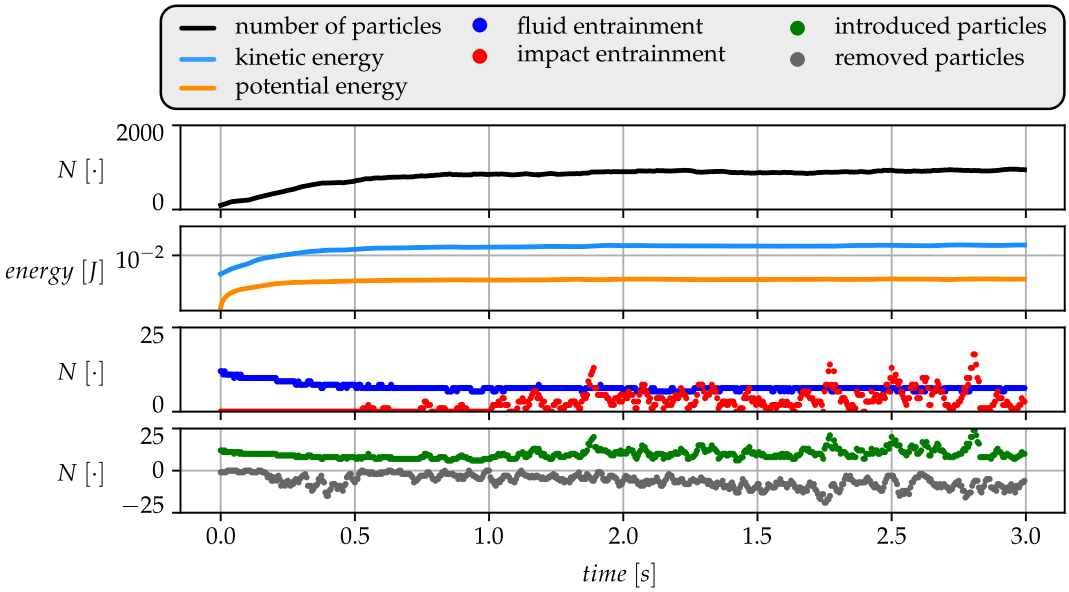

Figure 6.33: Numerical result using the default setup of Table 6.5.

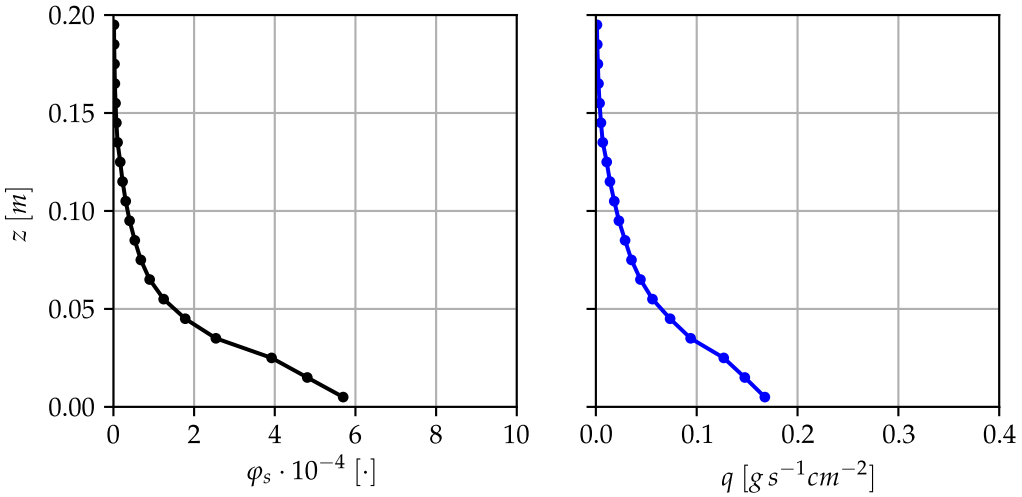

Figure 6.34: Particles concentration and flux using the default setup of Table 6.5.

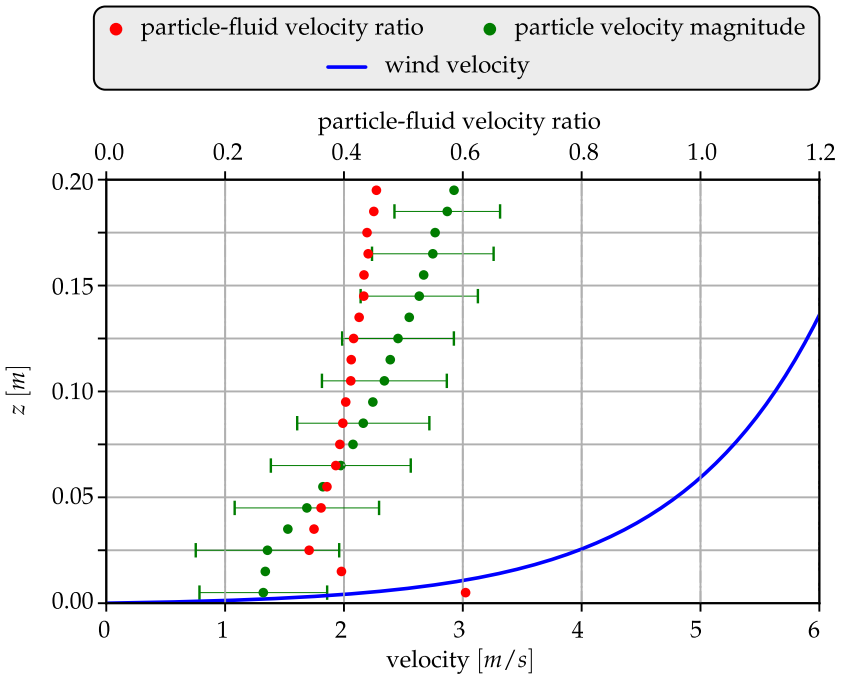

Figure 6.35: Particles velocity using the default setup of Table 6.5.

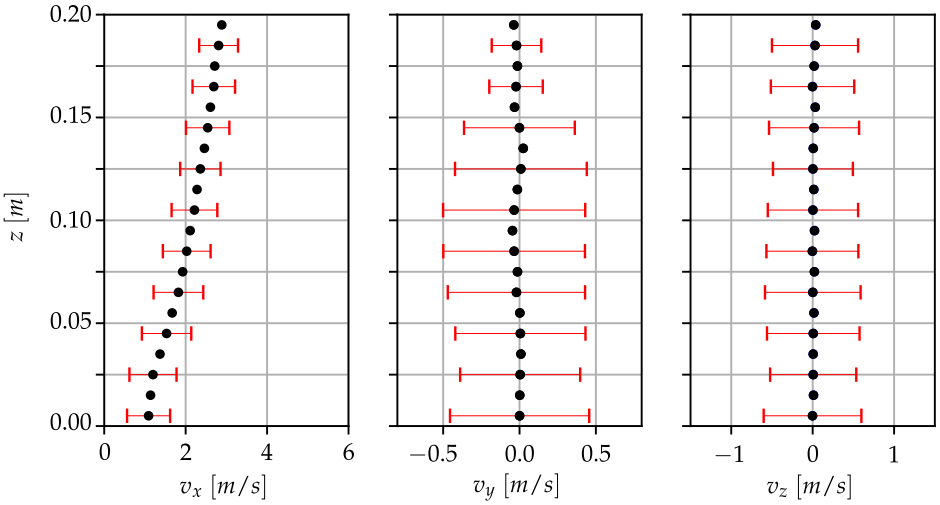

Figure 6.36: Mean and standard deviation of particles velocity components using the default setup of Table 6.5.

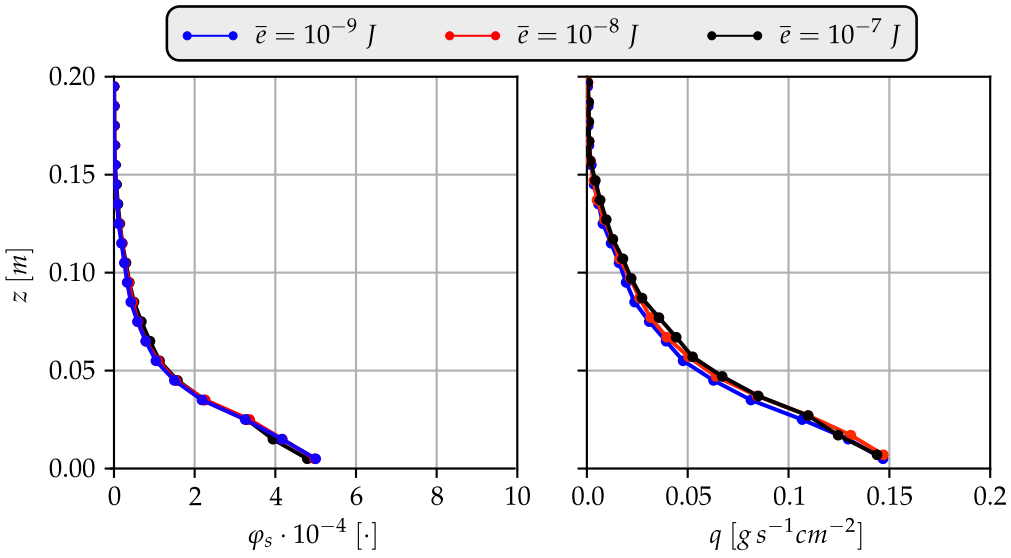

Figure 6.37: Test of the $dModel_2$ setting $e_{inf} = e_{sup} =: \bar{e}$ (see Eq. (6.16)). $\alpha_0^{inf} = 0.2$ and $\alpha_0^{sup} = 0.7$ in accordance to the default parameters.

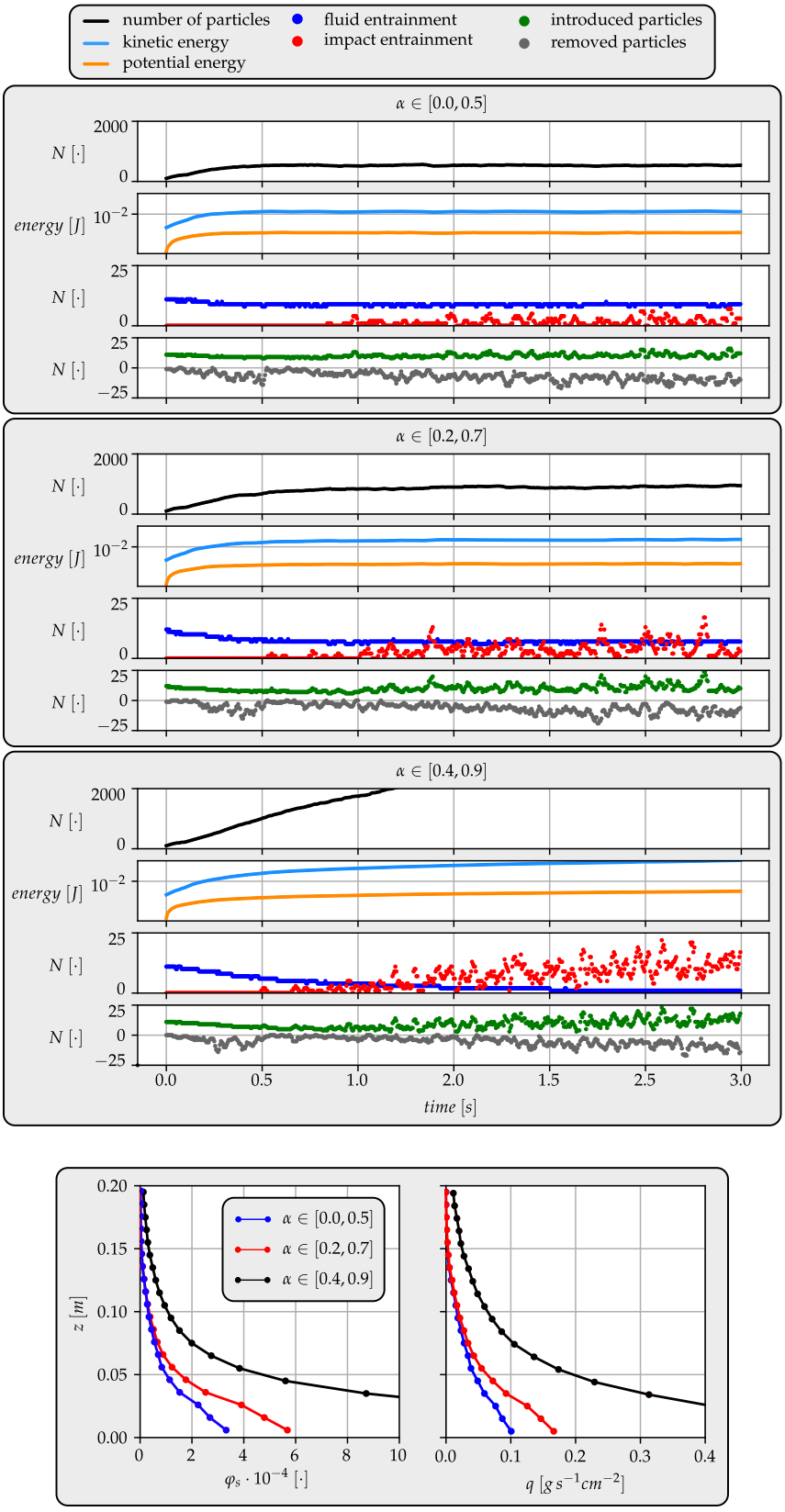

Figure 6.38: Effect of changing α.

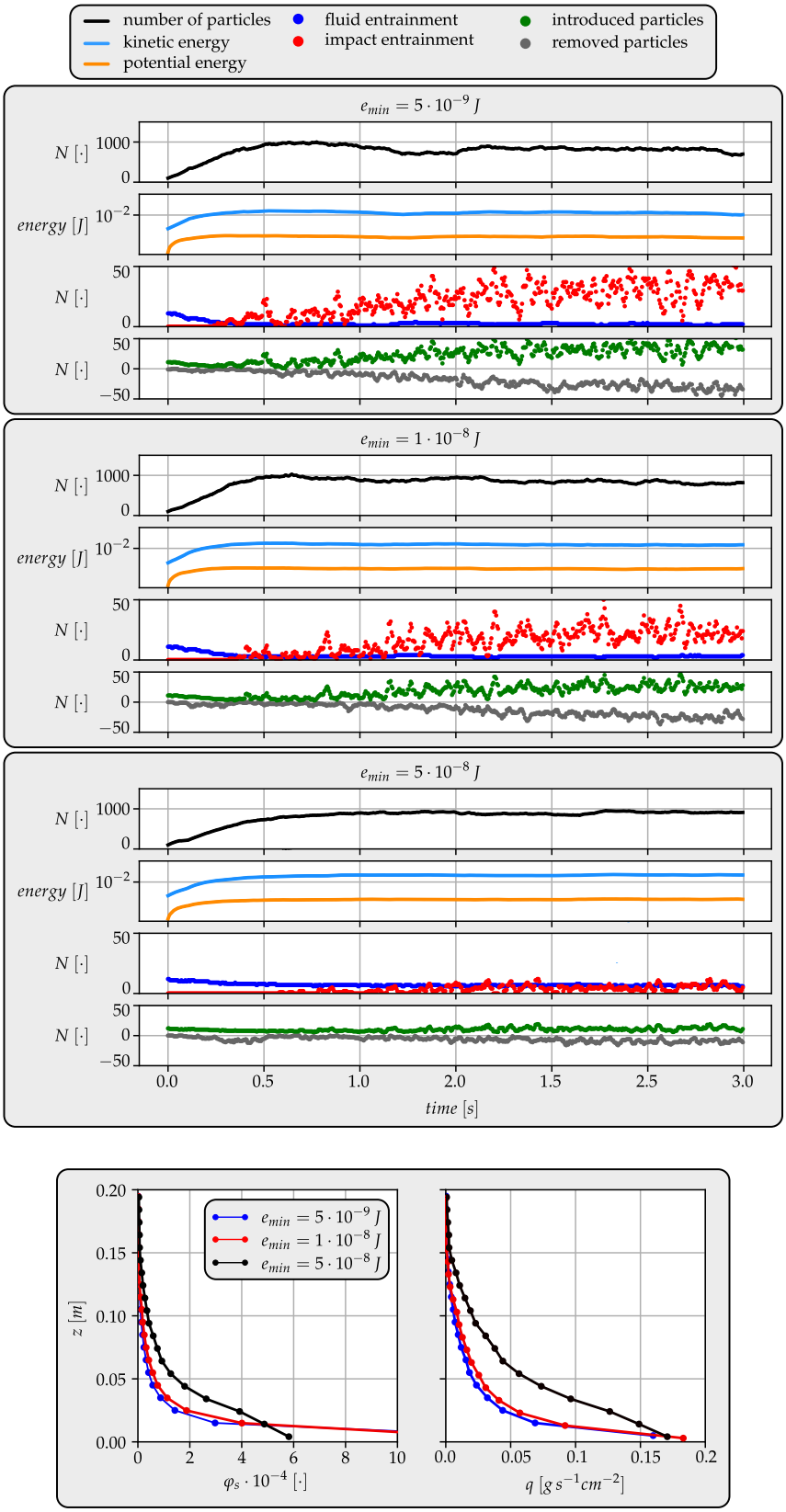

Figure 6.39: Effect of changing e_{min}.

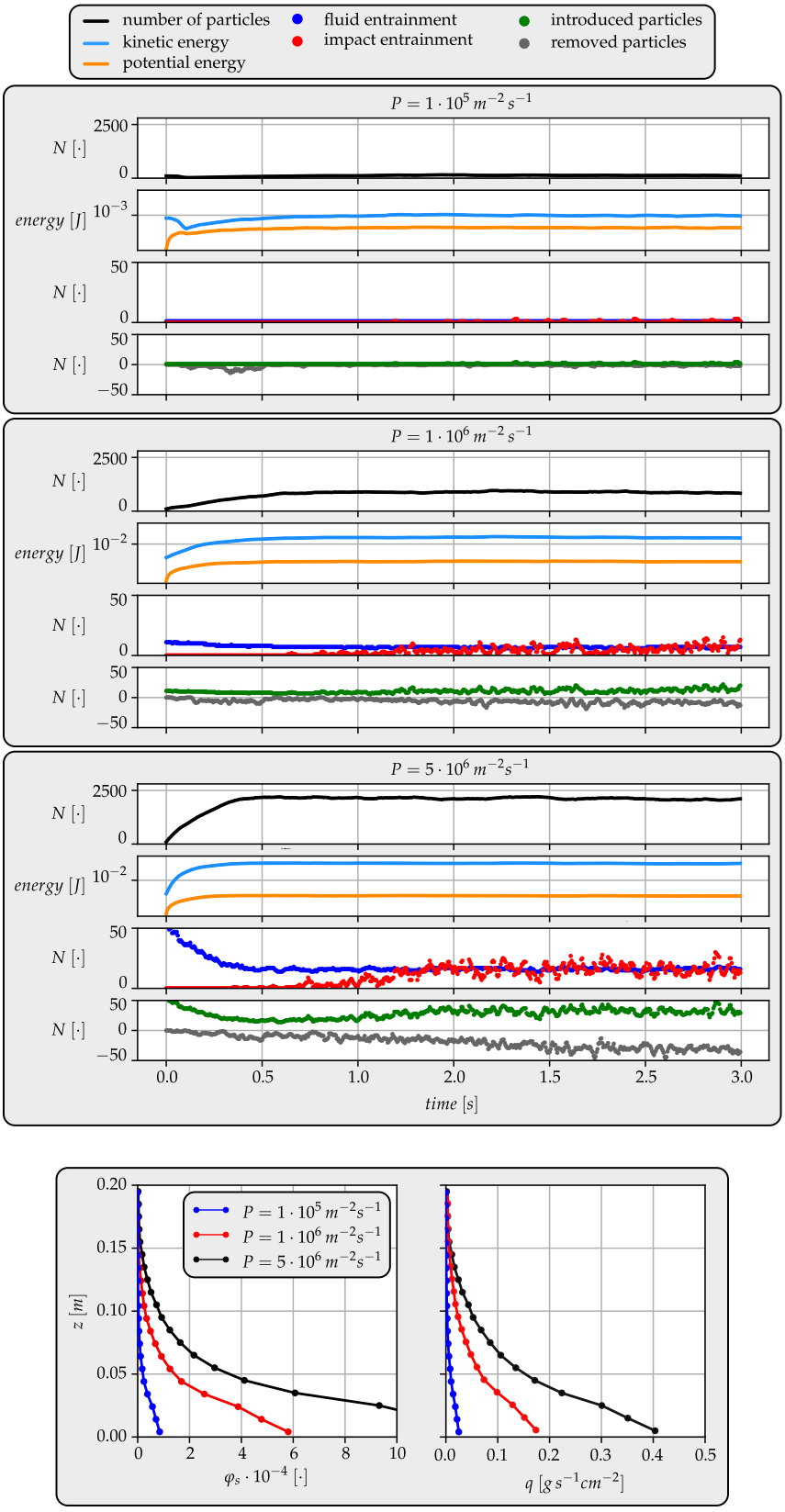

Figure 6.40: Effect of P (see (6.38)) using $dModel_1$.

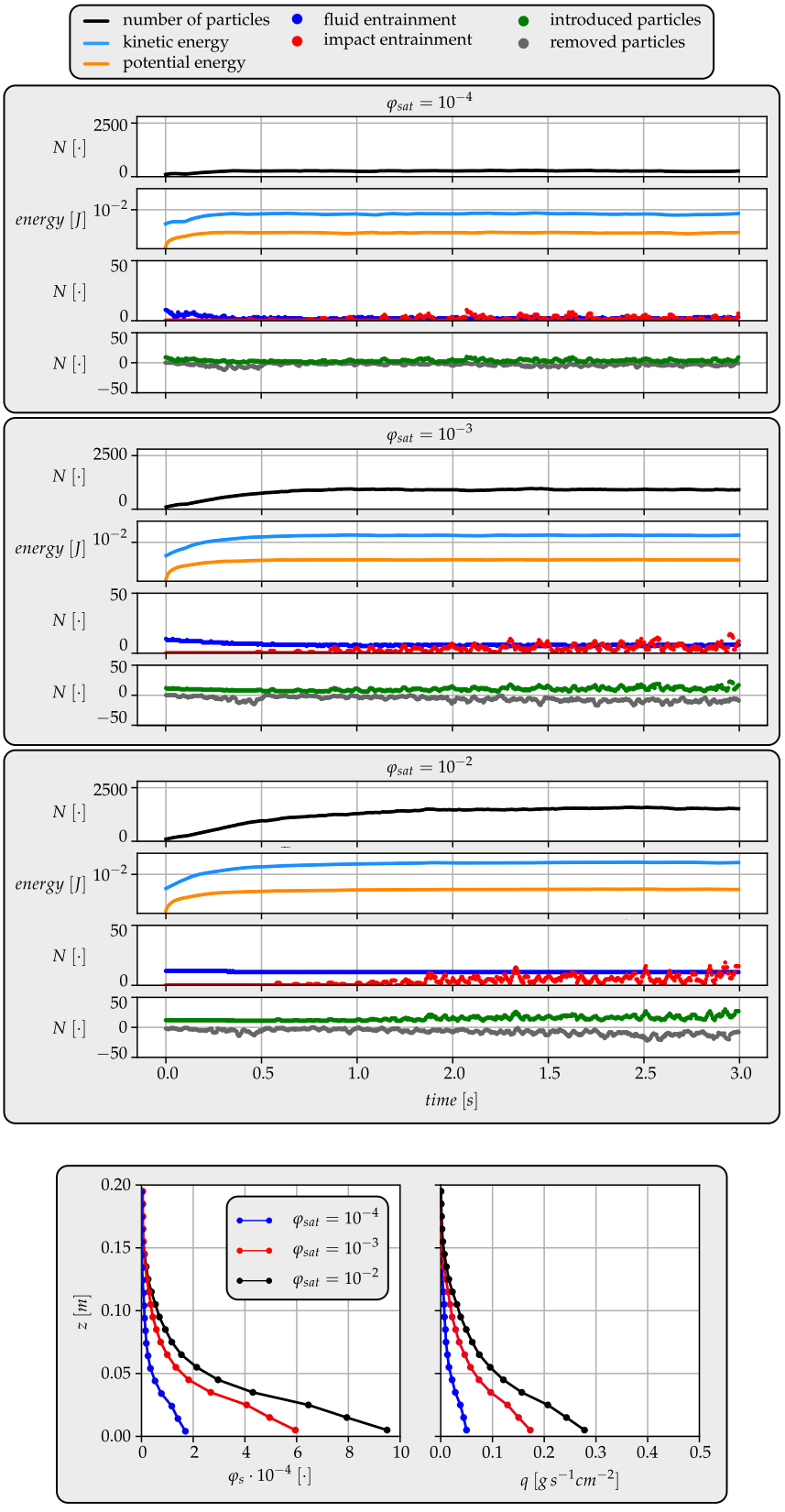

Figure 6.41: Effect of φ_{sat} (see (6.38)) using $dModel_1$.

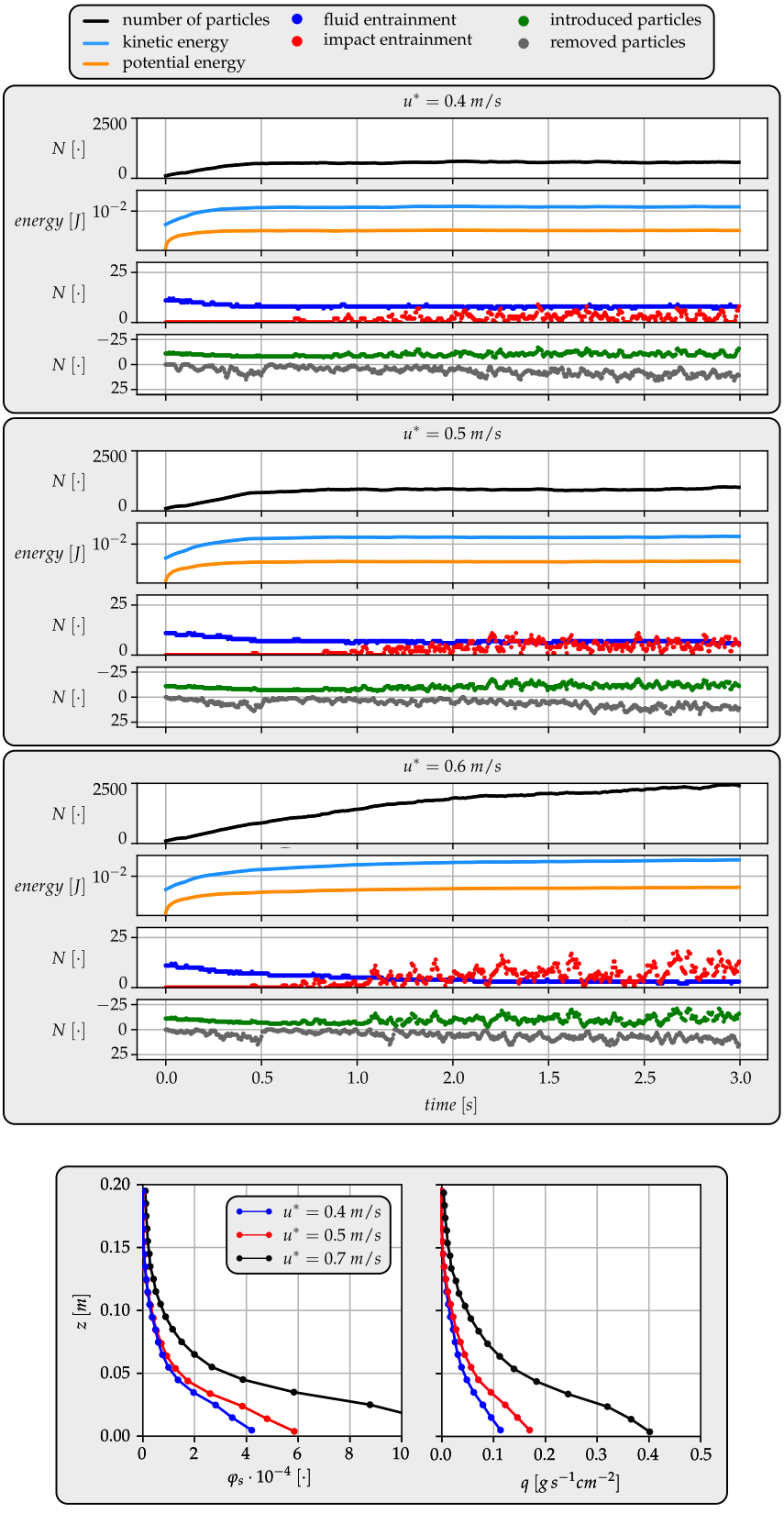

Figure 6.42: Effect of u^*.

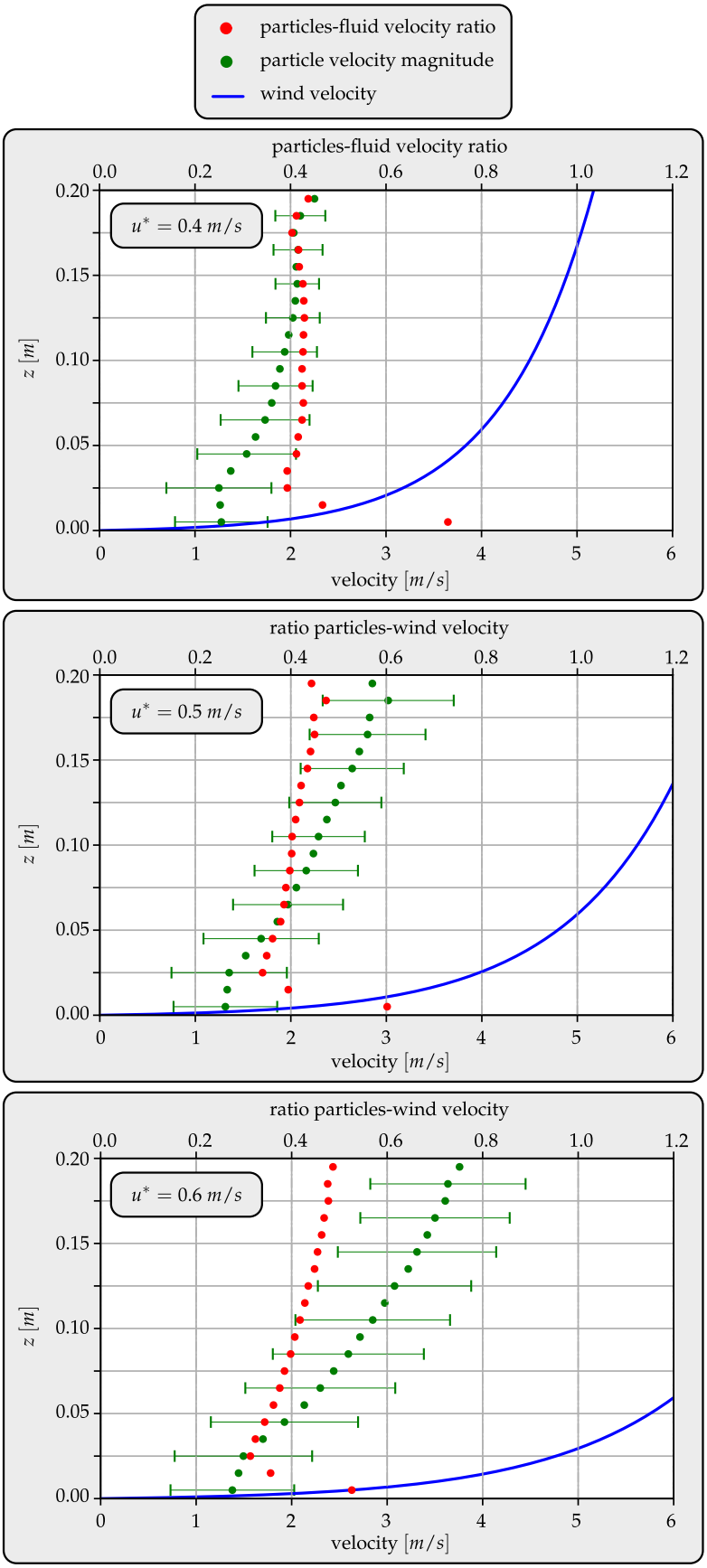

Figure 6.43: Effect of u^* on particles velocity.

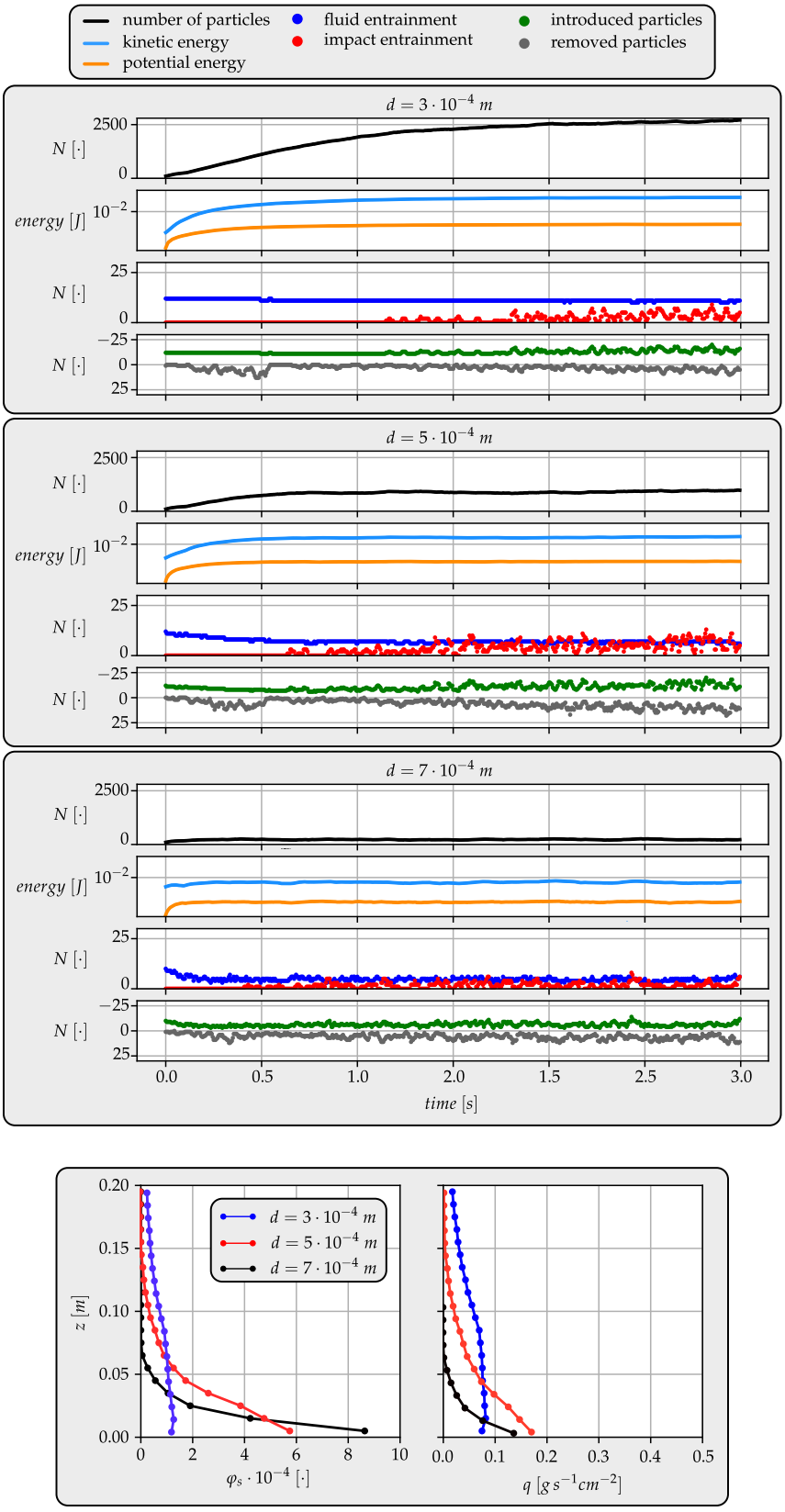

Figure 6.44: Effect of particle diameter.

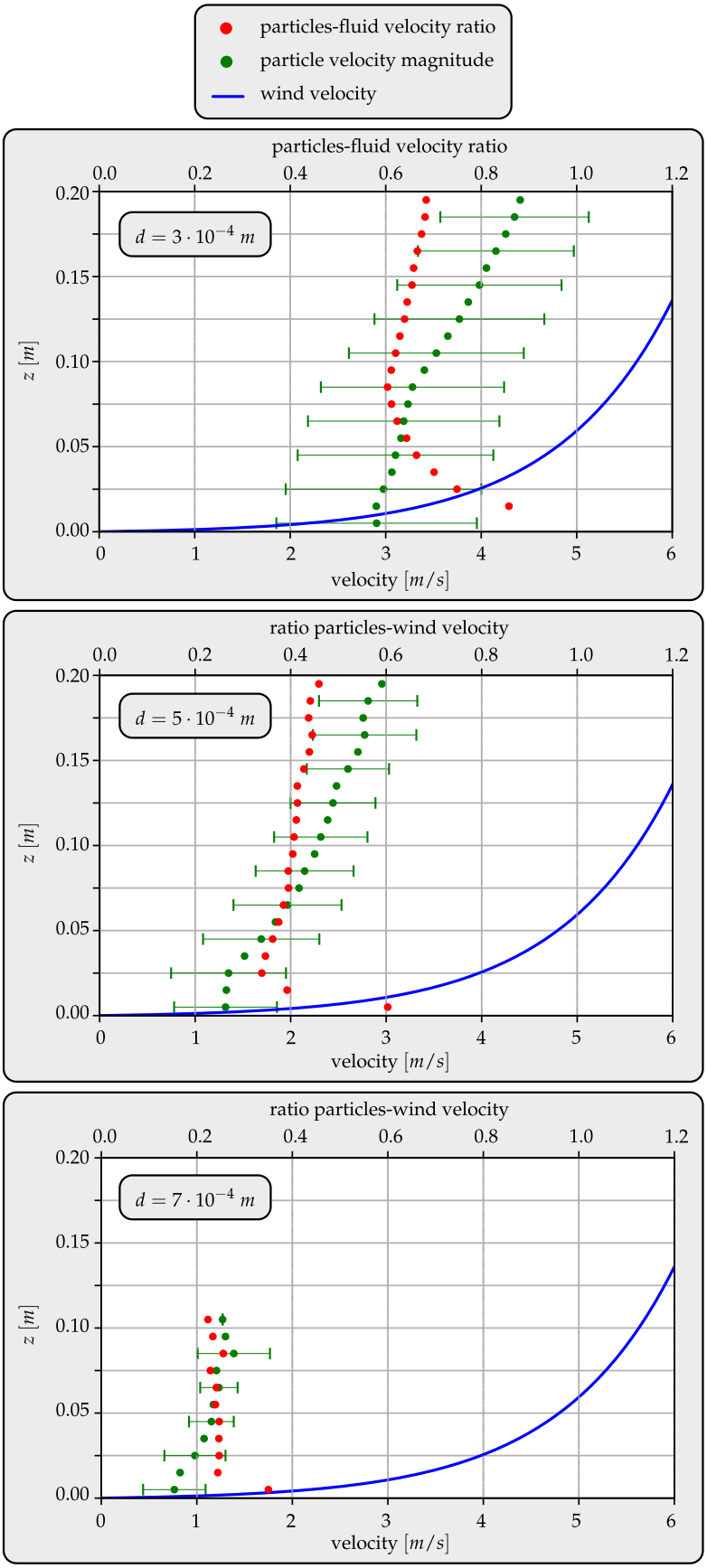

Figure 6.45: Effect of particle diameter.

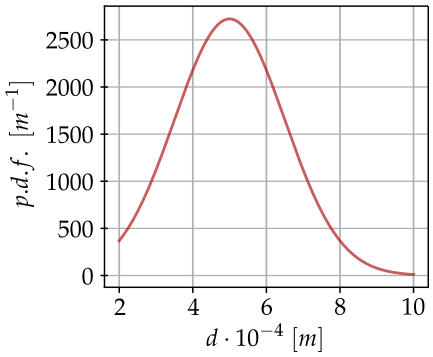

Figure 6.46: Truncated normal distribution in the interval $\left[2 \cdot 10^{-4}, 1 \cdot 10^{-3}\right]$ and mean $5 \cdot 10^{-4}$.

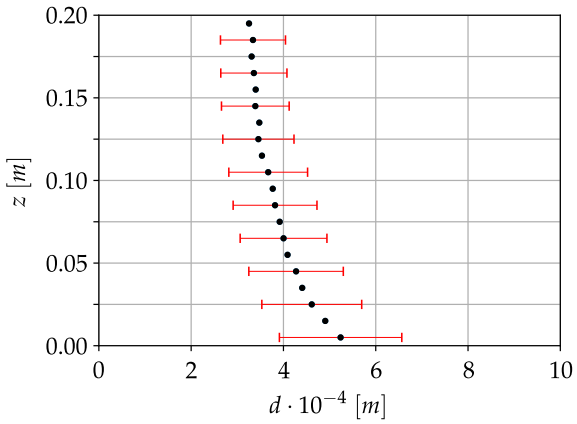

Figure 6.47: The mean and standard deviation of particles diameter distribution as a function of height from the ground.

6.4.2 Simulations in the Polidisperse Case

Our model is capable to treat the polidisperse case natively. In fact, one of the main purpose of the model is to explore the differences between different types of sand. For example we can study the behavior of a mix of sands and verify the truthfulness of the Eulerian polidisperse model presented in Section 5.5. We consider a sand characterized by the truncated normal distribution showed in figure 6.46. As a comparison we consider a monodisperce case where $\langle d \rangle = 5 \cdot 10^{-4}$. The rest of parameters are set as default values of Table 6.5. Figure 6.47 shows the mean and standard deviation of the particles diameter with respect to z direction. Larger diameters are confined near the ground, instead small particles can reach higher heights. This is in accordance with the observations on trajectories presented at the beginning of this Chapter. Figure 6.48 shows the particles concentration and flux in both the polidisperce and monodisperce cases. We can notice that the particles concentration of the polidisperse case is clearly weighted by the probability density function of the diameter. Figure 6.49 shows the particles velocity, the air velocity and their ratio both in the polidisperse and monodisperse case. We can notice that in the polidisperse case the standard deviation for the particles velocity is wider that the monodisperse case. This is probably due to the presence of particles with several sizes reacting very differently to the flow field.

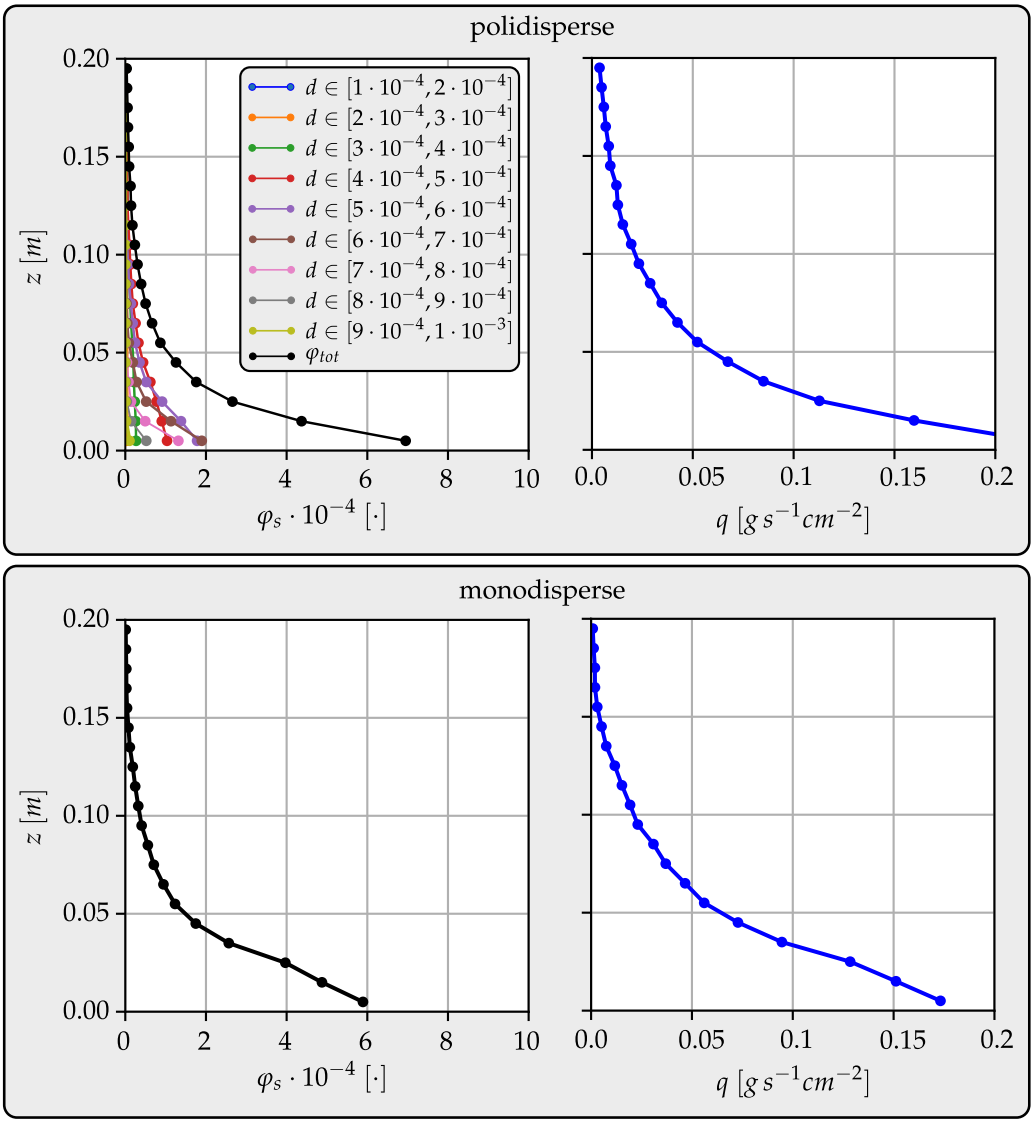

Figure 6.48: Solid volume concentration φ_s and mass flux. The top row refers to the polidisperse case with 6.46. The bottom row refers to the monodisperse case with $d = 5 \cdot 10^{-4}\,m$.

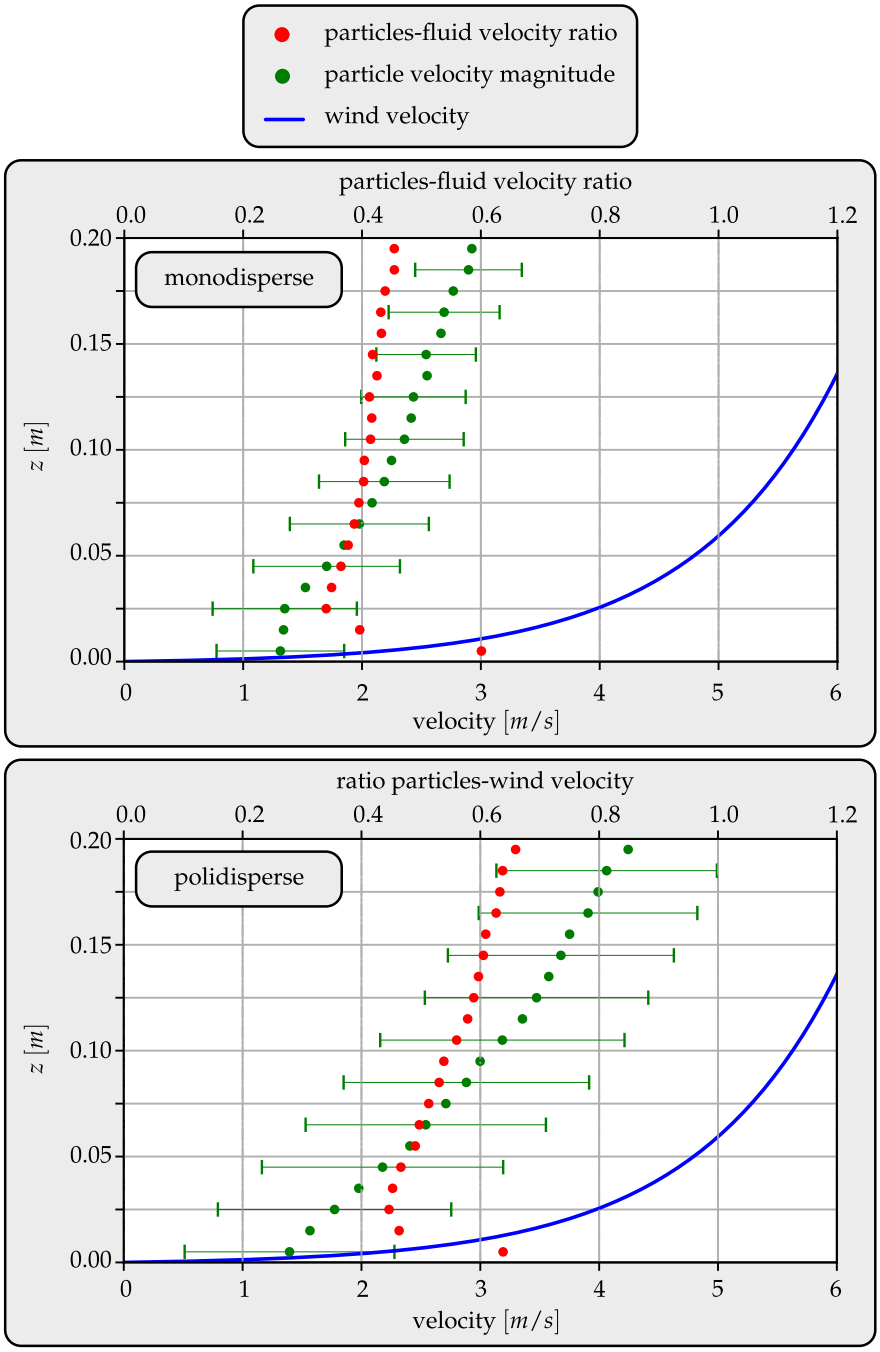

Figure 6.49: Particle velocity comparison between monodisperse and polidisperse case.

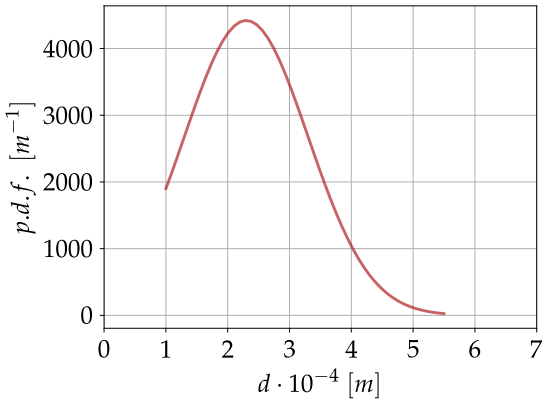

Figure 6.50: Approximation via the truncated normal distribution of the diameter probability density function presented in [122]. The mean value is 0.23 mm and extrema values are 0.1 mm and 0.55mm.

6.4.3 Comparison with Kang's experimental setup

We want to test the model in a wind tunnel setup. In Section 5.4.1 we reported some references to be used as data source for the derivation of the *First Order Model*. In [122] the authors provide the probability density function of the diameter, particles velocity and the distribution of the mean diameter over the saltation layer, solid concentration and mass flux. Therefore, we have multiple metrics to evaluate the algorithm efficacy in a polidisperse condition. Unfortunately, the air flow characterization is poor because only u^* and the free stream velocity is provided. No other info on the air velocity profile is given. Consequently, the numerical results can suffer from this uncertainty. This is also the reason why we discarded the usage of this article in the data-driven deduction of *First Order Model* parameters.

In this test we consider the case where the mean diameter is 0.23 mm and u^* is 0.66 m/s and the other parameters are set as the polidisperse case presented in the previous Section. Figure 6.50 shows the probability density function of the diameter as a truncated normal distribution used for the numerical test. Figure 6.51 show the comparison between numerical results and measurements for the solid concentration and mass flux. The matching for the concentration is quite good. Instead, the mass flux result less accurate in the first centimeter. However, in the very few millimeters measurements are usually not very reliable and values can considerably change with the measurement technique. We can also observe that the first three dots almost have the same coordinate z which is quite suspicious. Figure 6.53 shows mean diameter distribution over z. Also in this case the numerical result match as the available experimental data. Figure 6.52 shows the components of particles velocity together with the wind velocity profiles. We can notice a good match between the experimental data and the numerical result. In the figure the particles velocity is very sparse (see the errorbar in the figure i.e. the standard deviation), but the mean values match the experimental data. Unfortunately, in [122] the are no statistical characterization of measured quantities. The overall accuracy of the *Semi-Stochastic Periodic Box* results are very satisfactory to be in a preliminary stage. In particular for the particles velocity which is relevant

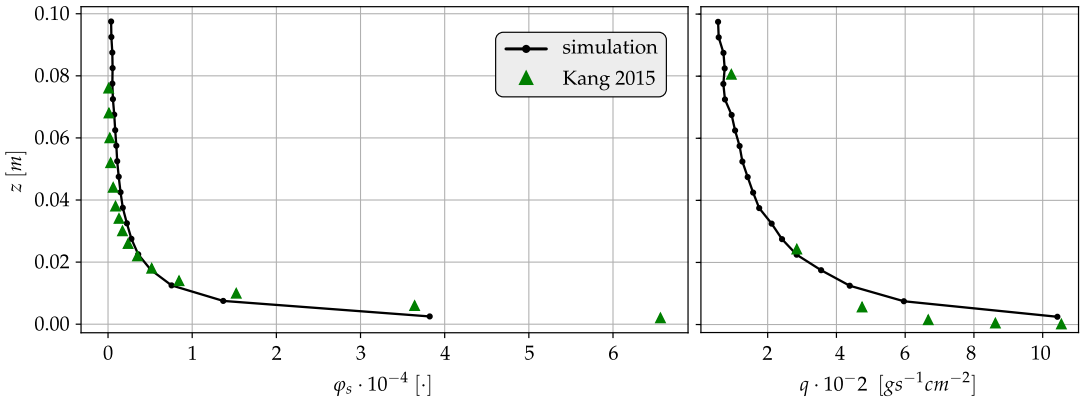

Figure 6.51: Comparison between the measurements in [122] and our numerical tests for the solid concentration and mass flux.

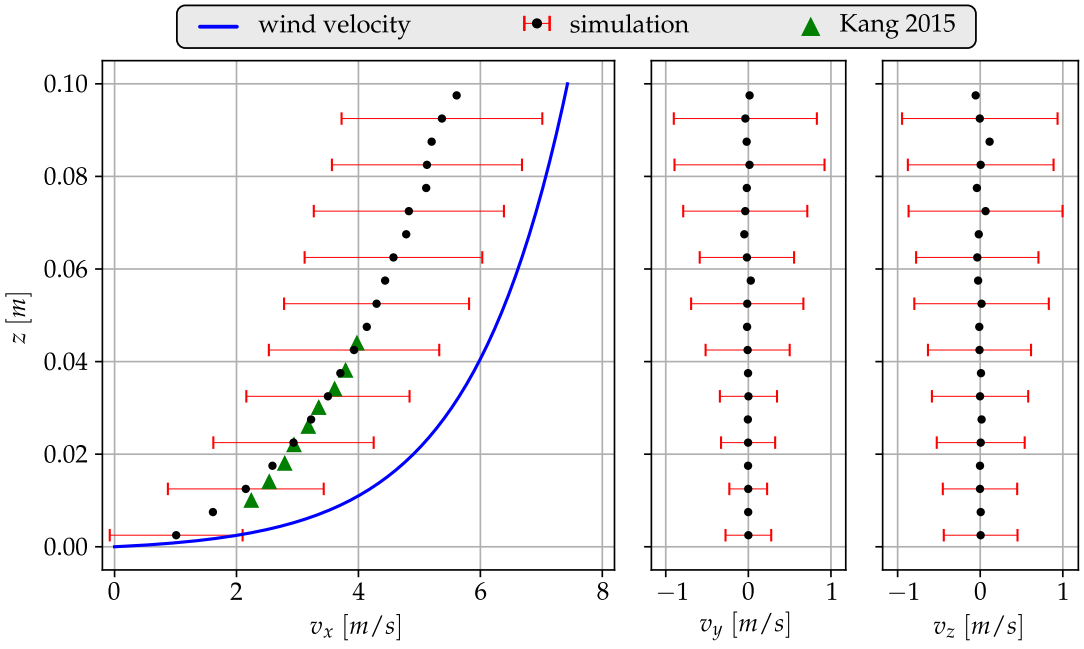

Figure 6.52: Mean and standard deviation of the particles velocity components. Experimental data from [122] only show x component of the particles vector velocity.

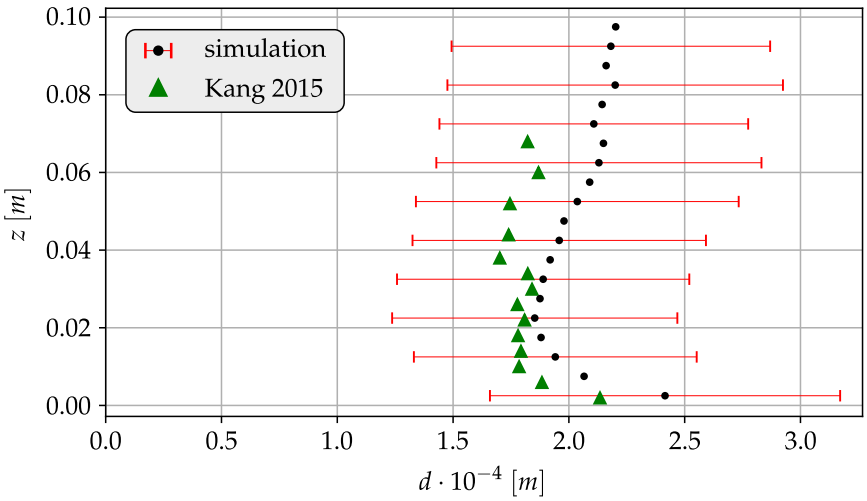

Figure 6.53: Comparison of measurements and numerical results (with standard deviation) of the mean diameter over z.

Chapter 7

Conclusion and Future Perspectives

The dissertation deals with mathematical and physical modeling aspects of aeolian sand transport. In particular, in accordance with the industrial character of the *SMaRT* project the topic is focused on the aeolian sand transport in large domains and on the interaction of sand with complex structures. The computational framework of the Eulerian solvers is based on the *OpenFOAM* platform, a set of finite volume based open-source APIs written in *C++* using high performance libraries for parallel computing.

In Chapter 2 we have summarized the foundational aspects of the continuum-like multiphase modeling. Furthermore, the Granular Kinetic Theory is recalled as example of closure model. We also highlighted some numerical issues in the solution of the two-phases approach with two momentum equations. In Chapter 3 the state of the art of fully Eulerian and Eulerian-Lagrangian models has been reviewed in order to find out deficiencies and relevant aspects of available models in literature. In Chapter 4 we have presented different closures of degenerate parabolic sliding models (DPSMs) to describe the morphology and evolution of sand piles studying similarities and differences. It is shown that DPSMs are reliable for many realistic situations characterized by negligible inertial effects and without massive motions of the granular material. The choice of the closure model is not crucial for the final configuration but affects the temporal evolution and the numerical convergence speed.

Fully Eulerian models are reasonably the best candidate class of models to be used in the simulation of sand transport in large domains. The main difficulties are represented by the complex analytical treatment of modeling terms and numerical methods for the model solutions. The classification of Eulerian models is related to the number of momentum equations for the particle constituent in the mathematical system. The *First Order Model* class consists of one momentum equation for air and all mass conservation equations for the constituents (plus the turbulence model). Chapter 5 described a procedure to define a convective-diffusive formulation with respect to the chosen turbulence model used to describe the dynamic of fluids. In order to insert the dynamics of sand grains the theory of mixtures (recalled in Chapter 2) is used. Also, a data-driven approach is integrated in the argument in order to properly evaluate the model coefficients. Its formulation allows to increase model accuracy once wind tunnel data or computational results from Lagrangian models increase in quantity and quality. The algorithm is designed with a modular

approach. Therefore, it can be easily modified to be used for other particles transport phenomena. We also proposed a polidisperse extension of the *First Order Model*.

A fundamental aspect in the correct model formulation regards surface morphing due to erosion and deposition patterns over time. In order to deal with this modeling aspect the sand surface description is discussed in Chapter 4 and integrated in the equations solver. However, this detail can be neglected for most industrial applications because the surface morphing velocity is globally very slow. Therefore, for industrial applications, it might be more effective to use a steady solution of the *First Order Model* and approximate surface morphing with a steady erosion/deposition surface field. Furthermore, from the pure numerical and computational point of view, the mesh moving has a monumental cost if compared with the other algorithm operations, and it is tricky to deal with. Hence whenever possible, steady simulations are preferred.

Some second order formulations were considered from literature models. However, it turns out that the model complexity and the computational cost to solve a two-momentum system of equations drastically decrease the efficiency and the accuracy of solution. Hence, they result not very interesting for the industrial perspective. Furthermore, similarly to the first order formulation the model validation becomes very difficult because of the lack of experimental data of additional quantities required in the second order formulation.

Despite these difficulties the study has determined some possible ways to model and simulate the sand transport phenomenon in different contexts. In particular, important pendant problems emerged and a clear overview of the problem allowed to plan a roadmap to face mathematical, numerical, physical and experimental issues. Thanks to this, right strategies can be defined for further developments. Some examples of studies that could be useful in the research flow are the following:

- embeding more accurate turbulence models such as LES or DES,
- designing tailored wind tunnel experiments in order to increase data quality. In particular, to measure the rate of erosion and deposition over time changing the wind conditions,
- considering a fixed grid formulation with an automatic three-dimensional refinement algorithm. This would allow to optimize computational resources in domain regions where Eulerian fields present high gradients,
- considering other numerical methods than finite volumes for the solution of partial differential equations and eventually to be able to describe interfaces with VOF-like approach,
- creating a reliable database of numerical solutions or experimental samplings in order to possibly apply reduced order approaches.

Finally in Chapter 6 the *Semi-Stochastic Lagrangian Box* is described with the purpose of exploring fundamental physical properties of particle transport at small scales. Its computational implementation has been done from scratch in *python-3* using basic libraries for scientific computing. The computational cost drastically reduces with respect to classical DEM solver by means of smart allocation of dynamic

lists in memory. Beside pure computational aspects, the main advantage of the approach consists in avoiding to solve directly Navier-Stokes equations and in treating the turbulence without the hassle of dealing with a divergence free fluctuating velocity field. The model also embed stochastic sub-models in order to describe the randomness associated to part of the collisional process. From the industrial perspective this model is not interesting, but it might be a fundamental scientific tool in the development of fully Eulerian models. Despite it is still in a prelimiary development stage, the numerical outputs show its efficacy. It results very modular and easily upgradable for future developments. A list of feasible developments are the following:

- implementing mid-air collisions,
- introducing the effect of a turbulence spectrum on the particles motion,
- introducing the effect of the particles drag on the velocity equilibrium profile of air. In particular, a momentum equation might be solved to compute the perturbation to apply to the equilibrium profile (e.g. using the perturbation theory),
- introducing the effect of particles on the turbulence spectrum,
- introducing the "ground memory function" presented in Section 5.5.1 modifying run-time the probability density function used for grains diameter,
- introducing a non-flat surface to study the sand transport over ripples using a periodic function,
- introducing rotational effects of particles,
- relaxing the mass conservation hypothesis in order to take into account the grains fragmentation due to collisions (very interesting in geomorphology).

Furthermore, most sub-models in this framework do not require wind tunnel tests to be validated. For this reason we consider the *Semi-Stochastic Lagrangian Box* a very promising tool for the study of particulate transport, not only for sand transport in air, but also in other contexts (e.g. sand in water or snow in air).

In conclusion, aeolian sand transport still appears a hard phenomenon to be described. In spite of that, taking into account new technologies and methods on experimental data sampling together with future computational capabilities, the computational and modeling infrastructure developed in this thesis has the potential to produce good results.

Bibliography

[1] M. O. Abadie and N. Mendes. "Numerical assessment of turbulence effect on the evaluation of wind-driven rain specific catch ratio". In: *International Communications in Heat and Mass Transfer* 35.10 (2008), pp. 1253–1261.

[2] S. Alhajraf. "Numerical simulation of drifting sand". PhD Thesis. Cranfield University, 2000.

[3] S. Alhajraf and P. Rubini. "Three-dimensional homogeneous two-phase flow modelling of drifting sand around an open gate". In: *WIT Trans Eng Sci* 30 (2001), pp. 309–325.

[4] R. S. Anderson and P. K. Haff. "Simulation of eolian saltation". In: *Science* 241.4867 (1988), pp. 820–823.

[5] R. S. Anderson and B. Hallet. "Sediment transport by wind: toward a general model". In: *Geol Society Am Bull* 97.5 (1986), pp. 523–535.

[6] B. Andreotti. "A two-species model of aeolian sand transport". In: *Journal of Fluid Mechanics* 510 (2004), pp. 47–70.

[7] B. Andreotti, P. Claudin, and S. Douady. "Selection of dune shapes and velocities Part 1: Dynamics of sand, wind and barchans". In: *Eur Phys J B* 28.3 (2002), pp. 321–339.

[8] B. Andreotti, P. Claudin, and S. Douady. "Selection of dune shapes and velocities Part 2: A two-dimensional modelling". In: *Eur Phys J B* 28.3 (2002), pp. 341–352.

[9] M. J. Andrews and P. J. O'rourke. "The multiphase particle-in-cell (MP-PIC) method for dense particulate flows". In: *Int J Multiph Flow* 22.2 (1996), pp. 379–402.

[10] A. Aradian, E. Raphaël, and P. G. de Gennes. "Surface flows of granular materials: a short introduction to some recent models". In: *C.R. Phys.* 3.2 (2002), pp. 187–196.

[11] H. Arastoopour, P. Pakdel, and M. Adewumi. "Hydrodynamic analysis of dilute gas-solids flow in a vertical pipe". In: *Powder Technol* 62.2 (1990), pp. 163–170.

[12] G. Aronsson, L. C. Evans, and Y. Wu. "Fast-slow diffusion and growing sandpiles". In: *SIAM J. Appl. Math.* 131 (1996), pp. 304–335.

[13] R. J. Atkin and R. E. Craine. "Continuum theories of mixtures: applications". In: *IMA Journal of Applied Mathematics* 17.2 (1976), pp. 153–207.

[14] R. J. Atkin and R. E. Craine. "Continuum theories of mixtures: basic theory and historical development". In: *The Quarterly Journal of Mechanics and Applied Mathematics* 29.2 (1976), pp. 209–244.

[15] G. Bagheri and C. Bonadonna. "On the drag of freely falling non-spherical particles". In: *Powder Technology* 301 (2016), pp. 526–544.

[16] R. A. Bagnold. *The physics of blown sand and desert dunes*. Methuen & Company, 1941.

[17] S. Balachandar and J. K. Eaton. "Turbulent Dispersed Multiphase Flow". In: *Annual Review of Fluid Mechanics* 42.1 (Dec. 2009), pp. 111–133.

[18] N. J. Balmforth and R. R. Kerswell. "Granular collapse in two dimensions". In: *Journal of Fluid Mechanics* 538 (2005), p. 399.

[19] B. Bang et al. "Computer simulation of wind speed, wind pressure and snow accumulation around buildings (SNOW-SIM)". In: *Energ Buildings* 21 (1994), pp. 235–243.

[20] E. Barnea and J. Mizrahi. "A generalized approach to the fluid dynamics of particulate systems: Part 1. General correlation for fluidization and sedimentation in solid multiparticle systems". In: *Chem Eng J* 5.2 (Jan. 1973), pp. 171–189.

[21] A. Bedford and D. S. Drumheller. "Theories of immiscible and structured mixtures". In: *International Journal of Engineering Science* 21.8 (1983), pp. 863–960.

[22] D. Beladjine et al. "Collision process between an incident bead and a three-dimensional granular packing". In: *Physical review. E, Statistical, nonlinear, and soft matter physics* 75 6 Pt 1 (2007), p. 061305.

[23] S. Benyahia, M. Syamlal, and T. J. O'Brien. "Extension of Hill–Koch–Ladd drag correlation over all ranges of Reynolds number and solids volume fraction". In: *Powder Technol* 162.2 (2006), pp. 166–174.

[24] C. M. Bessemoulin and F. Filbet. "A finite volume scheme for nonlinear degenerate parabolic equations". In: *SIAM J. Sci. Comput.* 34.5 (2012), B559–B583.

[25] J. H. M. Beyers and P. A. Sundsbø. "Numerical simulation of three-dimensional, transient snow drifting around a cube". In: *J Wind Eng Ind Aerod* 92.9 (2004), pp. 725–747.

[26] M. Beyers and B. Waechter. "Modeling transient snowdrift development around complex three-dimensional structures". In: *J Wind Eng Ind Aerod* 96.10-11 (2008), pp. 1603–1615.

[27] B. Blocken. "50 years of computational wind engineering: past, present and future". In: *J Wind Eng Ind Aerod* 129 (2014), pp. 69–102.

[28] B. Blocken and J. Carmeliet. "Overview of three state-of-the-art wind-driven rain assessment models and comparison based on model theory". In: *Building and Environment* (2010).

[29] B. Blocken, T. Stathopoulos, and J. Carmeliet. "CFD simulation of the atmospheric boundary layer: wall function problems". In: *Atmos Environ* 41.2 (2007), pp. 238–252.

[30] T. Börzsönyi, T. Halsey, and R. Ecke. "Avalanche dynamics on a rough inclined plane". In: *Phys. Rev. E* 78.1 (2008), p. 011306.

[31] J. P. Bouchaud, M. E. Cates, and J. R. Prakash. "A model for the dynamics of sandpile surfaces". In: *J. Phys. I* 4 (1994), pp. 1383–1410.

[32] J. P. Bouchaud et al. "Hysteresis and metastability in a continuum sandpile model". In: *Phys. Rev. Lett.* 74.11 (1995), pp. 1982–1985.

[33] N. Boulghobra. "Climatic data and satellite imagery for assessing the aeolian sand deposit and barchan migration, as a major risk sources in the region of In-Salah (Central Algerian Sahara)". In: *Arabian J. Geosci.* 9.6 (2016), p. 450.

[34] Z. Boutanios and H. Jasak. "Two-way coupled Eulerian-Eulerian simulations of drifting snow with viscous treatment of the snow phase". In: *J. Wind Eng. Ind. Aerodyn.* 169 (Oct. 2017), pp. 67–76.

[35] T. Boutreux and P. G. de Gennes. "Surface flows of granular mixtures: I. General principles and minimal model". In: *J. Phys. I* 6.10 (1996), pp. 1295–1304.

[36] T. Boutreux, E. Raphaël, and P. G. de Gennes. "Surface flows of granular materials: a modified picture for thick avalanches". In: *Phys. Rev. E* 58 (1998), pp. 4692–4700.

[37] R. M. Bowen. "A theory of constrained mixtures with multiple temperatures". In: *ArRMA* 70.3 (1979), pp. 235–250.

[38] R. M. Bowen. "Incompressible porous media models by use of the theory of mixtures". In: *International Journal of Engineering Science* 18.9 (1980), pp. 1129–1148.

[39] R. M. Bowen. *Theory of mixtures in continuum physics*. Vol. 3. Academic Press New York, 1976.

[40] M. Bretz et al. "Imaging of avalanches in granular materials". In: *Phys. Rev. Lett.* 69 (1992), p. 2431.

[41] P. P. Brown and D. F. Lawler. "Sphere Drag and Settling Velocity Revisited". In: *Journal of Environmental Engineering* 129.3 (2003), pp. 222–231.

[42] J. A. Businger et al. "Flux profile relationships in the atmospheric surface layer". In: *J Atmos Sci* 28 (1971), pp. 181–189.

[43] P. Cannarsa and P. Cardaliaguet. "Representation of equilibrium solutions to the table problem of growing sandpiles". In: *J. Eur. Math. Soc.* 6 (2004), pp. 1–30.

[44] P. Cannarsa, P. Cardaliaguet, and G. Crasta. "A boundary value problem for a PDE model in mass transfer theory: representation of solutions and applications". In: *Calc. Var.* 24.4 (2005), pp. 431–457.

[45] P. Cannarsa, P. Cardaliaguet, and C. Sinestrari. "On a differential model for growing sandpiles with non-regular sources". In: *Comm. Partial Diff. Eqs.* 34.7 (2009), pp. 656–675.

[46] C. Canuto and A. Lo Giudice. "A multi-timestep Robin-Robin domain decomposition method for time dependent advection-diffusion problems". In: *App Math Comput* (under review) (2018).

[47] S. Chapman and T. G. Cowling. *The Mathematical Theory of Non-uniform Gases*. Cambridge Mathematical Library, 1970.

[48] S. Chapman, T. G. Cowling, and D. Burnett. *The mathematical theory of non-uniform gases*. Cambridge university press, 1990.

[49] C. P. Chen and P. E. Wood. "A urbulence closure model for dilute gas particle flows". In: *Can J Chem Eng* 63.3 (1985), pp. 349–360.

[50] Z. Cheng, T. J. Hsu, and J. Calantoni. "SedFoam: A multi-dimensional Eulerian two-phase model for sediment transport and its application to momentary bed failure". In: *Coastal Engineering* 119 (2017), pp. 32–50.

[51] R. P. Chhabra and J. F. Richardson. *Non-Newtonian Flow in the Process Industry: Fundamentals and Engineering Applications*. Elsevier, 1999.

[52] E. C. C. Choi. "Numerical modelling of gust effect on wind-driven rain". In: *J Wind Eng Ind Aerod* 72 (1997), pp. 107–116.

[53] E. C. C. Choi. "Simulation of wind-driven-rain around a building". In: *Wind Engineers, JAWE* 1992.52 (1992), pp. 60–65.

[54] S. C. Colbeck. "Air Movement in Snow Due to Windpumping". In: *Journal of Glaciology* 35.120 (1989), pp. 209–213.

[55] R. M. Colombo, G. Guerra, and F. Monti. "Modelling the dynamics of granular matter". In: *IMA J. Appl. Math.* 77.2 (Apr. 2012), pp. 140–156.

[56] J. Crassous, D. Beladjine, and A. Valance. "Impact of a projectile on a granular medium described by a collision model". In: *Physical review letters* 99 24 (2007), p. 248001.

[57] G. Crasta and S. Finzi Vita. "An existence result for the sandpile problem on flat tables with walls". In: *Netw. Heterog. Media* 3 (2008), pp. 815–830.

[58] M. Creyssels et al. "Saltating particles in a turbulent boundary layer: experiment and theory". In: *J. Fluid Mech.* 625 (Apr. 2009), pp. 47–74.

[59] M. J. Crochet and P. M. Naghdi. "On constitutive equations for flow of fluid through an elastic solid". In: *International Journal of Engineering Science* 4.4 (1966), pp. 383–401.

[60] F. Dai and K. R. Rajagopal. "Diffusion of fluids through transversely isotropic solids". In: *Acta mechanica* 82.1-2 (1990), pp. 61–98.

[61] N. G. Deen et al. "Review of discrete particle modeling of fluidized beds". In: *Chem Eng Sci* 62.1 (2007), pp. 28–44.

[62] R. Di Felice. "The voidage function for fluid-particle interaction systems". In: *Int J Multiph Flow* 20.1 (1994), pp. 153–159.

[63] Z. Dong et al. "Aeolian sand transport: A wind tunnel model". In: *Sedimentary Geology* 161.1-2 (2003), pp. 71–83.

[64] Z. Dong et al. "Analysis of the mass flux profiles of an aeolian saltating cloud". In: *J. Geophys. Res. Atmos.* 111.D16 (Aug. 2006).

[65] Z. Dong et al. "Experimental investigation of the velocity of a sand cloud blowing over a sandy surface". In: *Earth Surface Processes and Landforms* 29.3 (2004), pp. 343–358.

[66] Z. Dong et al. "Height profile of particle concentration in an aeolian saltating cloud: A wind tunnel investigation by PIV MSD". In: *Geophysical Research Letters* 30.19 (2003).

[67] Z. Dong et al. "Velocity profile of a sand cloud blowing over a gravel surface". In: *Geomorphology* 45.3-4 (2002), pp. 277–289.

[68] S Douady, B Andreotti, and A Daerr. "On granular surface flow equations". In: *Eur. Phys. J. B* 11 (1999), pp. 131–142.

[69] D. A. Drew. "Mathematical modeling of two-phase flow". In: *Annual review of fluid mechanics* 15.1 (1983), pp. 261–291.

[70] D. A. Drew and S. L. Passman. *Theory of multicomponent fluids*. Vol. 135. Springer Science & Business Media, 2006.

[71] O. Durán, E. J. R. Parteli, and H. J. Herrmann. "A continuous model for sand dunes: Review, new developments and application to barchan dunes and barchan dune fields". In: *Earth Surf. Process. Landf.* 35.13 (2010), pp. 1591–1600.

[72] J. Dyer. "A review of flux profile relationships". In: *Boundary-Layer Meteorology* 7 (1974), pp. 363–372.

[73] S. Elghobashi. "On predicting particle-laden turbulent flows". In: *Appl Sci Res* 52.4 (1994), pp. 309–329.

[74] S. Elghobashi. "Particle-laden turbulent flows: direct simulation and closure models". In: *Computational fluid Dynamics for the Petrochemical Process Industry*. Springer, 1991, pp. 91–104.

[75] S. Ergun. "Fluid flow through packed columns". In: *Chem. Eng. Prog.* 48 (1952), pp. 89–94.

[76] R. Eymard, T. Gallouët, and R. Herbin. "Finite volume methods". In: *Handbook of numerical analysis* 7 (2000), pp. 713–1018.

[77] R. Eymard et al. "Convergence of a finite volume scheme for nonlinear degenerate parabolic equations". In: *Numer. Math.* 92.1 (2002), pp. 41–82.

[78] T. E. Faber. *Fluid Dynamics for Physicists*. Cambridge University Press, 1995.

[79] M. Falcone and S. Finzi Vita. "A finite-difference approximation of a two-layer system for growing sandpiles". In: *SIAM J. Sci. Comput.* 28 (2006), pp. 1120–1132.

[80] M. Falcone and S. Finzi Vita. "A numerical study for growing sandpiles on flat tables with walls". In: *IFIP Conference on System Modeling and Optimization* 202 (2005), pp. 127–137.

[81] M. Falcone and S. Finzi Vita. "A Semi-Lagrangian Scheme for the Open Table Problem in Granular Matter Theory". In: *Numerical Mathematics and Advanced Applications*. Ed. by K Kunisch, G Of, and O Steinbach. Springer, 2008, pp. 711–718.

[82] T. M. Farabee and M. J. Casarella. "Spectral features of wall pressure fluctuations beneath turbulent boundary layers". In: *Physics of Fluids A: Fluid Dynamics* 3.10 (Oct. 1991), pp. 2410–2420.

[83] A. B. Farimani, A. D. Ferreira, and A. C. M. Sousa. "Computational modeling of the wind erosion on a sinusoidal pile using a moving boundary method". In: *Geomorphology* 130.3-4 (2011), pp. 299–311.

[84] M. V. Gandhi, K. R. Rajagopal, and A. S. Wineman. "Some nonlinear diffusion problems within the context of the theory of interacting continua". In: *International journal of engineering science* 25.11-12 (1987), pp. 1441–1457.

[85] P. Gauer. "Blowing and drifting snow in alpine terrain: a physically-based numerical model and related field measurements". PhD thesis. ETH Zurich, 1999.

[86] P. G. de Gennes. "Dynamique superficielle d'un matériau granulaire". In: *C. R. Acad. Sci. II* 321.12 (1995), pp. 501–506.

[87] M. Germano et al. "A dynamic subgrid-scale eddy viscosity model". In: *Phys Fluids Fluid Dyn* 3.7 (1991), pp. 1760–1765.

[88] D. Gidaspow. *Multiphase flow and fluidization: continuum and kinetic theory descriptions*. Academic press, 1994.

[89] A. D. Gosman et al. "Multidimensional modeling of turbulent two-phase flows in stirred vessels". In: *AIChE Journal* 38.12 (1992), pp. 1946–1956.

[90] J. Gray. "Granular flow in partially filled slowly rotating drums". In: *J. Fluid Mech.* 441 (2001), pp. 1–29.

[91] A. E. Green and J. E. Adkins. *Large elastic deformations, Clarendon*. 1970.

[92] A. E. Green and P. M. Naghdi. "A dynamical theory of interacting continua". In: *International journal of engineering Science* 3.2 (1965), pp. 231–241.

[93] A. E. Green and P. M. Naghdi. "A note on mixtures". In: *International Journal of Engineering Science* 6.11 (1968), pp. 631–635.

[94] A. E. Green and P. M. Naghdi. "On basic equations for mixtures". In: *The Quarterly Journal of Mechanics and Applied Mathematics* 22.4 (1969), pp. 427–438.

[95] K. P. Hadeler and C. Kuttler. "Dynamical models for granular matter". In: *Granul Matter* 2.1 (1999), pp. 9–18.

[96] K. P. Hadeler and C. Kuttler. "Granular matter in a silo". In: *Granul Matter* 3 (2001), pp. 193–197.

[97] K. P. Hadeler and D. Schieborn. "Granular matter and the time-dependent viscous eikonal equation". In: *Physica D* 241.5 (2012), pp. 616–622.

[98] H. Hangan. "Wind-driven rain studies. A C-FD-E approach". In: *J Wind Eng Ind Aerod* 81.1-3 (1999), pp. 323–331.

[99] K. M. Hartung, P. Gilge, and F. Herbst. "Towards Immersed Boundary Methods For Complex Roughness Structures In Scale-Resolving Simulations." In: *ECMS*. 2018, pp. 359–365.

[100] T. D. Ho et al. "Aeolian sand transport: Length and height distributions of saltation trajectories". In: *Aeolian Res.* 12 (Mar. 2014), pp. 65–74.

[101] T. D. Ho et al. "Particle velocity distribution in saltation transport". In: *Phys. Rev. E* 85.5 (May 2012), p. 052301.

[102] T. D. Ho et al. "Scaling Laws in Aeolian Sand Transport". In: *Phys. Rev. Lett.* 106.9 (Mar. 2011), p. 094501.

[103] C. M. Hrenya and J. L. Sinclair. "Effects of particle-phase turbulence in gas-solid flows". In: *AlChE J.* 43.4 (Apr. 1997), pp. 853–869.

[104] T. J. Hsu, J. T. Jenkins, and P. L. F. Liu. "On two-phase sediment transport: sheet flow of massive particles". In: *Proceedings of the Royal Society of London A: Mathematical, Physical and Engineering Sciences* 460.2048 (Aug. 2004), pp. 2223–2250.

[105] N. Huang, P. He, and J. Zhang. "Large-eddy simulation of sand transport under unsteady wind". In: *Geomorphology* 358 (2020), p. 107105.

[106] S. H. Huang and Q. S. Li. "Large eddy simulations of wind-driven rain on tall building facades". In: *J Struct Eng* 138.8 (2011), pp. 967–983.

[107] S. H. Huang and Q. S. Li. "Numerical simulations of wind-driven rain on building envelopes based on Eulerian multiphase model". In: *J Wind Eng Ind Aerod* 98.12 (2010), pp. 843–857.

[108] S. Huang and Q. S. Li. "A new dynamic one-equation subgrid-scale model for large eddy simulations". In: *International Journal for Numerical Methods in Engineering* 81.7 (2010), pp. 835–865.

[109] J. D. Iversen et al. "Eolian erosion of the Martian surface, part 1: Erosion rate similitude". In: *Icarus* 26.3 (1975), pp. 321–331.

[110] J. Iversen and K. Rasmussen. "The effect of wind speed and bed slope on sand transport". In: *Sedimentology* 46.4 (1999), pp. 723–731.

[111] J. T. Jenkins and D. M. Hanes. "Collisional sheet flows of sediment driven by a turbulent fluid". In: *J. Fluid Mech.* 370 (Sept. 1998), pp. 29–52.

[112] J. T. Jenkins and S. B. Savage. "A theory for the rapid flow of identical, smooth, nearly elastic, spherical particles". In: *J. Fluid Mech.* 130 (May 1983), pp. 187–202.

[113] S. B. Ji, A. G. Gerber, and A. C. M. Sousa. "A convection-diffusion CFD model for aeolian particle transport". In: *Int J Numer Meth Fl* 45.8 (2004), pp. 797–817.

[114] H. Jiang, N. Huang, and Y. Zhu. "Analysis of wind-blown sand movement over transverse dunes". In: *Sci Rep-UK* 4 (2014), p. 7114.

[115] H. Jiang et al. "Sand transportation and reverse patterns over leeward face of sand dune". In: *Geomorphology* 283 (2017), pp. 41–47.

[116] W. P. Jones and B. E. Launder. "The prediction of laminarization with a two-equation model of turbulence". In: *Int J Heat Mass Tran* 15.2 (1972), pp. 301–314.

[117] L. Kang. "Discrete particle model of aeolian sand transport: Comparison of 2D and 2.5 D simulations". In: *Geomorphology* 139 (2012), pp. 536–544.

[118] L. Kang and L. Guo. "Eulerian–Lagrangian simulation of aeolian sand transport". In: *Powder Technol* 162.2 (2006), pp. 111–120.

[119] L. Kang, L. Guo, and D. Liu. "Experimental investigation of particle velocity distributions in windblown sand movement". In: *Science in China Series G: Physics, Mechanics and Astronomy* 51 (2008), pp. 986–1000.

[120] L. Kang and D. Liu. "Numerical investigation of particle velocity distributions in aeolian sand transport". In: *Geomorphology* 115.1-2 (2010), pp. 156–171.

[121] L. Kang and X. Zou. "Vertical distribution of wind–sand interaction forces in aeolian sand transport". In: *Geomorphology* 125.3 (2011), pp. 361–373.

[122] L. Kang et al. "An improved particle counting method for particle volume concentration in aeolian sand transport". In: *Powder Technol.* 280 (Aug. 2015), pp. 191–200.

[123] Th. von Kármán. "Mechanische Aenlichkeit und Turbulenz". In: *Nachrichten von der Gesellschaft der Wissenschaften zu Göttingen, Mathematisch-Physikalische Klasse* 1930 (1930), pp. 58–76.

[124] M. Kato and . Launder. "The modeling of turbulent flow around stationary and vibratingsquare cylinders". In: *Ninth Symp on Turbulent Shear Flows*. Vol. 10–4. American Society of Mechanical Engineers. 1993, pp. 1–6.

[125] E. Kermani, T. Qiu, and T. Li. "Simulation of collapse of granular columns using the discrete element method". In: *International Journal of Geomechanics* 15.6 (2015), p. 04015004.

[126] D. V. Khakhar et al. "Surface flow of granular materials: Model and experiments in heap formation". In: *J. Fluid Mech.* 441 (2001), pp. 255–264.

[127] H. Kobayashi. "The subgrid-scale models based on coherent structures for rotating homogeneous turbulence and turbulent channel flow". In: *Physics of Fluids* 17.4 (2005), p. 045104.

[128] H. Kobayashi, F. Ham, and X. Wu. "Application of a local SGS model based on coherent structures to complex geometries". In: *International Journal of Heat and Fluid Flow* 29.3 (2008). The Fifth International Symposium on Turbulence and Shear Flow Phenomena (TSFP5), pp. 640–653.

[129] J. F. Kok et al. "The physics of wind-blown sand and dust". In: *Reports on Progress in Physics* 75.10 (Sept. 2012), p. 106901.

[130] J. Kok and N. Renno. "A comprehensive numerical model of steady state saltation (COMSALT)". In: *Journal of Geophysical Research* 114 (2009).

[131] A. N. Kolmogorov. "The local structure of turbulence in incompressible viscous fluid for very large Reynolds numbers". In: *Dokl. Akad. Nauk SSSR*. Vol. 30. 4. 1941, pp. 299–303.

[132] A. Kubilay, J. Carmeliet, and D. Derome. "Computational fluid dynamics simulations of wind-driven rain on a mid-rise residential building with various types of facade details". In: *J Build Perform Simu* 10.2 (2017), pp. 125–143.

[133] A. Kubilay et al. "CFD simulation and validation of wind-driven rain on a building facade with an Eulerian multiphase model". In: *Build Environ* 61 (2013), pp. 69–81.

[134] A. Kubilay et al. "Numerical modeling of turbulent dispersion for wind-driven rain on building facades". In: *Environ Fluid Mech* 15.1 (2015), pp. 109–133.

[135] A. Kubilay et al. "Numerical simulations of wind-driven rain on an array of low-rise cubic buildings and validation by field measurements". In: *Build Environ* 81 (2014), pp. 283–295.

[136] A. Kubilay et al. "Wind-driven rain on two parallel wide buildings: field measurements and CFD simulations". In: *J Wind Eng Ind Aerod* 146 (2015), pp. 11–28.

[137] C. Kuttler. "On the competitive growth of two sand heaps". In: *Math. Methods Appl. Sci.* 26.17 (2003), pp. 1435–1449.

[138] D. Lakehal et al. "Eulero-Lagrangian simulation of raindrop trajectories and impacts within the urban canopy". In: *Atmospheric Environment* 29.23 (1995), pp. 3501–3517.

[139] Z. Li, Y. Wang, and Y. Zhang. "A numerical study of particle motion and two-phase interaction in aeolian sand transport using a coupled large eddy simulation - discrete element method". In: *Sedimentology* 61.2 (2014), pp. 319–332.

[140] Z. Li et al. "A Random Pairing Collision Model (RPCM) for Improving the DEM Simulation of Particle-Bed Collisions in Aeolian Sand Transport". In: *Particulate Science and Technology* 32 (2014), pp. 86–93.

[141] G. E. Liston, R. L. Brown, and J. D. Dent. "A two-dimensional computational model of turbulent atmospheric surface flows with drifting snow". In: *Ann Glaciol* 18 (1993), pp. 281–286.

[142] X. Liu and Z. Dong. "Experimental investigation of the concentration profile of a blowing sand cloud". In: *Geomorphology* 60.3 (June 2004), pp. 371–381.

[143] A. Lo Giudice and L. Preziosi. "A fully Eulerian multiphase model of wind-blown sand coupled with morphodynamic evolution: Erosion, transport, deposition, and avalanching". In: *Appl. Math. Model.* 79 (2020), pp. 68–84.

[144] A. Lo Giudice et al. "Modelling sand slides by a Mechanics-Based degenerate parabolic equation". In: *Math. Mech. Solids* 24 (2019), pp. 2558–2575.

[145] A. Lo Giudice et al. "Wind-blown particulate transport: A review of computational fluid dynamics models". In: *Mathematics in Engineering* 1.3 (July 2019), pp. 508–547.

[146] C. Y. Lo, M. Bolton, and Y. P. Cheng. "Discrete element simulation of granular column collapse". In: *AIP Conference Proceedings*. Vol. 1145. 1. American Institute of Physics. 2009, pp. 627–630.

[147] A. M. G. Lopes et al. "Numerical simulation of sand dune erosion". In: *Environ Fluid Mech* 13.2 (2013), pp. 145–168.

[148] G. Lube et al. "Axisymmetric collapses of granular columns". In: *Journal of Fluid Mechanics* 508 (2004), p. 175.

[149] G. Lube et al. "Collapses of two-dimensional granular columns". In: *Physical Review E* 72.4 (2005), p. 041301.

[150] G. Lube et al. "Granular column collapses down rough, inclined channels". In: *Journal of Fluid Mechanics* 675 (2011), p. 347.

[151] J. P. M. Lugo, R. L. Solorzano, and J. Curtis. "Numerical simulation of aeolian saltation within the sediment transport layer using Granular Kinetic Theory". In: *Revista de la Facultad de Ingenieria U.C.V.* 27.2 (2012), pp. 80–96.

[152] C. K. K. Lun and S. B. Savage. "A Simple Kinetic Theory for Granular Flow of Rough, Inelastic, Spherical Particles". In: *J. Appl. Mech.* 54.1 (Mar. 1987), pp. 47–53.

[153] C. K. K. Lun et al. "Kinetic theories for granular flow: inelastic particles in Couette flow and slightly inelastic particles in a general flowfield". In: *J. Fluid Mech.* 140 (Mar. 1984), pp. 223–256.

[154] C. W. Macosko. *Rheology: Principles, Measurements and Applications*. Wiley, 1994.

[155] J. P. Marval, R. L. R. Solórzano, and J. S. Curtis. "Two-dimensional numerical simulation of saltating particles using granular kinetic theory". In: *ASME/JSME 2007 5th Joint Fluids Engineering Conference*. American Society of Mechanical Engineers. 2007, pp. 929–939.

[156] F. R. Menter. "Two-equation eddy-viscosity turbulence models for engineering applications". In: *AIAA J* 32.8 (1994), pp. 1598–1605.

[157] F. R. Menter, M. Kuntz, and R. Langtry. "Ten years of industrial experience with the SST turbulence model". In: *Turbulence, heat and mass transfer* 4.1 (2003), pp. 625–632.

[158] F. R. Menter, M. Kuntz, and R. Langtry. "Ten Years of Industrial Experience with the SST Turbulence Model Turbulence heat and mass transfer". In: 4 (2003), pp. 625–632.

[159] A. Mochida and I. Lun. "Prediction of wind environment and thermal comfort at pedestrian level in urban area". In: *J Wind Eng Ind Aerod* 96.10-11 (2008), pp. 1498–1527.

[160] A. S. Monin and A. M. F. Obukhov. "Basic laws of turbulent mixing in the surface layer of the atmosphere". In: *Contrib. Geophys. Inst. Acad. Sci. USSR* 151 (1954), pp. 163–187.

[161] I. Moore. "Numerical modelling of blowing snow around buildings". PhD thesis. University of Leeds, 1995.

[162] I. Muller. "A new approach to thermodynamics of simple mixtures". In: *Zeitschrift fur Naturforschung A* 28.11 (1973), pp. 1801–1813.

[163] I. Muller. "A thermodynamic theory of mixtures of fluids". In: *Archive for Rational Mechanics and Analysis* 28.1 (1968), pp. 1–39.

[164] I. Muller. "Thermodynamics of mixtures of fluids". In: *J. Mécanique* 14.2 (1975), pp. 267–303.

[165] M. Naaim, N. F. Bouvet, and H. Martinez. "Numerical simulation of drifting snow: erosion and deposition models". In: *Ann Glaciol* 26 (1998), pp. 191–196.

[166] P. Nalpanis, J. C. R. Hunt, and C. F. Barrett. "Saltating particles over flat beds". In: *Journal of Fluid Mechanics* 251 (1993), pp. 661–685.

[167] N. Newmark. "A Method of Computation for Structural Dynamics". In: (1959).

[168] J. R. Ni, Z. S. Li, and C. Mendoza. "Vertical profiles of aeolian sand mass flux". In: *Geomorphology* 49.3-4 (2003), pp. 205–218.

[169] R. Nuca, A. Lo Giudice, and L. Preziosi. "Degenerate parabolic models for sand slides". In: *Applied Mathematical Modelling* 89 (2021), pp. 1627–1639.

[170] T. Okaze, H. Niiya, and K. Nishimura. "Development of a large-eddy simulation coupled with Lagrangian snow transport model". In: *J Wind Eng Ind Aerod* 183.Cryosphere 10 2016 (2018), pp. 35–43.

[171] T. Okaze et al. "Development of a new $\kappa\breve{}\epsilon$ model to reproduce the aerodynamic effects of snow particles on a flow field". In: *J Wind Eng Ind Aerod* 144 (2015), pp. 118–124.

[172] *OpenFOAM: User Guide: Implementation details*. [Online; accessed 16. Jul. 2020]. July 2020. URL: https://www.openfoam.com/documentation/guides/latest/doc/guide-schemes-laplacian-implementation-details.html.

[173] T. Pahtz and O. Durán. "Fluid forces or impacts: What governs the entrainment of soil particles in sediment transport mediated by a Newtonian fluid?" In: *arXiv: Geophysics* (2016).

[174] T. Pahtz et al. "The Physics of Sediment Transport Initiation, Cessation, and Entrainment Across Aeolian and Fluvial Environments". In: *Reviews of Geophysics* 58 (2020).

[175] E. J. R. Parteli et al. "Profile measurement and simulation of a transverse dune field in the Lençóis Maranhenses". In: *Geomorphology* 81.1-2 (2006), pp. 29–42.

[176] J. M. Pasini and J. T. Jenkins. "Aeolian transport with collisional suspension". In: *Philos T Roy Soc A* 363.1832 (July 2005), pp. 1625–1646.

[177] N. A. Patankar and D. D. Joseph. "Modeling and numerical simulation of particulate flows by the Eulerian–Lagrangian approach". In: *Int J Multiph Flow* 27.10 (2001), pp. 1659–1684.

[178] K. Pettersson et al. "Simulating wind-driven rain on building facades using Eulerian multiphase with rain phase turbulence model". In: *Build Environ* 106 (2016), pp. 1–9.

[179] M. Pischiutta, L. Formaggia, and F. Nobile. "Mathematical modelling for the evolution of aeolian dunes formed by a mixture of sands: entrainment-deposition formulation". In: *Communications in Applied and Industrial Mathematics* 2.2 (2011).

[180] J. W. Pomeroy and D. M. Gray. "Saltation of snow". In: *Water Resour Res* 26.7 (1990), pp. 1583–1594.

[181] M. C. Powers. "A new roundness scale for sedimentary particles". In: *Journal of Sedimentary Research* 23.2 (1953), pp. 117–119.

[182] L. Preziosi, D. Fransos, and L. Bruno. "A multiphase first order model for non-equilibrium sand erosion, transport and sedimentation". In: *Appl Math Lett* 45 (2015), pp. 69–75.

[183] L. Prigozhin. "Variational model of sandpile growth". In: *Eur. J. Appl. Math.* 7.3 (1996), pp. 225–235.

[184] L. Prigozhin and B. Zaltzman. "Two continuous models for the dynamics of sandpile surfaces". In: *Phys. Rev. E* 63 (2001), p. 041505.

[185] P. A. C. Raats and C. A. Truesdell. *Rational Thermodynamics*. 1984.

[186] L. Raffaele et al. "Windblown sand saltation: A statistical approach to fluid threshold shear velocity". In: *Aeolian Res.* 23 (Dec. 2016), pp. 79–91.

[187] L. Raffaele et al. "Windblown sand saltation: A statistical approach to fluid threshold shear velocity". In: *Aeolian Research* 23 (2016), pp. 79–91.

[188] K. R. Rajagopal and L. Tao. *Mechanics of mixtures*. Vol. 35. World scientific, 1995.

[189] K. R. Rajagopal, A. S. Wineman, and M. V. Gandhi. "On boundary conditions for a certain class of problems in mixture theory". In: *International Journal of Engineering Science* 24.8 (1986), pp. 1453–1463.

[190] K. R. Rasmussen and M. Sørensen. "Vertical variation of particle speed and flux density in aeolian saltation: Measurement and modeling". In: *Journal of Geophysical Research: Earth Surface* 113.2 (2008), pp. 1–12.

[191] P. J. Richards and S. E. Norris. "Appropriate boundary conditions for computational wind engineering models revisited". In: *J. Wind Eng. Ind. Aerodyn.* 99.4 (Apr. 2011), pp. 257–266.

[192] P. Sagaut. *Large eddy simulation for incompressible flows: an introduction*. Springer Science & Business Media, 2006.

[193] T. Sato et al. "Three dimensional numerical simulation of snowdrift". In: *Computational Wind Engineering 1*. Ed. by S. Murakami. Oxford: Elsevier, 1993, pp. 741–746. ISBN: 978-0-444-81688-7.

[194] G. Sauermann, K. Kroy, and H. J. Herrmann. "Continuum saltation model for sand dunes". In: 64.3 (2001), p. 031305.

[195] G. Sauermann et al. "Wind velocity and sand transport on a barchan dune". In: *Geomorphology* 54.3-4 (2003), pp. 245–255.

[196] SB Savage and K Hutter. "The motion of a finite mass of granular material down a rough incline". In: *J. Fluid Mech.* 199 (1989), pp. 177–215.

[197] H. Schlichting and K. Gersten. *Boundary-layer theory*. Springer, 2016.

[198] J. J. J. Shi, K. R. Rajagopal, and Alan S. Wineman. "Applications of the theory of interacting continua to the diffusion of a fluid through a non-linear elastic media". In: (1981).

[199] X. Shi, P. Xi, and J. Wu. "A lattice Boltzmann-Saltation model and its simulation of aeolian saltation at porous fences". In: *Theor Comp Fluid Dyn* 29.1-2 (2015), pp. 1–20.

[200] T. H. Shih et al. "A new k-ϵ eddy viscosity model for high reynolds number turbulent flows". In: *Comput Fluids* 24.3 (1995), pp. 227–238.

[201] J. Smagorinsky. "General circulation experiments with the primitive equations: I. The basic experiment". In: *Mon Weather Rev* 91.3 (1963), pp. 99–164.

[202] Catalin Stefan. *World Atlas of Sand*. 2020. URL: http://www.sand-atlas.com/en/.

[203] *Study on Sand Movement by Wind*. [Online; accessed 21. Mar. 2019]. 1951.

[204] Q. Sun, G. Wang, and Y. Xu. "DEM applications to aeolian sediment transport and impact process in saltation". In: *Particul Sci Technol* 19.4 (2001), pp. 339–353.

[205] X. Sun, R. He, and Y. Wu. "Numerical simulation of snowdrift on a membrane roof and the mechanical performance under snow loads". In: *Cold Reg Sci Technol* 150 (2018).

[206] P. A. Sundsbø. "Numerical simulations of wind deflection fins to control snow accumulation in building steps". In: *J Wind Eng Ind Aerod* 74 (1998), pp. 543–552.

[207] D. Surry et al. "Wind, rain and the building envelope: a status report of ongoing research at the University of Western Ontario". In: *Journal of Wind Engineering and Industrial Aerodynamics* 53.1-2 (1994), pp. 19–36.

[208] M. Syamlal and T. J. O Brien. "The derivation of a drag coefficient formula from velocity-voidage correlations". In: *Technical Note, US Department of energy, Office of Fossil Energy, NETL, Morgantown, WV* (1987).

[209] L. Tao and K. R. Rajagopal. "On boundary conditions in mixture theory". In: *Recent advances in elasticity and viscoelasticity* (1995), pp. 130–149.

[210] L. Tao, K. R. Rajagopal, and A. S. Wineman. "Unsteady diffusion of fluids through solids undergoing large deformations". In: *Mathematical Models and Methods in Applied Sciences* 1.03 (1991), pp. 311–346.

[211] T. K. Thiis. "A comparison of numerical simulations and full-scale measurements of snowdrifts around buildings". In: *Wind Struct* 3.2 (2000), pp. 73–81.

[212] E. L. Thompson and H. E. Huppert. "Granular column collapses: further experimental results". In: *Journal of Fluid Mechanics* 575 (2007), p. 177.

[213] Y. Tominaga, T. Okaze, and A. Mochida. "CFD modeling of snowdrift around a building: An overview of models and evaluation of a new approach". In: *Build Environ* 46.4 (2011), pp. 899–910.

[214] Y. Tominaga, T. Okaze, and A. Mochida. "Wind tunnel experiment and CFD analysis of sand erosion/deposition due to wind around an obstacle". In: *Journal of Wind Engineering and Industrial Aerodynamics* 182.September (Nov. 2018), pp. 262–271.

[215] D. Tong and N. Huang. "Numerical simulation of saltating particles in atmospheric boundary layer over flat bed and sand ripples". In: *J Geophys Res Atmos* 117.D16205 (2012).

[216] C. A. Truesdell. "Sulle basi della termodinamica II". In: *Atti Accad. Naz. Lincei: Rend. Sci. Fis. Mat. Nat* 22 (1957), pp. 33–38.

[217] T. Uematsu et al. "Three-dimensional numerical simulation of snowdrift". In: *Cold Reg Sci and Technol* 20.1 (1991), pp. 65–73.

[218] A. Valance and J. Crassous. "Granular medium impacted by a projectile: Experiment and model". In: *The European Physical Journal E* 30 (2009), pp. 43–54.

[219] A. Valance et al. "The physics of Aeolian sand transport". In: *Comptes Rendus Physique* 16.1 (2015), pp. 105–117.

[220] I. Vinkovic et al. "Large-eddy Simulation of the Dispersion of Solid Particles in a Turbulent Boundary Layer". In: *Boundary-layer Meteorol* 121.2 (2006), pp. 283–311.

[221] D. Wang et al. "Statistical analysis of sand grain/bed collision process recorded by high-speed digital camera". In: *Sedimentology* 55 (2008), pp. 461–470.

[222] H. T. Wang et al. "Experimental determination of saltating glass particle dispersion in a turbulent boundary layer". In: *Earth Surface Processes and Landforms* 31.14 (Dec. 2006), pp. 1746–1762.

[223] H. Wang, X. Hou, and Y. Deng. "Numerical simulations of wind-driven rain on building facades under various oblique winds based on Eulerian multiphase model". In: *J Wind Eng Ind Aerod* 142 (2015), pp. 82–92.

[224] C. Y. Wen and Y. H. Yu. "A generalized method for predicting the minimum fluidization velocity". In: *AIChE Journal* 12.3 (1966), pp. 610–612.

[225] B. T. Werner. "A Steady-State Model of Wind-Blown Sand Transport". In: *J Geology* 98.1 (1990), pp. 1–17.

[226] G. Wiggs et al. "Deliverable D3.4: Report on field tests of sand mitigation measure (SMM) designs". In: (July 2020).

[227] D. C. Wilcox. "Formulation of the k-ω Turbulence Model Revisited". In: *AIAA J* 46.11 (2008), pp. 2823–2838.

[228] D. C. Wilcox. "Reassessment of the scale-determining equation for advanced turbulence models". In: *AIAA J* 26.11 (1988), pp. 1299–1310.

[229] D. C. Wilcox. *Turbulence modeling for CFD*. Vol. 2. DCW industries La Canada, CA, 1998.

[230] F. Xiao et al. "Discrete particle simulation of mixed sand transport". In: *Particuology* 10.2 (2012), pp. 221–228.

[231] F. Xiao et al. "Sand particle lift-off velocity measurements and numerical simulation of mass flux distributions in a wind tunnel". In: *Journal of Arid Land* 9 (2017), pp. 331–344.

[232] M. Xing. "The harmonious character in equilibrium aeolian transport on mixed sand bed". In: *Geomorphology* 86.3-4 (2007), pp. 230–242.

[233] T. Xu and Y. C. Jin. "Modeling free-surface flows of granular column collapses using a mesh-free method". In: *Powder Technology* 291 (2016), pp. 20–34.

[234] V. Yakhot and S. A. Orszag. "Renormalization group analysis of turbulence. I. Basic theory". In: *J Sci Comput* 1.1 (1986), pp. 3–51.

[235] X. Yin et al. "Splash function for the collision of sand-sized particles onto an inclined granular bed, based on discrete-element-simulations". In: *Powder Technology* 378 (2021), pp. 348–358.

[236] C. You-Xing et al. "An Experimental Study on Splash Functions of Natural Sand-Bed Collision". In: *Journal of Geophysical Research* 124 (2019), pp. 7226–7235.

[237] W. Zhang, J. H. Kang, and S. J. Lee. "Visualization of saltating sand particle movement near a flat ground surface". In: *Journal of Visualization* 10 (2007), pp. 39–46.

[238] W. Zhang, Y. Wang, and S. J. Lee. "Two-phase measurements of wind and saltating sand in an atmospheric boundary layer". In: *Geomorphology* 88.1 (July 2007), pp. 109–119.

[239] X. Zhou et al. "3D numerical simulation of the evolutionary process of aeolian downsized crescent-shaped dunes". In: *Aeolian Res* 21 (2016), pp. 45–52.

[240] X. Zhou et al. "Numerical simulation and wind tunnel test for redistribution of snow on a flat roof". In: *J Wind Eng Ind Aerod* 153 (2016), pp. 92–105.

[241] X. Y. Zou et al. "The distribution of velocity and energy of saltating sand grains in a wind tunnel". In: *Geomorphology* 36.3-4 (2001), pp. 155–165.